PROTON COUPLED ELECTRON TRANSFER AND STRUCTURAL DYNAMICS IN BIOMIMETIC BETA HAIRPINS

A Dissertation
Presented to
The Academic Faculty

by

Tyler G. McCaslin

In Partial Fulfillment
of the Requirements for the Degree
Doctor of Philosophy in the
School of Chemistry and Biochemistry

Georgia Institute of Technology
May 2019

PROTON COUPLED ELECTRON TRANSFER AND STRUCTURAL DYNAMICS IN BIOMIMETIC BETA HAIRPINS

Approved by:

Dr. Bridgette A. Barry, Advisor
School of Chemistry and Biochemistry
Georgia Institute of Technology

Dr. John R. Reynolds
School of Chemistry and Biochemistry
Georgia Institute of Technology

Dr. David M. Collard
School of Chemistry and Biochemistry
Georgia Institute of Technology

Dr. Roger M. Wartell
School of Biological Sciences
Georgia Institute of Technology

Dr. Amit R. Reddi
School of Chemistry and Biochemistry
Georgia Institute of Technology

Date Approved: March 13, 2019

To the spirit of passing on what you have learned

ACKNOWLEDGEMENTS

First and foremost, I would like to thank my research advisor, Prof. Bridgette A. Barry. Her persistent advice to "be brave" has helped me overcome many technical challenges in scientific work. I am grateful to my thesis committee, Dr. David M. Collard, Dr. Amit R. Reddi, Dr. John R. Reynolds, and Dr. Roger M. Wartell, for their valuable insight, excellent questions, and careful guidance over my research career.

My colleagues in the Barry Lab have been a constant source of encouragement, scientific inquiry, and friendship throughout my time here. Dr. Cynthia Pagba was my mentor during the first few years of my graduate education experience. She taught me to be a careful scientist and a safe laser spectroscopist. Miranda McDaniel and Jiby Yohannan were incredibly talented undergraduate students who contributed to my projects. Dr. Udita Brahmachari, Dr. Jiafeng "Jeff" Geng, Dr. Zhanjun Guo, Jiayuan "Nancy" He, Sara Konecny, Emmanuela "Chichi" Obi, Dr. Adam Offenbacher, Dr. Brandon Polander, Dr. Yusuf Uddin and Dr. Ryan "Atlee" Watson were memorable scientific companions and I will cherish the experiences I shared with them.

TABLE OF CONTENTS

LIST OF TABLES

LIST OF FIGURES

LIST OF SYMBOLS AND ABBREVIATIONS

Å	angstrom
Abs	absorbance
AU	absorbance unit
CAPS	*N*-cyclohexyl-3-aminopropanesulfonic acid
EPR	electron paramagnetic resonance
HEPES	2-[4-(2-hydroxyethyl)piperazin-1-yl]ethanesulfonic acid
Hst5	histatin-5
MES	2-(*N*-morpholino)ethanesulfonic acid
PSII	photosystem II
RNR	ribonucleotide reductase
UV	ultraviolet
UVRR	ultraviolet resonance Raman
W48	tryptophan 48 of the beta subunit of *E coli* RNR
Y122	tyrosine 122 of the beta subunit of *E. coli* RNR
YD	tyrosine 160 of the D2 polypeptide in PSII
YZ	tyrosine 161 of the D1 polypepide in PSII

Additional abbreviations are explained in the text.

SUMMARY

Several crucial proteins required for the maintenance of life on earth utilize the potent oxidant of tyrosyl radical in their catalytic mechanism. This free radical species can have devastating effects, yet nature has crafted ways to control its reactivity. The means by which the thermodynamics and kinetics of proton-coupled electron transfer reactions of tyrosine and tryptophan are tuned is of profound importance. By utilizing biologically-inspired peptide-based model systems, or maquettes, one can measure the effect of the surrounding protein environment on the reactivity of tyrosyl radicals and redox-linked conformational changes that result from electron transfer and proton-coupled electron transfer. This work utilizes a wide variety of spectroscopic, electrochemical, and computational tools to characterize these reactions in a library of biomimetic peptide models. Factors of control of tyrosine-mediated electron transfer (including electronic coupling to the peptide backbone, proton coupling, aromatic-aromatic interactions, and metal-ion effects) will be investigated. Elucidating the mechanisms of controlling these radicals will inform the design of catalytic devices towards the goal of artificial solar energy conversion.

CHAPTER 1. INTRODUCTION

1.1 Proton-Coupled Electron Transfer (PCET)

1.1.1 Biological Electron Transfer (ET) and PCET Reactions

Electron transfer (ET) is a crucial biochemical process utilized by a number of enzymes required to sustain life. One prototypical example of biological ET is photosynthetic oxygen evolution, where several, light-driven redox reactions are coupled to convert water into molecular oxygen by the multi-subunit enzyme photosystem II (PSII).[1-3] In the process of DNA synthesis and repair, long-distance PCET reactions drive the turnover of ribonucleotides to deoxyribonucleotides in the heterodimeric protein ribonucleotide reducatase (RNR).[4-5] Aromatic amino acid radicals within these proteins facilitate these ET or proton-coupled electron transfer (PCET) reactions.[6-8]

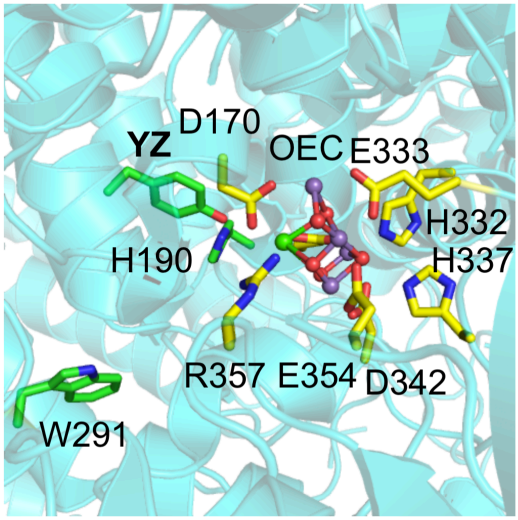

Figure 1.1 PSII oxygen evolving complex and YZ, PDB 4UB6[9]

In the case of photosystem II, the absorption of light by accessory chlorophylls generates a potent oxidant, P_{680}^{+}, which thereby oxidizes a critical tyrosine residue, YZ (Figure 1.1).[8, 10] This essential amino acid residue[7] is responsible for sequentially oxidizing a manganese-calcium-oxygen cluster (oxygen evolving complex, OEC)[9, 11] in a stepwise process. After four oxidation steps, molecular oxygen is generated from the oxidation of water.[12]

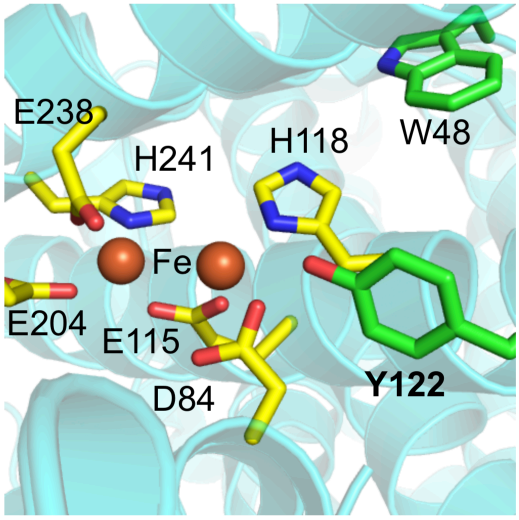

Figure 1.2 RNR β subunit di-iron cluster and Y122, PDB 1MXR[13]

For ribonucleotide reductase, a stable tyrosyl radical ($Y122O\cdot$)[6] is generated by a di-iron cluster[14] (Figure 1.2). This tightly regulated enzyme undergoes PCET over 35 Å, across a subunit interface facilitated by $Y122O\cdot$.[5] Along this PCET pathway, several additional tyrosine residues transfer this hole to an active site cysteine (C439) residue where reduction of the ribonucleotides to deoxyribonucleotides occurs.[5]

The exquisite control of these highly reactive aromatic amino acid radical species by the surrounding protein matrix is a profound observation. This work seeks to understand the mechanisms by which these high potential reactions are performed in biology and the

means by which these proteins have evolved to be protected from deleterious side reactions involving these intermediates. With a better understanding of how such powerful redox chemistry is controlled, this work may inform design strategies for the development of catalytic devices.

1.1.2 PCET of Aromatic Amino Acids As Models of Biological Electron Transfer

When considering PCET reactions of tyrosine, three possibilities arise concerning the transfer of an electron and/or proton from the phenol side chain (Figure 1.3). In one case, the deprotonation of tyrosine can occur first to produce tyrosinate. The pK_a of tyrosine is approximately 10.[15] Tyrosinate can then undergo electron transfer (~0.7 V vs NHE)[16] to form neutral tyrosyl radical. This process is referred to PTET, or the stepwise process of proton transfer followed by electron transfer. In another case, tyrosine can undergo electron transfer (~1.2 V vs NHE)[16] to produce tyrosyl radical cation. This radical cation has a pK_a below zero,[17] and thus proton transfer can follow to, again, form neutral tyrosyl radical. The stepwise process of electron transfer followed by proton transfer is termed ETPT. The estimation of the pK_a of the tyrosyl radical cation results in approximately 5 kcal/mol difference in energy of the PTET and ETPT paths in the square scheme in Figure 1.3, which should be equal[18-19] using an estimation of bond dissociation energy. It should be noted that the stepwise transfer of either proton or electron from tyrosine results in the generation of relatively high energy intermediates that are less likely to be prevalent under biological conditions. In either case, the biologically relevant radical is neutral.[20] One way to avoid such high energy intermediates is the concerted transfer of protons and electrons, CPET. This coupled process of a proton and an electron being transferred in one step is one

mechanism by which biology can access the power of neutral tyrosyl radical under mild conditions, though at a kinetic cost.[21]

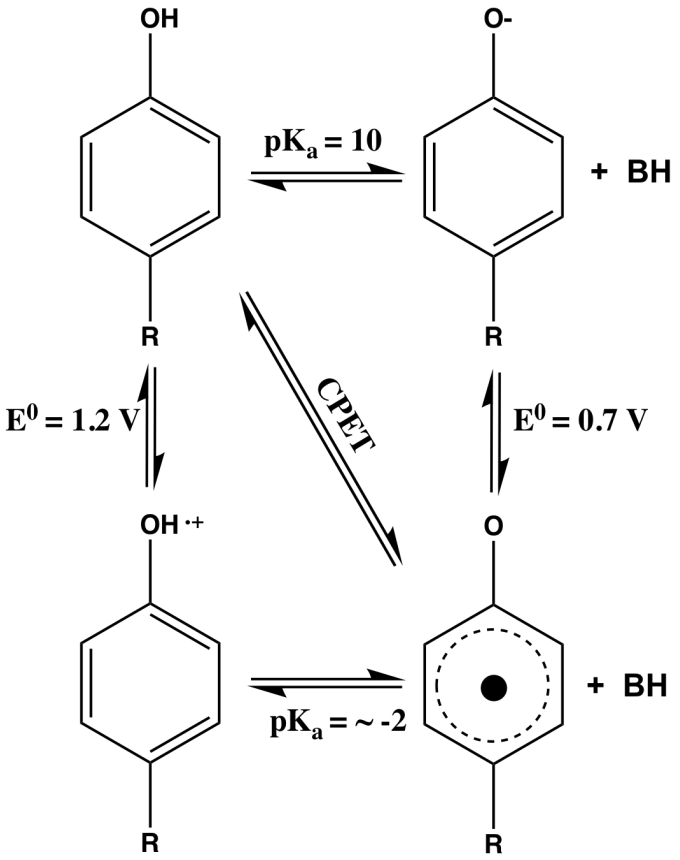

Figure 1.3 PCET scheme of tyrosine

Marcus Theory can predict the rate (Equation 1.1) of electron transfer.[22-23] The rate of electron transfer (k_{ET}) is governed by the driving force (ΔG°), reorganization energy (λ), the electronic coupling (V_{DA}) between the donor (D) and acceptor (A), the Boltzmann constant (k_B) and temperature (T). The magnitude of electronic coupling[24] (Equation 1.2) is distance-dependent between the donor and acceptor (R_{DA}). The protein matrix can modulate this donor-acceptor interaction and is represented with a decay factor (β).[22-24]

$|V_0|^2$ is defined as the maximum electronic coupling between the donor and acceptor wavefunctions. Marcus-like treatments have been used to understand PCET.[21, 25]

$$k_{ET} = \{[\pi/(\hbar^2 \lambda k_B T)]\}^{-1/2} |V_{DA}|^2 \, e^{-(\Delta G^\circ + \lambda)\hat{}2 \, / \, 4\lambda k_B T} \quad (1.1)$$

$$|V_{DA}|^2 = |V_0|^2 \, e^{-\beta R_{DA}} \quad (1.2)$$

1.2 Biomimetics

1.2.1 Protein Design

Broadly, protein design can be viewed in two contexts. One can redesign existing proteins to add new functionality or expand substrate scope.[26] On the other hand, one can explore *de novo* design and engineer a three-dimensional protein motif from first principles.[26] *De novo* protein design is capable of elucidating structure-function relationships as models of existing enzymes.[26]

1.2.2 Biomimetic Peptides

In this work, a spontaneously folding beta hairpin peptide library[27-34] is investigated. This library is designed to study the influence of non-covalent interactions on aromatic amino acids, tyrosine and tryptophan, and their corresponding radicals as well as metal-binding interactions on conformation. The parent peptide sequence is Peptide A (Figure 1.4).[27-28] Peptide A is an 18-mer beta hairpin that spontaneously folds and reversibly melts. The sequence contains two salt bridges, D3-R16 and R8-D11, and a turn promoter, N-G,

in the center of the strand.[27] In the core of the beta hairpin is Y5, which upon oxidation, engages in PCET across strand with H14 in the mid-pH range.[27-28] Sequence variants of Peptide A are characterized in this work through a variety of spectroscopic techniques.

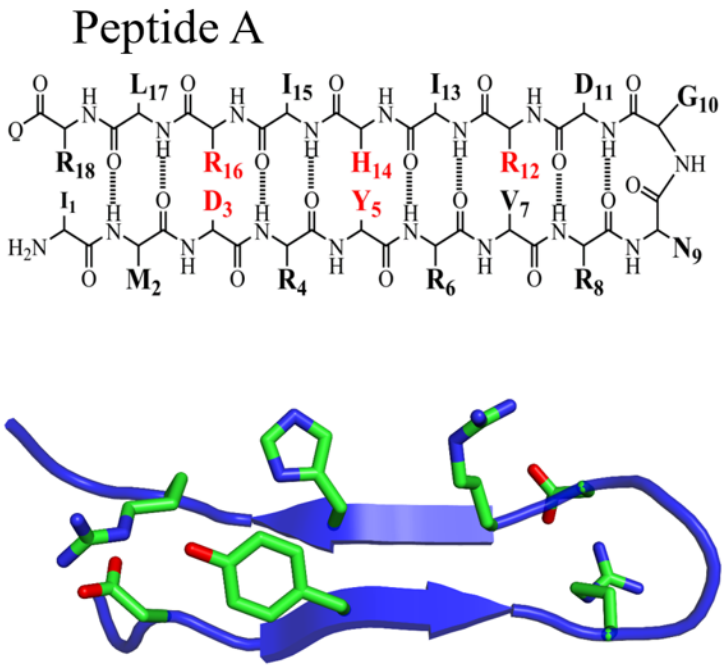

Figure 1.4 Sequence and secondary structure of Peptide A

1.3 UV Resonance Raman (UVRR) Spectroscopy

UV Resonance Raman spectroscopy is a vibrational spectroscopic technique that is complementary to infrared spectroscopy. This incisive method can probe non-covalent interactions and elucidate differences with high resolution.[35] Changes in redox state, hydrogen-bonding, or metal binding can influence the analyte spectrum. This work utilizes a laser wavelength on resonance with the UV absorbance of the aromatic amino acids within this peptide library. This is advantageous as the vibrational modes of aromatic amino acids are resonantly enhanced.[35] Additionally, to prevent UV degradation of the

analyte, a microcell device recirculates the aqueous peptide sample into a focused jet incident with the UV probe beam.[36] At 244 nm, using the second harmonic of a continuous wave Ar-ion laser, low background fluorescence and weak Raman scattering from water allows one to utilize difference spectroscopy to probe aforementioned interactions.[36-38] In this work, at high pH and high laser power, tyrosine/tyrosinate photolysis can be induced (Figure 1.5) and compared to a low power probe of the singlet state.[30]

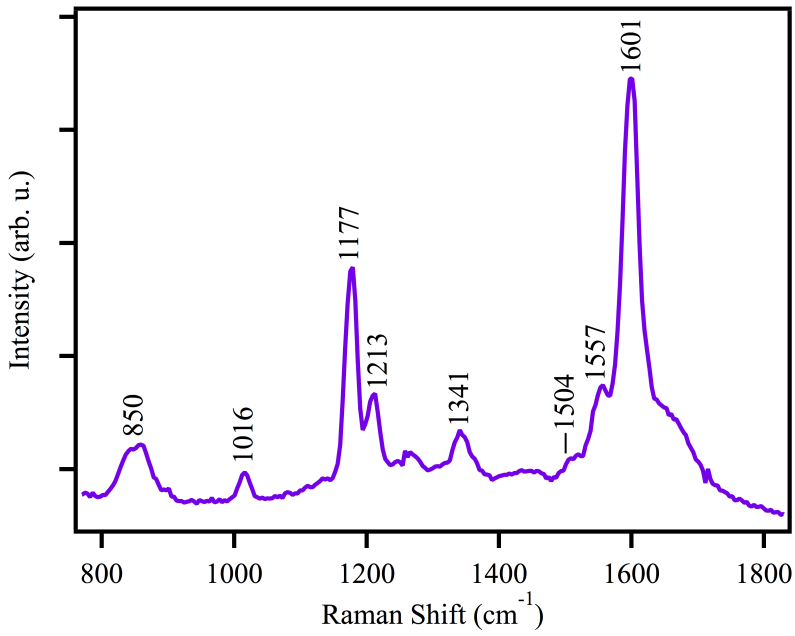

Figure 1.5 Representative high power UVRR spectrum of Peptide M at pH 11

1.4 Electron Paramagnetic Resonance (EPR) Spectroscopy

EPR spectroscopy is a powerful magnetic resonance technique for studying protein radicals.[39] In a magnetic field, the absorption of microwave light by paramagnetic species can be measured. In this work, spin ½ radicals are generated by UV photolysis using the fourth harmonic of a pulsed NdYAG laser source. At low temperature and in frozen aqueous solution using prior methods,[27] the EPR spectrum of aromatic amino acid radicals

can be measured. [20, 40] This spectrum (Figure 1.6) is influenced by coupling of the unpaired electron with nearby nuclei and is distinct between tyrosine and tryptophan and amongst different pH conditions. Perturbations of the radical environment can yield differences in intensity, lineshape, or g-value.[39]

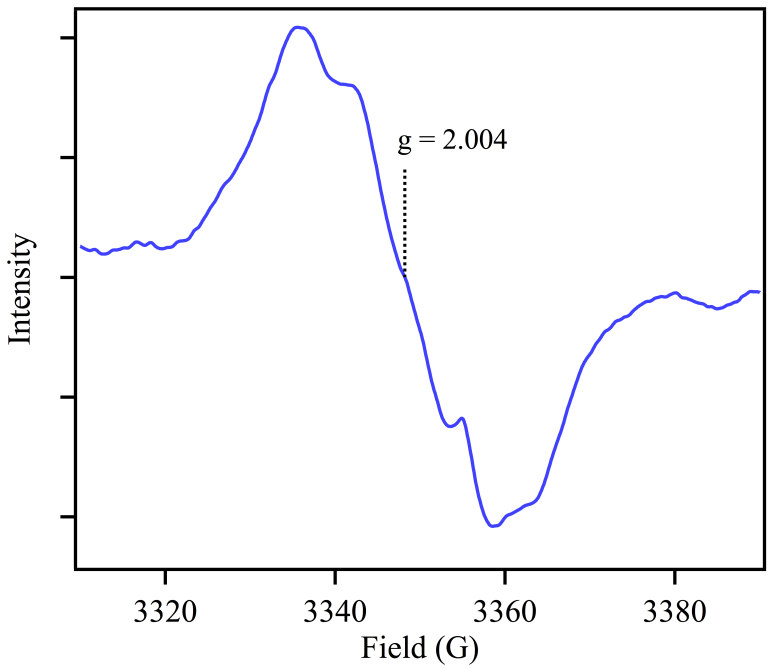

Figure 1.6 Representative EPR spectrum of tyrosine at pH 9

1.5 Transient Absorption Spectroscopy (TRAS)

Transient absorption spectroscopy, or time-resolved absorbance spectroscopy, operates on a pump-probe basis and, in this work adapted from prior methods[41], is capable of measuring picosecond kinetics of the decay of photogenerated radicals and excited states of tyrosine[31-32] and tryptophan. A regeneratively-amplified Ti:Sapphire laser provides the source of the pump beam as well as the probe beam (Figure 1.7). The majority of the 800 nm laser output is guided into an optical parametric amplifier (OPA) as the pumping

source. The fourth harmonic of the OPA is generated as 280 nm (referred to as pump beam). Less than 5% of the original 800 nm beam is directed to a mechanical delay stage to offset the beam in both space and therefore time. This delayed beam is focused onto a CaF_2 crystal to generate a white light continuum (WLC, 350-750 nm) and is focused on the sample (referred to as probe beam). The sample is flashed with the pump beam and then with the probe beam and the light is collected via a fiber optic cable lead to a CMOS sensor . The use of a chopper allows data acquisition with and without the 280 nm pump beam and a difference spectrum is generated to display the transient spectra (represented as Delta Absorbance or Delta Optical Density). With each time point collected, the mechanical delay stage is moved to elongate the beam path, thus separating the pump and probe beams in time. To prevent UV degradation of the samples, a magnetic stir bar was utilized within the cuvette.

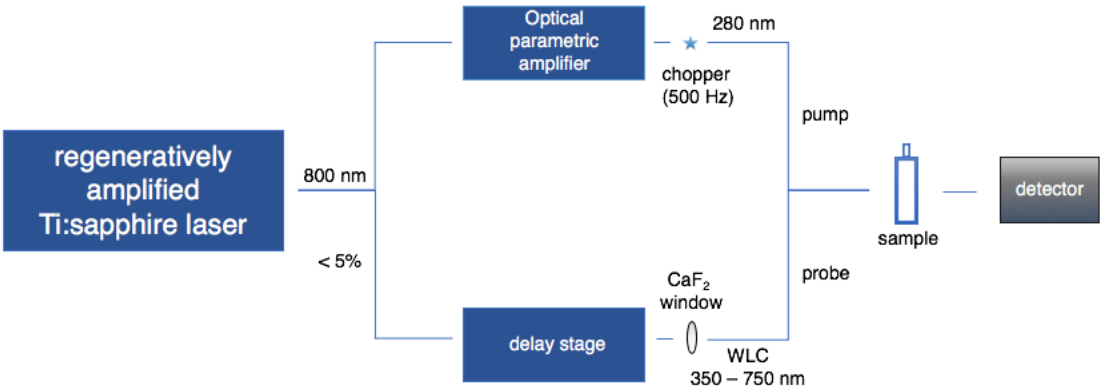

Figure 1.7 Schematic of TRAS instrument

1.6 Overview of Thesis

In Chapter 2[32], the picosecond kinetics of the formation decay of photogenerated tyrosyl radicals and tyrosine/tyrosinate excited states in tyrosine-containing, PSII-inspired, beta hairpin peptides were measured using TRAS. The absorption of tyrosyl radical was monitored at 410 nm, S_1 excited state of tyrosine/tyrosinate was monitored at 520 nm, and the solvated electron was monitored at 650 nm. Three models were compared: aqueous tyrosine/tyrosinate, Peptide A, and Peptide C. Peptide A was engineered with a Y5 – H14 cross strand interaction that can conduct PCET in the mid-pH range. Peptide C is a H14Cha mutant of the Peptide A sequence and cyclohexylalanine (Cha) is not capable of conducting PCET with Y5. Both electron transfer (pL 11) and proton-coupled electron transfer (pL 9) were accelerated compared to model tyrosinate/tyrosine. This was interpreted as increased electronic coupling by the peptide backbone to rationalize the increase in ET and PCET rate. D_2O exchange did not significantly alter the rates, thus there was no significant solvent isotope effect measured in the peptides. At pL 9, the PCET rate was decreased upon H14Cha mutation suggesting that Cha increases the reorganization energy of the reaction. In PSII, a non-essential, but long-lived tyrosyl radical, YD, is hydrogen-bonded to H189. Mutations at H189 have been shown to decrease the rate of YD• decay. The alterations of decay kinetics in mutants of Peptide A are reminiscent of YD in PSII and suggest that H189 mutations can alter the reorganization energy and thus decrease the CPET rate of YD.

In Chapter 3[29], prior UVRR studies of Peptide A and Peptide C were shown to undergo conformational changes taking place upon oxidation of tyrosine. Characteristic changes in the UVRR difference spectra of the peptides were observed in the amide II' region in different redox states of tyrosine. These bands were previously attributed to a reversible conformational change in the peptide backbone secondary structure. Molecular

dynamics simulations of Peptide A and Peptide C investigated three different charge states of Y5: tyrosine (YH), tyrosinate (Y-), and neutral tyrosyl radical (Y•). The simulations revealed that Peptide A-YH and Peptide A-Y- states retained the beta hairpin secondary structure and maintained Y5-H14 non-covalent interactions, while the Peptide A-Y• state was unstable and lead to an unfolding of the peptide. In the simulations of Peptide C, both Peptide C-Y- and Peptide C-Y• were unstable. These results suggest the Y5-H14 π-π interaction stabilize the secondary structure of Peptide A-Y•. The simulations were consistent with the UVRR experiments.

In Chapter 4[33], a beta hairpin peptide, Peptide M, was characterized as a model of RNR Y122O• and W48. In Peptide M, a cross-strand interaction between Y5 and W14 was engineered into the parent Peptide A sequence as a tyrosine-tryoptophan dyad. The NMR structure of Peptide M indicates that no direct hydrogen bond exists between the phenol (Y5) and indole (W14) rings. Electronic coupling between Y5 and W14 was detected. Additionally, downshifted ring and C-O UVRR frequencies were measured in the radical state of Peptide M. Peptide M is the first model to account for similarly downshifted bands in the UVRR spectrum of the RNR β2 subunit. These results are consistent with charge transfer from tyrosyl radical to tryptophan or another nearby residue and implies a role for the Y-W dyad in RNR electron transfer.

In Chapter 5, the Y-W dyad in Peptide M was further investigated. A hypochromic effect in the UV absorbance of Peptide M and an excitonic coupling signal were observed in the peptide. Spectral shifts in the singlet, excited (W*) and fluorescence emission spectrum were observed. A sequence variant of Peptide M was engineered, Peptide MW,

whereby the Y5-W13 dyad was formed diagonally across the strand as a perturbation of the Y5-W14 dyad of Peptide M. This sequence variation distorts the backbone of Peptide MW in MD simulations. Picosecond decay of W* was measured using TRAS and is similar in the peptides, but accelerated compared to aqueous amino acid solutions. Alterations of the Peptide MW W* transient spectra are consistent with increased conformational flexibility of the peptide. EPR spectra of Peptide M and Peptide MW following UV photolysis reveal the formation of tyrosyl and tryptophan radical species at 160 K. The radical photolysis yield is decreased in Peptide M and Peptide MW at pH 9 compared to aqueous amino acid controls. This protective effect is not observed at pH 11, nor in peptide sequences lacking the YW dyad. The protective effect by the dyad is attributed to an increase in the recombination rate of the radical and solvated electron and is facilitated by hydrogen-bonding interactions in the peptide. These interactions lower the barrier for PCET at pH 9. These results suggest more broadly that YW dyads in oxidoreductases may promote radical quenching under oxidative stress.

In Chapter 6, histatin-5 (Hst5), a salivary immune peptide was characterized spectroscopically. Hst5 is an intrinsically disordered, antimicrobial protein capable of binding zinc, copper, and nickel. Intrinsically disordered proteins are inherently challenging to study as their structures adopt an ensemble of conformations in solution. Hst5 is disordered in aqueous solution and adopts a helical conformation in non-aqueous solvent. UVRR and CD spectroscopy detect metal-binding interactions in Hst5. Characteristic UVRR shifts of histidine vibrational modes confirm the binding of zinc. Upon binding of zinc, nearby tyrosine ring modes are downshifted indicating a pK_a shift. Zinc and copper binding in Hst5 is perturbed in the H18A/H19A mutant as measured by

CD and UVRR spectroscopy. Hst5 H18A/H19A has been shown to reduce antifungal activity. Sequence variants of Peptide A were engineered with zinc binding sites inspired by Hst5 and reproduce similar spectroscopic characteristics of metal-protein interactions. This work illustrates that a combination of spectroscopic techniques identifies low affinity metal-binding in disordered peptides and suggest a role of zinc in the antimicrobial properties of Hst5.

1.7 References

1. McEvoy, J. P.; Brudvig, G. W. Water-Splitting Chemistry of Photosystem Ii. *Chem. Rev.* **2006,** *106*, 4455-4483.

2. Shen, J.-R. The Structure of Photosystem Ii and the Mechanism of Water Oxidation in Photosynthesis. *Annual Review of Plant Biology* **2015,** *66*, 23-48.

3. Vinyard, D. J.; Ananyev, G. M.; Dismukes, G. C. Photosystem Ii: The Reaction Center of Oxygenic Photosynthesis. *Annual Review of Biochemistry* **2013,** *82*, 577-606.

4. Nordlund, P.; Reichard, P. Ribonucleotide Reductases. *Ann. Rev. Biochem.* **2006,** *75*, 681-706.

5. Minnihan, E. C.; Nocera, D. G.; Stubbe, J. Reversible, Long-Range Radical Transfer in *E. Coli* Class Ia Ribonucleotide Reductase. *Acc. Chem. Res.* **2013,** *46*, 2524-35.

6. Sjoberg, B.-M.; Reichard, P.; Graslund, A.; Ehrenberg, A. The Tyrosine Free Radical in Ribonucleotide Reductase from *Escherichia Coli*. *J. Biol. Chem.* **1978,** *253*, 6863-6865.

7. Barry, B. A.; Babcock, G. T. Tyrosine Radicals Are Involved in the Photosynthetic Oxygen-Evolving System. *Proc. Nat. Acad. Sci. USA* **1987,** *84*, 7099-7103.

8. Boerner, R. J.; Barry, B. A. Isotopic Labeling and Epr Spectroscopy Show That a Tyrosine Residue Is the Terminal Electron Donor, Z, in Manganese-Depleted Photosystem Ii Preparations. *J. Biol. Chem.* **1993,** *268*, 17151-17154.

9. Suga, M.; Akita, F.; Hirata, K.; Ueno, G.; Murakami, H.; Nakajima, Y.; Shimizu, T.; Yamashita, K.; Yamamoto, M.; Ago, H., et al. Native Structure of Photosystem Ii at 1.95 a Resolution Viewed by Femtosecond X-Ray Pulses. *Nature* **2015,** *517*, 99-103.

10. Barry, B. A. The Role of Redox Active Amino Acids in the Photosynthetic Water-Oxidizing Complex. *Photochemistry and Photobiology* **1993,** *57*, 179-188.

11. Umena, Y.; Kawakami, K.; Shen, J.-R.; Kamiya, N. Crystal Structure of Oxygen-Evolving Photosystem Ii at a Resolution of 1.9 Angstrom. *Nature* **2011,** *473*, 55-60.

12. Kok, B.; Forbush, B.; McGloin, M. Cooperation of Charges in Photosynthetic O2 Evolution–I. A Linear Four Step Mechanism. *Photochemistry and Photobiology* **1970,** *11*, 457-475.

13. Högbom, M.; Galander, M.; Andersson, M.; Kolberg, M.; Hofbauer, W.; Lassmann, G.; Nordlund, P.; Lendzlan, F. Displacement of the Tryosyl Radical Cofactor in Ribonucleotide Reductase Obtained by Single-Crystal High-Field Epr and 1.4-a X-Ray Data. *Proc. Nat. Acad. Sci. USA* **2003,** *100*, 3209-3214.

14. BollingerJr., J. M.; Edmondson, D. E.; Huynh, B. H.; Filley, J.; Norton, J. R.; Stubbe, J. Mechanism of Assembly of the Tyrosyl Radical-Dinuclear Iron Cluster Cofactor of Ribonucleotide Reductase. *Science* **1991,** *253*, 292-298.

15. Edsall, J. T.; Martin, R. B.; Hollingworth, B. R. Ionization of Individual Groups in Dibasic Acids, with Application to the Amino and Hydroxyl Groups of Tyrosine *Proc. Natl. Acad. Sci. USA* **1958,** *44*, 505-519.

16. Harriman, A. Further Comments on the Redox Potentials of Tryptophan and Tyrosine. *J. Phys. Chem.* **1987,** *91*, 6102-6104.

17. Dixon, W. T.; Murphy, D. Determination of the Acidity Constants of Some Phenol Radical Cations by Means of Electron Spin Resonance. *J. Chem. Soc. London, Faraday Trans. II* **1976,** *72*, 1221-1230.

18. Mayer, J. M.; Rhile, I. J. Thermodynamics and Kinetics of Proton-Coupled Electron Transfer: Stepwise Vs. Concerted Pathways. *Biochim Biophys Acta* **2004,** *1655*, 51-8.

19. Mayer, J. M. Proton-Coupled Electron Transfer: A Reaction Chemist's View. *Ann. Rev. Phys. Chem.* **2004,** *55*, 363-90.

20. Barry, B. A.; El-Deeb, M. K.; Sandusky, P. O.; Babcock, G. T. Tyrosine Radicals in Photosystem Ii and Related Model Compounds. *J. Biol. Chem.* **1990,** *265*, 20139-20143.

21. Rhile, I. J.; Markle, T. F.; Nagao, H.; DiPasquale, A. G.; Lam, O. P.; Lockwood, M. A.; Rotter, K.; Mayer, J. M. Concerted Proton-Electron Transfer in the Oxidation of Hydrogen Bonded Phenols. *J. Am. Chem. Soc.* **2006,** *128*, 6075-6088.

22. Dempsey, J. L.; Winkler, J. R.; Gray, H. B. Proton-Coupled Electron Flow in Protein Redox Machines. *Chem. Rev.* **2010,** *110*, 7024-39.

23. Marcus, R. A. Electron Transfer Reactions in Chemistry: Theory and Experiment. *Pure Appl. Chem.* **1997,** *69*, 13-29.

24. Moser, C. C.; Keske, J. M.; Warncke, K.; Farid, R. S.; Dutton, P. L. Nature of Biological Electron Transfer. *Nature* **1992,** *355*, 796-802.

25. Mayer, J. M. A Simple Marcus-Theory Type Model for Hydrogen Atom Transfer/Proton-Coupled Electron Transfer. *J .Phys. Chem. Lett.* **2011,** *2*, 1481-1489.

26. Yu, F.; Cangelosi, V. M.; Zastrow, M. L.; Tegoni, M.; Plegaria, J. S.; Tebo, A. G.; Mocny, C. S.; Ruckthong, L.; Qayyum, H.; Pecoraro, V. L. Protein Design: Toward Functional Metalloenzymes. *Chemical Reviews* **2014,** *114*, 3495-3578.

27. Sibert, R.; Josowicz, M.; Porcelli, F.; Veglia, G.; Range, K.; Barry, B. A. Proton-Coupled Electron Transfer in a Biomimetic Peptide as a Model of Enzyme Regulatory Mechanisms. *J Am Chem Soc* **2007,** *129*, 4393-400.

28. Sibert, R. S.; Josowicz, M.; Barry, B. A. Control of Proton and Electron Transfer in De Novo Designed, Biomimetic Beta Hairpins. *ACS Chem Biol* **2010,** *5*, 1157-68.

29. Hwang, H.; Tyler G. McCaslin; Pagba, C. V.; Nevin, C. M.; Pavlova, A.; Barry, B. A.; Gumbart, J. C. Redox-Driven Conformational Dynamics in a Photosystem-Ii-Inspired B-Hairpin Maquette Determined through Spectroscopy and Simulation. *J. Phys. Chem. B* **2017,** *121*, 3536-3545.

30. Pagba, C. V.; Barry, B. A. Redox-Induced Conformational Switching in Photosystem-Ii-Inspired Biomimetic Peptides: A Uv Resonance Raman Study. *J. Phys. Chem. B* **2012,** *116*, 10590-9.

31. Pagba, C. V.; Chi, S. H.; Perry, J.; Barry, B. A. Proton-Coupled Electron Transfer in Tyrosine and a Beta-Hairpin Maquette: Reaction Dynamics on the Picosecond Time Scale. *J Phys Chem B* **2015,** *119*, 2726-36.

32. Pagba, C. V.; McCaslin, T. G.; Chi, S. H.; Perry, J. W.; Barry, B. A. Proton-Coupled Electron Transfer and a Tyrosine-Histidine Pair in a Photosystem Ii-Inspired Beta-Hairpin Maquette: Kinetics on the Picosecond Time Scale. *J Phys Chem B* **2016,** *120*, 1259-72.

33. Pagba, C. V.; McCaslin, T. G.; Veglia, G.; Porcelli, F.; Yohannan, J.; Guo, Z.; McDaniel, M.; Barry, B. A. A Tyrosine-Tryptophan Dyad and Radical-Based Charge Transfer in a Ribonucleotide Reductase-Inspired Maquette. *Nature Comm.* **2015,** *10010*.

34. Barry, B. A.; Chen, J.; Keough, J.; Jenson, D. L.; Offenbacher, A. R.; Pagba, C. V. Proton Coupled Electron Transfer and Redox Active Tyrosines: Structure and Function of the Tyrosyl Radicals in Ribonucleotide Reductase and Photosystem Ii. *J. Phys. Chem. Lett.* **2012,** *3*, 543-554.

35. Oladepo, S. A.; Xiong, K.; Hong, Z.; Asher, S. A. Elucidating Peptide and Protein Structure and Dynamics: Uv Resonance Raman Spectroscopy. *J. Phys. Chem. Lett.* **2011,** *2*, 334-344.

36. Chen, J.; Barry, B. Ultraviolet Resonance Raman Microprobe Spectroscopy of Photosystem Ii. *Photochem. Photobiol.* **2008,** *84*, 815-818.

37. Chen, J.; Bender, S. L.; Keough, J. M.; Barry, B. A. Tryptophan as a Probe of Photosystem I Electron Transfer Reactions: A Uv Resonance Raman Study. *J. Phys. Chem. B Letters* **2009,** *113*, 11367-11370.

38. Offenbacher, A. R.; Chen, J.; Barry, B. A. Perturbations of Aromatic Amino Acids Are Associated with Iron Cluster Assembly in Ribonucleotide Reductase. *J. Am. Chem. Soc.* **2011,** *133*, 6978-88.

39. Jeschke, G. Epr Techniques for Studying Radical Enzymes. *Biochimica et Biophysica Acta (BBA) - Bioenergetics* **2005,** *1707*, 91-102.

40. Stoll, S.; Shafaat, H. S.; Krzystek, J.; Ozarowski, A.; Tauber, M. J.; Kim, J. E.; Britt, R. D. Hydrogen Bonding of Tryptophan Radicals Revealed by Epr at 700 Ghz. *J Am Chem Soc* **2011,** *133*, 18098-101.

41. Chaudhry, A. F.; Verma, M.; Morgan, M. T.; Henary, M. M.; Siegel, N.; Hales, J. M.; Perry, J. W.; Fahrni, C. J. Kinetically Controlled Photoinduced Electron Transfer Switching in Cu (I)-Responsive Fluorescent Probes. *Journal of the American Chemical Society* **2009,** *132*, 737-747.

CHAPTER 2. PROTON-COUPLED ELECTRON TRANSFER AND A TYROSINE-HISTIDINE PAIR IN A PHOTOSYSTEM II-INSPIRED β-HAIRPIN: KINETICS ON THE PICOSECOND TIME SCALE

Reprinted with permission from *The Journal of Physical Chemistry B*

Pagba, C. V.; McCaslin, T. G.; Chi, S- H.; Perry, J. W.; Barry, B. A. Proton-Coupled Electron Transfer and a Tyrosine-Histidine Pair in a Photosystem II-Inspired β-Hairpin Maquette. *J. Phys. Chem. B* **2016**, *120*, 1259-1272

2.1 Abstract

Photosystem II (PSII) and ribonucleotide reductase employ oxidation and reduction of the tyrosine aromatic ring in radical transport pathways. Tyrosine-based reactions involve either proton-coupled electron transfer (PCET) or electron transfer (ET) alone, depending on the pH and the pKa of tyrosine's phenolic oxygen. In PSII, a subset of the PCET reactions are mediated by a tyrosine–histidine redox-driven proton relay, YD His189. Peptide A is a PSII- inspired β-hairpin, which contains a single tyrosine (Y5) and histidine (H14). Previous electrochemical characterization indicated that Peptide A conducts a net PCET reaction between Y5 and H14, which have a cross-strand π–π interaction. The kinetic impact of H14 has not yet been explored. Here, we address this question through time-resolved absorption spectroscopy and 280-nm photolysis, which generates a neutral tyrosyl radical. The formation and decay of the neutral tyrosyl radical at 410 nm were monitored in Peptide A and its variant, Peptide C, in which H14 is replaced by cyclohexylalanine (Cha14). Significantly, both electron transfer (ET, pL 11, L = lyonium) and PCET (pL 9) were accelerated in Peptide A and C, compared to model tyrosinate or tyrosine at the same pL. Increased electronic coupling, mediated by the peptide backbone, can account for this rate acceleration. Deuterium exchange gave no significant solvent isotope effect in the peptides. At pL 9, but not at pL 11, the reaction rate decreased when H14 was mutated to Cha14. This decrease in rate is attributed to an increase in reorganization energy in the Cha14 mutant. The Y5–H14 mechanism in Peptide A is reminiscent of proton- and electron-transfer events involving YD-H189 in PSII. These results document a mechanism by which proton donors and acceptors can regulate the rate of PCET reactions.

2.2 Introduction

Proton-coupled electron transfer (PCET) and electron-transfer (ET) reactions play a critical role in a number of biologically important processes, such as DNA synthesis, respiration, and photosynthesis. These reactions can be mediated by redox-active aromatic amino acids, such as tyrosine and tryptophan, which serve as charge carriers in the radical transport pathway[1-5]. For example, tyrosine is known to facilitate high- potential PCET reactions in ribonucleotide reductase (RNR) and photosystem II (PSII).[6-7] In this article, we use the term PCET to refer to any reaction in which an electron and proton are transferred, regardless of mechanism. The biologically relevant PCET and ET processes occur in complex biomolecules. Biomimetic modeling of these reactions is helpful, because model compounds provide a structurally tractable system in which to study mechanism. In the examination of tyrosine-based PCET and ET, a wide variety of useful model compounds and biomimetic approaches has been reported.[8-20]

UV photolysis can be used to ionize tyrosine or tyrosinate. Previous studies of phenol and tyrosine in aqueous solution showed that UV photoexcitation leads to the production of a neutral phenoxyl radical and a solvated electron.[21-26] Production of the neutral tyrosyl radical is expected in aqueous solutions because of the low pK value (−2) of the tyrosyl radical.[23] In gas-phase, phenol–water clusters, a net hydrogen-atom transfer occurs, with water functioning as the proton acceptor.[21, 27] At pH 9, the phenolic oxygen of tyrosine is protonated, and oxidation and reduction of tyrosine after UV photolysis occur as PCET, forming a neutral tyrosyl radical.[23, 28] At pH 11, the phenolic oxygen of tyrosinate is deprotonated, and oxidation and reduction of tyrosinate, through the neutral tyrosyl radical, occurs as ET after photolysis.

According to the Marcus equation (Equation 2.1),[4, 29] the electron-transfer (ET) rate is dependent on driving force ($\Delta G°$), reorganization energy (λ), and electronic coupling between donor (D) and acceptor (A) (V_{DA}). Electronic coupling (Equation 2.2)[30], in turn, depends exponentially on the distance between donor and acceptor (R_{DA}) with a decay factor (β) that is influenced by the medium (e.g., protein matrix).[4, 29-30] $|V_0|^2$ in Equation 2.2 is the maximum electronic coupling. A Marcus-type formalism has also been used to rationalize the rate of hydrogen-atom transfer and PCET reactions.[31-32]

$$k_{ET} = \{[\pi/(\hbar^2 \lambda k_B T)]\}^{-1/2} |V_{DA}|^2 \, e^{-(\Delta G° + \lambda)^2 / 4\lambda k_B T} \quad (2.1)$$

$$|V_{DA}|^2 = |V_0|^2 \, e^{-\beta R_{DA}} \quad (2.2)$$

Noncovalent interactions between tyrosine and its protein environment are known to alter the kinetics and thermodynamics of tyrosine-based PCET and ET. For example, the hydrophobic environment in the tyrosine-containing peptide α3 shifts the midpoint potential of tyrosine and gives rise to reversible redox reactions,[33] which are not observed for tyrosine/tyrosinate in solution.[34] Further, in PSII, there are two redox-active tyrosines, YZ and YD, with different potentials and radical lifetimes, mediated by alterations in the environment.[7]

To describe factors that alter the rate of tyrosine-based PCET and ET reactions, we have studied β-hairpin models. Previous electrochemical studies of a β-hairpin, Peptide A (IMDRYRVRNGDRIHIRLR, Figure 2.1), , showed that this peptide conducts a net

orthogonal PCET reaction. When tyrosine (Y5) is oxidized in a physiological pH range, the pK_a of histidine (H14) increases dramatically.[17] The NMR structure of Peptide A (Figure 2.1A) reveals that this peptide forms a β-hairpin. Y5 and H14 have a cross-strand, π–π stacked interaction but are not directly hydrogen-bonded in the averaged, minimized structure.[16]

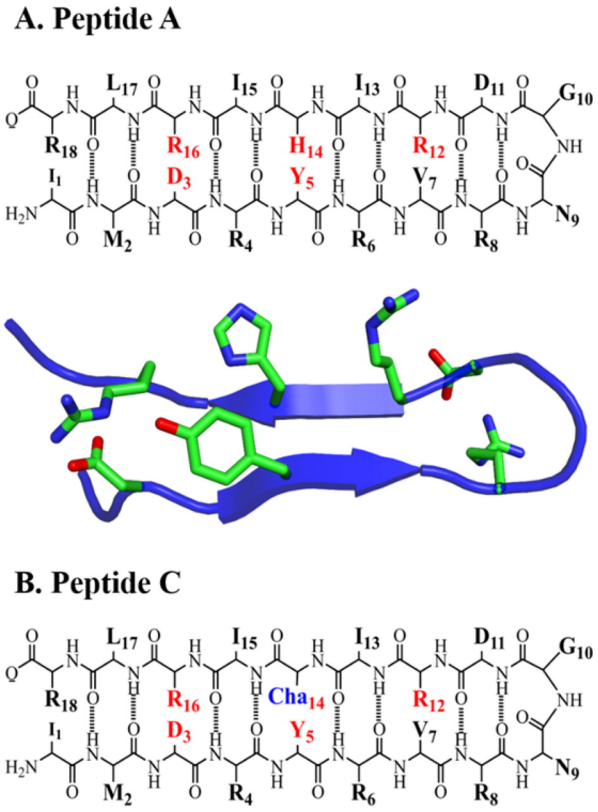

Figure 2.1 Primary sequences and secondary structures of (A) Peptide A and (B) Peptide C. Three-dimensional, (A) averaged, and minimized structure of Peptide A was determined by NMR spectroscopy and reported previously.[16]

The effect of H14 on tyrosyl radical kinetics has not yet been investigated in the β-hairpin model system. Also, the mechanism of the PCET reaction in Peptide A is not known. Recently, we employed time-resolved absorption spectroscopy (TRAS) in an initial study of the picosecond reaction dynamics of Peptide A tyrosyl radical.[8] In our TRAS

studies, photolysis of either tyrosine or Peptide A with a 280-nm femtosecond pulse yielded a short-lived excited state (S_1) with a pH-dependent absorption spectrum.[8] A narrow band at ~410 nm and a broad band at ~600 nm, assigned to the neutral tyrosyl radical and solvated electron, respectively, were also observed. These spectral assignments agree with previous time-resolved studies of phenol and phenolate.[13, 35] In our previous work, the decay profiles of all three species (S_1 state, tyrosyl radical, and solvated electron) were fit with biexponential kinetics. When the peptide was compared to model tyrosine (pH 9) or tyrosinate (pH 11), the decay of the S_1 state, the tyrosyl radical, and the solvated electron were accelerated in the peptide. This acceleration was observed at pH 9 and 11 and was attributed either to increased electronic coupling or to specific noncovalent interactions in the peptide.

To distinguish these possibilities and to assess any effect of H14 on the kinetics of tyrosyl radical decay, here, we present TRAS experiments on Peptide C in H_2O and D_2O buffers (Figure 2.1B). Peptide C (IMDRYRVRNGDRIChaIRLR, Figure 2.1) is a sequence variant of Peptide A in which H14 is substituted by a cyclohexylalanine (Cha). Cha14 is not active in proton transfer.[17] The Peptide C variant was shown to form a stable β-hairpin by circular dichroism (CD). Comparison of Peptide C results to Peptide A data supports the conclusion that electronic coupling influences the PCET rate. Importantly, H14 is observed to accelerate the PCET reaction, but not the ET reaction.

2.3 Materials and Methods

2.3.1 Samples

Boric acid (99% purity), HEPES [4-(2-hydroxyethyl)-1-piperazineethanesulfonic acid, 99.5%], sodium hydroxide (99.5%), and tyrosine (99.9%) were purchased from Sigma (St. Louis, MO). d,l-Dithiothreitol (DTT, 99.5%) was purchased from MP Biomedicals (Santa Ana, CA). Deuterium oxide (D_2O, 99.9%) and sodium deuteroxide (NaOD, 99.5%) were purchased from Cambridge Isotope Laboratories (Andover, MA). Peptide A (IMDRYRVRNGDRIHIRLR) and Peptide C (IMDRYRVRNGDRIChaIRLR) were synthesized by solid-state synthesis and were purchased from Genscript (Piscataway, NJ; >95% purity).[16-17] The pL values (where L refers to the lyonium ion) in D_2O buffers are reported as the uncorrected meter readings, because of the compensating effects of D_2O on the pK_a values of acids and bases and the response of the glass pH electrode.[36-37]

2.3.2 TRAS

TRAS data were acquired with a pump–white-light-continuum probe spectroscopy system (HELIOS, Ultrafast Systems, Sarasota, FL)[38]. The system consists of a regeneratively amplified titanium sapphire laser (Solstice, Spectra-Physics, 800 nm, 3.7 W average power, 100 fs pulse width, 1 kHz repetition rate) and a computer-controlled optical parametric amplifier (OPA) (Spectra-Physics, TOPAS, wavelength range of 266–2600 nm, pulse width of ~75 fs $HW_{1/e}$) pumped by the amplified laser. The 280-nm photolysis pulse was generated using the fourth-harmonic output of the OPA. A white-light-continuum (WLC) probe beam with a spectral range of 350–750 nm was generated by focusing less than 5% of the 800-nm amplified beam into a CaF_2crystal. The probe signal was collected using a fiber-optic cable coupled to a spectrometer with a multichannel CMOS (complementary metal–oxide–semiconductor) sensor (spectral range of 300–900 nm). The maximum time delay was 3.2 ns. The pump beam was chopped at 500 Hz to obtain the

WLC spectrum without the pump and alternately with the 280-nm pump. These data were used to calculate the transient spectra, represented as the changes in optical density or absorbance units (AU). Each transient spectrum at a given time delay was averaged for 4 s. A chirp correction function for the WLC probe was determined using the coherent artifact of the organic solvent, tetrahydrofuran, and was applied to all transient spectra.[39] The excitation pulse energy was 2–3 μJ. The averaged beam waist ($HW_{1/e}$) was ~160 μm for the pump and ~80 μm for the WLC probe. The optical path length of the quartz cuvette was 2 mm. The solutions had an optical density at 280 nm (OD_{280}) of 0.25–0.50 in 2-mm-path-length cuvettes and were stirred throughout data acquisition to prevent photoinduced degradation. The tyrosyl radical was not generated at pH values less than 9 under these conditions. It was reported previously that triplet-state formation is not expected in oxygenated samples.[40] To verify the integrity of the sample, steady-state absorption spectra were recorded before and after the ultrafast measurements on a Shimadzu UV-3101PC spectrophotometer. No significant change in the steady-state spectrum was observed. Data were fit using IGOR 6.43A software (Wavemetrics Inc., Oswego, OR). In some cases, sinusoidal oscillations were observed as noise on the kinetic transients; these oscillations were not fit during data analysis. To verify the integrity of the sample, steady-state absorption spectra were recorded before and after the ultrafast measurements on a Shimadzu UV-3101PC spectrophotometer. No significant change in the steady-state spectrum was observed. Data were fit using IGOR 6.43A software (Wavemetrics Inc., Oswego, OR). In some cases, sinusoidal oscillations were observed as noise on the kinetic transients; these oscillations were not fit during data analysis.

2.4 Results

2.4.1 Samples and Spectroscopy

Peptide A and Peptide C (Figure 2.1) were synthesized by solid-state synthesis. Previously, Peptides A and C were shown to form thermally stable β-hairpins.[16-17] TRAS was performed using a pump–WLC probe spectroscopy system (HELIOS, Ultrafast Systems) described previously.[38] Measurements were carried out in H_2O and D_2O buffers at pL 9 and 11. Comparing the expected differential effects of pL 9 and 11 on the peptides, this change titrates the phenolic oxygen of Y5 (pK_a 10)[41] and the amino terminus (pK_a 9.3)[42]. When tyrosine is oxidized in Peptide A, the pK_a of H14 changes from 6 to 9, as assessed by square-wave voltammetry.[16-17] Square-wave voltammetry was also used previously to study Peptide C. Characteristic inflection points, associated with the pK_a shifts of H14, were absent. However, the peak potentials of Y5 in Peptides A and C were found to be similar at both pL 9 and 11.[16-17]

2.4.2 Overview of TRAS Results

Figure 2.2 presents spectra, derived from time-resolved measurements and acquired from tyrosinate and Peptides A and C in D_2O buffer at pL 11. Figure 2.3 presents the corresponding spectra acquired from tyrosine and Peptides A and C in D_2O buffer at pL 9. Spectra of tyrosine/tyrosinate and Peptide A in H_2O buffers at pL 9 and 11 were reported previously.[8] TRAS data derived from Peptide C in H_2O buffers at pL 9 and 11 are presented in Figure 2.4. The formation of the S_1 state, which is monitored at 520 nm, is evident in these spectra. Production of the tyrosyl radical (410-nm narrow band) and of the solvated electron (broad band starting at ~600 nm) is also observed.

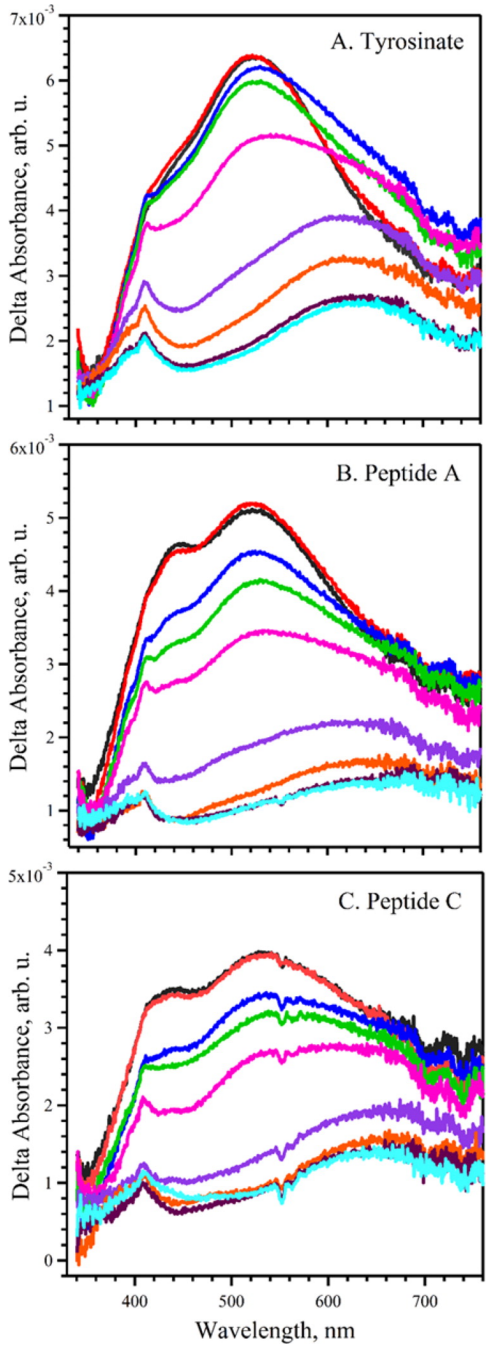

Figure 2.2 Transient absorption spectra of (A) tyrosinate, (B) Peptide A, (C) and Peptide C at pL 11 (where L refers to the lyonium ion) in D_2O buffer. Spectra were obtained (black) 2, (red) 3, (blue) 10, (green) 15, (pink) 30, (violet) 100, (orange) 500, (purple) 1500, and (cyan) 2000 ps after 280-nm photolysis. The spectra were averaged from at least three independent measurements. Analyte concentration, 1 mM; borate-NaOD, 5 mM.

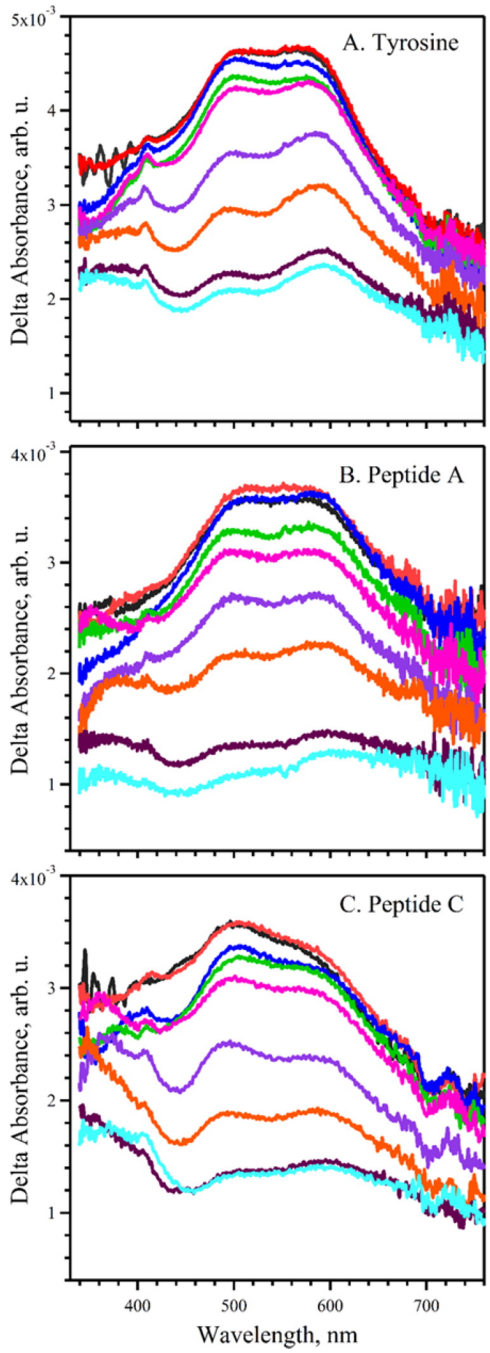

Figure 2.3 Transient absorption spectra of (A) tyrosine, (B) Peptide A, and (C) Peptide C at pL 9 (where L refers to the lyonium ion) in D_2O buffer. Spectra were obtained (black) 2, (red) 3, (blue) 10, (green) 15, (pink) 30, (violet) 100, (orange) 500, (purple) 1500, and (cyan) 2000 ps after 280-nm photolysis. The spectra were averaged from at least three independent measurements. Analyte concentration, 1 mM; borate-NaOD, 5 mM.

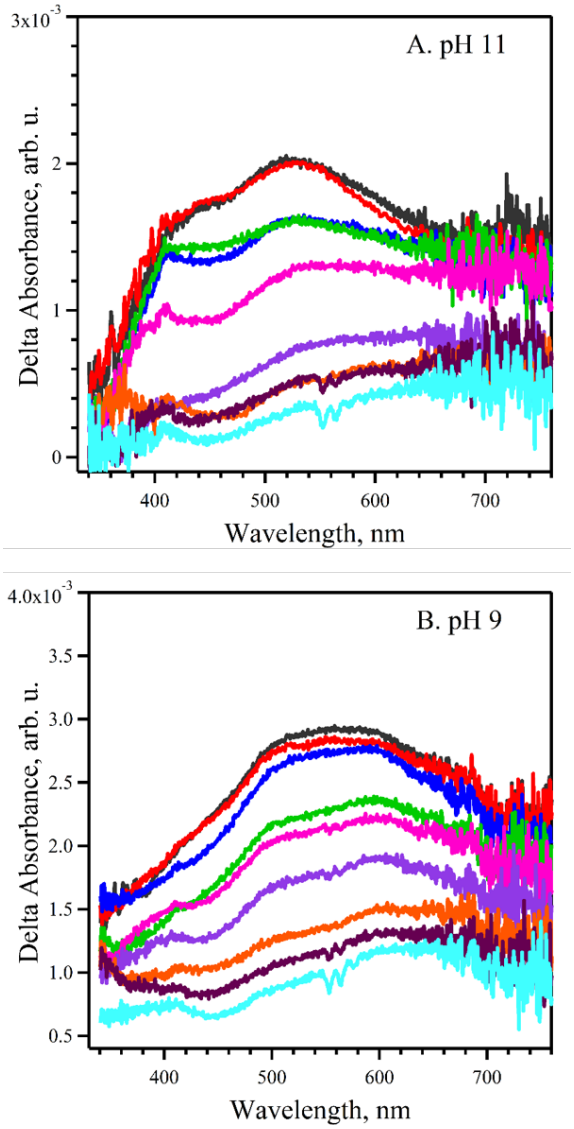

Figure 2.4 Transient absorption spectra of Peptide C at pL 11 (A) and at pL 9 (B) (where L refers to the lyonium ion) in H_2O buffers. Spectra were obtained at 2 (black), 3 (red), 10 (blue), 15 (green), 30 (pink), 100 (violet), 500 (orange), 1500 (purple) and 2000 ps (cyan) after 280-nm photolysis. The spectra were averaged from at least three independent measurements. Analyte concentration, 1 mM; 5 mM borate-NaOH.

2.4.3 TRAS Spectra at pL 11

Spectra derived from tyrosinate in D_2O buffer at pL 11 (Figure 2.2A) were indistinguishable from those reported previously for tyrosinate in H_2O buffer at pL 11.[8] The spectra of Peptide A and Peptide C (Figure 2.2B,C) were similar to each other in D_2O

at pL 11 but distinct from those of tyrosinate in D_2O at pL 11 (Figure 2.2A). In the peptide spectra, an additional band at ~450 nm was observed in the first 10 ps. This band might be due to a structural reorientation, specific to the peptides.[12] This band does not complicate the kinetic analysis below, because the signal decayed by 10 ps and the fits to the data used 20 ps as the initial point.

2.4.4 TRAS Spectra at pL 9

At pL 9 in D_2O, the spectra from tyrosine, Peptide A, and Peptide C (Figure 2.3) were not dissimilar and resembled data obtained in H_2O at pL 9 (Figure 2.4 and reported previously[8]).

2.4.5 Formation Profiles

The formations of the S_1 excited state, the neutral tyrosyl radical, and the solvated electron were monitored in all samples at 520, 410, and 650 nm, respectively. Examples for tyrosinate at pL 11 in H_2O and D_2O buffers are shown in panels A and B, respectively, of Figure 2.5. The formation profiles indicate that the S_1 excited state and the tyrosyl radical are fully formed in 4 ps whereas the fully solvated electron is formed in 10–15 ps. Other samples gave similar results (data not shown). The formation profiles in Figure 2.5 illustrate that the signals from the S_1 state, the tyrosyl radical, and the solvated electron do not begin to decay until ~20 ps.

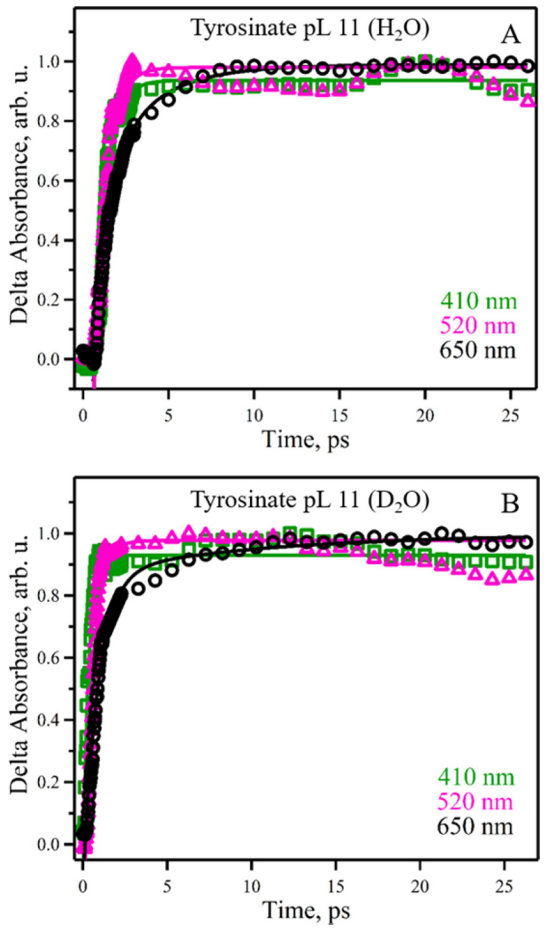

Figure 2.5 Formation kinetics obtained after 280-nm photolysis of tyrosinate at pL 11 in (A) H_2O and (B) D_2O buffers. In each sample, the absorption of the neutral tyrosyl radical was monitored at 410 nm (green), the absorption of the S_1 excited state was monitored at 520 nm (pink), and the absorption from the solvated electron was monitored at 650 nm (black). The data were averaged from at least three independent measurements. The averaged data were normalized with respect to the maximum absorbance, which occurred at ~3–4 ps at 410 and 520 nm and at ~15 ps at 650 nm. Analyte concentration, 1 mM; buffer, borate-NaOH/NaOD, 5 mM.

2.4.6 Kinetics at pL 9: PCET

Figure 2.6 (left) presents the decay kinetics of the tyrosyl radical (410 nm, A), the S_1 excited state (520 nm, B), and the solvated electron (650 nm, C) in tyrosine, Peptide A, and Peptide C in D_2O buffer at pL 9. Kinetic data acquired in H_2O buffers at pL 9 are shown in Figure 2.7 (left) At this pL, the radical reduction reaction, monitored at 410 nm,

involves both proton and electron transfer. The decay profiles were fit starting at 20 ps, based on analysis that showed that the signals do not begin to decay until this time point (see Figure 2.5 and discussion above). The decay profiles were fit well with biphasic kinetics, as assessed by the residuals (Figure 2.6 and 2.7) and χ^2 values (Table 2.1). We attribute the biphasic kinetics to the presence of multiple conformational states in tyrosine/tyrosinate and in the peptides.[43] Inspection of the decay profiles, time constants, and amplitudes suggests that the decay of the tyrosyl radical, the S_1 excited state, and the solvated electron is accelerated in the peptides relative to tyrosine/tyrosinate. For example, in D_2O, when Peptides A and C are compared to tyrosine, the fast phase of tyrosyl radical decay has similar time constants in all three samples ($\tau_{1/2}$ = 13–22 ps), but the amplitude of the fast phase was increased in Peptide A. In addition, a change in the slow phase was observed in the peptides, corresponding to an increased decay rate. A similar result was obtained in H_2O buffer (Table 2.1).

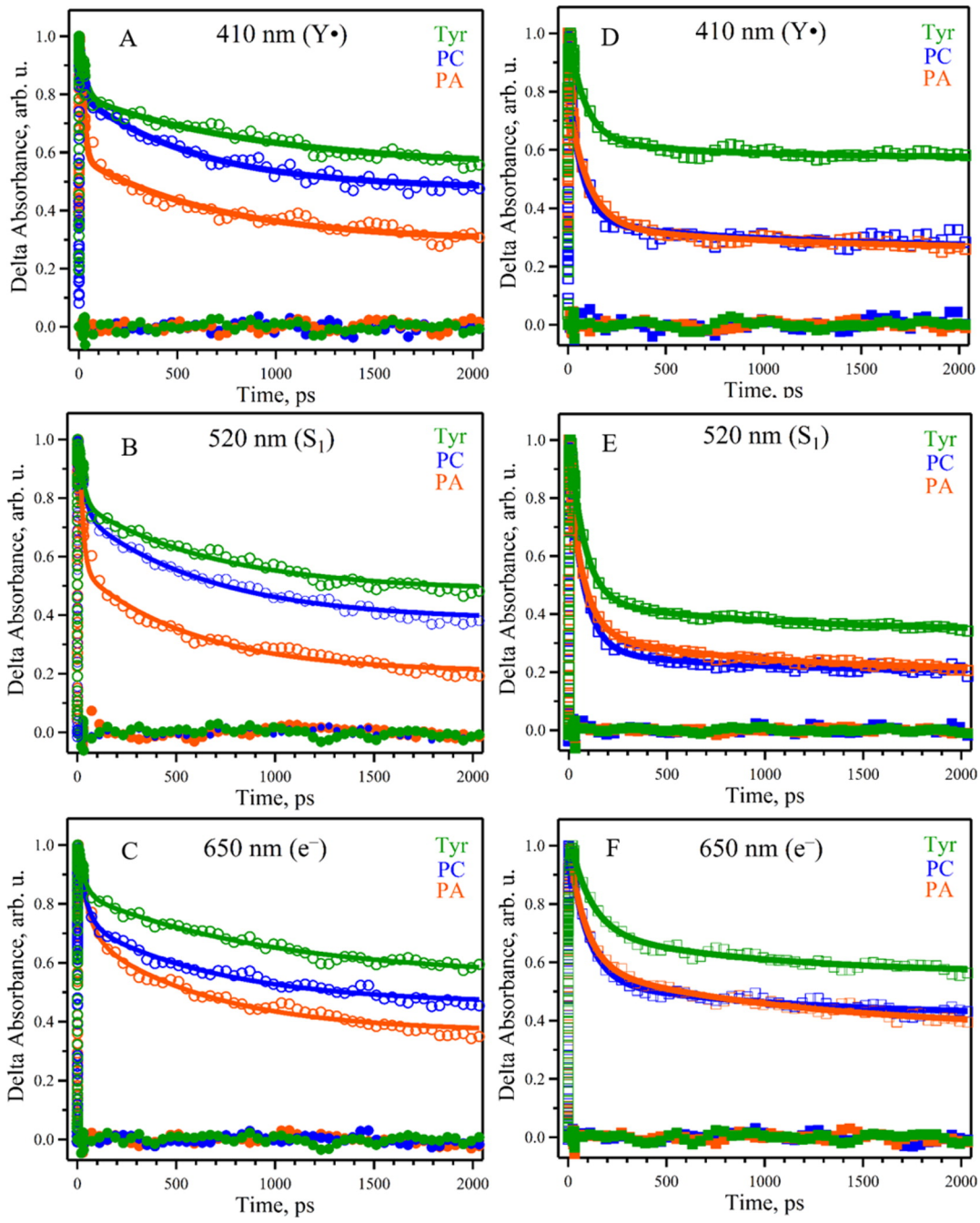

Figure 2.6 Decay kinetics, derived from tyrosine and peptides in D_2O buffers, after 280-nm photolysis at (A–C) pL 9 (open circles) or (D–F) pL 11 (open squares). Samples were tyrosine/tyrosinate (green), Peptide A (orange), or Peptide C (blue). In each sample, (A,D) the absorption of the neutral tyrosyl radical was monitored at 410 nm, (B,E) the absorption of the S_1 excited state was monitored at 520 nm, and (C,F) the absorption from the solvated electron was monitored at 650 nm. Double-exponential fits (starting from 20 ps) are superimposed as solid lines, and the solid circles and squares are the corresponding residuals. Fitting parameters are presented

in Table 2.1. The data were averaged from at least three independent measurements. The averaged data were normalized with respect to the maximum absorbance, which occurred at ~3–4 ps at 410 and 520 nm and at ~10–15 ps at 650 nm. Analyte concentration, 1 mM; borate-NaOD, 5 mM.

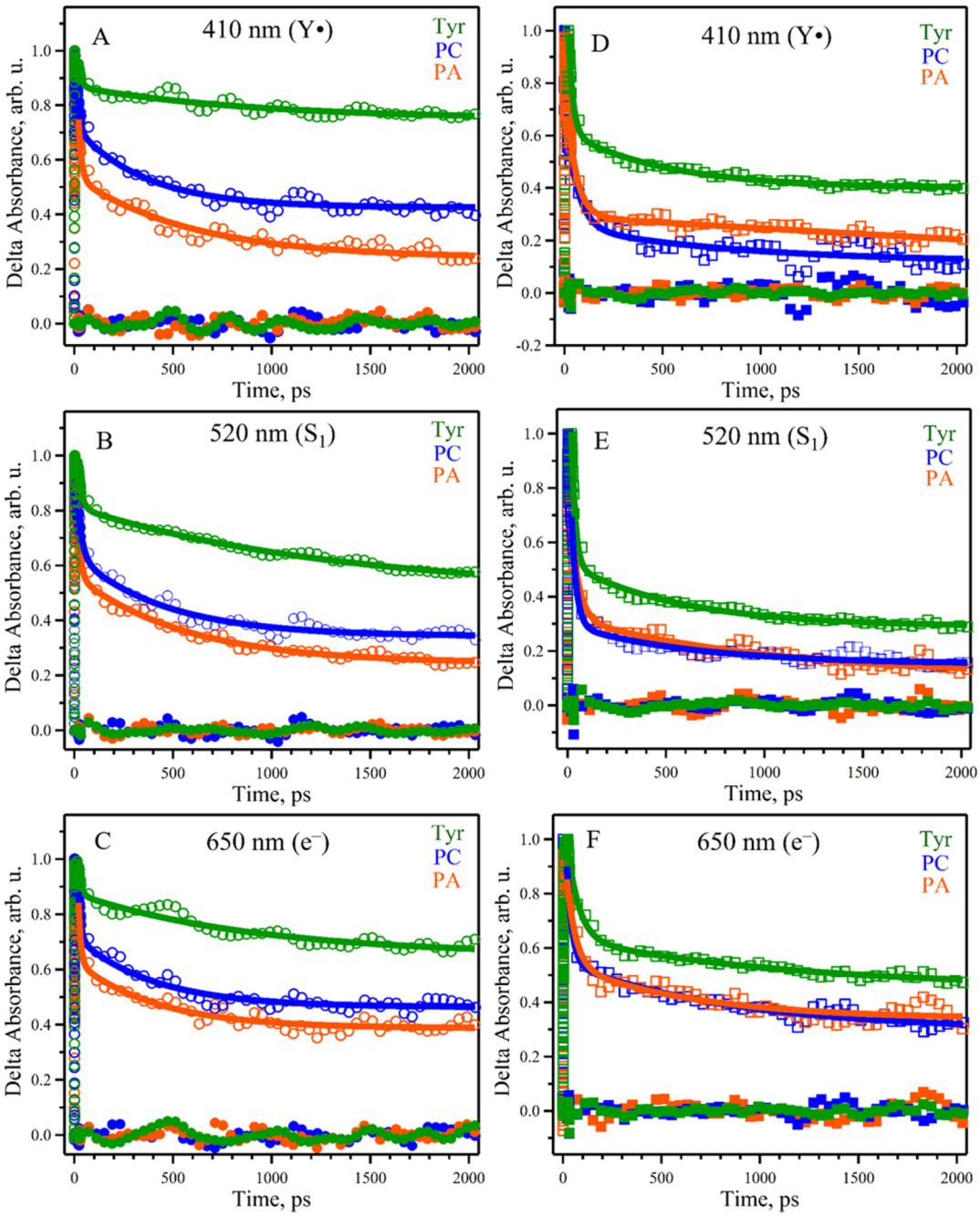

Figure 2.7 Decay kinetics, derived from tyrosine and peptides in H_2O buffers, after 280-nm photolysis at (A–C) pL 9 (open circles) or (D–F) pL 11 (open squares). Samples were tyrosine/tyrosinate (green), Peptide A (orange), or Peptide C (blue). In

each sample, (A,D) the absorption of the neutral tyrosyl radical was monitored at 410 nm, (B,E) the absorption of the S_1 excited state was monitored at 520 nm, and (C,F) the absorption from the solvated electron was monitored at 650 nm. Double-exponential fits (starting from 20 ps) are superimposed as solid lines, and the solid circles and squares are the corresponding residuals. Fitting parameters are presented in Table 2.1. The data were averaged from at least three independent measurements. The averaged data were normalized with respect to the maximum absorbance, which occurred at ~3–4 ps at 410 and 520 nm and at ~10–15 ps at 650 nm. Analyte concentration, 1 mM; 5 mM borate-NaOH.

Table 2.1 Kinetic Parameters derived from tyrosine, tyrosinate, Peptide A, and Peptide C

		τ_1	A_1 (%)	τ_2	A_2 (%)	y_0 (%)	χ^2
pL 9							
Tyrosine							
410 (H_2O)	nm	16 ± 6	0.08 (8)	910 ± 87	0.12 (12)	0.76 (80)	0.0140
410 (D_2O)	nm	22 ± 8	0.12 (13)	832 ± 54	0.23 (25)	0.56 (62)	0.0230
520 (H_2O)	nm	18 ± 2	0.14 (15)	1300 ± 150	0.31 (32)	0.50 (53)	0.0049

Table 2.1 continued

520 (D_2O)	nm	23 ± 7	0.15 (16)	684 ± 36	0.30 (32)	0.48 (52)	0.0223
650 (H_2O)	nm	14 ± 5	0.11 (11)	910 ± 190	0.22 (23)	0.65 (66)	0.0207
650 (D_2O)	nm	30 ± 10	0.10 (11)	869 ± 35	0.27 (29)	0.56 (60)	0.0115
Peptide A							
410 (H_2O)	nm	16 ± 3	0.22 (30)	600 ± 37	0.29 (38)	0.24 (32)	0.0275
410 (D_2O)	nm	14 ± 2	0.28 (33)	703 ± 41	0.28 (33)	0.29 (34)	0.0282

Table 2.1 continued

520 (H_2O)	nm	14 ± 2	0.19 (25)	530 ± 20	0.31 (42)	0.25 (33)	0.0109
520 (D_2O)	nm	18 ± 2	0.28 (34)	576 ± 27	0.34 (42)	0.20 (24)	0.0208
650 (H_2O)	nm	13 ± 2	0.22 (26)	410 ± 35	0.23 (28)	0.39 (46)	0.0241
650 (D_2O)	nm	49 ± 9	0.20 (22)	626 ± 18	0.34 (38)	0.36 (40)	0.0203
Peptide C							
410 (H_2O)	nm	14 ± 4	0.12 (15)	405 ± 23	0.28 (34)	0.42 (51)	0.0243

Table 2.1 continued

410 (D_2O)	nm	13 ± 4	0.10 (11)	598 ± 24	0.31 (35)	0.48 (54)	0.0139
520 (H_2O)	nm	24 ± 6	0.18 (22)	473 ± 24	0.28 (35)	0.34 (43)	0.0230
520 (D_2O)	nm	30 ± 7	0.15 (17)	652 ± 22	0.36 (40)	0.38 (43)	0.0120
650 (H_2O)	nm	14 ± 4	0.17 (19)	441 ± 29	0.25 (29)	0.45 (52)	0.0278
650 (D_2O)	nm	40 ± 8	0.16 (18)	695 ± 22	0.28 (31)	0.46 (51)	0.0111

pL 11

Tyrosinate

Table 2.1 continued

410 (H_2O)	nm	23 ± 2	0.37 (38)	500 ± 59	0.21 (21)	0.40 (41)	0.0117
410 (D_2O)	nm	81 ± 6	0.30 (32)	724 ± 95	0.06 (6)	0.58 (62)	0.0124
520 (H_2O)	nm	19 ± 1	0.49 (49)	576 ± 31	0.22 (22)	0.29 (29)	0.0121
520 (D_2O)	nm	73± 3	0.45 (50)	792 ± 41	0.11 (12)	0.34 (38)	0.0084
650 (H_2O)	nm	54 ± 7	0.34 (35)	820 ± 76	0.18 (18)	0.47 (47)	0.0186
650 (D_2O)	nm	113 ± 7	0.28 (29)	858 ± 37	0.14 (14)	0.56 (57)	0.0095

Table 2.1 continued

Peptide A

410 (H_2O)	nm	46 ± 6	0.36 (53)	980 ± 150	0.10 (16)	0.21 (31)	0.0221
410 (D_2O)	nm	101 ± 6	0.36 (51)	1081 ± 94	0.08 (11)	0.26 (37)	0.0140
520 (H_2O)	nm	38 ± 6	0.34 (49)	720 ± 69	0.22 (31)	0.14 (20)	0.0297
520 (D_2O)	nm	76 ± 4	0.42 (56)	858 ± 72	0.13 (17)	0.20 (27)	0.0064
650 (H_2O)	nm	51 ± 10	0.36 (40)	1100 ± 140	0.22 (24)	0.32 (36)	0.0586
650 (D_2O)	nm	90 ± 8	0.34 (37)	1137 ± 78	0.21 (23)	0.37 (42)	0.0116

Table 2.1 continued

Peptide C

410 (H_2O)	nm	55 ± 9	0.33 (57)	896 ± 110	0.14 (24)	0.11 (19)	0.0579
410 (D_2O)	nm	72 ± 7	0.36 (51)	1072 ± 120	0.09 (13)	0.26 (37)	0.0262
520 (H_2O)	nm	25 ± 3	0.40 (58)	625 ± 57	0.14 (20)	0.15 (22)	0.0360
520 (D_2O)	nm	73 ± 3	0.48 (63)	750 ± 64	0.08 (11)	0.20 (26)	0.0128
650 (H_2O)	nm	26 ± 4	0.36 (40)	857 ± 64	0.25 (27)	0.30 (33)	0.0328
650 (D_2O)	nm	94 ± 5	0.39 (42)	1095 ± 56	0.12 (13)	0.41 (45)	0.0104

[a]$y = y_0 + A_1\exp\{-(x-x_0)/\tau_1\} + A_2\exp\{-(x-x_0)/\tau_2\}$; A = Amplitude, τ = time constant (ps), x_0 = 20 ps. The transients were normalized with respect to the maximum absorbance in

each averaged data set, which occurs ~ 3-4 ps at 410 and 520 nm and ~ 10-15 ps at 650 nm, before fitting with Igor Pro 6.34A software (Wavemetrics Inc., Lake Oswego, OR).

[b]Kinetic parameters for tyrosine and Peptide A in H_2O were obtained from previous work.[8]

The substitution of Cha for H14 was observed to decrease the reduction rates at pL 9. Similar effects were observed when the decays of the S_1 state, the tyrosyl radical, and the solvated electron were monitored (Figures 2.6 and 2.7). In Peptide A in H_2O buffer, the decay of tyrosyl radical was described with two time constants, 16 ± 3 ps (30% of the amplitude) and 600 ± 37 ps (38%) (Table 2.1). In Peptide C in H_2O buffer, the fast phase had a smaller amplitude and the nondecaying component had a larger amplitude relative to Peptide A. These effects rationalize the overall observed decrease of the rate when Peptide C and Peptide A are compared. In D_2O buffer at pL 9, the Cha14 mutation also significantly decreased the amplitude of the fast phase and increased the amplitude of the non-decaying component, relative to Peptide A, resulting in an overall lower reaction rate.

2.4.7 Kinetics at pL 11: ET

Figure 2.6 (right) presents the decay kinetics of the tyrosyl radical (410 nm, D), the S_1 excited state (520 nm, E), and the solvated electron (650 nm, F) in tyrosinate, Peptide A, and Peptide C in D_2O buffer at pL 11. Kinetic data acquired in H_2O buffers at pL 11 are shown in Figure 2.7 (right). At this pL, the radical reduction reaction, monitored at 410 nm, involves only ET, because the pH is above the pK_a of the phenolic oxygen. Biexponential fits to the decay profiles are reported in Table 2.1. For model tyrosinate in H_2O, the first time constant is derived as 23 ± 2 ps, which is 38% of the amplitude, and the second time constant is derived as 500 ± 59 ps, which is 21% of the amplitude. Again,

decay of the tyrosyl radical was accelerated in the peptide samples relative to that in model tyrosinate. This is evident in the biexponential fits to the data, which show, for example, an increased contribution from the fast phase in Peptides A and C relative to that in tyrosinate (Table 2.1). Interestingly, at this pL, the kinetic data in Figure 2.6 and 2.7 and the fits in Table 2.1 show that the H14-to-Cha14 substitution has no significant effect on the reaction rate. We conclude that, whereas the PCET reaction rate is sensitive to H14 substitution, the ET reaction rate is not.

2.4.8 Solvent Isotope Effects

Exchange into D_2O was used to measure the solvent isotope effect on decay kinetics (Figures 2.8, 2.9, and 2.10). The effects of D_2O on the rates of tyrosyl radical, S_1 excited state, and solvated electron decay are complex when judged from the amplitudes and time constants in the biexponential fits. These detailed effects are presented in Table 2.1. As a simpler method of assessing the impact of D_2O, the effect of solvent isotope exchange on the percentage of the signal decaying by the 2-ns time point was determined (Table 2.2). Comparison of pL 9 and 11 identifies the solvent isotope effects (SIEs) specific for PCET and ET, respectively.

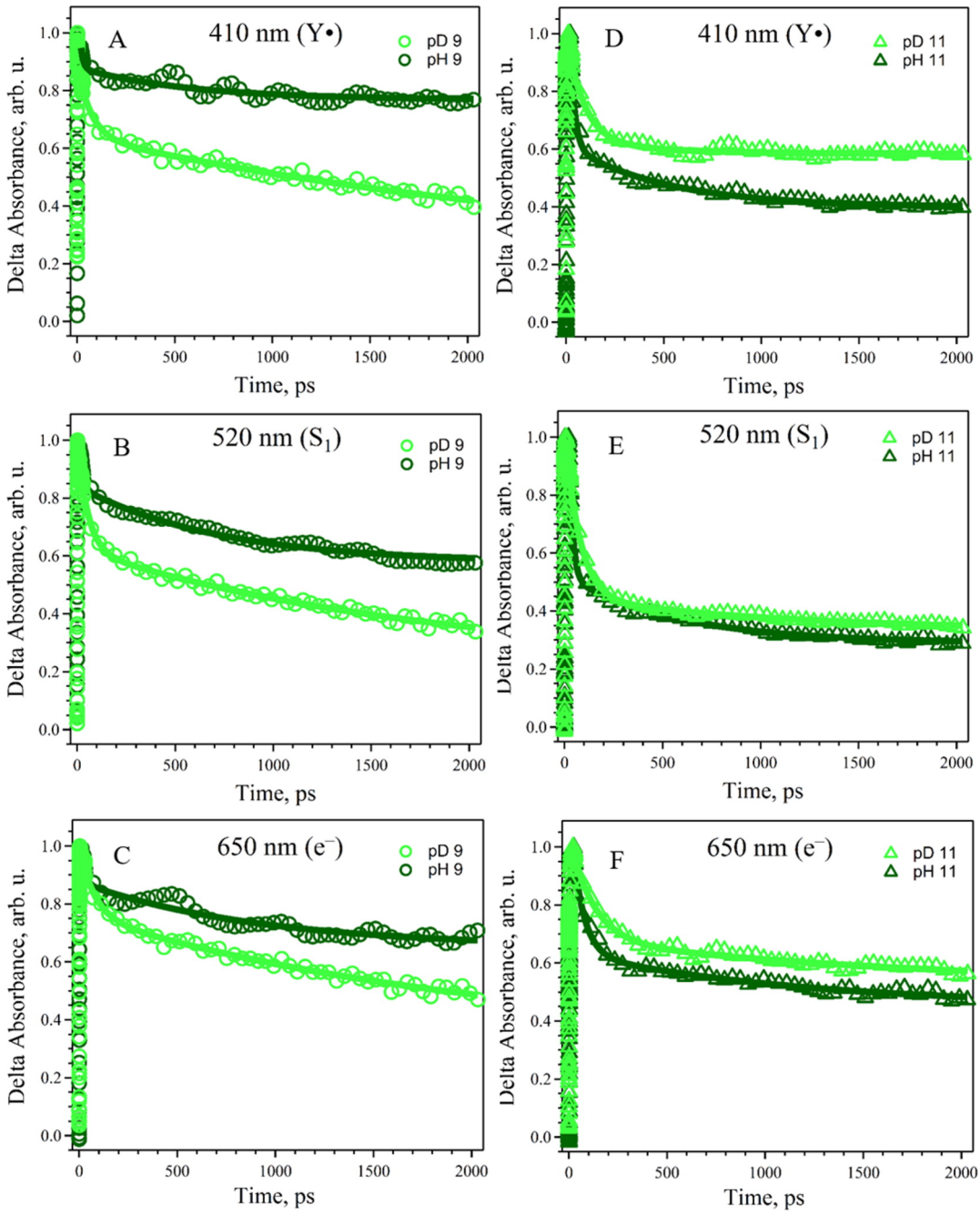

Figure 2.8 Decay kinetics, derived from model tyrosine and tyrosinate, after 280-nm photolysis. The samples were (A–C) tyrosine (pL 9, open circles) or (D–F) tyrosinate (pL 11, open triangles) in H_2O (dark green) or D_2O (light green). The solid lines are the superimposed double-exponential fits (starting from 20 ps). Fitting parameters are presented in Table 2.1. The data were averaged from at least three independent measurements. The averaged data were normalized with respect to the maximum absorbance in each averaged data set. Analyte concentration, 1 mM; borate-NaOH/NaOD, 5 mM. Data for tyrosine at pH 9 and 11 are reproduced from a

previous report. The notation inside the panels uses pH to refer to pL in H_2O buffer and pD to refer to pL in D_2O buffer.

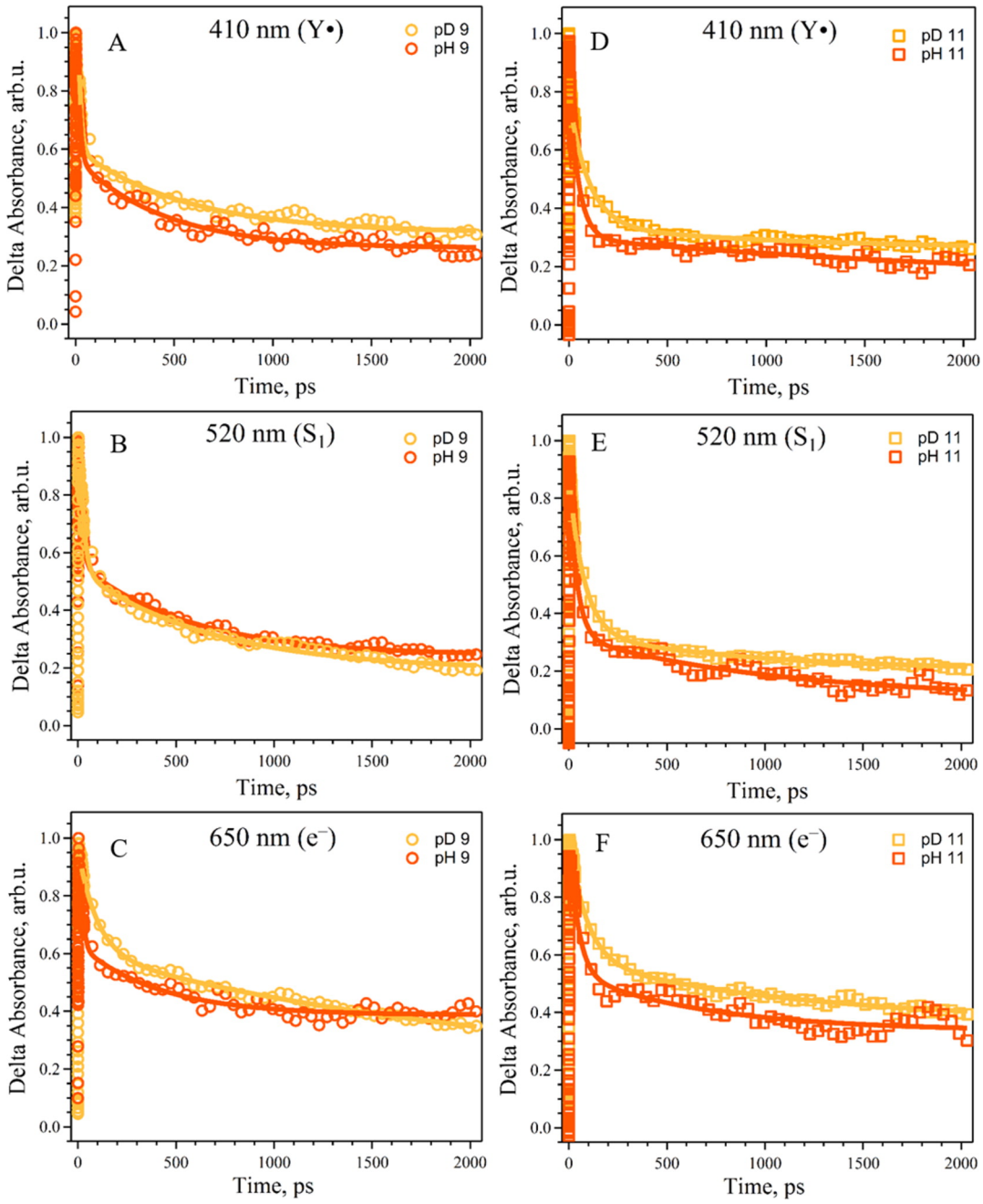

Figure 2.9 Decay kinetics, derived from Peptide A, after 280-nm photolysis. The sample was (A–C) pL 9 (open circles) or (D–F) pL 11 (open squares) in H_2O (dark orange) or D_2O (light orange). The solid lines are the superimposed double-exponential fits (starting from 20 ps). The data were averaged from at least three independent measurements. The averaged data were normalized with respect to the maximum absorbance in each averaged data set. Analyte concentration, 1 mM;

borate-NaOH/NaOD, 5 mM. Data for Peptide A at pL 9 and 11 in H_2O buffer are reproduced from a previous report.

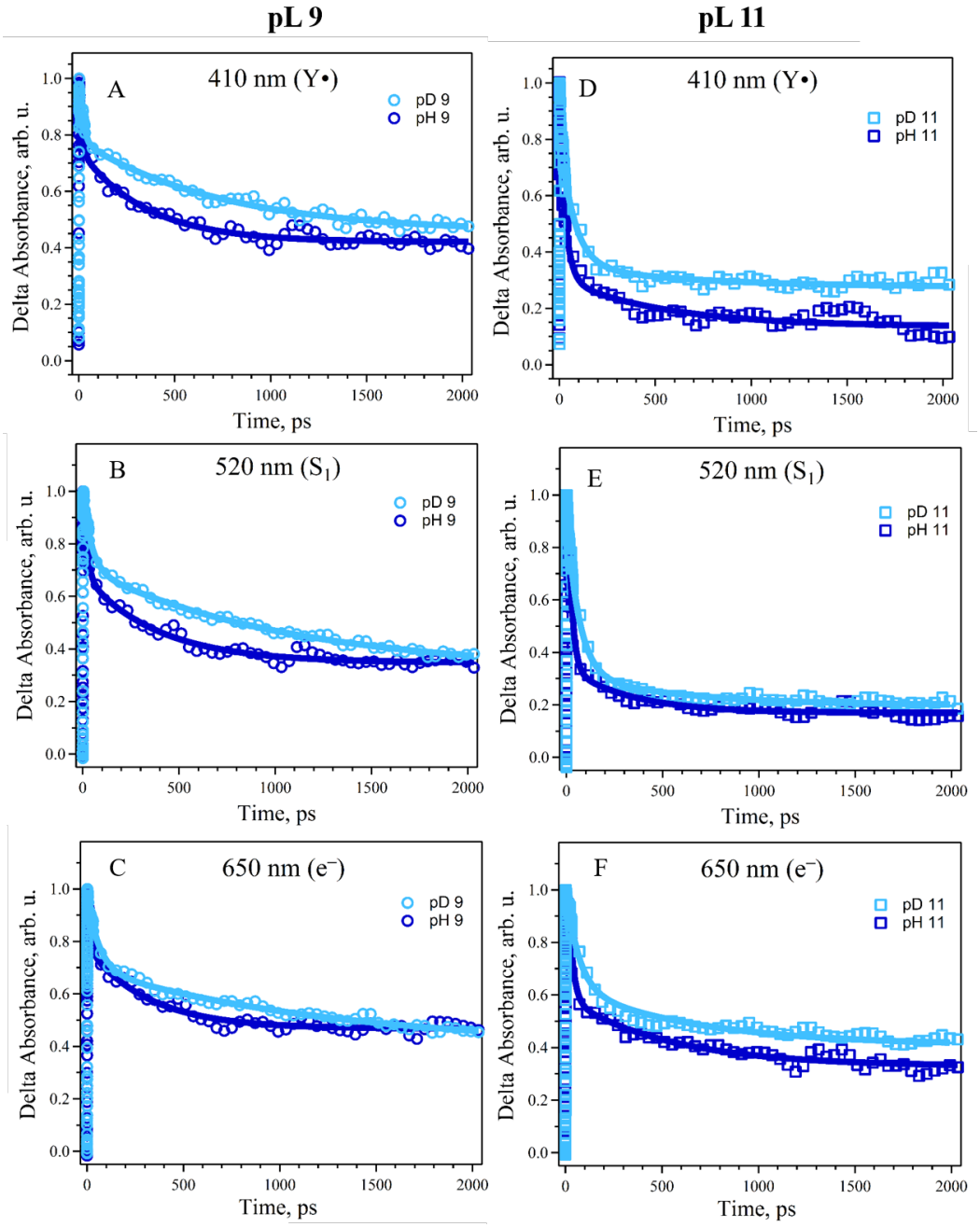

Figure 2.10 Decay kinetics in the picosecond to nanosecond regime, acquired after 280-nm photolysis of Peptide C at pL 9 (A-C, open circles) or pL 11 (D-F, open squares). Samples were suspended in H_2O (dark blue, pH) or in D_2O (light blue, pD) buffers. The solid lines are the superimposed double exponential fits (starting from 20 ps). Fitting parameters are presented in Table S1. The data were averaged from

at least three independent measurements. The averaged data were normalized with respect to the maximum absorbance in each averaged data set. Analyte concentration, 1 mM; buffer, 5 mM borate-NaOH/NaOD.

Table 2.2 Solvent Isotope Effect (SIE) on the Decays of the Tyrosyl Radical (410 nm), the S_1 Excited State (520 nm), and the Solvated Electron (650 nm) at pL 9 and pL 11[a]

	% Overall Decay[2]	SIE[2]	% Overall Decay[2]	SIE[2]
	pL 9		pL 11	
Tyrosine/Tyrosinate				
410 nm (H_2O)	23.9	0.54	59.7	1.41
410 nm (D_2O)	44.2		42.2	
520 nm (H_2O)	43.1	0.86	70.4	1.08
520 nm (D_2O)	50.2		64.7	
650 nm (H_2O)	32.6	0.77	51.7	1.22

Table 2.2 continued

650 nm (D_2O)	42.4		42.4	
Peptide A				
410 nm (H_2O)	75.0	1.09	79.6	1.09
410 nm (D_2O)	69.0		72.9	
520 nm (H_2O)	74.8	0.95	86.5	1.10
520 nm (D_2O)	78.5		78.4	
650 nm (H_2O)	61.1	0.98	65.3	1.10
650 nm (D_2O)	62.1		59.6	
Peptide C				

Table 2.2 continued

410 nm (H_2O)	57.3	1.12	87.0	1.20
410 nm (D_2O)	51.3		72.4	
520 nm (H_2O)	65.4	1.08	84.2	1.06
520 nm (D_2O)	60.2		79.4	
650 nm (H_2O)	53.5	1.02	68.1	1.20
650 nm (D_2O)	52.5		56.7	

[a] Values derived from the decay profiles of tyrosine, Peptide A, and Peptide C at pL 9 and 11. Data from tyrosine and Peptide A in H2O were reported previously.[8]

[b]Percent overall decay (POD) evaluated at the 2-ns time point, SIE = $POD(H_2O)/POD(D_2O)$.

The SIE for model tyrosine and tyrosinate is presented in Table 2.2. The corresponding data are presented in Figure 2.8. Considering the effect on tyrosyl radical decay (as monitored at 410 nm), an inverse isotope effect is observed for PCET at pL 9 (SIE = 0.54) but not ET at pL 11 (SIE = 1.41). At pL 9, small inverse isotope effects were also observed for the decay of the S_1 excited state (SIE = 0.86) and of the solvated electron

(SIE = 0.77). At pL 11, the SIE values for the S_1 excited state and solvated electron were close to one (1.22–1.08).

The SIEs on decay profiles derived from Peptides A and C are also presented in Table 2.2. The corresponding data are presented in Figure 2.9 (Peptide A) and Figure 2.10 (Peptide C). For tyrosyl radical decay through PCET at pL 9, SIE values close to one (1.09–1.12) were measured in both peptides. A similar result was obtained for tyrosyl radical decay by ET at pL 11 in the peptides. SIE values close to one (0.95–1.2) were also measured for the decays of the S_1 excited state and solvated electron in both peptides and at both pL values (Table 2.2). We conclude that there is a negligible SIE on decay kinetics in the peptide samples.

2.5 Discussion

In this study, we investigate the formation and decay of the neutral tyrosyl radical, S_1 excited state, and solvated electron on the picosecond to nanosecond time scale after photoionization. By monitoring the absorption at different wavelengths, the kinetic contributions of the tyrosyl radical, the S_1 excited state, and the solvated electron can be monitored independently.

2.5.1 Formation of Neutral Tyrosyl Radical, the S_1 Excited State, and the Solvated Electron

After UV photolysis, the S_1 excited state and the tyrosyl radical are fully formed at ~4 ps, and the signal from the solvated electron is fully formed at ~15 ps. These formation times agree with results obtained previously in aqueous phenolate.[13] In that work, the

solvated electron signal was formed in 15 ps, and the neutral phenoxyl radical signal grew in at ~3 ps. In a recent study[35] of aqueous phenol, a 400-nm signal from a neutral radical was reported to be produced by 200 fs. A 425-nm signature of a protonated phenoxyl radical was also detected, but this signal decayed on the subpicosecond time scale.[35] This time scale is not accessible in our experiment, and the 425-nm signature of the protonated tyrosyl radical was not detected here.

2.5.2 Mechanism of Tyrosyl Radical Formation

The mechanism of photoionization of tyrosine/tyrosinate and phenol/phenolate is an area of active investigation.[13, 22, 24, 26, 35, 40, 44-48] When photoexcited to the S_1 excited state, electron ejection is one of the relaxation processes available.[13, 35] The yield of the triplet state due to intersystem crossing was reported to be low.[13] Photoionization has been attributed to a reaction on the excited-state surface with a mechanism that depends on the excitation wavelength.[13, 24, 40, 44, 47, 49-51] For example, using 266-nm excitation in phenolate, the precursors of the radical were proposed to be the vibrationally excited S_1 state and the relaxed S_1 state.[13] For phenol in aqueous solution, the mechanism of phenoxyl radical formation has been attributed to a photoinduced autoionization process on the excited-state surface, followed by a rapid deprotonation. For aqueous phenol, the same photoproducts were observed with 200- and 267-nm excitation wavelengths but with different formation times. The 200-nm yield of neutral phenoxyl radical was reported as 13% at 800 ps; the 267-nm yield of radical was reported as 13% at 13 ns.[35] No SIE was observed for the formation of products at 267 nm. In this previous study at 267 nm, no spectral signatures attributable to phenoxyl radical or solvated electron were observed at times less than 1 ns. However, under the conditions employed here, which use a much lower concentration of

analyte and 280-nm excitation, the yield of neutral tyrosyl radical is complete in approximately 4 ps.

2.5.3 Summary of Results Concerning Decay Kinetics

In the studies reported here, recombination between the tyrosyl radical and the solvated electron occurs on the picosecond to nanosecond time scale. At pL 9, the transfer of the electron is accompanied by transfer of a proton in a PCET reaction. At pL 11, ET occurs, forming tyrosinate. In tyrosine, but not in tyrosinate, the decay of tyrosyl radical was accompanied by an inverse isotope effect. The decays of the S_1 state and solvated electron also exhibited inverse SIE values in tyrosine, but not in tyrosinate. In both Peptides A and C, the tyrosyl radical reduction rate at pL 9 (PCET) was significantly decreased compared to that at pL 11 (ET). This effect was also observed when model tyrosine at pL 9 was compared to tyrosinate. No significant SIE was found on any of the decay reactions in the peptide samples. We report that the rate of tyrosyl radical decay is increased in both peptides compared to that in model tyrosine/tyrosinate. Corresponding increases were observed in the rates of decay of the S_1 excited state and solvated electron. Finally, at pL 9, we found that the reaction rate was altered when H14 in Peptide A was replaced with Cha in Peptide C. ET rates at pL 11 were insensitive to this substitution, implying that the mutation alters the PCET reaction mechanism but not the ET reaction mechanism.

2.5.4 Mechanism of the Tyrosyl-Radical PCET Reaction

The decay of tyrosyl radical at pL 9 is an orthogonal PCET reaction, in which the radical recombines with the solvated electron. In model tyrosine solutions, the source of the proton is the borate buffer ($pK_a = 9.2$). In the averaged, minimized structure of Peptide

A, there is no direct hydrogen bond between Y5 and H14. Instead, Y5 makes a short hydrogen bond to R16. Structural dynamics in Peptide A can be assessed in a preliminary fashion by examining distances in the 20 lowest-energy structures.[52] When examining the ensemble, Y5 and H14 sample distances of less than 3 Å in a significant number of these structures; hydrogen bonds to arginine are formed in most of the remaining set. However, all intramolecular hydrogen bonds in the peptide compete with hydrogen-bonding interactions with solvating water. Therefore, in Peptide A, the source of the proton in the PCET reaction is likely to be either histidine or borate buffer, in competing proton-donation pathways. In Peptide C, H14 is not present, and borate buffer is expected to be the proton donor.

PCET reactions can proceed by three different mechanisms (Figure 2.11): proton first (PTET), electron first (ETPT), and a concerted pathway (CPET) in which electron and proton are transferred through the same transition state and no intermediate is produced.[1, 53-54] A PTET mechanism seems unlikely for the reactions studied here, given the low pK_a value of the tyrosyl radical.[23] Also, the generation of a protonated tyrosyl cation radical is spectroscopically distinguishable from that of the neutral tyrosyl radical,[26, 35, 55-56] and the protonated tyrosyl radical was not observed in our TRAS experiments.

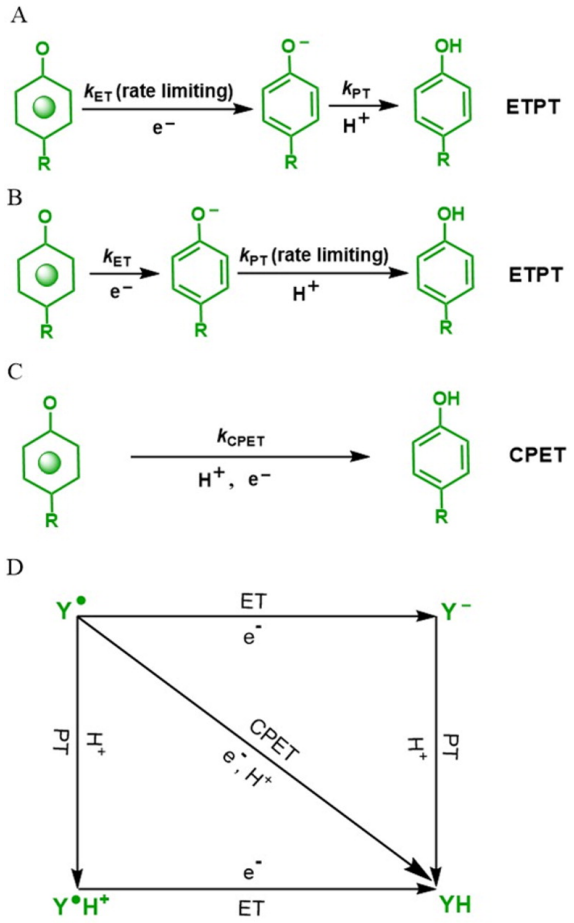

Figure 2.11(A–C) Mechanisms for tyrosyl radical reduction by PCET: (A) ETPT (ET is rate-limiting), (B) ETPT (PT is rate-limiting), and (C) CPET. (D) Overview of PCET for tyrosyl radical (Y•) decay, corresponding to stepwise ETPT (top to right), concerted PT and ET (CPET, diagonal), or stepwise PTET (top to bottom).

For the ETPT mechanism, there are two possibilities (Figure 2.11); either electron transfer or proton transfer can be rate-limiting. However, rate-limiting proton transfer seems unlikely. For ETPT, there will be a favorable driving force for proton transfer at pL 9, once the tyrosyl radical is reduced to tyrosinate (pK_a 10). Also, for ETPT with a rate-limiting PT step, a solvent isotope effect and an increase in rate at low pH values are expected; neither result was obtained in our study. Therefore, an ETPT mechanism with a rate-limiting proton-transfer step seems improbable.

This leaves two possible mechanisms (Figure 2.11): ETPT, in which electron transfer is rate-limiting, and CPET, in which proton and electron are transferred through the same transition state with no intermediate. For rate-limiting ET, solvent isotope effects are expected to be small, as observed in this study. However, while the ETPT mechanism, with ET rate-limiting, can account for the lack of a solvent isotope effect, this mechanism cannot readily account for the decrease in rate when the pH decreases or for the effect of the H14-to-Cha14 mutation.

Therefore, a CPET mechanism seems the most likely explanation for these data. This coupled mechanism (Figure 2.11) can account for the effect of the H14-to-Cha mutation (see below) and the decrease of the rate at pL 9 compared to pL 11. The slowing of the CPET reaction at pL 9 relative to ET at pL 11 is explained by the higher solvent reorganization energies[32], which are known to determine the rates of CPET reactions[57-59]. Note that the question of the expected pH dependence of CPET reactions is complex and has been much discussed.[60-65]

Although detailed theoretical treatments have been applied to CPET reactions,[57, 66-70] a Marcus-type treatment has also been used.[31-32] Employing a Marcus-type treatment and assuming a CPET mechanism, the accelerating effect of H14 on the reaction can be rationalized. The electron acceptor, the neutral tyrosyl radical, is the same in both Peptides A and C. Further, the Y5 peak potentials are similar in Peptides A and C.[16-17] Also, the distances for proton and electron transfer to tyrosyl radical are assumed to be comparable in the two peptides, because these reactions involve the solvated electron and solvating borate buffer in both cases. However, note that H14 can function as a proton donor to tyrosyl radical in some members of the dynamic ensemble. The pK_a values of the primary

proton donors (borate buffer and histidine) are similar in the two peptide samples. The pK_a of borate buffer is 9.2; the pK_a of H14 has been modeled as ~9 in the tyrosyl radical state of Peptide A.[17] Based on this predicted pK_a value, H14 is expected to be protonated in approximately one-half of the tyrosyl-radical-containing sample at pL 9.

Based on these considerations and assumptions, we propose that H14 increases the rate by decreasing the reorganization energy necessary for CPET in Peptide A. This can be rationalized with a microscopic explanation that proposes two roles for H14 in CPET. In a subset of molecules in the dynamic ensemble, H14 serves as a direct proton donor to the Y5 tyrosyl radical. In this subset, H14 and Y5 radical are within hydrogen-bonding distance. In other members of the ensemble, in which Y5 radical is closer to R16, H14 facilitates proton transfer through hydrogen-bonded water molecules to the Y5 tyrosyl radical. The imidazolium cation is known to form strong hydrogen bonds as a proton donor to water.[71-72] Therefore, protonated H14 will facilitate proton transfer through these adjacent water molecules to the tyrosyl radical. Substitution of Cha at position 14 eliminates both of these interactions and thus decreases the rate of CPET in Peptide C. Providing precedent for this interpretation, a site-directed mutation in an enzyme, methylamine dehydrogenase, has been shown to decrease reorganization energy for ET by changing the position of bound water molecules.[73]

2.5.5 Decay Kinetics of the S_1 State and the Solvated Electron Correlate with Tyrosyl Radical Kinetics

The decay rates of the S_1 excited state and the solvated electron correlate with the alterations observed in the rate of tyrosyl radical decay under different conditions and in

different samples. A correlation between the kinetics of the solvated electron and tyrosyl radical is expected because the mechanism of decay involves their recombination.[13, 35] Assuming that ionization to form the radical is fast and rate-limiting, the correlation with S_1 decay kinetics is due to competition of radical generation with parallel decay pathways. As tyrosyl radical decay slows, S_1 decay slows, because the rate-limiting step in excited-state deactivation has decreased in rate.

2.5.6 Comparison of ET and PCET Decay Rates at pL 9 and 11

In all samples examined here, the rates of tyrosyl radical reduction, S_1 decay, and solvated electron decay were decreased at pL 9 relative to those at pL 11. The driving forces for the reaction at pL 9 and 11 differ. However, as we previously discussed,[8] when this factor is considered, ET rates are actually predicted to be higher at pH 9. Therefore, changes in the driving force alone do not account for this observation. This acceleration is observed both in Peptide A and Peptide C and thus seems to be independent of noncovalent interactions with the tyrosyl radical. Indeed, the same decrease in low-pH rate is observed in model tyrosine. Another possibility is that the protonation of the amino terminus has an electrostatic effect, decreasing the rate of electron transfer at pH 9. However, the expectation would be that the presence of the positive charge on the tyrosine amino group or peptide amino terminus would increase the reduction rate of the radical.[18] Considering all of these factors, our interpretation is that the decrease of the rate at pL 9 is due to the increase in solvent reorganization energy, which is known to accompany a CPET reaction but is not associated with ET at pL 11.

2.5.7 Solvent Isotope Effects

CPET reactions can be accompanied by substantial solvent isotope effects. However, solvent isotope effects for CPET reactions are variable and have been shown to depend on donor–acceptor distance[58, 74-78] and driving force.[64, 74, 79-80] Previous work showed that CPET reactions can be accompanied by small or insignificant solvent isotope effects under some conditions.[11, 32] Therefore, our results on the peptides, which had SIE values of approximately 1 at pL 9, can be rationalized by a CPET mechanism with a negligible SIE. However, more experiments are necessary to address this point.

One intriguing result presented here concerns the inverse SIE in model tyrosine at pL 9. This observation distinguishes the tyrosine CPET mechanism from the Peptide C mechanism, although the sources of electron (solvated electron) and proton (borate buffer) are the same. An inverse isotope effect can be caused by an inverse fractionation factor, favoring the X–D bond.[37] Reactions involving metal-bound water molecules or cysteine side chains are known to have low reactant-state fractionation factors[81] and can give rise to inverse solvent isotope effects, but neither explanation can rationalize the results obtained here. Other possible explanations for inverse solvent isotope effects are low-barrier hydrogen bonds, which can exhibit a preference for deuterium[82] and a decrease in reaction entropy, caused by a change in hydrogen bonding, solvation, and librational frequencies.[83]

At pL 9, model tyrosine experiences intramolecular interactions between the π electrons of the phenol ring and the protonated amino terminus.[84] This interaction is likely to persist in the radical state of model tyrosine. This change in hydrogen-bonding interaction is a key distinguishing feature when tyrosine and the peptides are compared and might account for the unique, inverse SIE in tyrosine. Note that no SIE was observed in a

recent report concerning aqueous phenol photoionization.[35] Because phenol lacks the terminal amino group of tyrosine, that previous report supports the interpretation that the inverse isotope effect in tyrosine results from a phenolic–ammonium group interaction. We hypothesize that the phenolic–ammonium group interaction produces a low reactant-state fractionation factor. The inverse SIE is not observed at pL 11; this would be expected because the amino group is not protonated at this pL value. As precedent for this interpretation, a low fractionation factor and an inverse isotope effect were observed in the methanolysis and hydrolysis of β-lactams in a β-lactamase. This result was attributed to the interaction of an active-site tyrosine with two lysine-derived ammonium groups.[85]

2.5.8 Electronic Coupling Increases the Rate of Tyrosyl Radical Reduction in Peptides A and C

The results presented here confirm that the rates of the PCET and ET reactions are increased in peptides, regardless of a change in sequence, relative to those in model tyrosine/tyrosinate. This supports our earlier suggestion[8] that an increase in electronic coupling, mediated by the peptide backbone, may increase the rates of ET and PCET reactions. This explanation was based on previous reports showing that the peptide bond can increase coupling for ET reactions (reviewed in refs [86-87]). However, an additional rate effect due to a change in reorganization energy cannot be ruled out at this time.

2.5.9 Peptide Conformational Changes Associated with PCET

Our previous UV Raman results provided evidence that PCET in Peptides A and C is accompanied by a redox-induced conformational change.[12] This change was detected as a loss of amide II intensity in D_2O buffers, which was associated with radical formation

and was more pronounced for Peptide A at pL 9 than at pL 11. This spectral change was also observed in Peptide C at pL 9 but not at pL 11. This result was attributed to a partial loss of β-strand character in the radical state of the peptides. Importantly, the conformational change was found to be reversible.[12] This conformational change could alter the distance between H14 and Y5. However, the possibility of this structural rearrangement does not alter our interpretation of the mechanism or of the impact of H14. H14 remains in close structural proximity to Y5 in the radical state, as judged by the effect of Y5 oxidation on the pK_a value of H14.[16-17]

2.5.10 Comparison to CPET in PSII

Our results suggest that specific donor–acceptor interactions can increase the rate of a CPET reaction through a decrease in reorganization energy. This result has important implications for understanding PCET in complex enzymes and has an interesting parallel in PSII mechanism. In PSII, a long-lived YD radical, located on position Y160 of the D2 subunit, is hydrogen-bonded to His189 in D2.[7] Proton transfer from YD radical to His189 occurs and was observed as infrared-detectable changes in the N–H stretching bands of the imidazole side chain.[88] In parallel with the results reported here, mutations at His189 were shown to decrease the rate of tyrosyl radical decay (at pH 7.5). These rate changes were partially reversed by chemical complementation with imidazole. A subsequent pH study and proton inventory showed that this YD radical reduction reaction occurs by a CPET mechanism at pH values greater than 7.5. [36, 89] At low pH, the rate of YD radical reduction increases, and the reaction converts to a PTET mechanism.[89] Fits to the proton inventory data (at pL 8) suggested that the YD CPET reaction is mediated by two proton-transfer pathways. One involves a single proton, which might originate from His189, and the

second involves multiple protons, which might originate from water.[36] This interpretation of the PSII data is similar to the mechanism proposed here for CPET in Peptide A. This comparison suggests that mutations at His189 can decrease the YD CPET rate through an alteration in reorganization energy.

2.6 Conclusions

We found that CPET and ET reactions in the maquettes are facilitated by electronic coupling in the peptide backbone. Although there is no significant SIE on CPET in the peptides, CPET in model tyrosine proceeds with an inverse solvent isotope effect. A comparison of Peptides A and C yields new information concerning the mechanism of PCET in Peptide A and the kinetic consequences of H14 and its cross-strand interaction with Y5. These results rationalize and parallel previous observations concerning a His-Tyr pair in PSII.

2.7 References

1. Warren, J. J.; Mayer, J. M. Moving Protons and Electrons in Biomimetic Systems. *Biochemistry* **2015,** *54*, 1863-1878.

2. Migliore, A.; Polizzi, N. F.; Therien, M. J.; Beratan, D. N. Biochemistry and Theory of Proton-Coupled Electron Transfer. *Chem Rev* **2014,** *114*, 3381-465.

3. Weinberg, D. R.; Gagliardi, C. J.; Hull, J. F.; Murphy, C. F.; Kent, C. A.; Westlake, B. C.; Paul, A.; Ess, D. H.; McCafferty, D. G.; Meyer, T. J. Proton-Coupled Electron Transfer. *Chem. Rev.* **2012,** *112*, 4016-93.

4. Dempsey, J. L.; Winkler, J. R.; Gray, H. B. Proton-Coupled Electron Flow in Protein Redox Machines. *Chem. Rev.* **2010,** *110*, 7024-39.

5. Reece, S. Y.; Hodgkiss, J. M.; Stubbe, J.; Nocera, D. G. Proton-Coupled Electron Transfer: The Mechanistic Underpinning for Radical Transport and Catalysis in Biology. *Phil. Trans. Roy. Soc. B* **2006,** *361*, 1351-1364.

6. Minnihan, E. C.; Nocera, D. G.; Stubbe, J. Reversible, Long-Range Radical Transfer in *E. Coli* Class Ia Ribonucleotide Reductase. *Acc. Chem. Res.* **2013,** *46*, 2524-35.

7. Barry, B. A. Proton Coupled Electron Transfer and Redox Active Tyrosines in Photosystem Ii. *J. Photochem. Photobiol. B* **2011,** *104*, 60-71.

8. Pagba, C. V.; Chi, S. H.; Perry, J.; Barry, B. A. Proton-Coupled Electron Transfer in Tyrosine and a Beta-Hairpin Maquette: Reaction Dynamics on the Picosecond Time Scale. *J Phys Chem B* **2015,** *119*, 2726-36.

9. Koo, B. J.; Huynh, M.; Halbach, R. L.; Stubbe, J.; Nocera, D. G. Modulation of Phenol Oxidation in Cofacial Dyads. *J Am Chem Soc* **2015,** *137*, 11860-3.

10. Glover, S. D.; Jorge, C.; Liang, L.; Valentine, K. G.; Hammarstrom, L.; Tommos, C. Photochemical Tyrosine Oxidation in the Structurally Well-Defined Alpha3y Protein: Proton-Coupled Electron Transfer and a Long-Lived Tyrosine Radical. *J. Am Chem Soc* **2014,** *136*, 14039-51.

11. Megiatto Jr, J. D.; Méndez-Hernández, D. D.; Tejeda-Ferrari, M. E.; Teillout, A.-L.; Llansola-Portolés, M. J.; Kodis, G.; Poluektov, O. G.; Rajh, T.; Mujica, V.; Groy, T. L. A Bioinspired Redox Relay That Mimics Radical Interactions of the Tyr–His Pairs of Photosystem Ii. *Nature chemistry* **2014,** *6*, 423.

12. Pagba, C. V.; Barry, B. A. Redox-Induced Conformational Switching in Photosystem-Ii-Inspired Biomimetic Peptides: A Uv Resonance Raman Study. *J. Phys. Chem. B* **2012,** *116*, 10590-9.

13. Chen, X.; Larsen, D. S.; Bradforth, S. E.; van Stokkum, I. H. Broadband Spectral Probing Revealing Ultrafast Photochemical Branching after Ultraviolet Excitation of the Aqueous Phenolate Anion. *J. Phys .Chem. A* **2011,** *115*, 3807-19.

14. Costentin, C.; Robert, M.; Savéant, J.-M.; Tard, C. H-Bond Relays in Proton-Coupled Electron Transfers. Oxidation of a Phenol Concerted with Proton Transport to a Distal Base through an Oh Relay. *Physical Chemistry Chemical Physics* **2011,** *13*, 5353-5358.

15. Hammarström, L.; Styring, S. Proton-Coupled Electron Transfer of Tyrosines in Photosystem Ii and Model Systems for Artificial Photosynthesis: The Role of a Redox-Active Link between Catalyst and Photosensitizer. *Energy & Environmental Science* **2011,** *4*, 2379-2388.

16. Sibert, R.; Josowicz, M.; Porcelli, F.; Veglia, G.; Range, K.; Barry, B. A. Proton-Coupled Electron Transfer in a Biomimetic Peptide as a Model of Enzyme Regulatory Mechanisms. *J Am Chem Soc* **2007,** *129*, 4393-400.

17. Sibert, R. S.; Josowicz, M.; Barry, B. A. Control of Proton and Electron Transfer in De Novo Designed, Biomimetic Beta Hairpins. *ACS Chem Biol* **2010,** *5*, 1157-68.

18. Reece, S. Y.; Stubbe, J.; Nocera, D. G. Ph Dependence of Charge Transfer between Tryptophan and Tyrosine in Dipeptides. *Biochim. Biophys. Acta* **2005,** *1706*, 232-8.

19. Carra, C.; Iordanova, N.; Hammes-Schiffer, S. Proton-Coupled Electron Transfer in a Model for Tyrosine Oxidation in Photosystem Ii. *Journal of the American Chemical Society* **2003,** *125*, 10429-10436.

20. Sjödin, M.; Styring, S.; Akermark, B.; Sun, L.; Hammarström, L. The Mechanism for Proton-Coupled Electron Transfer from Tyrosine in a Model Complex and Comparisons with Yz Oxidation in Photosystem Ii. *Phil. Trans. Royal Soc. B* **2002,** *357*, 1471-1478.

21. Sobolewski, A.; Domcke, W.; Dedonder-Lardeux, C.; Jouvet, C. Excited-State Hydrogen Detachment and Hydrogen Transfer Driven by Repulsive 1 Πσ* States: A New Paradigm for Nonradiative Decay in Aromatic Biomolecules. *Physical Chemistry Chemical Physics* **2002,** *4*, 1093-1100.

22. Creed, D. The Photophysics and Photochemistry of the near-Uv Absorbing Amino Acids–Ii. Tyrosine and Its Simple Derivatives. *Photochemistry and photobiology* **1984,** *39*, 563-575.

23. Dixon, W. T.; Murphy, D. Determination of the Acidity Constants of Some Phenol Radical Cations by Means of Electron Spin Resonance. *J. Chem. Soc. London, Faraday Trans. II* **1976,** *72*, 1221-1230.

24. Feitelson, J.; Hayon, E. Electron Ejection and Electron Capture by Phenolic Compounds. *The Journal of Physical Chemistry* **1973,** *77*, 10-15.

25. Atherton, N.; Land, E.; Porter, G. Relative Electron Spin Distributions in Anilino and Phenoxyl Radicals. *Transactions of the Faraday Society* **1963,** *59*, 818-823.

26. Land, E. J.; Porter, G.; Strachan, E. Primary Photochemical Processes in Aromatic Molecules. *Trans. Faraday Soc.* **1961,** *57*, 1885-1893.

27. Sobolewski, A. L.; Domcke, W. Photoinduced Electron and Proton Transfer in Phenol and Its Clusters with Water and Ammonia. *The Journal of Physical Chemistry A* **2001,** *105*, 9275-9283.

28. Barry, B. A.; Babcock, G. T. Tyrosine Radicals Are Involved in the Photosynthetic Oxygen-Evolving System. *Proc. Nat. Acad. Sci. USA* **1987,** *84*, 7099-7103.

29. Marcus, R. A. Electron Transfer Reactions in Chemistry: Theory and Experiment. *Pure Appl. Chem.* **1997,** *69*, 13-29.

30. Moser, C. C.; Keske, J. M.; Warncke, K.; Farid, R. S.; Dutton, P. L. Nature of Biological Electron Transfer. *Nature* **1992,** *355*, 796-802.

31. Mayer, J. M. A Simple Marcus-Theory Type Model for Hydrogen Atom Transfer/Proton-Coupled Electron Transfer. *J .Phys. Chem. Lett.* **2011,** *2*, 1481-1489.

32. Rhile, I. J.; Markle, T. F.; Nagao, H.; DiPasquale, A. G.; Lam, O. P.; Lockwood, M. A.; Rotter, K.; Mayer, J. M. Concerted Proton-Electron Transfer in the Oxidation of Hydrogen Bonded Phenols. *J. Am. Chem. Soc.* **2006,** *128*, 6075-6088.

33. Berry, B. W.; Martínez-Rivera, M. C.; Tommos, C. Reversible Voltammograms and a Pourbaix Diagram for a Protein Tyrosine Radical. *Proceedings of the National Academy of Sciences* **2012,** *109*, 9739-9743.

34. Harriman, A. Further Comments on the Redox Potentials of Tryptophan and Tyrosine. *J. Phys. Chem.* **1987,** *91*, 6102-6104.

35. Oliver, T. A.; Zhang, Y.; Roy, A.; Ashfold, M. N.; Bradforth, S. E. Exploring Autoionization and Photoinduced Proton-Coupled Electron Transfer Pathways of Phenol in Aqueous Solution. *The journal of physical chemistry letters* **2015,** *6*, 4159-4164.

36. Jenson, D. L.; Barry, B. A. Proton-Coupled Electron Transfer in Photosystem Ii: Proton Inventory of a Redox Active Tyrosine. *J Am Chem Soc* **2009,** *131*, 10567-73.

37. Schowen, K. B.; Schowen, R. L. Solvent Isotope Effects of Enzyme Systems. *Methods in Enzymology* **1982,** *87*, 551-606.

38. Chaudhry, A. F.; Verma, M.; Morgan, M. T.; Henary, M. M.; Siegel, N.; Hales, J. M.; Perry, J. W.; Fahrni, C. J. Kinetically Controlled Photoinduced Electron Transfer Switching in Cu (I)-Responsive Fluorescent Probes. *Journal of the American Chemical Society* **2009,** *132*, 737-747.

39. Kovalenko, S.; Dobryakov, A.; Ruthmann, J.; Ernsting, N. Femtosecond Spectroscopy of Condensed Phases with Chirped Supercontinuum Probing. *Physical review A* **1999,** *59*, 2369.

40. Bent, D. V.; Hayon, E. Excited State Chemistry of Aromatic Amino Acids and Related Peptides. I. Tyrosine. *Journal of the American Chemical Society* **1975,** *97*, 2599-2619.

41. Martin, R. B.; Edsall, J. T.; Wetlaufer, D. B.; Hollingworth, B. R. A Complete Ionization Scheme for Tyrosine, and the Ionization Constants of Some Tyrosine Derivatives. *Journal of Biological Chemistry* **1958,** *233*, 1429-1435.

42. Edsall, J. T.; Martin, R. B.; Hollingworth, B. R. Ionization of Individual Groups in Dibasic Acids, with Application to the Amino and Hydroxyl Groups of Tyrosine *Proc. Natl. Acad. Sci. USA* **1958,** *44*, 505-519.

43. Range, K.; Ayala, I.; York, D.; Barry, B. A. Normal Modes of Redox-Active Tyrosine: Conformation Dependence and Comparison to Experiment. *J. Phys. Chem. B* **2006,** *110*, 10970-10981.

44. Zhang, Y.; Oliver, T. A.; Ashfold, M. N.; Bradforth, S. E. Contrasting the Excited State Reaction Pathways of Phenol and Para-Methylthiophenol in the Gas and Liquid Phases. *Faraday Discuss* **2012,** *157*, 141-63; discussion 243-84.

45. Hermann, R.; Mahalaxmi, G.; Jochum, T.; Naumov, S.; Brede, O. Balance of the Deactivation Channels of the First Excited Singlet State of Phenols: Effect of Alkyl Substitution, Sterical Hindrance, and Solvent Polarity. *The Journal of Physical Chemistry A* **2002,** *106*, 2379-2389.

46. Baugher, J.; Grossweiner, L. Photolysis Mechanism of Aqueous Tyrosine and Tyrosyl Peptides. *Photochemistry and Photobiology* **1978,** *28*, 175-184.

47. Feitelson, J. On the Mechanism of Fluorescence Quenching. Tyrosine and Similar Compounds. *The Journal of Physical Chemistry* **1964,** *68*, 391-397.

48. Land, E.; Porter, G. Primary Photochemical Processes in Aromatic Molecules. Part 7.—Spectra and Kinetics of Some Phenoxyl Derivatives. *Transactions of the Faraday Society* **1963,** *59*, 2016-2026.

49. Iqbal, A.; Pegg, L.-J.; Stavros, V. G. Direct Versus Indirect H Atom Elimination from Photoexcited Phenol Molecules. *The Journal of Physical Chemistry A* **2008,** *112*, 9531-9534.

50. Tseng, C.-M.; Lee, Y. T.; Lin, M.-F.; Ni, C.-K.; Liu, S.-Y.; Lee, Y.-P.; Xu, Z.; Lin, M. Photodissociation Dynamics of Phenol. *The Journal of Physical Chemistry A* **2007,** *111*, 9463-9470.

51. Guzow, K.; Ganzynkowicz, R.; Rzeska, A.; Mrozek, J.; Szabelski, M.; Karolczak, J.; Liwo, A.; Wiczk, W. Photophysical Properties of Tyrosine and Its Simple Derivatives Studied by Time-Resolved Fluorescence Spectroscopy, Global Analysis, and Theoretical Calculations. *The Journal of Physical Chemistry B* **2004,** *108*, 3879-3889.

52. Pagba, C. V.; McCaslin, T. G.; Veglia, G.; Porcelli, F.; Yohannan, J.; Guo, Z.; McDaniel, M.; Barry, B. A. A Tyrosine-Tryptophan Dyad and Radical-Based Charge Transfer in a Ribonucleotide Reductase-Inspired Maquette. *Nature Comm.* **2015,** *10010*.

53. Huynh, M. H.; Meyer, T. J. Proton-Coupled Electron Transfer. *Chem Rev* **2007,** *107*, 5004-64.

54. Mayer, J. M.; Rhile, I. J. Thermodynamics and Kinetics of Proton-Coupled Electron Transfer: Stepwise Vs. Concerted Pathways. *Biochim Biophys Acta* **2004,** *1655*, 51-8.

55. Das, T. N. Oxidation of Phenol in Aqueous Acid: Characterization and Reactions of Radical Cations Vis-a-Vis the Phenoxyl Radical. *The Journal of Physical Chemistry A* **2005,** *109*, 3344-3351.

56. Gadosy, T.; Shukla, D.; Johnston, L. Generation, Characterization, and Deprotonation of Phenol Radical Cations. *The Journal of Physical Chemistry A* **1999,** *103*, 8834-8839.

57. Hammes-Schiffer, S.; Stuchebrukhov, A. A. Theory of Coupled Electron and Proton Transfer Reactions. *Chem. Rev.* **2010,** *110*, 6939-60.

58. Edwards, S. J.; Soudackov, A. V.; Hammes-Schiffer, S. Analysis of Kinetic Isotope Effects for Proton-Coupled Electron Transfer Reactions. *J Phys Chem A* **2009,** *113*, 2117-26.

59. Navrotskaya, I.; Hammes-Schiffer, S. Electrochemical Proton-Coupled Electron Transfer: Beyond the Golden Rule. *J Chem Phys* **2009,** *131*, 024112.

60. Savéant, J.-M. Concerted Proton-Electron Transfers: Fundamentals and Recent Developments. *Annual review of analytical chemistry* **2014,** *7*, 537-560.

61. Keough, J.; Zuniga, A.; Jenson, D. L.; Barry, B. A. Redox Control and Hydrogen Bonding Networks: Proton-Coupled Electron Transfer Reactions and Tyrosine Z in the Photosynthetic Oxygen-Evolving Complex. *J. Phys. Chem. B* **2013,** *117*, 1296−1307.

62. Bonin, J.; Costentin, C.; Louault, C.; Robert, M.; Saveant, J. M. Water (in Water) as an Intrinsically Efficient Proton Acceptor in Concerted Proton Electron Transfers. *J. Am. Chem. Soc.* **2011,** *133*, 6668-74.

63. Keough, J.; Jenson, D. L.; Zuniga, A.; Barry, B. A. Proton Coupled Electron Transfer and Redox-Active Tyrosine Z in the Photosynthetic Oxygen Evolving Complex. *J. Am. Chem. Soc.* **2011,** *133*, 11084-11087.

64. Bonin, J.; Costentin, C.; Louault, C.; Robert, M.; Routier, M.; Savéant, J.-M. Intrinsic Reactivity and Driving Force Dependence in Concerted Proton-Electron Transfers to Water Illustrated by Phenol Oxidation. *Proc. Nat. Acad. Sci. USA* **2010,** *107*, 3367-3372.

65. Irebo, T.; Reece, S. Y.; Sjödin, M.; Nocera, D. G.; Hammarström, L. Proton-Coupled Electron Transfer of Tyrosine Oxidation: Buffer Dependence and Parallel Mechanisms. *J. Am. Chem. Soc.* **2007,** *129*, 15462-15464.

66. Liu, Y.; Liu, H.; Song, K.; Xu, Y.; Shi, Q. Theoretical Study of Proton Coupled Electron Transfer Reactions: The Effect of Hydrogen Bond Bending Motion. *The Journal of Physical Chemistry B* **2015,** *119*, 8104-8114.

67. Cukier, R. In *Proton-Coupled Electron Transfer Reactions: A Theoretical Approach*, ACS Symp. Ser, 2004; pp 145-158.

68. Cukier, R. I. Theory and Simulation of Proton-Coupled Electron Transfer, Hydrogen Atom Transfer, and Proton Translocation in Proteins. *Biochimica et Biophysica Acta* **2004,** *1655*, 37-44.

69. Hammes-Schiffer, S. Theoretical Perspectives on Proton-Coupled Electron Transfer Reactions. *Accounts of chemical research* **2001,** *34*, 273-281.

70. Cukier, R. I.; Nocera, D. G. Proton-Coupled Electron Transfer. *Annual review of physical chemistry* **1998,** *49*, 337-369.

71. Jain, A.; Ramanathan, V.; Sankararamakrishnan, R. Lone Pair··· Π Interactions between Water Oxygens and Aromatic Residues: Quantum Chemical Studies Based on High-Resolution Protein Structures and Model Compounds. *Protein Science* **2009,** *18*, 595-605.

72. Scheiner, S.; Kar, T.; Pattanayak, J. Comparison of Various Types of Hydrogen Bonds Involving Aromatic Amino Acids. *Journal of the American Chemical Society* **2002,** *124*, 13257-13264.

73. Davidson, V. L. Electron Transfer in Quinoproteins. *Archives of biochemistry and biophysics* **2004,** *428*, 32-40.

74. Hammes-Schiffer, S. Proton-Coupled Electron Transfer: Moving Together and Charging Forward. *J Am Chem Soc* **2015,** *137*, 8860-71.

75. Markle, T. F.; Rhile, I. J.; Mayer, J. M. Kinetic Effects of Increased Proton Transfer Distance on Proton-Coupled Oxidations of Phenol-Amines. *J Am Chem Soc* **2011,** *133*, 17341-52.

76. Hatcher, E.; Soudackov, A. V.; Hammes-Schiffer, S. Proton-Coupled Electron Transfer in Soybean Lipoxygenase: Dynamical Behavior and Temperature Dependence of Kinetic Isotope Effects. *J Am Chem Soc* **2007,** *129*, 187-96.

77. Klinman, J. P. The Role of Tunneling in Enzyme Catalysis of C-H Activation. *Biochimica et Biophysica Acta* **2006,** *1757*, 981-987.

78. Hatcher, E.; Soudackov, A. V.; Hammes-Schiffer, S. Proton-Coupled Electron Transfer in Soybean Lipoxygenase. *J Am Chem Soc* **2004,** *126*, 5763-75.

79. Edwards, S. J.; Soudackov, A. V.; Hammes-Schiffer, S. Driving Force Dependence of Rates for Nonadiabatic Proton and Proton-Coupled Electron Transfer: Conditions for Inverted Region Behavior. *J Phys Chem B* **2009,** *113*, 14545-8.

80. Rhile, I. J.; Mayer, J. M. One-Electron Oxidation of a Hydrogen-Bonded Phenol Occurs by Concerted Proton-Coupled Electron Transfer. *J. Am. Chem. Soc.* **2004,** *126*, 12718-12719.

81. Quinn, D. M.; Sutton, L. D. Theoretical Basis and Mechanistic Utility of Solvent Isotope Effects. *Enzyme mechanism from isotope effects* **1991,** *3*, 73-126.

82. Cleland, W. Low-Barrier Hydrogen Bonds and Low Fractionation Factor Bases in Enzymic Reactions. *Biochemistry* **1992,** *31*, 317-319.

83. Mitton, C. G.; Gresser, M.; Schowen, R. L. Catalysis in Ester Cleavage. Iii. Solvent Isotope Effects and Transition-State Solvation in the Basic Methanolysis of Esters. *Journal of the American Chemical Society* **1969,** *91*, 2045-2047.

84. Zhang, M.; Huang, Z.; Lin, Z. Systematic Ab Initio Studies of the Conformers and Conformational Distribution of Gas-Phase Tyrosine. *The Journal of chemical physics* **2005,** *122*, 134313.

85. Page, M. I.; Vilanova, B.; Layland, N. J. Ph Dependence of and Kinetic Solvent Isotope Effects on the Methanolysis and Hydrolysis Of. Beta.-Lactams Catalyzed by Class C. Beta.-Lactamase. *Journal of the American Chemical Society* **1995,** *117*, 12092-12095.

86. Giese, B.; Graber, M.; Cordes, M. Electron Transfer in Peptides and Proteins. *Current opinion in chemical biology* **2008,** *12*, 755-759.

87. Beratan, D. N.; Onuchic, J. N.; Winkler, J. R.; Gray, H. B. Electron-Tunneling Pathways in Proteins. *Science* **1992,** *258*, 1740-1742.

88. Kim, S.; Liang, J.; Barry, B. A. Chemical Complementation Identifies a Proton Acceptor for Redox-Active Tyrosine D in Photosystem Ii. *Proc. Nat. Acad. Sci. USA* **1997,** *94*, 14406-14411.

89. Jenson, D. L.; Evans, A.; Barry, B. A. Proton-Coupled Electron Transfer and Tyrosine D of Photosystem Ii. *J Phys Chem B* **2007,** *111*, 12599-604.

CHAPTER 3. REDOX-DRIVEN CONFORMATIONAL DYNAMICS IN A PHOTOSYSTEM-II-INSPIRED β-HAIRPIN MAQUETTE DETERMINED THROUGH SPECTROSCOPY AND SIMULATION

Reprinted with permission from *The Journal of Physical Chemistry B*

Hwang, H.; McCaslin, T. G.; Hazel, A.; Pagba, C. V.; Nevin, C. M.; Pavlova, A.; Barry, B. A.; Gumbart, J. C. *J. Phys. Chem. B* **2017**, *121*, 3536-3545

3.1 Abstract

Tyrosine-based radical transfer plays an important role in photosynthesis, respiration, and DNA synthesis. Radical transfer can occur either by electron transfer (ET) or proton coupled electron transfer (PCET), depending on the pH. Reversible conformational changes in the surrounding protein matrix may control reactivity of radical intermediates. De novo designed Peptide A is a synthetic 18 amino-acid β-hairpin, which contains a single tyrosine (Y5) and carries out a kinetically significant PCET reaction between Y5 and a cross-strand histidine (H14). In Peptide A, amide II′ (CN) changes are observed in the UV resonance Raman (UVRR) spectrum, associated with tyrosine ET and PCET; these bands were attributed previously to a reversible change in secondary structure. Here, we use molecular dynamics simulations to define this conformational change in Peptide A and its H14-to-cyclohexylalanine variant, Peptide C. Three different Y5 charge states, tyrosine (YH), tyrosinate (Y^-), and neutral tyrosyl radical ($Y\cdot$), are considered. The simulations show that Peptide A-YH and A-Y^- retain secondary structure and noncovalent interactions, whereas A-$Y\cdot$ is unstable. In contrast, both Peptide C-Y^- and Peptide C-$Y\cdot$ are unstable, due to the loss of the Y5-H14 π–π interaction. These simulations are consistent with previous UVRR experimental results on the two β-hairpins. Furthermore, they demonstrate the ability of simulations using fixed-charge force fields to accurately capture redox-linked conformational dynamics in a β-strand peptide.

3.2 Introduction

Photosynthesis, respiration, and DNA synthesis involve essential electron transfer (ET) reactions. When these reactions operate at high potential, aromatic amino acids can

play important roles in the mechanism. Redox-active tyrosine residues are known to be catalytically important in cytochrome c oxidase,[1-2] ribonucleotide reductase (RNR),[3] photosystem II (PSII),[4-5] and other enzymes, such as prostaglandin H synthase,[6] galactose oxidase,[7] glyoxyl oxidase,[8] and *Mycobacterium tuberculosis* catalase-peroxidase.[9] Tyrosine side chains can participate in ET reactions either by tunneling or by hopping (multistep tunneling) mechanisms (reviewed in refs [10-12]). For outer sphere reactions, Marcus ET theory[13] predicts the dependence of the electron transfer rate (k_{ET}) on temperature (T), driving force (ΔG^o), nuclear reorganization energy (λ), and the electronic coupling (H_{AB}) between the reactants and products.

The pK_a of the tyrosine phenolic group is approximately 10,[14] while the pK_a of the phenolic group is below zero after oxidation of tyrosine.[15] Therefore, oxidation of tyrosine forms a neutral radical both at low and high pH. When the pH is above the pK_a of tyrosine (>10, Figure 3.1), oxidation of tyrosine proceeds by an ET reaction.[16] When the pH is below the pK_a, (<10, Figure 3.1), oxidation occurs via a proton coupled electron transfer (PCET) reaction, yielding both an electron and a proton. The PCET reaction can occur by three distinct mechanisms, proton first (PTET), electron first (ETPT), or a coupled movement of proton and electron (CPET) through the same transition state. The factors that control PCET reactions have been the focus of theory and experiment in a wide variety of model systems and proteins.[10-12, 17]

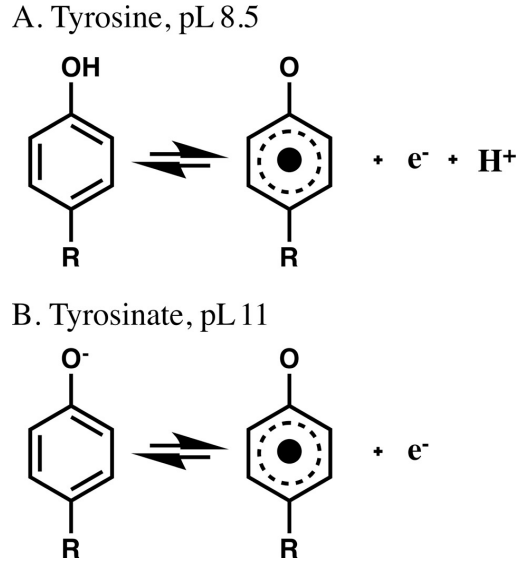

Figure 3.1(A) Tyrosine and its PCET reaction to form a neutral tyrosyl radical and (B) tyrosinate and its ET reaction to form a neutral tyrosyl radical. The reaction in (A) occurs at pL/pD 8.5; the reaction in (B) occurs at pL/pD 11 (L is the lyonium ion).

In the investigation of ET and PCET mechanisms, peptides provide simple, water-soluble scaffolds. The use of unnatural amino acids in these scaffolds opens up new avenues for chemistry. The construction and study of such peptide models or maquettes has provided valuable insight into biological reactions (for previous examples, see refs [18-30]).

To model tyrosine-based PCET in a β-hairpin, an 18-amino-acid sequence, Peptide A (Figure 3.2C), which contains a single tyrosine (Y5) and a histidine (H14),[25, 27] was synthesized and characterized. The NMR structure of the peptide was determined, and it was shown that the peptide folds to form a β-hairpin. The Y5 and H14 are π–π stacked but not hydrogen bonded in the averaged, minimized structure.[31] Electrochemical data are consistent with a PCET reaction between histidine and tyrosine, when the tyrosyl radical is generated in the mid-pH range from singlet tyrosine. Oxidation of tyrosine results in a

change in histidine pK_a, which leads to a proton transfer to the imidazole side chain. This reaction has been shown to be kinetically important in time-resolved absorption measurements on the picosecond time scale.[32-33] Interestingly, UV resonance Raman (UVRR) studies, which maintained the oxidized state for orders of magnitude greater time scales, have suggested that the tyrosine PCET/ET reaction is accompanied by a reversible conformational change, attributed to a loss of β-strand interactions in Peptide A.[34] While the change could be observed in Peptide A either at pD 8.5 or 11, in a variant of Peptide A, in which H14 is replaced with cyclohexylalanine (Cha14, Peptide C, Figure 3.2D), the amide II′ bands were only detected at the lower pD value. Previous CD studies showed that both peptides experienced a reversible thermal transition at low and high pH values.[25, 27]

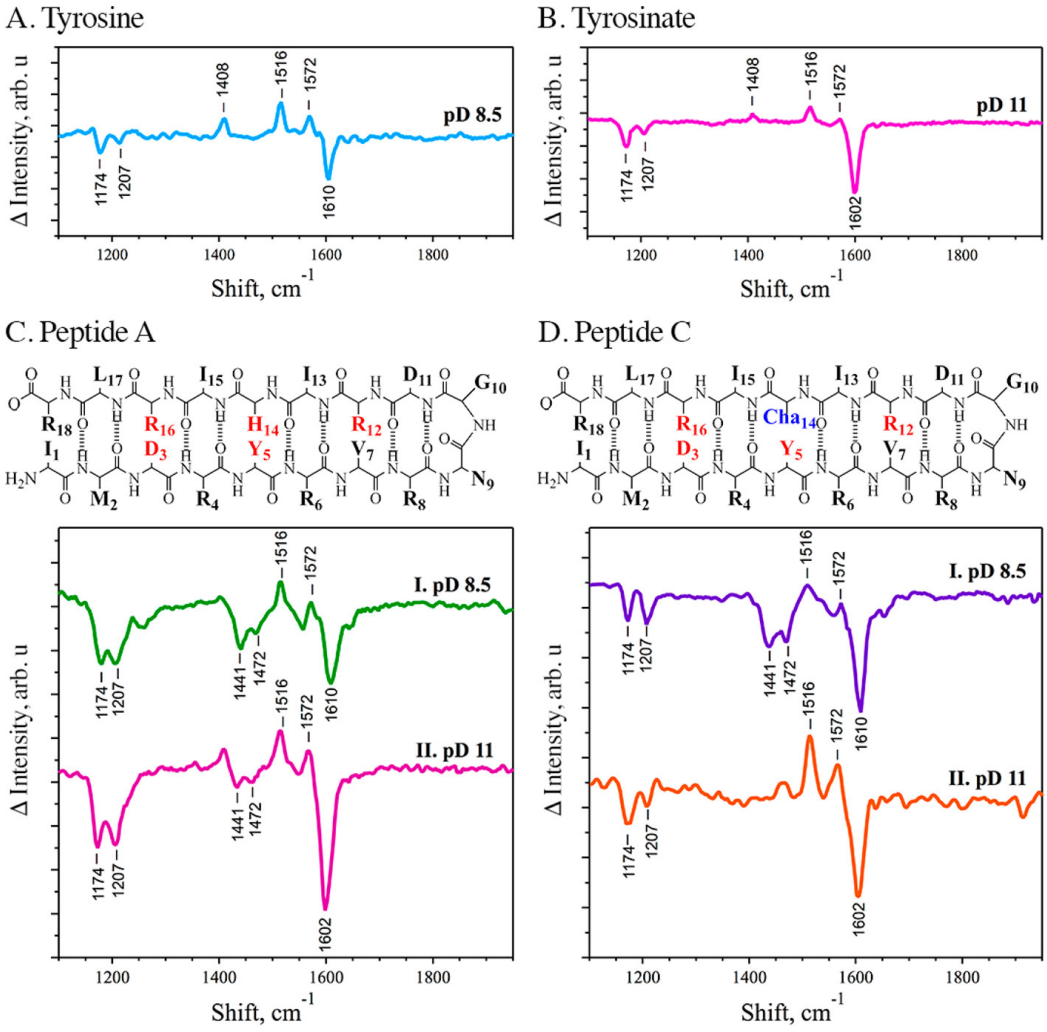

Figure 3.2 UVRR difference spectra, primary sequences, and predicted secondary structures. UVRR difference spectra (radical-minus-singlet) acquired from (A) tyrosine, pD 8.5, or (B) tyrosinate, pD 11 solution. Sequences and predicted fold of Peptide A (C) and its His14 to Cha14 variant, Peptide C (D). UVRR difference spectra (radical-minus-singlet) acquired from (C) Peptide A-YH at pD 8.5 (I) or Peptide A-Y^- at pD 11 (II) and from (D) Peptide C-YH at pD 8.5 (I) or Peptide C-Y^- at pD 11 (II). The difference spectra were calculated as radical-minus-singlet. A 244 nm Raman probe beam was utilized. The data are reproduced from ref [34].

The potential contribution of protein motions in ET and PCET reactions has been discussed extensively.[11, 17, 35-38] Here, we investigate those motions using molecular dynamics simulations. In the simulations, we observed redox-induced conformational

changes in two β-hairpin maquettes, Peptide A and Peptide C, which rationalize experimental spectroscopic data.

3.3 Methods

3.3.1 Molecular Dynamics Simulations

The three-dimensional, averaged, and minimized structure of Peptide A (sequence IMDRYRVRNGDRIHIRLR), determined by NMR spectroscopy,[31] was used as an initial structure. In Peptide A, H14 is singly protonated at the epsilon nitrogen. Because this histidine has an estimated pK_a of 7.0 when Y5 is in a reduced state and 8.0 when Y5 is in an oxidized, radical state,[25] roughly 3% of His14 in Peptide A-YH and 25% of His14 in Peptide A-Y· are doubly protonated at pD 8.5 in the UVRR experiments. Therefore, we also built a system in which H14 is doubly protonated.

Peptide C was built by replacing H14 with cyclohexylalanine (Cha14). For each variant, three different conditions were simulated to observe the conformational change and stability depending on the charge state of Y5. We denote these charge states Peptide A/C-YH (tyrosine), Peptide A/C-Y^- (charged tyrosine, tyrosinate), and Peptide A/C-Y· (neutral tyrosyl radical) based on the charge state of Y5 (see Figure 3.1).

Because parameters for the tyrosyl radical are not present for the CHARMM protein force field, we optimized the partial atomic charges for this residue using the Force Field Toolkit in VMD.[39-40] A reduced model for the side chain, truncated at CG (see Figure 3.3) , was used. We fitted the interaction energies with water molecules in molecular dynamics to those in quantum chemical calculations, as is standard in the CHARMM force

field.[41] Because the restricted open-shell approach was shown to be more accurate than the unrestricted one for phenoxyl radical calculations with MP2 and HF methods,[42] this approach was used for geometry optimization of the radical state and for determining the interaction energies with water molecules. The geometry was optimized at the ROMP2(6-31G*) level of theory and the interaction energies with water molecules were calculated at the ROHF(6-31G*) level of theory. Gaussian09 was used for all QM calculations.[43] Only the charges of the phenol group were modified; the resulting MM interaction energies with water were within 0.2 kcal/mol of the target QM energies, as recommended for CHARMM parameters.[41] The resulting charges for Y·, shown in Table 3.1 and Figure 3.3, produce an electrostatic potential qualitatively similar to one previously determined based on hybrid-functional calculations using B3LYP/6-311++G(3df,2p).[25]

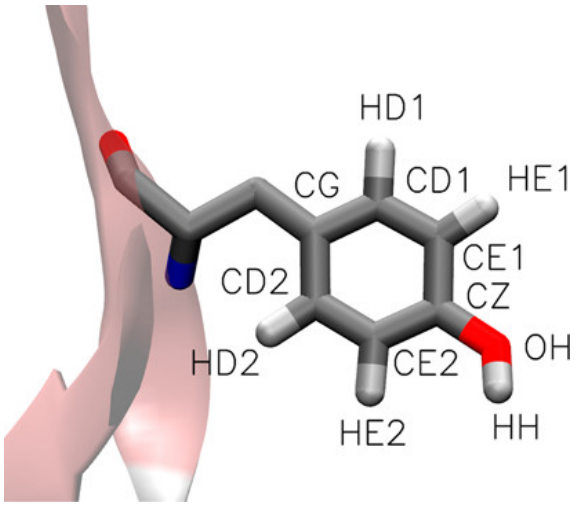

Figure 3.3 Phenol group of YH/Y⁻/Y·, with labels matching those in Table 3.1

Table 3.1 Partial Atomic Charges of the Side Chain of YH/Y⁻/Y·[a]

NAME	Tyrosine (YH)	Tyrosinate (Y−)	Radical (Y•)
HH	0.43		
OH	-0.54	-0.76	-0.205
CZ	0.11	0.40	-0.994
CE1/CE2	-0.115	-0.60	0.344
HE1/HE2	0.115	0.28	0.134
CD1/CD2	-0.115	-0.115	0.369
HD1/HD2	0.115	0.115	0.027
CG	0.00	0.00	-0.549

[a] The charges for YH and Y− are directly taken from CHARMM36.

All peptide models were solvated with TIP3P water and ions to neutralize the system in 100 mM NaCl. The initial size of the periodic box was 55 × 55 × 51 Å, providing 20–30 Å between periodic images of the protein in all three directions. Each system was minimized for 1000 steps, and the solvent was equilibrated while the peptide backbone was restrained for 2 ns. All analysis was done on 200-ns unrestrained production runs. Molecular dynamics simulations were carried out with NAMD[44] using the CHARMM36 force field[45]. A 2-fs time step was used. Bonded and short-range nonbonded interactions

were calculated every time step, while long-range electrostatics were calculated every other time step using the particle-mesh Ewald (PME) method.[46] The long-range cutoff was set to 12 Å with a potential-based switching function starting at 10 Å. The temperature was maintained at 300 K using Langevin dynamics, and the pressure was kept constant at 1 atm using the Langevin piston method. System setup and analysis were performed in VMD.[40]

3.3.2 UV Resonance Raman Spectroscopy

The 18-mer peptides were synthesized by solid state synthesis and were obtained from Genscript USA Inc. (Piscataway, NJ) or New England Peptide (Gardner, MA). Samples were suspended in a D_2O buffer containing 5 mM sodium borate and *N*-cyclohexyl-3-aminopropanesulfonic acid (CAPS), pD 11, or 5 mM *N*-tris(hydroxymethyl)-methyl-3-aminopropanesulfonic acid (TAPS), pD 8.5, to give 1 mM solutions. The pD is reported as the uncorrected meter reading because the small solvent isotope effects on weak acid pK_a values are compensated for by the D_2O-induced changes in the response of the glass electrode.[47-48] The use of D_2O buffer is necessary to observe the amide II′ band, which results from uncoupling of the ND stretch and CN stretch of the amide bond. The frequency of the amide II′ band is sensitive to secondary structure.[34]

Spectra were obtained at room temperature using a 244 nm probe beam generated from an intracavity frequency-doubled argon ion laser (Cambridge LEXEL 95, Fremont, CA). The method has been described previously.[34, 49] The probe was coupled to a Raman microscope (Renishaw inVia, Hoffman Estates, IL) equipped with UV-coated, deep depletion charge-coupled device. The sample (1 mL) was recirculated at a rate of 4.5 mL/min using a peristaltic pump and a focused jet to prevent UV degradation of the sample.

The radical was generated by UV photolysis with increasing power of the probe beam, described previously. The high power-minus-low power (radical-minus-singlet) difference spectrum was obtained by subtracting an averaged 340 μW from an averaged 3.4 mW scan. A total of 16 low-power scans (240 s) and 8 high-power scans (120 s) were averaged from an 8 mL sample. Previous control experiments have shown that the peptide mass is not altered by procedure. Additional details of the experimental procedures have been described previously.[34]

3.4 Results

3.4.1 Samples and UV Resonance Raman Spectroscopy

For Peptides A and C, three charge states of the tyrosine side chain were considered. In the first, predominant at pD 8.5, Y5 is in the protonated form (YH). In the second, predominant at pD 11, the Y5 side chain is anionic (Y^-). In the third, the tyrosine side chain is oxidized by one electron and deprotonated, forming a neutral radical ($Y\cdot$) at both pD values.

Figure 3.2A,B presents UVRR difference spectra, associated with oxidation of tyrosine/tyrosinate model compounds to form a neutral tyrosyl radical. The data were obtained at two different pD values in D_2O buffer. These different spectra are associated with the generation of the radical by UV photolysis under continuous illumination.[34, 50] With UV laser probes, the vibrational spectrum of phenolic compounds is resonantly enhanced.[51] Assignments of the tyrosine, tyrosinate, and tyrosyl radical spectra have been established by previous experimental and theoretical work.[50, 52-53] Tyrosine or tyrosinate oxidation leads to spectral changes including a decrease in the frequency of the Y8a ring

stretching mode and a dramatic increase in the frequency of the CO stretching mode. Positive bands reflect unique bands of the radical state; negative bands reflect unique bands of the starting, singlet YH or Y^- state. At pD 8.5 (Figure 3.2A), characteristic negative bands of tyrosine at 1174, 1207, and 1610 cm^{-1} were observed; characteristic positive bands of tyrosyl radical were observed at 1408, 1516, and 1572 cm^{-1}. The spectrum at pD 11 (Figure 3.2B) is similar to the spectrum acquired at pD 8.5, except for the expected shift of the Y8a ring stretching mode to 1602 cm^{-1}, due to deprotonation of the side chain.[50, 54] See refs for reviews of normal mode assignments.[50, 52-53]

UVRR difference spectra were also obtained from Peptides A and C at pD 8.5 (Figure 3.2C, I, and D, I). At this pD value, both peptides are in the YH state. The spectrum derived from Peptide A-YH (Figure 3.2C, I) contains negative bands at 1441 and 1472 cm^{-1}, which are not observed in tyrosinate or tyrosine model compound (see Figure 3.2A,B) Previous work has established that these negative bands are assignable to amide II′ bands.[34] These bands are negative due to a loss of Raman intensity in the radical state with 244 nm excitation. This loss of intensity was attributed previously to a red shift of the UV electronic spectrum of the peptide backbone.[34] Such a red shift can be associated with a loss of β-strand structure,[55-56] which is driven by the YH to Y· reaction in Peptide A. Negative amide II′ bands are also observed in the Peptide A-Y^-spectrum at pD 11, indicating that the putative change in structure may also occur in the Y^- to Y· reaction. However, for Peptide C (Figure 3.2D, I and II), the amide II′ bands are not observed at pD 11 (Y^- to Y·), although the bands are present at pD 8.5 (YH to Y·). This result implies that the YH to Y· reaction causes a conformational change in Peptide C, but that the Y^- to Y· reaction does not result in the same hydrogen bonding rearrangement in Peptide C.

3.4.2 Molecular Dynamics Simulations

We focus our analysis and presentation on β-hairpin stability and its dynamics to provide a detailed view of molecular interactions and structural information probed in the CD and UVRR experiments presented above. The conformational stability of the β-hairpin conformation of Peptide A and Peptide C and their variants was examined for three independent conventional MD simulations and one accelerated MD simulation of each system, giving a total of 7.0 μs for all simulations reported here. The below figures include the number of interchain backbone hydrogen bonds, radius of gyration, and distance between Y5 and residue 14 (histidine or cyclohexylalanine). The data are reported for all simulation runs on Peptide A and Peptide C in their three charge states: YH, Y^-, and $Y^\cdot$. Although the $Y^\cdot$ state is extremely short-lived in vitro (picoseconds), it is maintained in the UVRR experiments for time scales exceeding those of the simulations.

3.4.3 Simulations of Peptide A

To describe the model's conformational dynamics, the per-residue secondary structure assignment as a function of time was examined over the entire simulation. Figure 3.4A shows that Peptide A-YH retained its β-hairpin structure, i.e., the secondary structure of residues 4–7 and 12–15 exhibited no change in two out of three runs. In run 3, although Peptide A-YH lost β-sheet structure after 50 ns, it did not unfold but rather showed a propensity to recover its β-hairpin structure, preserving a long β-turn in the middle. Similarly, two out of three runs for Peptide A-Y^- were consistent with a stable β-hairpin conformation (see Figure 3.4B).

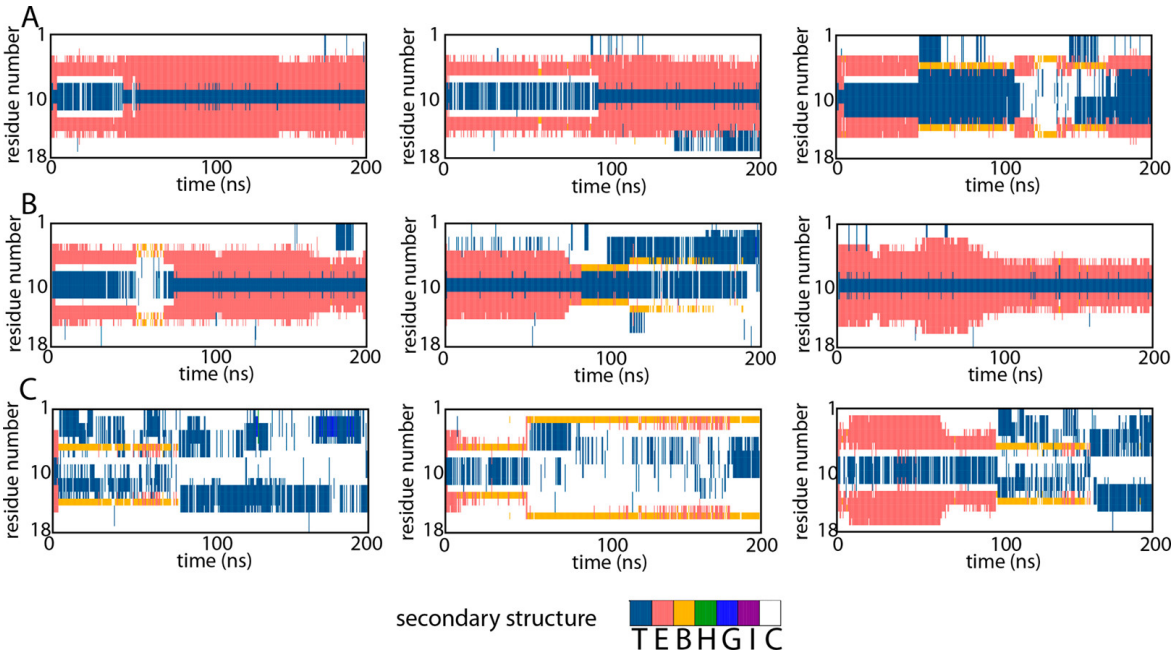

Figure 3.4 Time evolution of secondary-structure assignment per residue of Peptide A charge states for all three runs. Extension of the first run to 400 ns is presented in Figure 3.5. The legend at the bottom uses DSSP classification as implemented in Stride[57] where T is β turn, E is β sheet, B is β bridge, H is α helix, G is 3_{10} helix, I is π helix, and C is unstructured coil. (A) Peptide A-YH. (B) Peptide A-Y^{-}. (C) Peptide A-Y·.

In contrast to Peptide A-YH and A-Y^{-}, Peptide A-Y· was observed to unfold, with loss of β-hairpin structure in all three runs (see Figures 3.4C and 3.6). However, during the first 50 ns of run 3, the peptide retained some β-bridge structure, interstrand hydrogen bonds, a stable Y5-H14 distance, and a relatively low radius of gyration. Retention of the overall fold immediately after radical generation is consistent with time-resolved absorption experiments on the 20-ps to 2-ns time scale, which have been used to study tyrosyl radical PCET in these peptides.[32-33] However, the peptide reaches the unfolded state on time scales greater than 50 ns, in agreement with the longer-time-scale UVRR experiments, supporting the experimental implication that oxidation of tyrosine results in a conformational transition from β-strand to extended form in Peptide A. Because we

estimate ~3% of His14 is doubly protonated when Y5 is in a reduced state and ~25% is doubly protonated when Y5 is in a radical state, we also simulated Peptide A-YH and Peptide A-Y· with a charged His14 for 200-ns each. Similar to their neutral His14 variants, we found Peptide A-YH to maintain its β-hairpin, while Peptide A-Y· unfolded (see Figure 3.7).

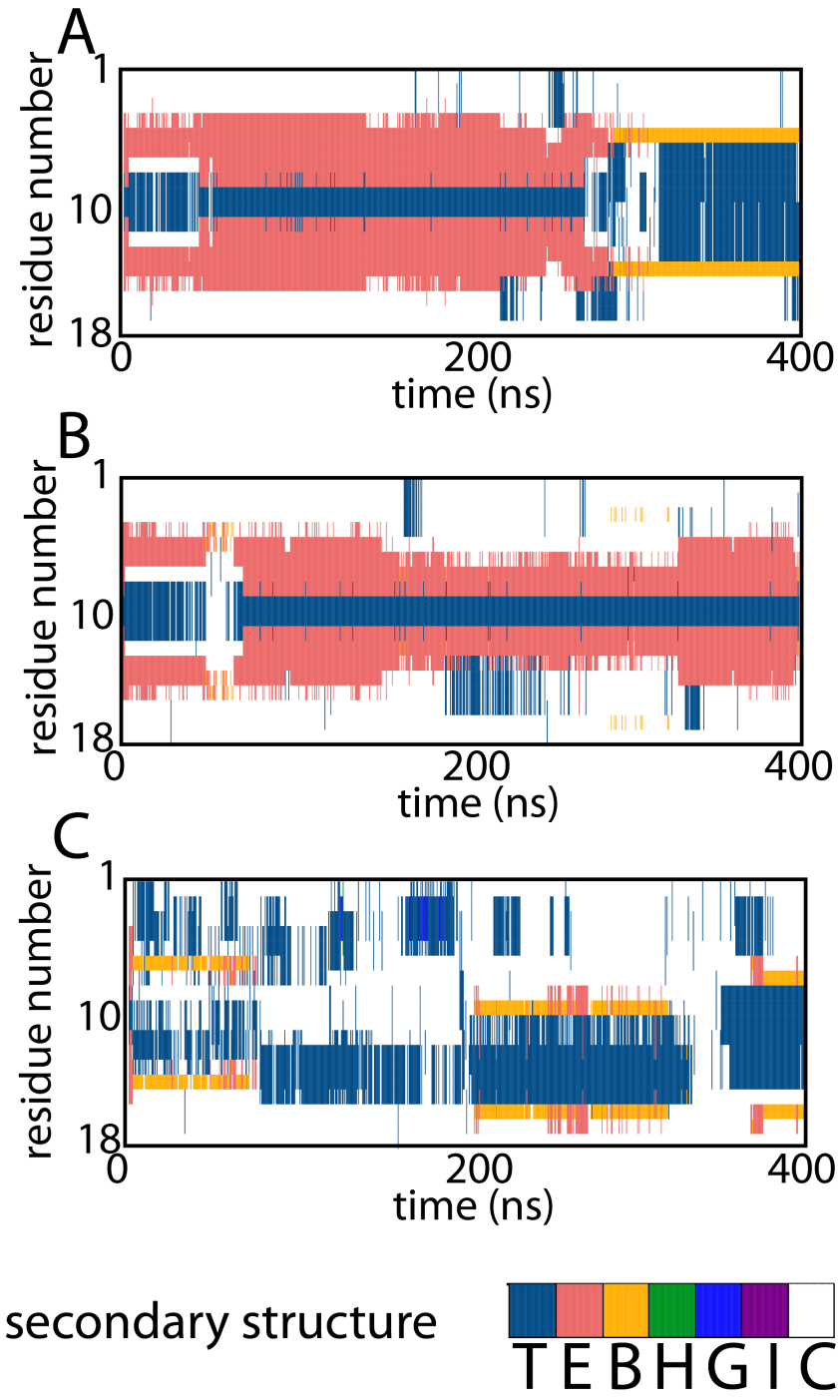

Figure 3.5 Time evolution of secondary-structure assignment per residue of Peptide A charge states for the first run extended to 400ns. The legend at the bottom uses DSSP classification as implemented in Stride where T is β turn, E is β sheet, B is β bridge, H is α helix, G is 310 helix, I is π helix, and C is unstructured coil. (A) Peptide A-YH. (B) Peptide A-Y–. (C) Peptide A-Y•.

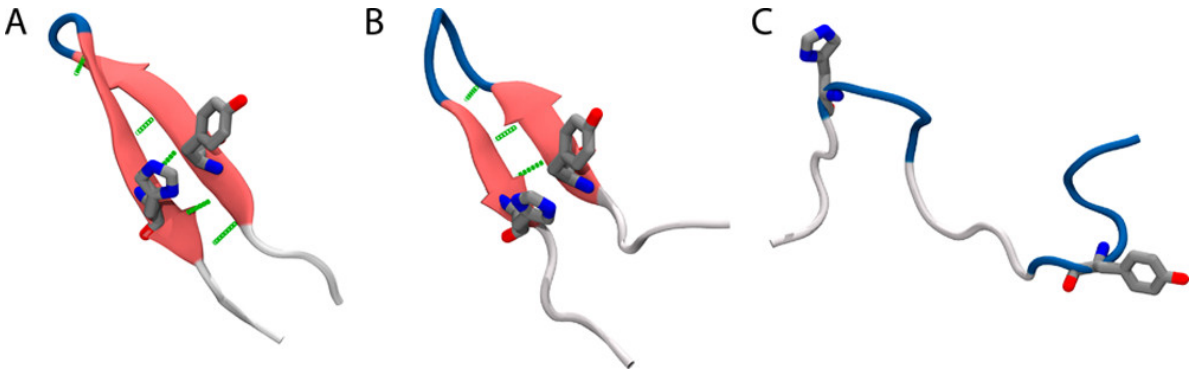

Figure 3.6 Examples of observed structures of (A) Peptide A-YH, (B) Peptide A-Y^{-}, and (C) Peptide A-Y$^{\cdot}$ from run 1 of each.

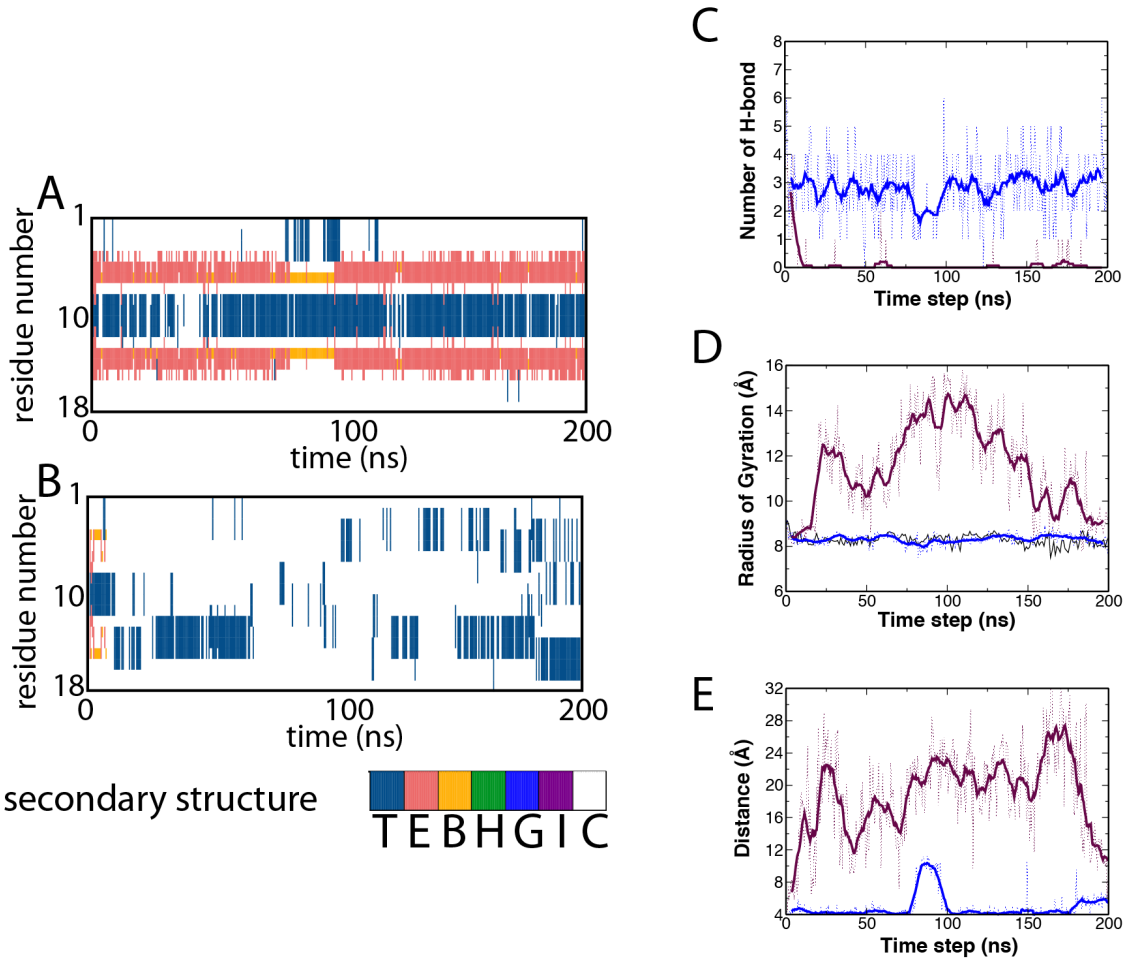

Figure 3.7 Protonated His14 variants. (A,B) Time evolution of secondary-structure assignment per residue of (A) Peptide A-YH and (B) Peptide A-Y•. (C) Number of backbone hydrogen bonds vs. time for Peptide A-YH (blue) and Peptide A-Y•

(maroon). (D) Radius of gyration vs. time for Peptide A-YH (blue) and Peptide A-Y• (maroon). (E) Distance between Y5/Y• and H14 vs. time for Peptide A-YH (blue) and Peptide A-Y• (maroon).

Because the 200 ns simulations may not be converged, we took two alternative approaches. First, we extended one of the three runs for an additional 200 ns (400 ns total). Shown in Figure 3.5, Peptide A-YH switches from a predominantly β-strand to β-turn structure after approximately 250 ns, while Peptide A-Y^- and Peptide A-$Y^{\cdot}$ remain the same. Second, we ran 300 ns accelerated MD (aMD) simulations, in which a "boost" potential is applied to enhance sampling of high-energy configurations.[58] The probability of the number of native hydrogen bonds was determined after reweighting the trajectories (see Figures 3.8 and 3.9). Peptide A-YH had the highest average number of backbone hydrogen bonds (6.7 out of a possible 8), while Peptide A-Y^- and Peptide A-$Y^{\cdot}$ had averages of 2.9 and 3.7, respectively. Although the average number of hydrogen bonds for Peptide A-$Y^{\cdot}$ is apparently increased relative to Peptide A-Y^-, we note that the probability for more than 4 hydrogen bonds is predicted to be zero only for Peptide A-$Y^{\cdot}$ (see Figure 3.9). However, given that a few samples dominate the probability distribution after reweighting (see Figure 3.9) , a known problem,[59-60] the aMD simulations are also unlikely to be converged.

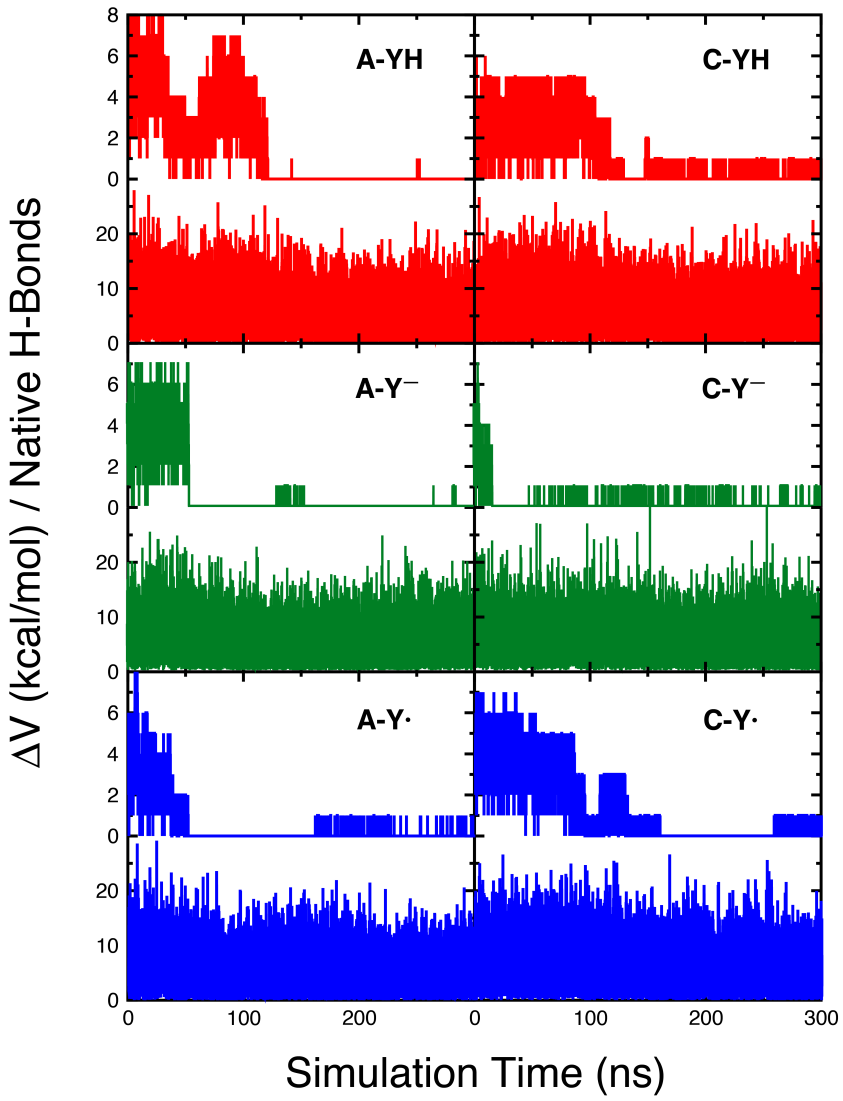

Figure 3.8 aMD trajectories. For each system, number of hydrogen bonds (top) and aMD boost (ΔV) values (bottom) were calculated every 10 ps. Peptide A-YH and Peptide C-YH are shown in red. Peptide A-Y– and Peptide C-Y– are shown in green. Peptide A-Y• and Peptide C-Y• are shown in blue.

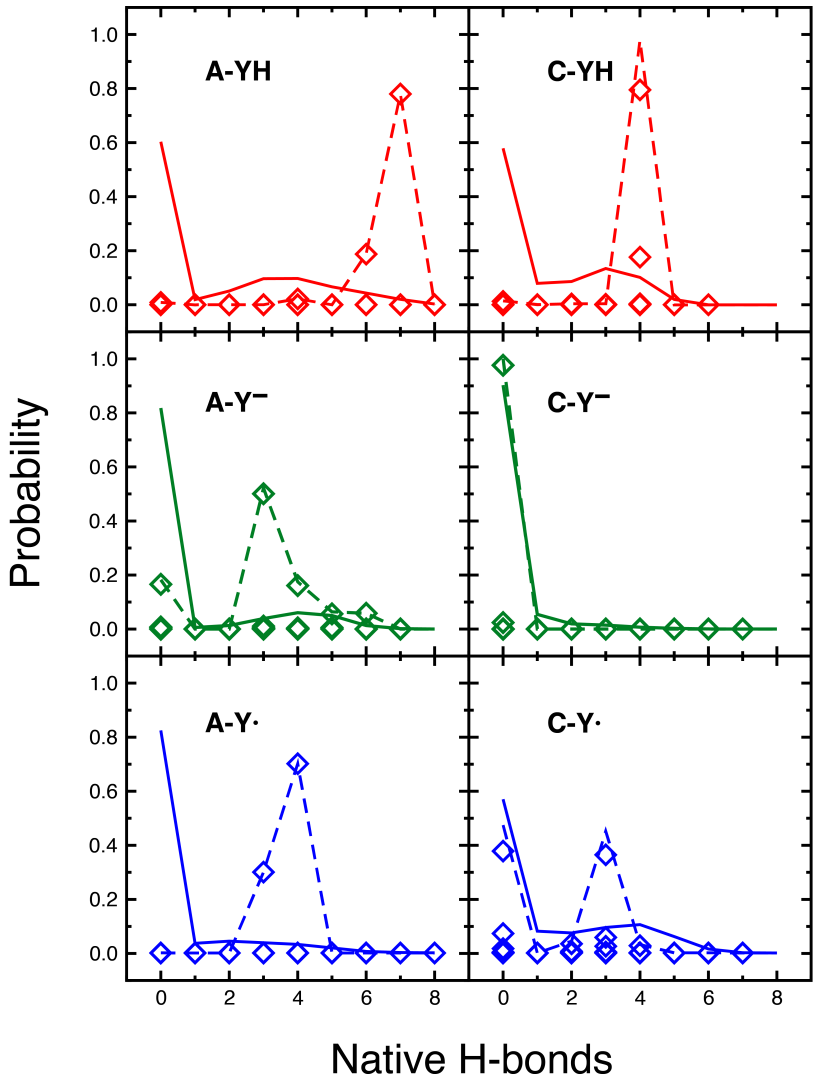

Figure 3.9 aMD trajectory weights, unweighted distributions, and reweighted distributions. (Diamonds) Weights, w_i calculated for all aMD trajectory points. (Solid lines) Unweighted probability distributions for each aMD trajectory. (Dashed lines) Peptide A-YH and Peptide C-YH are shown in red. Peptide A-Y– and Peptide C-Y– are shown in green. Peptide A-Y• and Peptide C-Y• are shown in blue.

Analyses of backbone hydrogen bonding support the results of the secondary structure analysis and are consistent with a redox-induced change in the Peptide-A β-hairpin. Figure 3.10A shows that interstrand hydrogen bonds are stable, enabling Peptide A-YH and Peptide A-Y$^-$ to remain folded in a β-hairpin conformation during their entire trajectory, while there were almost no interstrand hydrogen bonds for Peptide A-Y$\cdot$ after

100 ns (see Figure 3.10A, red). This result is further supported by analysis of the radius of gyration (R_g), which is an indicator of compactness of a protein (see Figure 3.10B). Peptide A-YH and Peptide A-Y^- remained compact, with R_g values that did not change by more than 2 Å from their native state. The folded-to-unfolded state transition of Peptide A-$Y^{\cdot}$ is characterized by a significant increase in R_g (see Figure 3.10B, red). This increase in R_g after 75 ns reflects the structural changes associated with the loss of backbone hydrogen bonding.

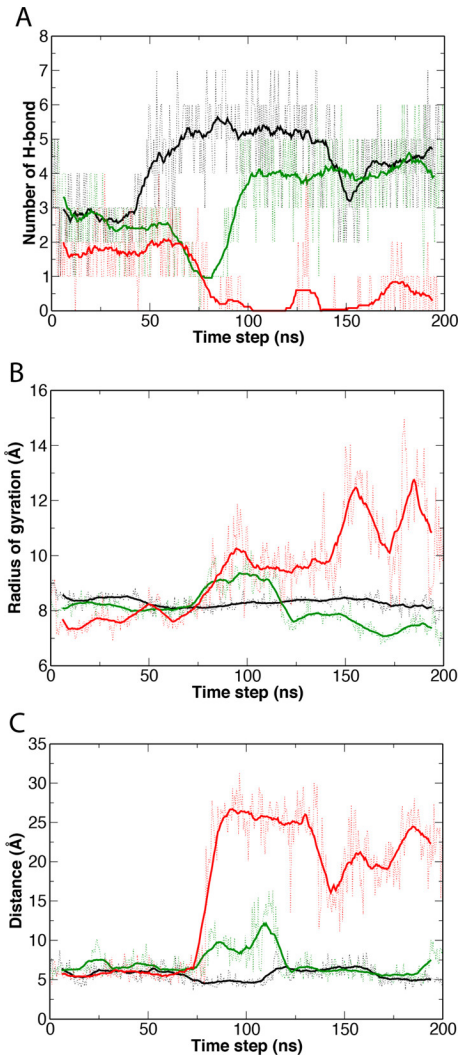

Figure 3.10 Structural parameters measured during simulations of Peptide A. In all panels, black curves are from run 1 of Peptide YH, green from Peptide A-Y^{-}, and red from Peptide A-$Y^{\cdot}$. Other runs are presented in Figure 3.11, 3.12, 3.13. (A) Number of backbone hydrogen bonds for each Peptide-A variant. (B) Radius of gyration. (C) Distance between Y5/$Y5^{-}$/$Y5^{\cdot}$ and H14 of Peptide A.

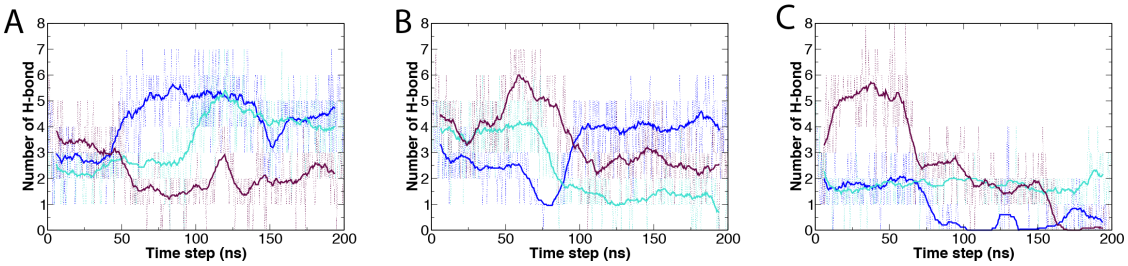

Figure 3.11 Number of backbone hydrogen bonds for each Peptide-A variant. In each panel, the three colors denote three independent runs. (A) Peptide A-YH. (B) Peptide A-Y–. (C) Peptide A-Y•.

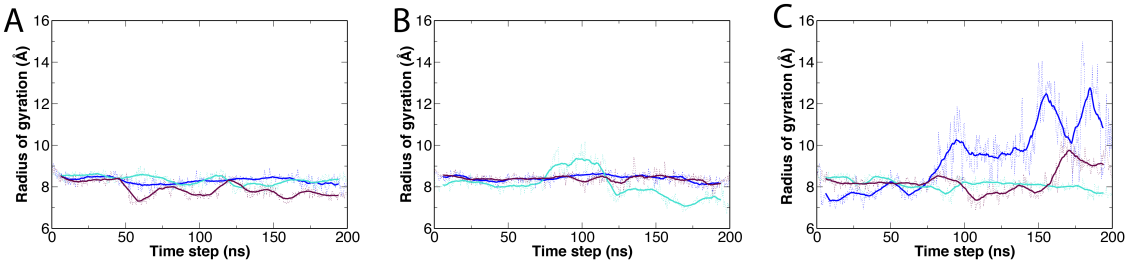

Figure 3.12 Radius of gyration for each Peptide-A variant. In each panel, the three colors denote three independent runs. (A) Peptide A-YH. (B) Peptide A-Y–. (C) Peptide A-Y•.

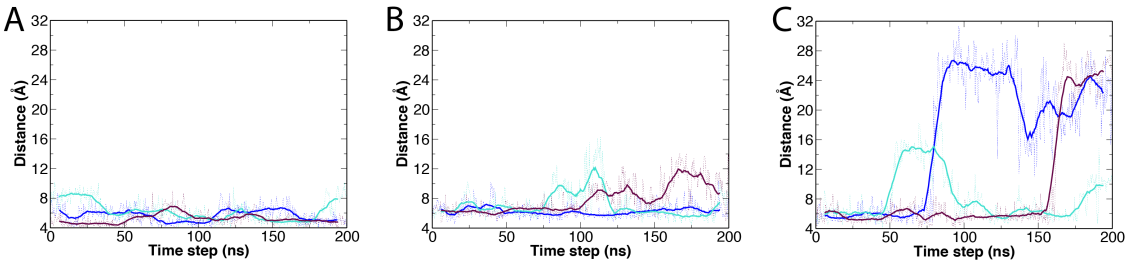

Figure 3.13 Distance between Y5/Y–/Y• and H14 for each Peptide-A variant. In each panel, the three colors denote three independent runs. (A) Peptide A-YH. (B) Peptide A-Y–. (C) Peptide A-Y•.

We hypothesized that the stabilities of Peptide A-YH and Peptide A-Y^{-} are a result of the π–π interaction between Y5/$Y5^{-}$ and H14. Consistent with this hypothesis, over most

of the simulation period, the distance between Y5/Y5^{-} and H14 remained within 5–10 Å (see Figure 3.10C, black/green), due to a parallel-offset (more common) or perpendicular T-shaped (less common) stacking arrangement as seen in Figure 3.14. However, the distance between these two residues for Peptide A-Y$\cdot$ increases to greater than 10 Å as the peptide begins to unfold, consistent with a loss of the noncovalent interaction (see Figure 3.10C, red). Loss of this interaction is driven by unfavorable interaction energies between the two side chains; the energies for one instance of parallel-offset stacking are −0.8 kcal/mol for Peptide A-YH, −1.5 kcal/mol for Peptide A-Y^{-}, and +0.8 kcal/mol for Peptide A-Y$\cdot$ (all in identical conformations).

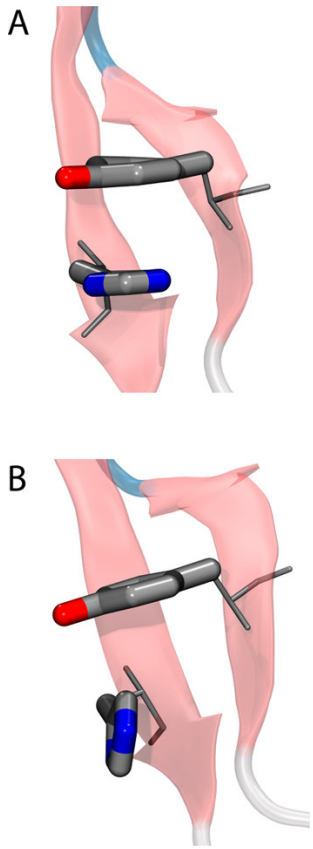

Figure 3.14 Arrangements for the (A) parallel offset and (B) perpendicular T-shaped π–π stacking.

3.4.4 Simulations of Peptide C

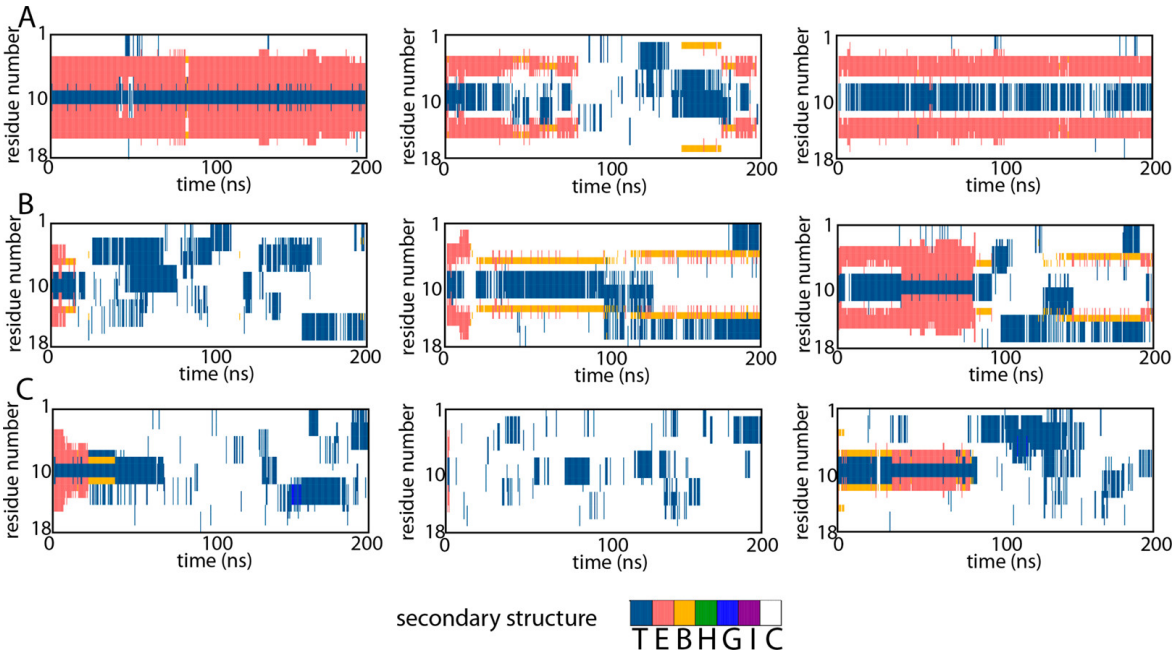

Figure 3.15 Time evolution of secondary-structure assignment per residue of Peptide C charge states for all three runs. Extension of the first run to 400 ns is presented in Figure 3.16. The legend at the bottom uses DSSP classification as implemented in Stride[57] where T is β turn, E is β sheet, B is β bridge, H is α helix, G is 3_{10} helix, I is π helix, and C is unstructured coil. (A) Peptide C-YH. (B) Peptide C-Y^{-}. (C) Peptide C-$Y^{\cdot}$.

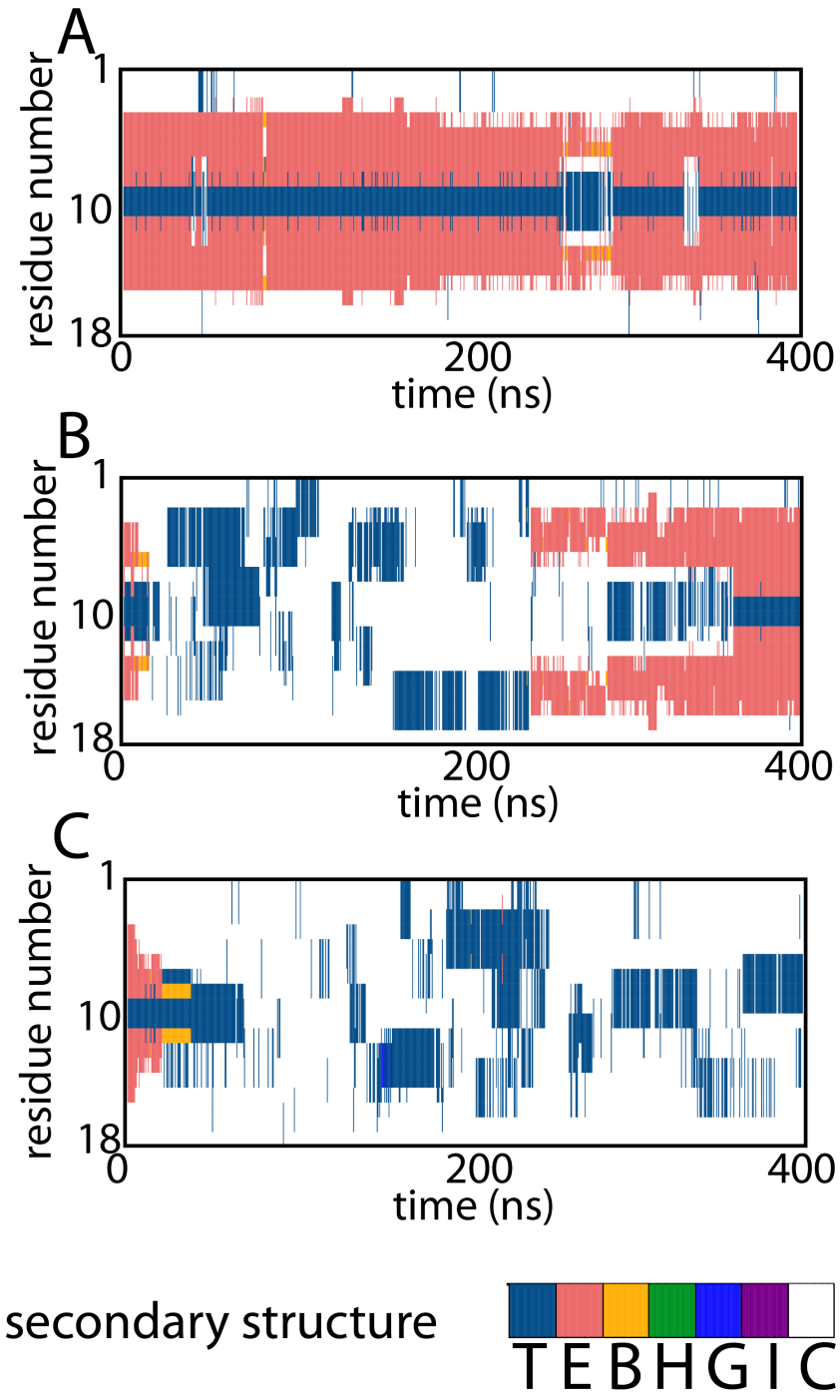

Figure 3.16 Time evolution of secondary-structure assignment per residue of Peptide C charge states for the first run extended to 400ns. The legend at the bottom uses DSSP classification as implemented in Stride where T is β turn, E is β sheet, B is β bridge, H is α helix, G is 310 helix, I is π helix, and C is unstructured coil. (A) Peptide C-YH. (B) Peptide C-Y–. (C) Peptide C-Y•.

In Peptide C, H14 is substituted by a cyclohexylalanine (Cha14), and the π–π interaction between Y5 and the cross-strand imidazole side chain is not present. Simulations were conducted on models of Peptide C to assess its stability and to account for the pH dependence observed in the UVRR spectra. The simulations were consistent with a stable β-hairpin core in Peptide C-YH involving residues 5–8 and 11–14 (see Figure 3.15A), similar to the fold observed in Peptide A-YH. Even though Peptide C-YH lost its β-hairpin conformation after 80 ns in run 2 (see Figure 3.15B), the model reattained its β-turn between residues 6–12 and a single backbone hydrogen bond between residue 2 and 17 at 150 ns. The model then formed a looplike structure and finally recovered its β-hairpin conformation. The stability of Peptide C-YH is also evident from analysis of its hydrogen bonds and R_g (see Figure 3.17). Figure 3.17A shows that interstrand hydrogen bonds in the β-hairpin formed in the initial state are maintained during in the entire 200 ns of run 1, while Figure 3.17B reflects a constant R_g value.

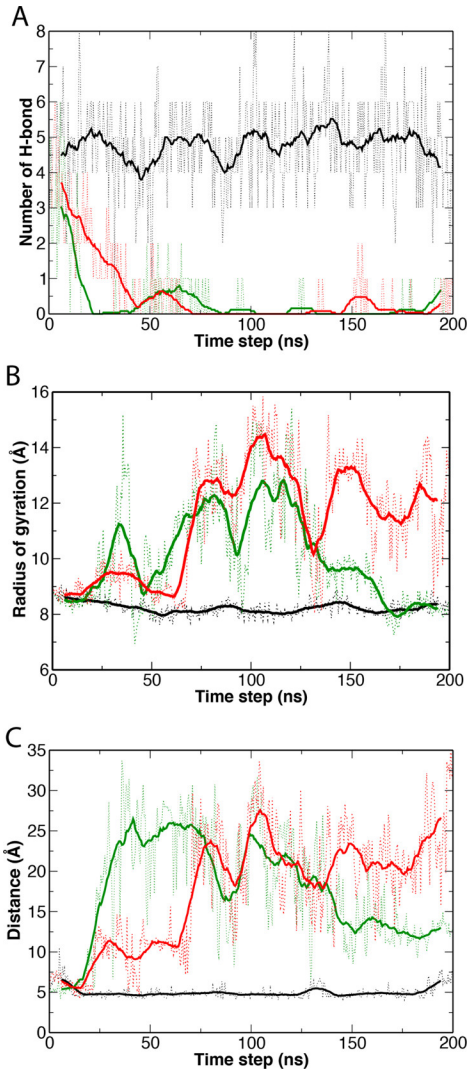

Figure 3.17 Structural parameters measured during simulations of Peptide C. In all panels, black curves are from run 1 of Peptide C-YH, green from Peptide C-Y^{-}, and red from Peptide C-Y·. Other runs are presented in Figures 3.18, 3.19, and 3.20. (A) Number of backbone hydrogen bonds for each Peptide-C variant. (B) Radius of gyration. (C) Distance between Y5/Y5^{-}/Y5· and Cha14 of Peptide C.

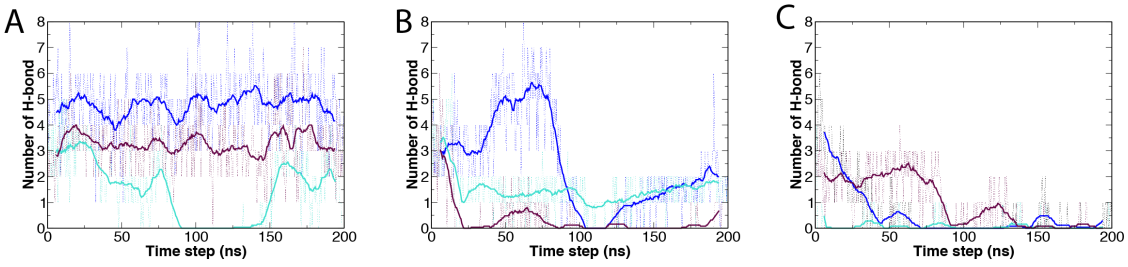

Figure 3.18 Number of backbone hydrogen bonds for each Peptide-C variant. In each panel, the three colors denote three independent runs. (A) Peptide C-YH. (B) Peptide C-Y–. (C) Peptide C-Y•.

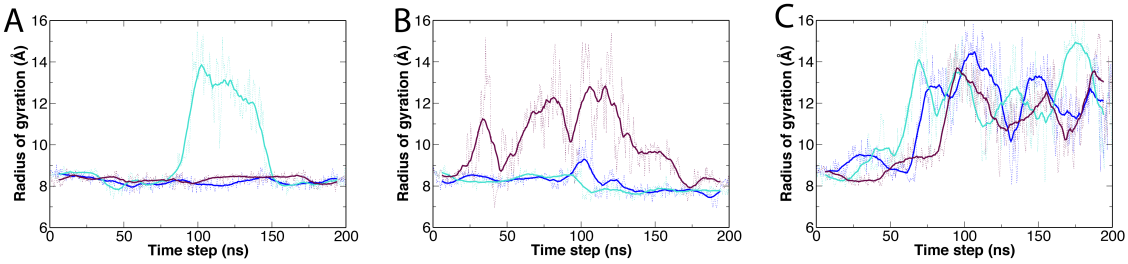

Figure 3.19 Radius of gyration for each Peptide-C variant. In each panel, the three colors denote three independent runs. (A) Peptide C-YH. (B) Peptide C-Y–. (C) Peptide C-Y•.

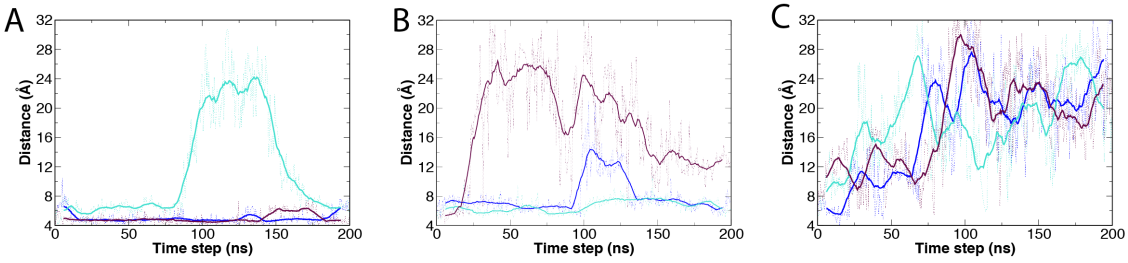

Figure 3.20 Distance between Y5/Y–/Y• and Cha14 for each Peptide-C variant. In each panel, the three colors denote three independent runs. (A) Peptide C-YH. (B) Peptide C-Y–. (C) Peptide C-Y•.

Peptide C-Y^- and Peptide C-$Y^{\cdot}$ showed behaviors distinct from Peptide C-YH (see Figure 3.15B,C). Unlike Peptide A-Y^-, which maintains its secondary structure over most

of the simulations, Peptide C-Y^- is not as stable in a β-sheet conformation. While the Y5–Cha14 distance and radius of gyration were stable for the first few nanoseconds, large increases in both were observed by 35 ns (see Figure 3.17B, C, green). Interchain hydrogen bonds were lost much more quickly, within 20 ns (see Figure 3.17A, green). These observations suggest that the lack of π–π stacking, which is present between Y^- and H14 in Peptide A-Y^-, destabilizes the folded state of Peptide C-Y^-. However, two of three runs indicate that Peptide C-Y^- retains a β-turn during part of the simulation (Figure 3.15).

A loss of the β-hairpin conformation is evident in Peptide C-$Y^{\cdot}$. This peptide completely loses its secondary structure within 30 ns, and never comes back to a folded β-hairpin conformation. An increase in R_g and in the distance between $Y5^{\cdot}$ and Cha14 (see Figure 3.17B, C, red) also indicate that Peptide C-$Y^{\cdot}$ becomes extended toward the end of the simulation. Taken together, the simulations suggest that while Peptide C-YH undergoes a hydrogen bonding change upon conversion to Peptide C-$Y^{\cdot}$ at pH 8.5, Peptide C-Y^- does not. Singlet Peptide C-Y^- samples nonhydrogen-bonded states, and thus the structure does not change substantially when compared to Peptide C-$Y^{\cdot}$, as assessed by UVRR. These simulations provide an explanation of the pD-dependent UVRR results presented above for Peptide C. Note that CD spectra derived from Peptide C exhibited negative ellipticity at pH 5 and 11 with a minimum wavelength similar to that of Peptide A, but with decreased amplitude. Thermal melting gave results suggesting a reversible unfolding transition in Peptide C at both pH values.[27] We attribute the previous CD results to retention of a thermostable β-turn in Peptide C in the YH and Y^- states, even though interstrand hydrogen-bonding distances have increased. Thus, we propose that while the UVRR

reflects the strength of hydrogen bonding interactions, through shifts of the UV absorption band, CD reflects the presence of the β-turn,[61] which is partially retained in Peptide C-Y^{-}.

We also extended one of the three runs for each Peptide-C variant to 400 ns (see Figure 3.16). Peptide C-YH maintained its β-sheet structure for the entire simulation. Peptide C-Y^{-} gained a folded structure for the last 150 ns, while Peptide C-Y$^{\cdot}$ only exhibited sporadic β-turn structure. The aMD results, given in Figure 3.9, also show that Peptide C-Y^{-} and Peptide C-Y$^{\cdot}$ are unstable; the average numbers of backbone-hydrogen bonds after reweighting the 300-ns aMD simulations were 3.9 (Peptide C-YH), 0 (Peptide C-Y^{-}), and 1.6 (Peptide C-Y$^{\cdot}$). Here again, we note that the probabilities tend to be dominated by a few rare events, as these high-energy states contribute the most during reweighting (see Figure 3.9).[59-60]

3.5 Discussion

The design of Peptide A was inspired by two enzymes, RNR and PSII. RNR plays a pivotal role in nucleic acid metabolism and cell division,[62] and PCET reactions are important in its function.[63] In class 1a RNR, found in *E. coli* and mammals, a long-range radical transfer links the essential Y122O$^{\cdot}$ in the β-subunit with the active site in the α-subunit.[64-67] Tyrosine-based radical transfer is also important in PSII, which has two redox-active tyrosines, YZ and YD, with different protein environments and different roles in electron transfer.[4, 68] EPR experiments on YD and YZ suggest that PCET distinguishes the two tyrosines.[47-48, 69] There are no structures available of the radical states. YZ and YD are oxidized on the nanosecond time scale,[70] while the decay times of the radicals vary from microseconds (YZ) to hours or even days (YD) (reviewed in ref [71]).

Aerobic organisms require reactions such as these, which operate at high potential, but they must also protect themselves from toxic side effects. There are many unanswered questions concerning these protective mechanisms. For example, high-potential ET and PCET reactions are associated with the generation of highly reactive radical intermediates, which can irreversibly damage polypeptides. However, proteins have evolved methods to protect themselves from this oxidative damage; one mechanism may involve radical transfer to solvent through tyrosine-tryptophan dyads.[31, 72-73] In addition, the structured protein environment is able to extend the lifetime of radical intermediates. While the lifetime of tyrosyl radicals in solution is on the microsecond time scale, in proteins, these lifetimes can be extended to hours or days. These control mechanisms are not understood, but may involve modulation of water access to the tyrosyl radical site (reviewed in ref [50]). Finally, proteins have devised mechanisms to trigger the tyrosyl radical to initiate an ET or PCET reaction.[61-63]

In this article, we simulated a redox-driven conformational change in a tyrosine-containing maquette, a β-hairpin peptide. Our molecular dynamics simulations provide evidence that oxidation of tyrosine in the β-hairpin maquettes, Peptide A-YH, Peptide A-Y^-, and Peptide C-YH is associated with a substantial change in secondary structure on the 100 ns time scale. In comparison to the others, Peptide C-Y^- is more dynamic, and tyrosinate oxidation in this peptide does not drive a net change in hydrogen bonding. Overall, the simulations provide evidence that the redox-driven conformational change in Peptide A is associated with a change in distance between H14 and Y5, as well as a loss of interstrand amide hydrogen bonding. This change in distance is induced, in part, by a loss

of favorable π–π stacking between H14 and Y5, due to the rearrangement of charge on the Y5 side chain in the radical state.

The kinetics of PCET have also been investigated in the β-hairpin peptides, where tyrosyl radical formation and decay occur on the picosecond time scale. In the peptides, a femtosecond UV photolysis pulse was used to generate the Peptide A- or Peptide C-Y· state, which is formed in 3 ps. The time course of radical decay was then monitored out to 2 ns (see Figure 3.21B).[32-33] The radicals decay either by recombination with the solvated electron alone (ET) or by recombination with the solvated electron and a proton (PCET), depending on the pH. This time-resolved absorption spectroscopy has shown that the decay time of the tyrosyl radical is accelerated in the β-hairpin, compared to model tyrosine or tyrosinate in solution. This effect was attributed to increased electronic coupling in the peptide.[32-33] The substitution of Cha14 (Peptide C) for H14 (Peptide A) was observed to decrease the decay rate of tyrosyl radical on this time scale at pD 9, but not at pD 11. This change shows that H14 is kinetically significant in the picosecond PCET reactions that occur at pD 9. The decrease in rate was attributed to an increase in reorganization energy in the Cha14 mutant.[33] On the time scale of these time-resolved absorption experiments, the simulated unfolding reaction is not predicted to be significant in Peptides A and C. However, in the UVRR difference experiment, which produces a photosteady state (see Figure 3.21A), the predicted altered conformational state can be maintained.

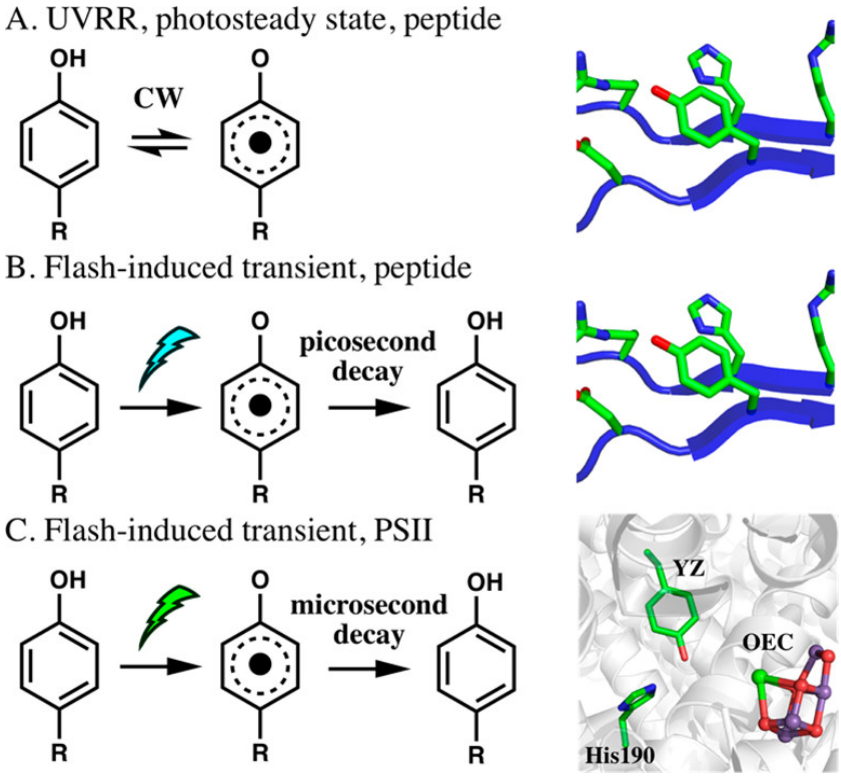

Figure 3.21 PCET reaction schemes for tyrosyl radical generation. (A) UVRR experiments produce a photosteady state in a peptide sample. Tyrosyl radical is generated by continuous wave (CW) illumination using 244 nm illumination and sample circulation by a peristaltic pump. Spectral subtraction ($UV_{high} - UV_{low}$) generates the radical-minus-singlet UVRR difference spectrum.[25, 34] (B) Time-resolved absorption spectroscopy (TRAS) generates a transient tyrosyl radical in a peptide sample. A femtosecond 280 nm pump and a stirred sample are used. The decay of radical is monitored as a transient on the picosecond time scale.[25, 32-33] (C) In PSII, photoexcitation of chlorophyll with a visible, 532 nm pump and time-resolved absorption spectroscopy are used to measure the rate of electron transfer from tyrosine, YZ, to oxidized chlorophyll. The generation of YZ radical occurs on the nanosecond time scale and its reduction by the PSII oxygen-evolving complex (OEC) occurs on the microsecond to millisecond time scale. His190 in the D1 polypeptide is hydrogen bonded to YZ (PDB 4UB6).[70, 74-76]

In photosynthetic water oxidation, a subset of the visible light-driven PCET reactions occur on the nanosecond time scale.[5] For example, the oxidation of YZ by the primary chlorophyll donor, P_{680}^{+}, is multiphasic and occurs on this time scale in active, oxygen-evolving PSII (see Figure 3.21C).[70] The reduction reaction occurs on the

microsecond to millisecond time scale (Figure 3.21C). In an ETPT or PTET mechanism, which involves rate-limiting proton transfer mechanism, or in a coupled proton electron transfer, the rate of tyrosyl radical decay would be expected to decrease as distance increases.[13, 77] Therefore, a redox-induced increase in side chain-side chain distance, as described here, could play a critical role in modulation of proton transfer rate on the hundreds of nanoseconds time scale. Note that the details of the conformational change are expected to be sequence and structure dependent. Future work will explore the impact of these factors.

3.6 Conclusions

Although not fully converged, the molecular dynamics simulations presented here provide support for the hypothesis that tyrosyl radical reactions can alter hydrogen-bonding interactions in proteins. In addition, critical distances between amino-acid side chains are shown to respond to the oxidation reaction. Such redox-coupled conformational changes may occur and be of significance in complex proteins.

3.7 References

1. Ostermeier, C.; Harrenga, A.; Ermler, U.; Michel, H. Structure at 2.7 Å Resolution of the *Paracoccus Denitrificans* Two-Subunit Cytochrome *C* Oxidase Complexed with an Antibody Fv Fragment. *Proc. Natl. Acad. Sci. USA* **1997,** *94*, 10547-10553.

2. Yoshikawa, S.; Shinzawa-Itoh, K.; Nakashima, R.; Yaono, R.; Yamashita, E.; Inoue, N.; Yao, M.; Fei, M. J.; Libeu, C. P.; Mizushima, T., et al. Redox-Coupled Crystal Structural Changes in Bovine Heart Cytochrome C Oxidase. *Science* **1998,** *280*, 1723-1729.

3. Stubbe, J. Ribonucleotide Reductases: Amazing and Confusing. *J. Biol. Chem.* **1990,** *265*, 5329-5332.

4. Barry, B. A.; Babcock, G. T. Tyrosine Radicals Are Involved in the Photosynthetic Oxygen-Evolving System. *Proc. Nat. Acad. Sci. USA* **1987,** *84*, 7099-7103.

5. Pujols-Ayala, I.; Barry, B. A. Tyrosyl Radicals in Photosystem Ii. *Biochim. Biophys. Acta* **2004,** *1655*, 205-216.

6. Kulmacz, R. J.; Ren, Y.; Tsai, A.-L.; Palmer, G. Prostaglandin H Synthase: Spectroscopic Studies of the Interaction with Hydroperoxides and with Indomethacin. *Biochemistry* **1990,** *29*, 8760-8771.

7. Whittaker, M. M.; Whittaker, J. W. Tyrosine-Derived Free Radical in Apogalactose Oxidase. *J. Biol. Chem.* **1990,** *265*, 9610-9613.

8. Whittaker, M. M.; Kersten, P. J.; Nakamura, N.; Sanders-Loehr, J.; Schweizer, E. S.; Whittaker, J. W. Glyoxal Oxidase from *Phanerochaete Chrysosporium* Is a New Radical-Copper Oxidase. *J. Biol. Chem.* **1996,** *271*, 681-687.

9. Chouchane, S.; Girotto, S.; Yu, S.; Magliozzo, R. S. Identification and Characterization of Tyrosyl Radical Formation in *Mycobacterium Tuberculosis* Catalase-Peroxidase (Katg). *J. Biol. Chem.* **2002,** *277*, 42633 -42638.

10. Huynh, M. H.; Meyer, T. J. Proton-Coupled Electron Transfer. *Chem Rev* **2007,** *107*, 5004-64.

11. Dempsey, J. L.; Winkler, J. R.; Gray, H. B. Proton-Coupled Electron Flow in Protein Redox Machines. *Chem. Rev.* **2010,** *110*, 7024-39.

12. Migliore, A.; Polizzi, N. F.; Therien, M. J.; Beratan, D. N. Biochemistry and Theory of Proton-Coupled Electron Transfer. *Chem Rev* **2014,** *114*, 3381-465.

13. Marcus, R. A. Electron Transfer Reactions in Chemistry: Theory and Experiment. *Pure Appl. Chem.* **1997,** *69*, 13-29.

14. Edsall, J. T.; Martin, R. B.; Hollingworth, B. R. Ionization of Individual Groups in Dibasic Acids, with Application to the Amino and Hydroxyl Groups of Tyrosine *Proc. Natl. Acad. Sci. USA* **1958,** *44*, 505-519.

15. Dixon, W. T.; Murphy, D. Determination of the Acidity Constants of Some Phenol Radical Cations by Means of Electron Spin Resonance. *J. Chem. Soc. London, Faraday Trans. II* **1976,** *72*, 1221-1230.

16. Barry, B. A.; El-Deeb, M. K.; Sandusky, P. O.; Babcock, G. T. Tyrosine Radicals in Photosystem Ii and Related Model Compounds. *J. Biol. Chem.* **1990,** *265*, 20139-20143.

17. Hammes-Schiffer, S.; Soudackov, A. V. Proton-Coupled Electron Transfer in Solution, Proteins, and Electrochemistry. *J. Phys. Chem. B* **2008,** *112*, 14108-14123.

18. Jones II, G.; Vullev, V.; Braswell, E. H.; Zhu, D. Multistep Photoinduced Electron Transfer in a *De Novo* Helix Bundle: Multimer Self-Assembly of Peptide Chains Including a Chromophore Special Pair. *J. Am. Chem. Soc.* **2000,** *122*, 388-389.

19. Lombardi, A.; Nastri, F.; Pavone, V. Peptide-Based Heme-Protein Models. *Chem. Rev.* **2001,** *101*, 3165-3190.

20. Gibney, B. R.; Huang, S. S.; Skalicky, J. J.; Fuentes, E. J.; Wand, A. J.; Dutton, P. L. Hydrophobic Modulation of Heme Properties in Heme Protein Maquettes. *Biochemistry* **2001,** *40*, 10550-10561.

21. Discher, B. M.; Noy, D.; Strzalka, J.; Ye, S.; Moser, C. C.; Lear, J. D.; Blasie, J. K.; Dutton, P. L. Design of Amphiphilic Protein Maquettes: Controlling Assembly, Membrane Insertion, and Cofactor Interactions. *Biochemistry* **2005,** *44*, 12329-12343.

22. Cochran, F. V.; Wu, S. P.; Wang, W.; Nanda, V.; Saven, J. G.; Therien, M. J.; DeGrado, W. F. Computational *De Novo* Design and Characterization of a Four-Helix Bundle Protein That Selectively Binds a Nonbiological Cofactor. *J. Am Chem Soc* **2005,** *127*, 1346-1347.

23. Tommos, C.; Skalicky, J. J.; Pilloud, D. L.; Wand, A. J.; Dutton, P. L. De Novo Proteins as Models of Radical Enzymes. *Biochemistry* **1999,** *38*, 9495-507.

24. Di Bilio, A. J.; Crane, B. R.; Wehbi, W. A.; Kiser, C. N.; Abu-Omar, M. M.; Carlos, R. M.; Richards, J. H.; Winkler, J. R.; Gray, H. B. Properties of Photogenerated Tryptophan and Tyrosyl Radicals in Structurally Characterized Proteins Containing Rhenium(I) Tricarbonyl Diimines. *J. Am. Chem. Soc.* **2001,** *123*, 3181-2.

25. Sibert, R.; Josowicz, M.; Porcelli, F.; Veglia, G.; Range, K.; Barry, B. A. Proton-Coupled Electron Transfer in a Biomimetic Peptide as a Model of Enzyme Regulatory Mechanisms. *J Am Chem Soc* **2007,** *129*, 4393-400.

26. Li, S.; Su, Y.; Luo, W.; Hong, M. Water-Protein Interactions of an Arginine-Rich Membrane Peptide in Lipid Bilayers Investigated by Solid-State Nuclear Magnetic Resonance Spectroscopy. *J. Phys. Chem. B* **2010,** *114*, 4063-9.

27. Sibert, R. S.; Josowicz, M.; Barry, B. A. Control of Proton and Electron Transfer in De Novo Designed, Biomimetic Beta Hairpins. *ACS Chem Biol* **2010,** *5*, 1157-68.

28. Martinez-Rivera, M. C.; Berry Bruce, W.; Valentine, K. G.; Westerlund, K.; Hay, S.; Tommos, C. Electrochemical and Structural Properties of a Protein System Designed to Generate Tyrosine Pourbaix Diagrams *J. Am. Chem. Soc.* **2011,** *133*, 17786-17795

29. Ravichandran, K. R.; Liang, L.; Stubbe, J.; Tommos, C. Formal Reduction Potential of 3,5-Difluorotyrosine in a Structured Protein: Insight into Multistep Radical Transfer. *Biochemistry* **2013,** *52*, 8907-15.

30. Glover, S. D.; Jorge, C.; Liang, L.; Valentine, K. G.; Hammarstrom, L.; Tommos, C. Photochemical Tyrosine Oxidation in the Structurally Well-Defined Alpha3y Protein: Proton-Coupled Electron Transfer and a Long-Lived Tyrosine Radical. *J. Am Chem Soc* **2014,** *136*, 14039-51.

31. Pagba, C. V.; McCaslin, T. G.; Veglia, G.; Porcelli, F.; Yohannan, J.; Guo, Z.; McDaniel, M.; Barry, B. A. A Tyrosine-Tryptophan Dyad and Radical-Based Charge Transfer in a Ribonucleotide Reductase-Inspired Maquette. *Nature Comm.* **2015,** *10010*.

32. Pagba, C. V.; Chi, S. H.; Perry, J.; Barry, B. A. Proton-Coupled Electron Transfer in Tyrosine and a Beta-Hairpin Maquette: Reaction Dynamics on the Picosecond Time Scale. *J Phys Chem B* **2015,** *119*, 2726-36.

33. Pagba, C. V.; McCaslin, T. G.; Chi, S. H.; Perry, J. W.; Barry, B. A. Proton-Coupled Electron Transfer and a Tyrosine-Histidine Pair in a Photosystem Ii-Inspired Beta-Hairpin Maquette: Kinetics on the Picosecond Time Scale. *J Phys Chem B* **2016,** *120*, 1259-72.

34. Pagba, C. V.; Barry, B. A. Redox-Induced Conformational Switching in Photosystem-Ii-Inspired Biomimetic Peptides: A Uv Resonance Raman Study. *J. Phys. Chem. B* **2012,** *116*, 10590-9.

35. Bixon, M.; Jortner, J. Coupling of Protein Modes to Electron Transfer in Bacterial Photosynthesis. *J. Phys. Chem.* **1986,** *90*, 3795–3800.

36. Moser, C. C.; Keske, J. M.; Warncke, K.; Farid, R. S.; Dutton, P. L. Nature of Biological Electron Transfer. *Nature* **1992,** *355*, 796-802.

37. Mayer, J. M. Proton-Coupled Electron Transfer: A Reaction Chemist's View. *Ann. Rev. Phys. Chem.* **2004,** *55*, 363-90.

38. Cukier, R. I. Theory and Simulation of Proton-Coupled Electron Transfer, Hydrogen Atom Transfer, and Proton Translocation in Proteins. *Biochimica et Biophysica Acta* **2004,** *1655*, 37-44.

39. Mayne, C. G.; Saam, J.; Schulten, K.; Tajkhorshid, E.; Gumbart, J. C. Rapid Parameterization of Small Molecules Using the Force Field Toolkit. *J .Comput. Chem.* **2013,** *34*, 2757-70.

40. Humphrey, W.; Dalke, A.; Schulten, K. Vmd: Visual Molecular Dynamics. *Journal of molecular graphics* **1996,** *14*, 33-38.

41. Vanommeslaeghe, K.; Hatcher, E.; Acharya, C.; Kundu, S.; Zhong, S.; Shim, J.; Darian, E.; Guvench, O.; Lopes, P.; Vorobyov, I. Charmm General Force Field: A Force Field for Drug-Like Molecules Compatible with the Charmm All-Atom Additive Biological Force Fields. *Journal of computational chemistry* **2010,** *31*, 671-690.

42. Bally, T.; Borden, W. T. Calculations on Open-Shell Molecules: A Beginner's Guide. *Reviews in computational chemistry* **1999**, 1-97.

43. Frisch, M.; Trucks, G.; Schlegel, H.; Scuseria, G.; Robb, M.; Cheeseman, J.; Scalmani, G.; Barone, V.; Mennucci, B.; Petersson, G. Gaussian09 Revision D. 01, Gaussian Inc. Wallingford Ct. *See also: URL: http://www. gaussian. com* **2009**.

44. Phillips, J. C.; Braun, R.; Wang, W.; Gumbart, J.; Tajkhorshid, E.; Villa, E.; Chipot, C.; Skeel, R. D.; Kale, L.; Schulten, K. Scalable Molecular Dynamics with Namd. *Journal of computational chemistry* **2005,** *26*, 1781-1802.

45. Best, R. B.; Zhu, X.; Shim, J.; Lopes, P. E.; Mittal, J.; Feig, M.; MacKerell Jr, A. D. Optimization of the Additive Charmm All-Atom Protein Force Field Targeting Improved Sampling of the Backbone Φ, Ψ and Side-Chain X1 and X2 Dihedral Angles. *Journal of chemical theory and computation* **2012,** *8*, 3257-3273.

46. Darden, T.; York, D.; Pedersen, L. Particle Mesh Ewald: An N· Log (N) Method for Ewald Sums in Large Systems. *The Journal of chemical physics* **1993,** *98*, 10089-10092.

47. Jenson, D. L.; Barry, B. A. Proton-Coupled Electron Transfer in Photosystem Ii: Proton Inventory of a Redox Active Tyrosine. *J Am Chem Soc* **2009,** *131*, 10567-73.

48. Jenson, D. L.; Evans, A.; Barry, B. A. Proton-Coupled Electron Transfer and Tyrosine D of Photosystem Ii. *J Phys Chem B* **2007,** *111*, 12599-604.

49. Chen, J.; Barry, B. Ultraviolet Resonance Raman Microprobe Spectroscopy of Photosystem Ii. *Photochem. Photobiol.* **2008,** *84*, 815-818.

50. Barry, B. A.; Chen, J.; Keough, J.; Jenson, D. L.; Offenbacher, A. R.; Pagba, C. V. Proton Coupled Electron Transfer and Redox Active Tyrosines: Structure and Function of the Tyrosyl Radicals in Ribonucleotide Reductase and Photosystem Ii. *J. Phys. Chem. Lett.* **2012,** *3*, 543-554.

51. Asher, S. A. Uv Resonance Raman Spectroscopy for Analytical, Physical, and Biophysical Chemistry. *Analytical Chemistry* **1993,** *65*, A59-A66.

52. Johnson, C. R.; Ludwig, M.; Asher, S. A. Ultraviolet Resonance Raman Characterization of Photochemical Transients of Phenol, Tyrosine, and Tryptophan. *J. Am. Chem. Soc.* **1986,** *108*, 905-912.

53. Range, K.; Ayala, I.; York, D.; Barry, B. A. Normal Modes of Redox-Active Tyrosine: Conformation Dependence and Comparison to Experiment. *J. Phys. Chem. B* **2006,** *110*, 10970-10981.

54. Barry, B. A. Reaction Dynamics and Proton Coupled Electron Transfer: Studies of Tyrosine-Based Charge Transfer in Natural and Biomimetic Systems. *Biochim. Biophys. Acta* **2015,** *1847*, 46-54.

55. Rosenheck, K.; Doty, P. T. The Far Ultraivolet Absorption Spectrum of Polypeptide and Protein Solutoins and Their Dependence on Conformation *Proc Natl Acad Sci U S A* **1961,** *47*, 1775-1785.

56. Copeland, R. A.; Spiro, T. G. Secondary Structure Determination in Proteins from Deep (192-223-Nm) Ultraviolet Raman Spectroscopy. *Biochemistry* **1987,** *26*, 2134-9.

57. Frishman, D.; Argos, P. Knowledge-Based Protein Secondary Structure Assignment. *Proteins: Structure, Function, and Bioinformatics* **1995,** *23*, 566-579.

58. Hamelberg, D.; Mongan, J.; McCammon, J. A. Accelerated Molecular Dynamics: A Promising and Efficient Simulation Method for Biomolecules. *The Journal of chemical physics* **2004,** *120*, 11919-11929.

59. Shen, T.; Hamelberg, D. A Statistical Analysis of the Precision of Reweighting-Based Simulations. *The Journal of chemical physics* **2008,** *129*, 034103.

60. Sinko, W.; Miao, Y.; de Oliveira, C. s. A. F.; McCammon, J. A. Population Based Reweighting of Scaled Molecular Dynamics. *The Journal of Physical Chemistry B* **2013,** *117*, 12759-12768.

61. M. Kawai, G. F. A Model .Beta. Turn. Circular Dichroism and Infrared Spectra of a Tetrapeptide. *J. Am .Chem. Soc.* **1978,** *100*, 3630-3632.

62. Jordan, A.; Reichard, P. Ribonucleotide Reductases. *Ann. Rev. Biochem.* **1998,** *67*, 71-98.

63. Minnihan, E. C.; Nocera, D. G.; Stubbe, J. Reversible, Long-Range Radical Transfer in *E. Coli* Class Ia Ribonucleotide Reductase. *Acc. Chem. Res.* **2013,** *46*, 2524-35.

64. Högbom, M.; Galander, M.; Andersson, M.; Kolberg, M.; Hofbauer, W.; Lassmann, G.; Nordlund, P.; Lendzlan, F. Displacement of the Tryosyl Radical Cofactor in Ribonucleotide Reductase Obtained by Single-Crystal High-Field Epr and 1.4-a X-Ray Data. *Proc. Nat. Acad. Sci. USA* **2003,** *100*, 3209-3214.

65. Offenbacher, A. R.; Burns, L. A.; Sherrill, C. D.; Barry, B. A. Redox-Linked Conformational Control of Proton-Coupled Electron Transfer: Y122 in the Ribonucleotide Reductase Beta2 Subunit. *J. Phys. Chem. B* **2013,** *117*, 8457-68.

66. Offenbacher, A. R.; Vassiliev, I. R.; Seyedsayamdost, M. R.; Stubbe, J.; Barry, B. A. Redox-Linked Structural Changes in Ribonucleotide Reductase. *J. Am. Chem. Soc.* **2009,** *131*, 7496-7497.

67. Kasanmascheff, M.; Lee, W.; Nick, T. U.; Stubbe, J.; Bennati, M. Radical Transfer in E. *Coli* Ribonucleotide Reductase: A Nh2y731/R411a-A Mutant Unmasks a New Conformation of the Pathway Residue 731. *Chem. Sci.* **2016,** *7*, 2170-2178

68. Boerner, R. J.; Barry, B. A. Isotopic Labeling and Epr Spectroscopy Show That a Tyrosine Residue Is the Terminal Electron Donor, Z, in Manganese-Depleted Photosystem Ii Preparations. *J. Biol. Chem.* **1993,** *268*, 17151-17154.

69. Keough, J.; Jenson, D. L.; Zuniga, A.; Barry, B. A. Proton Coupled Electron Transfer and Redox-Active Tyrosine Z in the Photosynthetic Oxygen Evolving Complex. *J. Am. Chem. Soc.* **2011,** *133*, 11084-11087.

70. Renger, G. Oxidative Photosynthetic Water Splitting: Energetics, Kinetics and Mechanism. *Photosyn. Res.* **2007,** *92*, 407-425.

71. Barry, B. A. Proton Coupled Electron Transfer and Redox Active Tyrosines in Photosystem Ii. *J. Photochem. Photobiol. B* **2011,** *104*, 60-71.

72. Winkler, J. R.; Gray, H. B. Could Tyrosine and Tryptophan Serve Multiple Roles in Biological Redox Processes? *Philos Trans A Math Phys Eng Sci* **2015,** *373*.

73. Gray, H. B.; Winkler, J. R. Hole Hopping through Tyrosine/Tryptophan Chains Protects Proteins from Oxidative Damage. *Proc Natl Acad Sci USA* **2015,** *112*, 10920-5.

74. Ahlbrink, R.; Haumann, M.; Cherepanov, D.; Bogershausen, O.; Mulkidjanian, A.; Junge, W. Function of Tyrosine Z in Water Oxidation by Photosystem Ii: Electrostatical Potential Instead of Hydrogen Abstractor. *Biochemistry* **1998,** *37*, 1131-1142.

75. Umena, Y.; Kawakami, K.; Shen, J.-R.; Kamiya, N. Crystal Structure of Oxygen-Evolving Photosystem Ii at a Resolution of 1.9 Angstrom. *Nature* **2011,** *473*, 55-60.

76. Suga, M.; Akita, F.; Hirata, K.; Ueno, G.; Murakami, H.; Nakajima, Y.; Shimizu, T.; Yamashita, K.; Yamamoto, M.; Ago, H., et al. Native Structure of Photosystem Ii at 1.95 a Resolution Viewed by Femtosecond X-Ray Pulses. *Nature* **2015,** *517*, 99-103.

77. Mayer, J. M. A Simple Marcus-Theory Type Model for Hydrogen Atom Transfer/Proton-Coupled Electron Transfer. *J .Phys. Chem. Lett.* **2011,** *2*, 1481-1489.

CHAPTER 4. A TYROSINE–TRYPTOPHAN DYAD AND RADICAL-BASED CHARGE TRANSFER IN A RIBONUCLEOTIDE REDUCTASE-INSPIRED MAQUETTE

Reprinted with permission from Nature Communications

Pagba, C. V.; McCaslin, T. G.; Veglia, G.; Porcelli, F.; Yohannan, J.; Guo, Z.; McDaniel, M.; Barry, B. A. A tyrosine–tryptophan dyad and radical-based charge transfer in a ribonucleotide reductase-inspired maquette. *Nat. Commun.* **2015**, *6*, 10010.

4.1 Abstract

In class 1a ribonucleotide reductase (RNR), a substrate-based radical is generated in the α2 subunit by long-distance electron transfer involving an essential tyrosyl radical (Y122O·) in the β2 subunit. The conserved W48 β2 is ∼10 Å from Y122OH; mutations at W48 inactivate RNR. Here, we design a beta hairpin peptide, which contains such an interacting tyrosine–tryptophan dyad. The NMR structure of the peptide establishes that there is no direct hydrogen bond between the phenol and the indole rings. However, electronic coupling between the tyrosine and tryptophan occurs in the peptide. In addition, downshifted ultraviolet resonance Raman (UVRR) frequencies are observed for the radical state, reproducing spectral downshifts observed for β2. The frequency downshifts of the ring and CO bands are consistent with charge transfer from YO· to W or another residue. Such a charge transfer mechanism implies a role for the β2 Y-W dyad in electron transfer.

4.2 Introduction

The aromatic amino-acid residues, tyrosine and tryptophan, mediate high potential electron transfer reactions in proteins.[1] For example, ribonucleotide reductase (RNR) employs a tyrosine-based charge relay to reduce ribonucleotides to deoxyribonucleotides.[2] The reaction is initiated by H atom abstraction at the substrate 3′-carbon; this process employs an active site cysteine radical in the α2 subunit. Class Ia RNRs, such as the *Escherichia coli* RNR, use a tyrosyl radical (Y122O·)-diferric cofactor in the β2 subunit to generate the cysteine radical. The charge transfer between Y122 and C439 occurs over 35 Å and is mediated by a conserved pathway of tyrosine side chains.[3] Y122O·

is required for activity[4] and is formed via oxygen-requiring reactions at the diferric cluster.[4-6]

Although there is no high-resolution structure of Y122O·-diferric β2, in structures of the met state (Y122OH-diferric state)[7], Y122OH is buried in a hydrophobic environment and is ~10 Å (Figure 4.1a) from a surface-exposed tryptophan, β2 W48. This tryptophan is highly conserved in class 1a β2 sequences.[8] Mutations at W48 in *E. coli* β2 or at the homologous position, W103 in mouse β2 (Figure 4.1b)[9], inactivate RNR.[8, 10-12] This residue has been shown to participate in cofactor assembly.[10] However, its role in proton-coupled electron transfer (PCET) has not been established.[3] The orientations of Y122OH and W48 in the crystal structure of the Y122OH-diferric state suggest the possibility of electronic, dipole–dipole interaction between the two side chains. In addition, the resonance Raman spectrum of Y122O· reveals downshifted CO and aromatic ring stretching frequencies. The low ring stretching frequency is not readily explained by existing model compounds.[13]

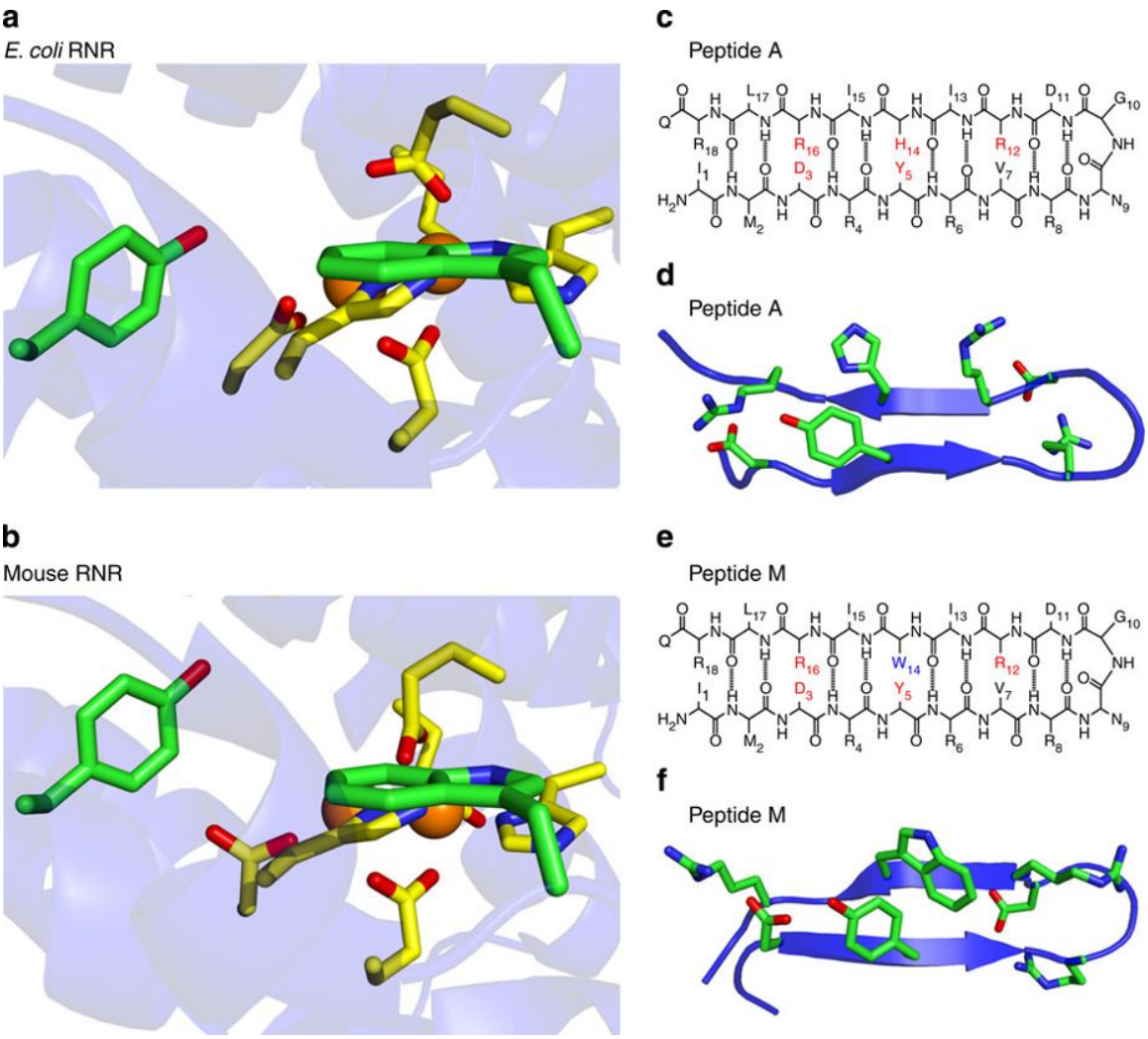

Figure 4.1 The environments of redox active tyrosine residues in class 1a met β2 subunits from *E. coli* and mouse RNR. The structures were generated with Pymol from 1MXR (*E. coli,* a) and 1W69 (mouse, b). In a, Y122 and W48 are shown, along with iron cluster ligands, D84, E115, H118, E204, E238 and H241 in *E. coli*. In b, Y177 and W103 are shown, along with iron ligands D139, E170, H173, E233, E267 and H270 in mouse. The distance between the phenolic oxygen and the indole nitrogen is 9.7 Å in *E. coli* and 9.9 Å in mouse. Primary sequences and NMR structures of Peptide A (c,d) and Peptide M (e,f). (d,f) The averaged, minimized NMR structures. The Peptide A structure was reported previously[14], and the Peptide M structure is derived from this work. Structural analyses for the ensemble of 20 low energy NMR models are presented in Table 4.1 (Peptide M) and Table 4.2 (Peptide A). as well as side chain–side chain distances in the averaged, minimized structures.

Table 4.1 Distances (Å) derived from the 20 lowest energy structural models and the averaged, minimized NMR structure of Peptide M

Model #	Y5O-W14NH	Y5O-R16NεH	Y5OH-R16Nε	Y5O-R16NH*	Y5OH-R16N*
1	6.1	9.3	9.7	9.7	10.9
2	5.9	6.4	7.2	8.2	9.2
3	6.2	5.4	5.2	1.5	3.1
4	6.0	9.3	9.7	7.9	9.6
5	6.4	2.8	3.7	1.4	3.1
6	6.3	4.2	4.2	1.5	3.1
7	6.3	8.5	6.9	5.5	5.4
8	6.5	5.1	5.3	1.4	3.2
9	6.7	5.7	4.2	3.7	3.3
10	6.2	4.9	4.4	2.9	2.9

11	6.5	5.1	4.8	7.3	6.8
12	6.4	7.0	6.0	7.4	7.0
13	6.4	8.4	7.5	9.5	9.0
14	6.9	7.8	8.0	7.7	8.8
15	6.7	4.8	4.4	2.7	2.8
16	6.7	6.5	6.1	5.0	5.3
17	6.0	9.2	7.6	7.1	6.5
18	6.6	6.9	5.7	5.7	5.8
19	6.6	4.9	5.1	1.4	3.1
20	6.3	6.7	6.0	7.3	7.1
AVE, MIN.	6.4	8.2	6.8	6.3	5.5

*For simplicity, only the distances from the closer of the other two –NH groups (η^1 or η^2) of R16 are presented.

Table 4.2 Distances (Å) derived from the 20 lowest energy structural models and the averaged, minimized NMR structure of Peptide A [14]

Model #	Y5O-H14NH	Y5O-R16NεH	Y5OH-R16Nε	Y5O-R16NH*	Y5OH-R16N*
1	3.8	1.8	2.8	3.8	3.8
2	3.8	1.8	2.8	3.9	3.8
3	3.8	1.9	2.6	4.0	3.7
4	2.2	5.6	5.3	6.2	5.9
5	4.0	1.5	3.0	4.0	4.1
6	2.3	5.6	5.2	5.8	6.0
7	2.3	5.6	5.2	6.0	6.2
8	2.1	4.3	5.1	3.8	3.6
9	3.7	3.9	4.1	1.4	3.1
10	2.3	5.6	5.3	6.1	6.3

11	2.2	5.6	5.3	6.2	6.3
12	3.8	4.4	3.4	1.5	2.6
13	2.5	4.8	4.9	3.0	4.3
14	3.2	5.5	5.1	5.9	6.0
15	3.3	5.5	4.0	5.8	5.9
16	2.4	4.0	4.0	1.5	2.9
17	2.5	4.0	3.4	1.5	2.9
18	3.8	4.1	4.3	1.5	3.0
19	2.1	5.1	4.3	3.8	3.7
20	3.8	3.0	3.1	1.4	4.1
AVE, MIN.	4.0	1.6	2.9	3.8	3.9

*For simplicity, only the distances from the closer of the other two –NH groups (η^1 or η^2) of R16 are presented.

Despite the low sequence similarity between the *E. coli* and mammalian β2 subunits, the staggered T-shaped arrangement of tyrosine and tryptophan is similar when *E. coli*[7], mouse[9] and human p53 (ref [15]) β2 subunits are compared. Also, other metalloproteins containing redox active tyrosines, such as photosystem II (ref. [16]) and galactose oxidase[17], contain tyrosine–tryptophan dyads with a similar structure.

In this study, we designed a β hairpin peptide, Peptide M, to characterize the functional and spectroscopic consequences of such an interacting tyrosine–tryptophan pair. Peptide M is an 18-mer and is a variant of Peptide A (Figure 4.1c), previously shown to form a β-hairpin (Figure 4.1d).[14, 18] Peptide M (Figure 4.1e) contains a single tyrosine and a single tryptophan, which form a dyad (Y5-W14), as established here by NMR, ultraviolet absorption and circular dichroism (CD) spectropolarography. The ultraviolet resonance Raman (UVRR) spectrum of Peptide M is unique and provides a framework in which to interpret the Raman spectra, previously reported for Y122O· in class 1a *E. coli* β2. Although there were earlier studies of (for example, see refs [19-20]) singlet states in model tyrosine–tryptophan peptides, we describe the first peptide in which interactions between the tyrosyl radical and the tryptophan sidechain are probed. The results are relevant to RNR and to other metalloproteins that employ redox-active tyrosines in high potential charge transfer pathways.[21-22]

4.3 Materials and Methods

4.3.1 Material

Peptides were synthesized by solid-state synthesis and were obtained from Genscript USA Inc. ^2H_2O and NaO^2H were purchased from Cambridge Isotopes (99.9% D).

When ^2H_2O was used, the p^{2}H was adjusted to the uncorrected metre reading.[23] 2-(*N*-morpholino)ethanesulfonic acid (MES), *N*-cyclohexyl-3-aminopropanesulfonic acid (CAPS), 2-[4-(2-hydroxyethyl)piperazin-1-yl]ethanesulfonic acid (HEPES), tyrosine and tryptophan were purchased from Sigma-Aldrich. Sodium borate was purchased from Mallinckrodt Pharmaceuticals, and boric acid was purchased from J.T. Baker Avantor Performance Materials. Hexamine ruthenium (III) chloride was purchased from Strem Chemicals.

4.3.2 NMR

The NMR samples were prepared by dissolving 1 mg of peptide in 350 µM sodium phosphate buffer (pH ~5) containing 5% ^2H_2O. The spectra were acquired on a 700-MHz Bruker spectrometer equipped with a triple-resonance cryogenic probe. A [^{1}H,^{1}H]-total correlation spectroscopy (TOCSY) experiment with 70 ms mixing time and spectral widths of 7,122.5 Hz for both dimensions was utilized to assign all of the peptide resonances. MLEV17 with field strength of 9 kHz was used as a mixing sequence.[24] To determine the inter-nuclear distances, we utilized a series of [^{1}H,^{1}H]-rotating frame nuclear Overhauser effect spectroscopy (ROESY) experiments with spectral widths identical to the TOCSY experiments, and with a continuous wave mixing sequence using 100, 200, 250, 350 and 400 ms mixing times.[25] The NMR spectra were processed using NMRPipe[26] and analysed using Sparky[27] software packages. The spectra were referenced to the water resonance at 4.7 p.p.m. TOCSY and ROESY spectra were assigned using the standard approach described by Wuthrich.[28] Based on the build-up curve, ROESY cross-peaks at 350 ms were chosen for structure calculations. A total of 156 ROEs consisting of 65 intra-residue and 91 inter-residue correlations were used for structure determination. Peak intensities were

converted into distances using the following classifications: strong (1.8–2.9 Å), medium (1.8–3.6 Å) and weak (1.8–6.0 Å). For residues with $^{3}J_{NH\text{-}Ha}$>8.0 Hz φ, angles were restricted to the range of –160 to –80°. NMR conformers were calculated starting from an extended conformation of Peptide M and using a hybrid simulated annealing protocol available in the XPLOR-NIH package.[29] Briefly, calculations were carried out using an initial temperature of 1,000 K, 50,000 high temperature steps and 6,000 cooling steps with a step size of 5 fs decreasing the temperature from 1,000 to 100 K. The generated conformers were further minimized including the Lennard-Jones potential, with the Conjugated Gradients algorithm using an initial temperature of 300 K and 60,000 steps (step size 1 fs). A total of 50 conformers were generated; the 20 lowest energy conformers without NOE violations greater than 0.5 Å, no bond violations greater than 0.05 Å, and no bond violations greater than 4° were selected for further analysis. Measurements were conducted both at 278 and 298 K.

4.3.3 Circular Dichroism

A Jasco J-810 CD spectropolarimeter equipped with a Peltier-type cell was employed. Spectra were collected from 250 to 193 nm in 1 mm quartz cells. Eight accumulations per scan were averaged in three independent measurements for each of the conditions. Parameters used were: sensitivity, 100 mdeg; data pitch, 2 nm; scan speed, 50 nm min^{-1}; response time, 1 s; bandwidth, 1 nm.

4.3.4 Ultraviolet-Visible Spectroscopy

Ultraviolet absorption spectra were recorded on a Shimadzu UV-1700 spectrometer. The slit width was 1 nm, the resolution was 1 nm and the scan speed was 6.5 nm s^{-1}. The spectra were averaged from two independent measurements.

4.3.5 Ultraviolet Resonance Raman

UVRR spectra of 1 mM samples were obtained at room temperature using a 244-nm probe beam generated from an intracavity frequency-doubled Argon ion laser (Cambridge LEXEL 95).[30-31] Briefly, the probe beam was coupled to a Raman microscope system (Renishaw inVia) equipped with ultraviolet-coated, deep depletion charge-coupled device. Backscattering from the sample was collected by a 15 × ultraviolet (NA=0.32) objective (OFR division of Thorlabs, Inc.), assembled in a Leica Microsystems microscope. The spectral resolution was 6 cm^{-1}, and the interval between the data points was 3.8 cm^{-1}. The peak positions are reported to a precision of ±2 cm^{-1}. To prevent photodegradation, samples were re-circulated using a peristaltic pump and a nozzle (~120 μm inner diameter) to form a jet. The Raman difference spectrum was obtained by subtracting an averaged low power scan (340 μW) from an averaged high power scan (3.4 mW) using 244 nm beam. The data were averaged from at least two measurements on different samples. Mass spectrometry (ThermoFisher Scientific, LTQ Orbitrap XL, Electrospray ionization, Positive Ion Mode) before and after the Raman measurement gave the expected 1,195 *m*/*z* ratio for Peptide M, indicating that there was no significant oxidative modification of the peptide during the UVRR measurement.

4.4 Results

4.4.1 NMR Studies

Peptide M is a variant of β-hairpin, Peptide A (Figure 4.1c,d), in which H14 is replaced with W (Figure 4.1e,f). For Peptide A, the NMR structure has shown that the peptide is β hairpin, that H14 has a pi–pi cross-strand interaction with Y5, and that Y5 is hydrogen bonded to R16. To assess the structure of Peptide M in solution, we performed NMR experiments at pH ~5. The NMR data are summarized in Figure 4.2 and Tables 4.3, 4.4 and 4.5. The rotating frame Overhauser enhancement (ROE) pattern (Figure 4.2a) with several (*i, i+1*) connectivities and $^{3}J_{H\alpha\text{-}HN}$ coupling constants greater than 7 Hz for residues 5, 7, 10, 12, 13, 15 and 16 are typical of β strands. Also, several long-range dipolar contacts were observed between residues 2–17, 3–16, 5–14 and 6–13, supporting the β sheet fold of the peptide (Figure 4.3). The NMR data resulted in an ensemble of 20 selected conformers (Figure 4.2c) with a root-mean-square deviation of 0.59±0.17 and 1.68±0.31 Å for backbone and side chains heavy atoms. The average structure (Figures 4.1f and 4.2d) shows that the aromatic residues (Y5 and W14) are co-facially aligned, as supported by seven inter-residue contacts between the aromatics, including ROEs between the ε protons of Y5 and $CH_2\beta$ and ε of W14. These NMR experiments show that the tyrosine and tryptophan are ~6 Å apart and exhibit a pi-stacked, staggered interaction, which is reminiscent of the orientation observed in the β2 dyad. In Peptide M, tyrosine is not hydrogen bonded to tryptophan (distance greater than 5.9 Å in all models).

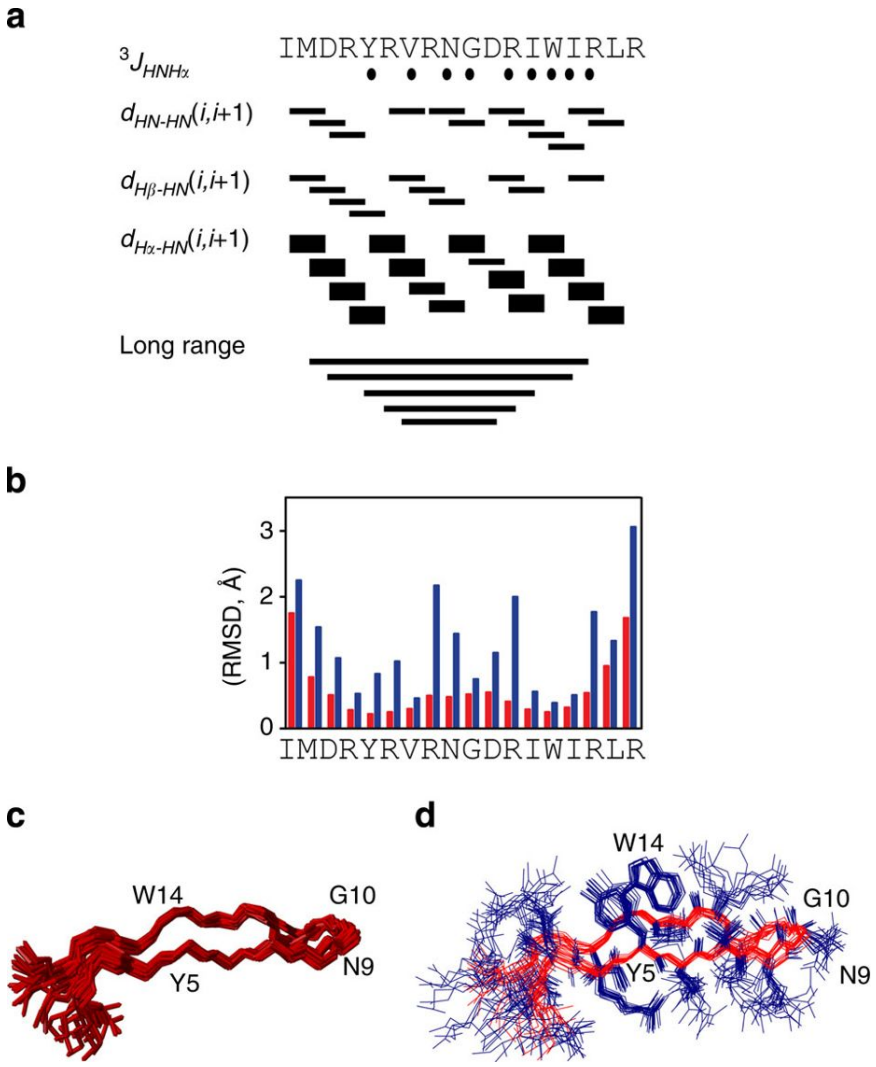

Figure 4.2 Summary of the NMR data on Peptide M. (a) Plot showing the short- and long-range ROEs for the backbone and the side chains, (b) root-mean-square deviations (RMSD) of the backbone atoms, (c) ensemble of 20 selected backbone conformers and (d) average structure of Peptide M. Resonance assignments were carried out using a combination of 2D [^{1}H–^{1}H]-TOCSY and [^{1}H–^{1}H]-ROESY experiments. All of the resonances were assigned, and 159 ROESY connectivities were detected. See Methods for more information, and Table 4.5 for ROE values used in calculations.

Table 4.3 Resonance assignments of *^1H* chemical shifts of Peptide M at pH 5.0 using solution NMR experiments.

Residue	NH (ppm)	CαH (ppm)	CβH (ppm)	Others (ppm)
I1	NA	3.882	1.954	NA
M2	8.717	4.516	2.021	γ -CH_2 2.558
D3	8.556	4.614	2.724	
R4	8.357	4.217	1.641	γ -CH_2 1.389
				δ-CH_2 3.081
				NH 7.090
Y5	8.113	4.609	3.027/2.905	δ-H 7.049
				ε -H 6.726

Table 4.3 continued

R6	8.056	4.356	1.735	γ -CH_2 1.538 δ-CH_2 3.154 NH 7.191
V7	8.160	4.126	2.012	γ -CH_3 0.9080
R8	8.485	4.360	1.702/1.795	γ -CH_2 1.568 δ-CH_2 3.140 NH 7.191
N9	8.585	4.630	2.793	
G10	8.440	3.930		
D11	8.207	4.650	2.774	

Table 4.3 continued

R12	8.240	4.237	1.654	γ -CH_2 1.442
				δ-CH_2 3.019
				NH 7.020
I13	8.094	4.162	1.775	γ -CH 1.114
				δ-CH_3 0.805
W14	8.312	4.695	3.256/3.137	δ-H 7.207
				ε -H 7.581
				ζ2-H 7.457
				ζ3-H 7.167
				ε -NH_3^+ 7.128
I15	7.980	4.086	1.731	γ-CH 1.034
				δ-CH_3 0.856

Table 4.3 continued

R16	8.223	4.237	1.757	γ -CH_2 1.523
				δ-CH_2 3.126
L17	8.223	4.339	1.620	γ -CH 0.888
				δ-CH_3 0.841
R18	7.973	4.197	1.851	γ -CH_2 1.576
				δ-CH_2 3.167

Table 4.4 Statistics for the 20 lowest energy NMR structures.

Parameter	Value
Distance and Angle Restraints	

Table 4.4 continued

Total NOEs	161
Intraresidual	73
Interresidual	88
Angles	9
Hydrogen bond restraints	--
Total restraints per residue	8.9
Statistics for Calculated Structures	
R.M.S.D. (Å)	
Backbone	0.59 ± 0.17
All Heavy Atoms	1.68 ± 0.31
Analysis (performed with Molprobity)	

% residues in most favored regions % residues in allowed regions % residues in generally allowed regions % residues in disallowed regions	

Table 4.5 NOEs used for calculations.

assign (residue 1 and name HA) (residue 1 and name HB#) 3.0 1.2 0.6 !m
assign (residue 1 and name HA) (residue 1 and name HG#) 5.0 2.2 1.0 !w
assign (residue 2 and name HA) (residue 2 and name HB#) 5.0 2.2 1.0 !w
assign (residue 2 and name HA) (residue 2 and name HG#) 5.0 2.2 1.0 !w
assign (residue 2 and name HA) (residue 2 and name HN) 5.0 2.2 1.0 !w
assign (residue 2 and name HA) (residue 3 and name HN) 2.5 0.7 0.4 !s
assign (residue 2 and name HB#) (residue 4 and name HB#) 5.0 2.2 1.0 !w
assign (residue 2 and name HA) (residue 17 and name HG#) 5.0 2.2 1.0 !w
assign (residue 2 and name HA) (residue 17 and name HA) 5.0 2.2 1.0 !w

Table 4.5 continued

assign (residue 2 and name HB#) (residue 2 and name HG#) 5.0 2.2 1.0 !w
assign (residue 2 and name HB#) (residue 3 and name HN) 5.0 2.2 1.0 !w
assign (residue 2 and name HG#) (residue 2 and name HN) 5.0 2.2 1.0 !w
assign (residue 3 and name HA) (residue 3 and name HN) 3.0 1.2 0.6 !m
assign (residue 3 and name HA) (residue 4 and name HN) 2.5 0.7 0.4 !s
assign (residue 3 and name HA) (residue 3 and name HB1#) 5.0 2.2 1.0 !w
assign (residue 3 and name HA) (residue 3 and name HB2#) 5.0 2.2 1.0 !w
assign (residue 3 and name HB#) (residue 3 and name HN) 5.0 2.2 1.0 !w
assign (residue 3 and name HA) (residue 4 and name HA) 5.0 2.2 1.0 !w
assign (residue 3 and name HB#) (residue 4 and name HN) 5.0 2.2 1.0 !w
assign (residue 3 and name HB#) (residue 4 and name HN) 5.0 2.2 1.0 !w
assign (residue 3 and name HA) (residue 16 and name HN) 5.0 2.2 1.0 !w
assign (residue 3 and name HB#) (residue 16 and name HD#) 5.0 2.2 1.0 !w
assign (residue 3 and name HA) (residue 16 and name HA) 5.0 2.2 1.0 !w

Table 4.5 continued

assign (residue 3 and name HA) (residue 16 and name HD#) 5.0 2.2 1.0 !w
assign (residue 3 and name HB#) (residue 5 and name HE#) 5.0 2.2 1.0 !w
assign (residue 4 and name HA) (residue 5 and name HN) 2.5 0.7 0.4 !s
assign (residue 4 and name HA) (residue 4 and name HD#) 5.0 2.2 1.0 !w
assign (residue 4 and name HA) (residue 4 and name HN) 5.0 2.2 1.0 !w
assign (residue 4 and name HA) (residue 4 and name HB#) 3.0 1.2 0.6 !m
assign (residue 4 and name HD#) (residue 4 and name HB#) 5.0 2.2 1.0 !w
assign (residue 4 and name HD#) (residue 4 and name HG#) 5.0 2.2 1.0 !w
assign (residue 4 and name HG#) (residue 15 and name HG#) 5.0 2.2 1.0 !w
assign (residue 4 and name HB#) (residue 5 and name HN) 5.0 2.2 1.0 !w
assign (residue 4 and name HG#) (residue 15 and name HA#) 5.0 2.2 1.0 !w
assign (residue 4 and name HB#) (residue 15 and name HN) 5.0 2.2 1.0 !w
assign (residue 4 and name HA) (residue 15 and name HB#) 5.0 2.2 1.0 !w
assign (residue 4 and name HG#) (residue 6 and name HG#) 5.0 2.2 1.0 !w

Table 4.5 continued

assign (residue 5 and name HA) (residue 6 and name HN) 2.5 0.7 0.4 !s
assign (residue 5 and name HA) (residue 5 and name HB#) 5.0 2.2 1.0 !w
assign (residue 5 and name HA) (residue 5 and name HB#) 5.0 2.2 1.0 !w
assign (residue 5 and name HA) (residue 5 and name HN) 5.0 2.2 1.0 !w
assign (residue 5 and name HA) (residue 5 and name HD#) 5.0 2.2 1.0 !w
assign (residue 5 and name HB#) (residue 6 and name HN) 5.0 2.2 1.0 !w
assign (residue 5 and name HB1) (residue 5 and name HB2) 2.5 0.7 0.4 !s
assign (residue 5 and name HB#) (residue 5 and name HN) 5.0 2.2 1.0 !w
assign (residue 5 and name HB#) (residue 7 and name HG#) 5.0 2.2 1.0 !w
assign (residue 5 and name HA) (residue 5 and name HE#) 5.0 2.2 1.0 !w
assign (residue 5 and name HD#) (residue 14 and name HB#) 5.0 2.2 1.0 !w
assign (residue 5 and name HB#) (residue 14 and name HE#) 5.0 2.2 1.0 !w
assign (residue 5 and name HD#) (residue 5 and name HB#) 5.0 2.2 1.0 !w
assign (residue 5 and name HD#) (residue 14 and name HE#) 5.0 2.2 1.0 !w

Table 4.5 continued

assign (residue 5 and name HA) (residue 14 and name HB#) 5.0 2.2 1.0 !w
assign (residue 5 and name HB#) (residue 14 and name HZ#) 5.0 2.2 1.0 !w
assign (residue 5 and name HE#) (residue 14 and name HZ#) 5.0 2.2 1.0 !w
assign (residue 5 and name HE#) (residue 14 and name HD#) 5.0 2.2 1.0 !w
assign (residue 5 and name HB#) (residue 6 and name HN) 5.0 2.2 1.0 !w
assign (residue 6 and name HA) (residue 7 and name HN) 2.5 0.7 0.4 !s
assign (residue 6 and name HA) (residue 13 and name HB#) 5.0 2.2 1.0 !w
assign (residue 6 and name HA) (residue 6 and name HG#) 5.0 2.2 1.0 !w
assign (residue 6 and name HA) (residue 6 and name HB#) 5.0 2.2 1.0 !w
assign (residue 6 and name HA) (residue 6 and name HN) 5.0 2.2 1.0 !w
assign (residue 6 and name HD#) (residue 6 and name HG#) 2.5 0.7 0.4 !s
assign (residue 6 and name HA) (residue 13 and name HA) 5.0 2.2 1.0 !w
assign (residue 6 and name HG#) (residue 13 and name HB#) 5.0 2.2 1.0 !w
assign (residue 6 and name HD#) (residue 13 and name HB#) 5.0 2.2 1.0 !w

Table 4.5 continued

assign (residue 6 and name HG#) (residue 4 and name HG#) 5.0 2.2 1.0 !w
assign (residue 7 and name HA) (residue 7 and name HB#) 5.0 2.2 1.0 !w
assign (residue 7 and name HA) (residue 7 and name HN) 5.0 2.2 1.0 !w
assign (residue 7 and name HA) (residue 7 and name HG#) 5.0 2.2 1.0 !w
assign (residue 7 and name HA) (residue 8 and name HN) 2.5 0.7 0.4 !s
assign (residue 7 and name HB#) (residue 8 and name HN) 5.0 2.2 1.0 !w
assign (residue 7 and name HG#) (residue 7 and name HB#) 3.0 1.2 0.6 !m
assign (residue 7 and name HG#) (residue 8 and name HN) 5.0 2.2 1.0 !w
assign (residue 8 and name HA) (residue 8 and name HN) 2.5 0.7 0.4 !s
assign (residue 8 and name HA) (residue 9 and name HN) 3.0 1.2 0.6 !m
assign (residue 8 and name HB#) (residue 9 and name HN) 5.0 2.2 0.6 !w
assign (residue 8 and name HB#) (residue 6 and name HG#) 5.0 2.2 0.6 !w
assign (residue 8 and name HD#) (residue 8 and name HB#) 5.0 2.2 0.6 !m
assign (residue 8 and name HA) (residue 8 and name HB#) 5.0 2.2 1.0 !w

Table 4.5 continued

assign (residue 8 and name HA) (residue 8 and name HB#) 5.0 2.2 1.0 !w
assign (residue 9 and name HA) (residue 9 and name HN) 3.0 1.2 0.6 !m
assign (residue 9 and name HA) (residue 10 and name HN) 3.0 1.2 0.6 !m
assign (residue 9 and name HA) (residue 9 and name HB#) 5.0 2.2 1.0 !w
assign (residue 9 and name HB#) (residue 9 and name HN) 5.0 2.2 1.0 !w
assign (residue 9 and name HB#) (residue 10 and name HN) 5.0 2.2 1.0 !w
assign (residue 10 and name HA#) (residue 10 and name HN) 3.0 1.2 0.6 !m
assign (residue 10 and name HA#) (residue 11 and name HN) 2.5 0.7 0.4 !s
assign (residue 11 and name HA) (residue 12 and name HN) 2.5 0.7 0.4 !s
assign (residue 11 and name HA) (residue 11 and name HN) 5.0 2.2 1.0 !w
assign (residue 11 and name HA) (residue 11 and name HB#) 3.0 1.2 0.6 !m
assign (residue 11 and name HB#) (residue 11 and name HN) 3.0 1.2 0.6 !m
assign (residue 11 and name HA) (residue 12 and name HN) 5.0 2.2 1.0 !w
assign (residue 11 and name HB#) (residue 8 and name HG#) 5.0 2.2 1.0 !w

Table 4.5 continued

assign (residue 11 and name HB#) (residue 13 and name HB#) 5.0 2.2 1.0 !w
assign (residue 12 and name HA) (residue 13 and name HN) 2.5 0.7 0.4 !s
assign (residue 12 and name HA) (residue 12 and name HB#) 5.0 2.2 1.0 !w
assign (residue 12 and name HA) (residue 12 and name HD#) 5.0 2.2 1.0 !w
assign (residue 12 and name HA) (residue 12 and name HN) 5.0 2.2 1.0 !w
assign (residue 12 and name HB#) (residue 7 and name HG#) 5.0 2.2 1.0 !w
assign (residue 12 and name HD#) (residue 7 and name HG#) 5.0 2.2 1.0 !w
assign (residue 12 and name HD#) (residue 7 and name HB#) 5.0 2.2 1.0 !w
assign (residue 12 and name HG#) (residue 7 and name HG#) 5.0 2.2 1.0 !w
assign (residue 12 and name HB#) (residue 13 and name HN) 5.0 2.2 1.0 !w
assign (residue 12 and name HD#) (residue 14 and name HZ#) 5.0 2.2 1.0 !w
assign (residue 13 and name HA) (residue 14 and name HN) 2.5 0.7 0.4 !s
assign (residue 13 and name HA) (residue 13 and name HB#) 5.0 2.2 1.0 !w
assign (residue 13 and name HA) (residue 13 and name HG#) 5.0 2.2 1.0 !w

Table 4.5 continued

assign (residue 13 and name HA) (residue 13 and name HN) 5.0 2.2 1.0 !w
assign (residue 13 and name HA) (residue 14 and name HN) 2.5 0.7 0.4 !s
assign (residue 13 and name HB#) (residue 13 and name HN) 2.5 0.7 0.4 !s
assign (residue 13 and name HA) (residue 14 and name HZ#) 5.0 2.2 1.0 !w
assign (residue 13 and name HG#) (residue 13 and name HN) 5.0 2.2 1.0 !w
assign (residue 13 and name HB#) (residue 14 and name HN) 5.0 2.2 1.0 !w
assign (residue 14 and name HA) (residue 15 and name HN) 2.5 0.7 0.4 !s
assign (residue 14 and name HA) (residue 14 and name HB#) 5.0 2.2 1.0 !w
assign (residue 14 and name HB#) (residue 14 and name HE#) 5.0 2.2 1.0 !w
assign (residue 14 and name HB#) (residue 14 and name HZ#) 5.0 2.2 1.0 !w
assign (residue 15 and name HA) (residue 16 and name HN) 2.5 0.7 0.4 !s
assign (residue 15 and name HA) (residue 15 and name HB#) 5.0 2.2 1.0 !w
assign (residue 15 and name HA) (residue 15 and name HD#) 5.0 2.2 1.0 !w
assign (residue 15 and name HA) (residue 15 and name HN) 5.0 2.2 1.0 !w

Table 4.5 continued

assign (residue 15 and name HB#) (residue 15 and name HG#) 5.0 2.2 1.0 !w
assign (residue 15 and name HB#) (residue 15 and name HD#) 3.0 1.2 0.6 !m
assign (residue 15 and name HG#) (residue 15 and name HD#) 3.0 1.2 0.6 !m
assign (residue 15 and name HG#) (residue 14 and name HN) 5.0 2.2 1.0 !w
assign (residue 15 and name HB#) (residue 17 and name HD#) 5.0 2.2 1.0 !w
assign (residue 16 and name HA) (residue 16 and name HN) 2.5 0.7 0.4 !s
assign (residue 16 and name HA) (residue 17 and name HN) 2.5 0.7 0.4 !s
assign (residue 16 and name HD#) (residue 16 and name HB#) 5.0 2.2 1.0 !w
assign (residue 16 and name HB#) (residue 17 and name HN) 5.0 2.2 1.0 !w
assign (residue 16 and name HG#) (residue 18 and name HB#) 5.0 2.2 1.0 !w
assign (residue 17 and name HA) (residue 17 and name HN) 5.0 2.2 1.0 !w
assign (residue 17 and name HA) (residue 17 and name HB#) 3.0 1.2 0.6 !m
assign (residue 17 and name HA) (residue 17 and name HD#) 3.0 1.2 0.6 !m
assign (residue 17 and name HA) (residue 18 and name HN) 2.5 0.7 0.4 !s

Table 4.5 continued

assign (residue 17 and name HD#) (residue 15 and name HG#) 5.0 2.2 1.0 !w
assign (residue 17 and name HD#) (residue 17 and name HB#) 3.0 1.2 0.6 !m
assign (residue 18 and name HA) (residue 18 and name HN) 3.0 1.2 0.6 !m
assign (residue 18 and name HD#) (residue 16 and name HG#) 5.0 2.2 1.0 !w
assign (residue 18 and name HA) (residue 18 and name HB#) 5.0 2.2 1.0 !w
assign (residue 18 and name HA) (residue 18 and name HB#) 5.0 2.2 1.0 !w
assign (residue 18 and name HA) (residue 18 and name HD#) 5.0 2.2 1.0 !w
assign (residue 18 and name HB#) (residue 18 and name HD#) 5.0 2.2 1.0 !w
assign (residue 18 and name HA) (residue 18 and name HG#) 5.0 2.2 1.0 !w
assign (residue 18 and name HA) (residue 2 and name HA) 2.5 0.7 0.4 !s
! NH-NH
assign (residue 2 and name HN) (residue 3 and name HN) 5.0 2.2 1.0 !w
assign (residue 3 and name HN) (residue 4 and name HN) 5.0 2.2 1.0 !w
assign (residue 4 and name HN) (residue 5 and name HN) 5.0 2.2 1.0 !w

Table 4.5 continued

assign (residue 5 and name HN) (residue 6 and name HN) 5.0 2.2 1.0 !w
assign (residue 7 and name HN) (residue 8 and name HN) 5.0 2.2 1.0 !w
assign (residue 9 and name HN) (residue 10 and name HN) 5.0 2.2 1.0 !w
assign (residue 10 and name HN) (residue 11 and name HN) 5.0 2.2 1.0 !w
assign (residue 11 and name HN) (residue 12 and name HN) 5.0 2.2 1.0 !w
assign (residue 12 and name HN) (residue 13 and name HN) 5.0 2.2 1.0 !w
assign (residue 13 and name HN) (residue 14 and name HN) 5.0 2.2 1.0 !w
assign (residue 14 and name HN) (residue 15 and name HN) 5.0 2.2 1.0 !w
assign (residue 15 and name HN) (residue 16 and name HN) 5.0 2.2 1.0 !w
assign (residue 16 and name HN) (residue 17 and name HN) 5.0 2.2 1.0 !w
assign (residue 17 and name HN) (residue 18 and name HN) 5.0 2.2 1.0 !w
assign (residue 4 and name HN) (residue 15 and name HN) 5.0 2.2 1.0 !w
assign (residue 3 and name HN) (residue 16 and name HN) 5.0 2.2 1.0 !w

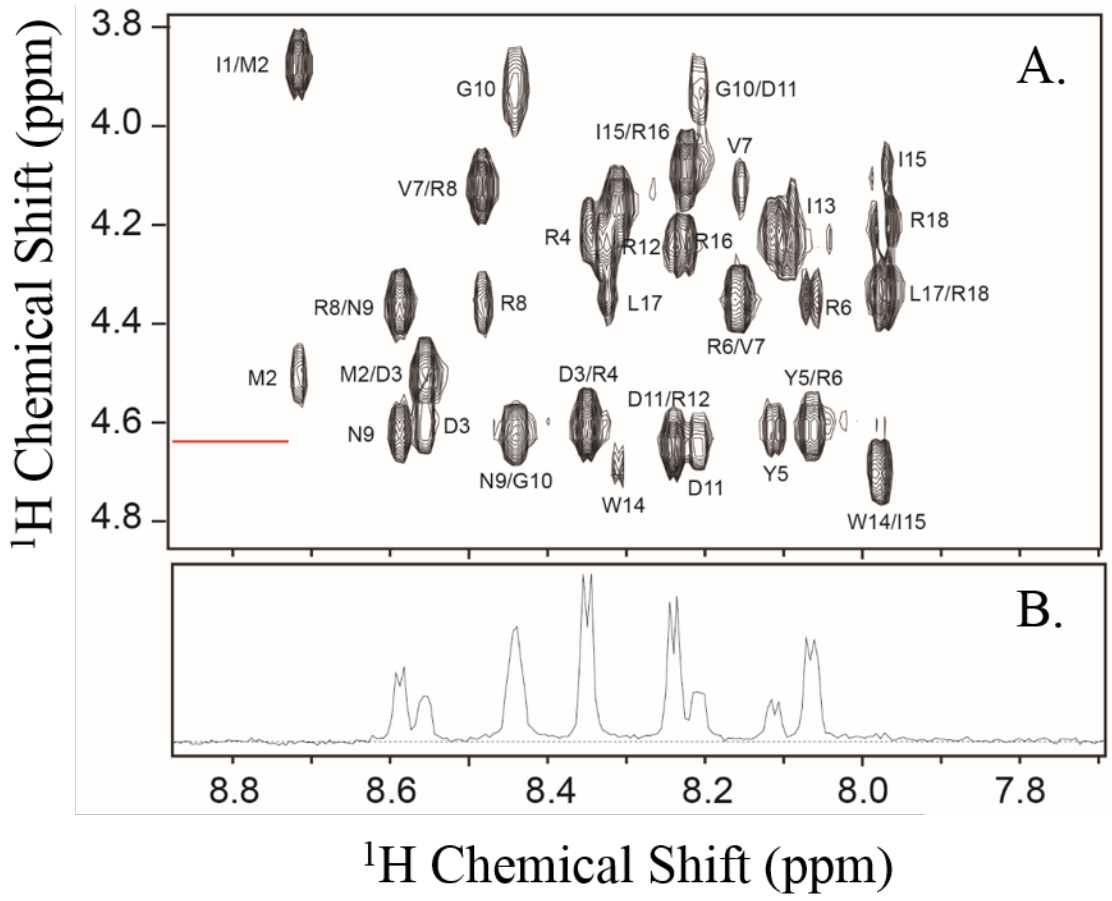

Figure 4.3 NMR data. Selected region of [^{1}H,^{1}H] ROESY (A) and ^{1H}-NMR (B) spectra showing several long-range dipolar contacts between residues.

Seven of the twenty lowest energy conformers of the Peptide M ensemble display distances consistent with a hydrogen bond between the hydroxyl group of Y5 and NH of R16 (distance less than 3.0 Å, Table 4.1). In Peptide A, Y5 is predicted to hydrogen bond as a proton acceptor to R16NH (distance less than 3 Å) in 6 of the 20 models and as a proton acceptor to R16NεH in 4 of the 20 models (Table 4.2). In the averaged, minimized structure of Peptide A, tyrosine is predicted to hydrogen bond to R16NεH (Table 4.2 and Figure 4.1d). These results indicate that there is some probability of a hydrogen-bonding interaction between Y5 and R16 in both peptides. The dynamic nature of the peptide

enables the formation of several stable as well as transient hydrogen bonds. Nonetheless, these residues are exposed to the bulk solvent, and intramolecular hydrogen bonds compete with formation of hydrogen bonds to water.

4.4.2 Circular Dichroism

Figure 4.4b,c presents CD data acquired from Peptide M. The characteristic β-hairpin CD signal has maximum negative ellipticity at 198 nm and arises from the n–pi* transition of the amide backbone.[14, 18] Similar to Peptide A (Figure 4.4a), Peptide M exhibits this characteristic β-hairpin band and reversibly folds both at pH 6.5 and 11. As shown, spectra obtained before (solid line) and after (dashed line) a thermal melt (80 °C, dot–dashed line) exhibit the characteristic negative 198 nm band of the β-hairpin. At both pH values, spectra obtained pre-melt (purple, solid line) and post-melt (purple, dashed line) are similar. Further, β-hairpin signal is lost at 80 °C (purple, dot–dashed line), consistent with thermal melting. These experiments establish that Peptide M has a stable, β-hairpin fold.

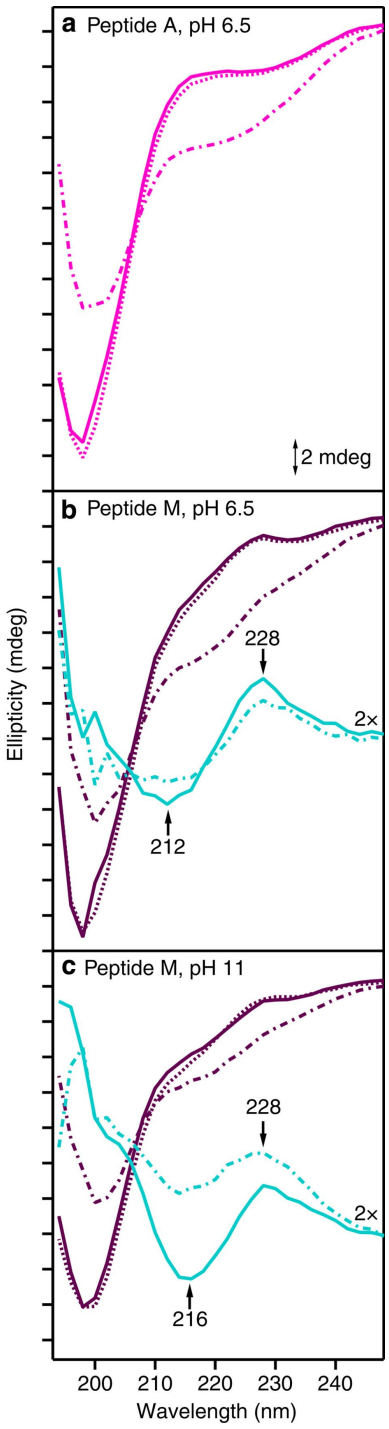

Figure 4.4 CD spectra of Peptide A and Peptide M. Data were acquired from Peptide A, pH 6.5 (a, pink) Peptide M, pH 6.5 (b, purple) and Peptide M, pH 11 (c, purple). The spectra were obtained at 20 °C (solid line, pre-melt), 80 °C (dot–dashed line) or at 20 °C (dashed line, post-melt). In b, difference CD spectra are shown in cyan, corresponding to Peptide M pH 6.5 (b, purple)–minus–Peptide A (a, pink). In c, difference spectra are shown in cyan, corresponding to Peptide M pH 11 (c, purple)–

minus–Peptide A (a, pink). Data were obtained at 20 °C (b,c, cyan, solid line, pre-melt) or at 80 °C (b,c, dot–dashed line). The analyte concentration was 200 µM, and the buffer contained 5 mM MES, pH 6.5 (a,b) or 5 mM borate, pH 11 (C). The spectra were averaged from three independent measurements. The tick marks denote 2 mdeg. Difference CD spectra (cyan) in b,c are multiplied by a factor of 2 for presentation purposes.

4.4.3 Ultraviolet-Visible Absorption Spectra

Figure 4.5a presents presents the ultraviolet absorption spectrum of Peptide M at pH 5 (I, purple) and pH 11 (II, purple). In the 200- to 300-nm region, the spectra of tyrosine (C) and tryptophan (B) are dominated by pi–pi* transitions of the phenol and indole rings. As expected, Peptide M (A) exhibits absorption bands similar to those of tyrosine and tryptophan. However, the Peptide M tyrosine spectrum is perturbed compared with solution models. Subtraction (D) of the aqueous tryptophan spectrum from that of Peptide M reveals a red-shift, both at pH 5 and 11 (I and II, black dashed line). Note that subtraction of the tyrosine spectrum from that of Peptide M yields spectra that resemble tryptophan (Figure 4.6, grey dotted line), with some minor perturbation, except for the region below 260 nm, which is the onset of the peptide bond absorption. Previous gas phase and computational studies of indole-benzene, indole-pyridine and indole-imidazole heterodimers have shown a stabilization of the S_0 state, attributed to NH hydrogen bonding, NH– and CH–pi interactions and pi–pi interactions in the dimers.[32-34] Thus, the red shift of the tyrosine ultraviolet spectrum in Peptide M is attributable to the close proximity of the cross-strand Y5 and W14 to form a Y5-W14 dyad.

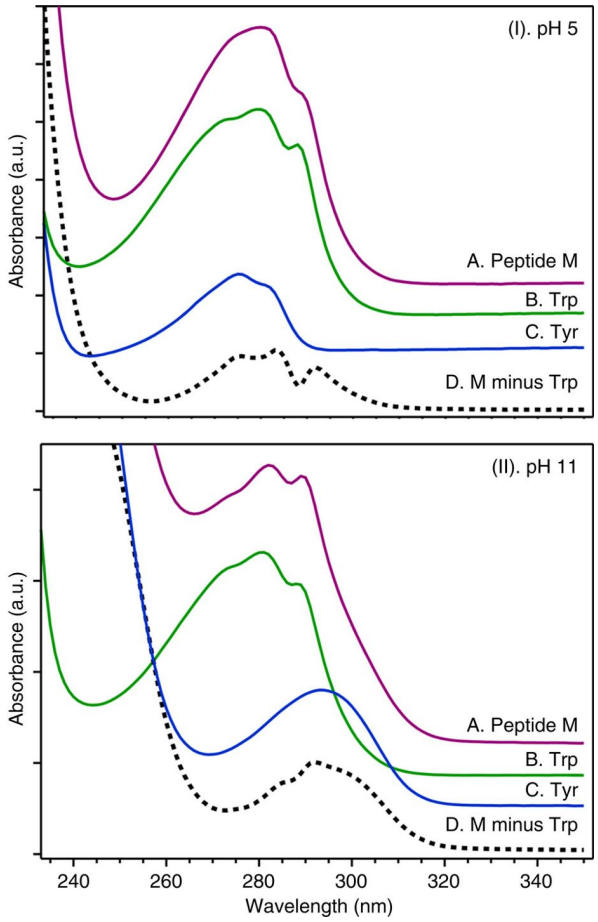

Figure 4.5 Ultraviolet absorption spectra of Peptide M and model compounds. Data were acquired from Peptide M (purple), tyrosine (Tyr; blue) and tryptophan (Trp; green) at pH 5 (I) and at pH 11 (II). The black dashed trace (D) was obtained by subtracting the tryptophan spectrum from that of Peptide M. The analyte concentration was 100 µM, and the buffer contained 5 mM acetate, pH 5 (I) or 5 mM borate, pH 11 (II). The spectra were averaged from two independent measurements. The tick marks denote 0.1 absorbance unit.

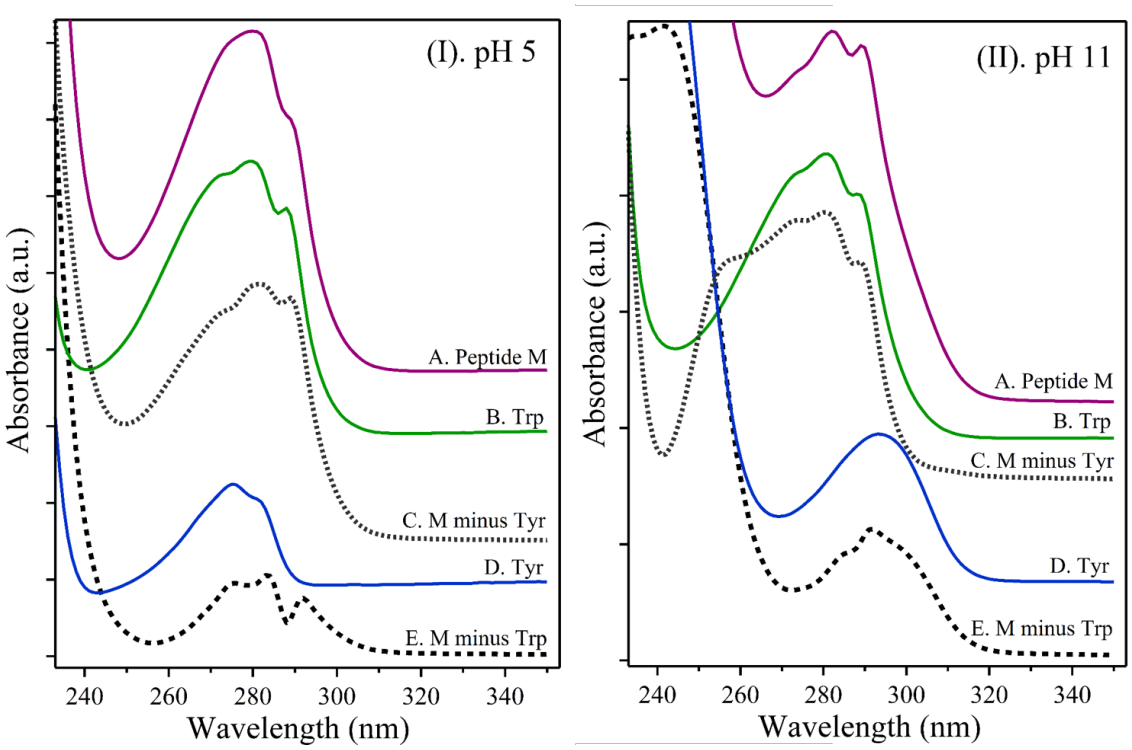

Figure 4.6 UV absorption spectra. Data were derived from Peptide M (purple), tyrosine (blue) and tryptophan (green) at pH 5 (I) and at pH 11 (II). The gray dotted trace (C) was obtained by subtracting the tyrosine spectrum from that of Peptide M. The black dashed trace (E) was obtained by subtracting the tryptophan spectrum from that of Peptide M. The analyte concentration was 100 µM, and the buffer contained 5 mM acetate, pH 5 (I) or 5 mM borate, pH (11). The spectra were averaged from two independent measurements. The tick marks denote 0.1 absorbance unit.

4.4.4 Excitonic Splitting

A through-space aromatic–aromatic interaction between two pi–pi* transitions with similar energies can result in excitonic splitting, which is detectable in the CD spectrum.[35] The red shift of the Peptide M tyrosine spectrum led us to search for characteristic exciton splitting in the CD spectra of this peptide. Examination of Figure 4.4b (pH 6.5) and Figure 4.4c (pH 11) showed a differential band, which is superimposed on the β strand 198 nm signal. Peptide A, which lacks the Y5-W14 dyad, did not exhibit this feature (Figure 4.4a).

This excitonic feature is clearly seen when the CD spectrum of Peptide A is subtracted from that of Peptide M, revealing the characteristic excitonic splitting with a negative feature at 212–216 nm and a positive component at 228 nm. The amplitude of this excitonic couplet signal decreased at 80 °C, indicating sensitivity to thermal melting of the peptide. Excitonic coupling leads to the splitting of the excited state into two components because of delocalization over the two monomers. Previous studies of PagP have identified an excitonic couplet (negative, ~225 nm; positive 230 nm) between Trp66 and Tyr26 (ref. [36]). Such an excitonic splitting between the ^1B_b band of tryptophan and the ^1L_a band of tyrosine can occur only if the indole and phenol side chains are in close proximity and fulfill geometric restraints on the orientations of the two transition moments. We conclude that the tryptophan and tyrosine in Peptide M form an excitonically interacting, aromatic pair via a dipole–dipole interaction.

4.4.5 Differential Pulse Voltammetry (DPV)

To characterize the properties of the dyad, we performed DPV, and the results are presented in Figure 4.7. The peak potential of tyrosine exhibits linear dependence on pH below the pK_a of the phenolic oxygen.[37] Using DPV, the peak potentials of tyrosine (blue) were determined to be 0.99±0.01 and 0.65±0.01 V at pH 5 and 11, respectively. The voltammograms acquired from tyrosine were irreversible, as previously reported, because of a contribution from competing reactions.[37] However, these peak potentials agree with reported midpoint potentials, implying that any correction factor is small.[14, 37-38] Y5 in Peptide A (pink) gave peak potentials of 1.00±0.01 V (pH 5) and 0.71±0.02 V (pH 11) versus normal hydrogen electrode (NHE), similar to peak potentials of aqueous tyrosine and to values previously reported for this peptide.[14]

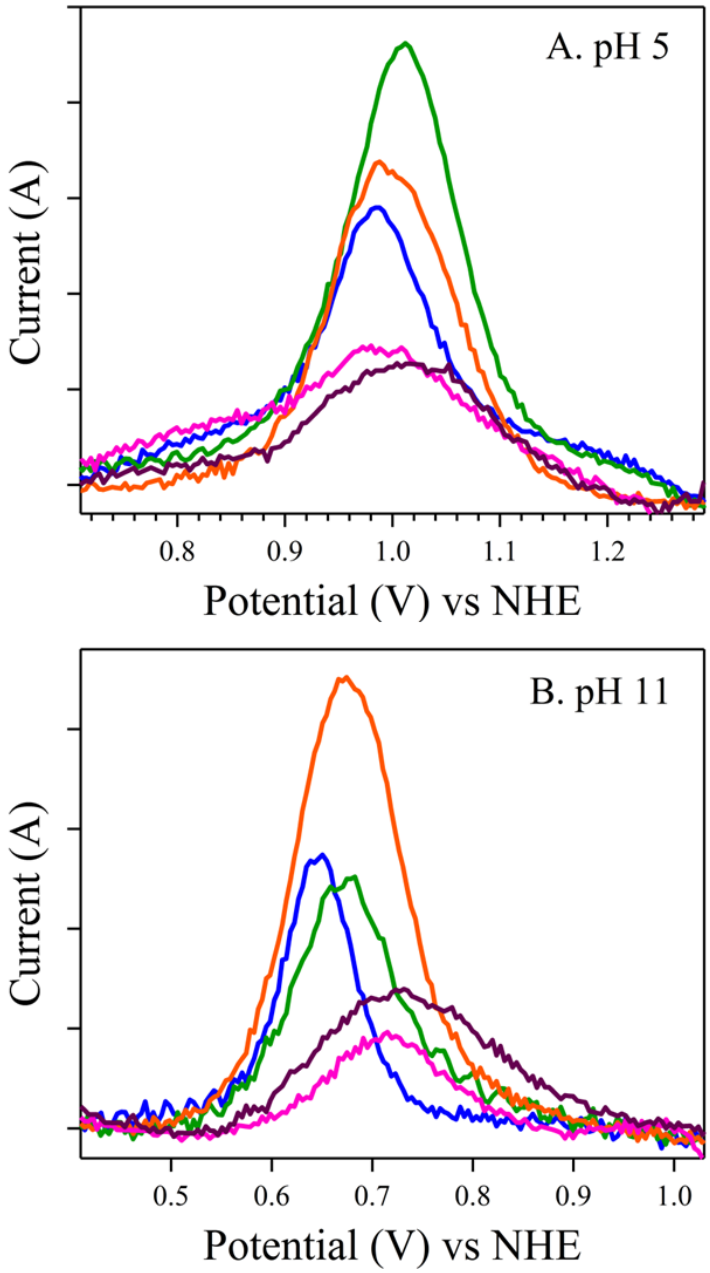

Figure 4.7 DPV. Data were derived from Peptide A (pink), Peptide M (purple), a tyrosine-tryptophan solution (orange), a tyrosine solution (blue) and a tryptophan solution (green) at pH 5 (A) or at pH 11 (B). The data were baseline corrected for presentation purposes. The analyte concentration was 100 µM. At pH 5, the buffer was 5 mM acetate, 200 mM KCl (A). At pH 11, the buffer was 5 mM borate, 200 mM KCl (B). The data were averaged from three independent measurements for peptides and from nine independent measurements for amino acid analytes. Potentials are given versus the normal hydrogen electrode (NHE) by adding 0.22 V to the values measured using a 1 M KCl-filled Ag/AgCl reference electrode. The tick marks denote 1 x 10-7 units. Peptide A (pink) and Peptide M (purple) voltammagrams are

multiplied by 2 for clarity. DPV measurements were performed on a computer-controlled Princeton Applied Research 273A potentiostat. Experiments were conducted in an argon-sparged, three-electrode cell (CH Instruments, Austin, TX) equipped with a 3 mm glassy carbon working electrode, platinum wire counter electrode, and a Ag/AgCl reference electrode in 1 M KCl (E = 0.22 V (NHE)). Data were collected in increments of ΔE = 4 mV at a scan rate of 32 mV/s. The differential pulse amplitude was 25 mV. Data were fit to a polynomial baseline using PeakFit 4 (Systat Software Inc, San Jose, CA) and smoothed using CorrView3 (Scribner, Southern Pines, NC). Data on the amino acids were averaged in triplicate and data on the peptides were averages of nine trials. The peak potentials reported in the text were determined from the centroid of the data before baseline correction. Hexamine ruthenium (III) chloride (200 µM, 1 M KCl)1 was used as standard in each trial and gave a peak potential of -0.200 ± 0.003 V versus Ag/AgCl (average of 20), as expected. In control experiments at pH 11, CAPS was used as a buffering agent. The substitution of the borate buffer by CAPS had no effect on the DPV measurement at pH 11.

The peak potentials of Peptide M, aqueous tryptophan and an aqueous mixture of tyrosine and tryptophan (Figure 4.7A,B) were similar both at pH 5 and pH 11, given the standard deviation of the measurements. The values obtained at pH 5 and 11 for Peptide M (1.02±0.02 and 0.72±0.01 V versus NHE, respectively) were in good agreement with values previously reported for the midpoint potential of tryptophan.[37-38] We conclude that the electronic interaction between tryptophan and tyrosine in Peptide M does not have a large effect on the peak potential of the amino-acid side chain. This implies that stabilization of the singlet and the radical state are similar in Peptide M, suggesting that Y5 interacts with W14 in both states.

4.4.6 Electron Paramagnetic Resonance (EPR) Spectroscopy

Next, we sought to examine the radical state of Y5 in order to establish whether tyrosyl radical structure is altered in Peptide M. To examine the radical state, ultraviolet photolysis and EPR spectroscopy can be performed. However, the breadth of the X-band EPR spectra precludes the detection of small differences in radical structure. This is

illustrated in Figure 4.8, in which photolysis at 266 nm was used to generate both tyrosyl (Figure 4.8D) and tryptophan (Figure 4.8C) radicals in frozen solutions or powders (160 K) of the isolated amino acids. The EPR of the tyrosyl and tryptophan radicals agree in lineshape and *g* value with earlier reports.[39-40] Ultraviolet photolysis of Peptide M (Figure 4.8B) gave an EPR lineshape similar to the spectrum of an aqueous mixture of tyrosine and tryptophan (Figure 4.8C) and of Peptide A (Figure 4.8A). However, small changes due to the environment are not detectable. Note that this procedure does not cause significant modification of the samples as assessed by the ultraviolet–visible absorption before and after photolysis (Figure 4.9).

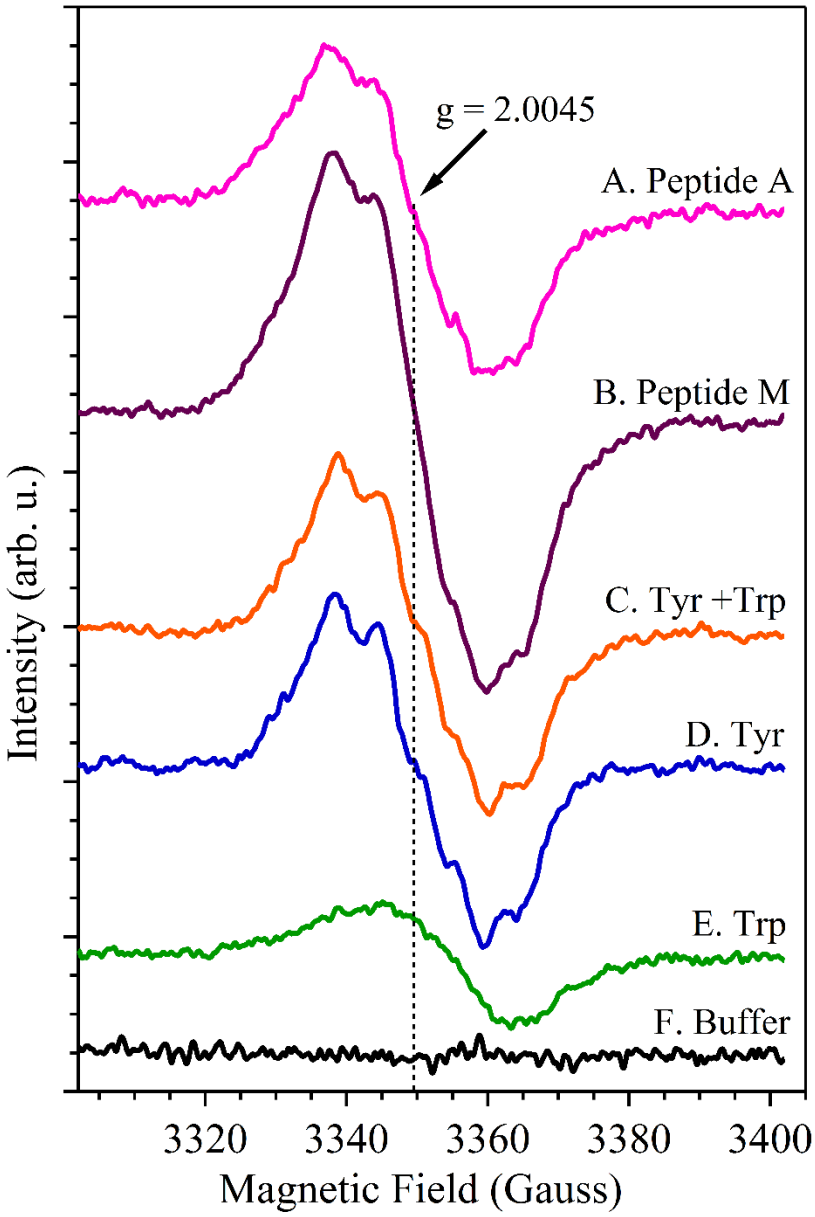

Figure 4.8 X-band EPR spectra. Data were acquired from Peptide A (A), Peptide M (B), tyrosine + tryptophan solution (C), tyrosine solution (D) and tryptophan solution (E). The buffer blank is shown in (F). EPR spectra2,3 were collected on a Bruker EMX spectrometer (Billerica, MA) at 160 K using the following conditions: microwave frequency, 9.2 GHz; microwave power, 200 µW; modulation amplitude, 1 G; modulation frequency, 100 kHz; scan time, 168 s; number of scans, 4; time constant, 655 ms. Radicals were generated using 50 flashes at 266 nm (50-60 mJ) generated by a Nd-YAG laser (Continuum Surelite III, Santa Clara, CA). The analyte concentration was 1 mM, and the buffer contained 10 mM borate, pH 11. The data were averaged from three independent measurements. The tick marks denote 500 units.

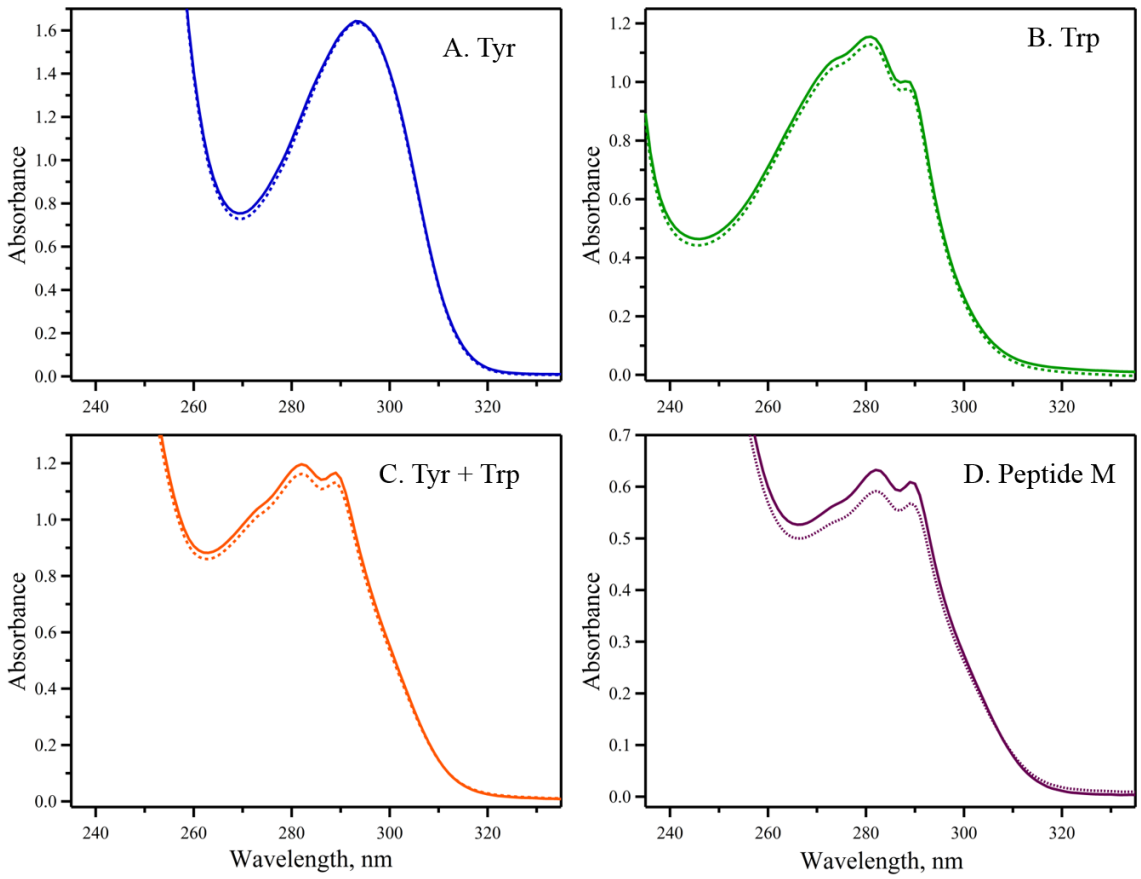

Figure 4.9 UV-Vis spectra. Data acquired from tyrosine (A), tryptophan (B), tyrosine-tryptophan solution (C) and Peptide M (D) before (solid line) and after (dashed-line) EPR measurements. The solutions of tryptophan (B), tyrosine-tryptophan mixture (C) and Peptide M (D) were diluted four fold before measurements due to the high absorbance of the original 1 mM solution.

4.4.7 Ultraviolet Resonance Raman Studies

To more incisively probe the structure of the tyrosyl radical and singlet state, UVRR spectra were acquired at pH 11 using 244 nm excitation. Previous work has shown that tyrosyl radical can be generated by 244 nm, continuous illumination of aqueous tyrosine at room temperature.[13, 30] This procedure does not result in modification of the peptide, as assessed by mass spectrometry. Raman excitation at 244 nm is specific for the tyrosyl radical and the tyrosine singlet, because of resonance enhancement of the tyrosine

electronic transition relative to that of tryptophan. The Raman bands due to tyrosyl radical and tyrosine singlet state are highlighted in difference spectra (high power scan minus low power scan). The positive bands correspond to the vibrational modes of the radical, whereas the negative bands correspond to the singlet vibrational modes.

The UVRR difference spectrum obtained from aqueous tyrosine is shown in Figure 4.10d. Positive bands at 1,410, 1,514 and 1,574 cm^{-1} are assigned to ring stretching (Y19a), C–O stretching (Y7a) and C–C ring (Y8a) stretching modes of the radical, respectively (Table 4.6). The negative bands at 1,172, 1,206 and 1,600 cm^{-1} arise from the CH bend (Y9a), ring C–CH2 (Y7a) and a ring Y8a mode of the singlet state.[13, 30] As expected, 244 nm excitation of aqueous tryptophan did not produce a Raman difference spectrum (Figure 4.10e). The difference spectrum of an aqueous tyrosine–tryptophan mixture (Figure 4.10c) was indistinguishable (±2 cm^{-1}) from that of tyrosine alone, again showing the specificity of this Raman probe wavelength for tyrosine.

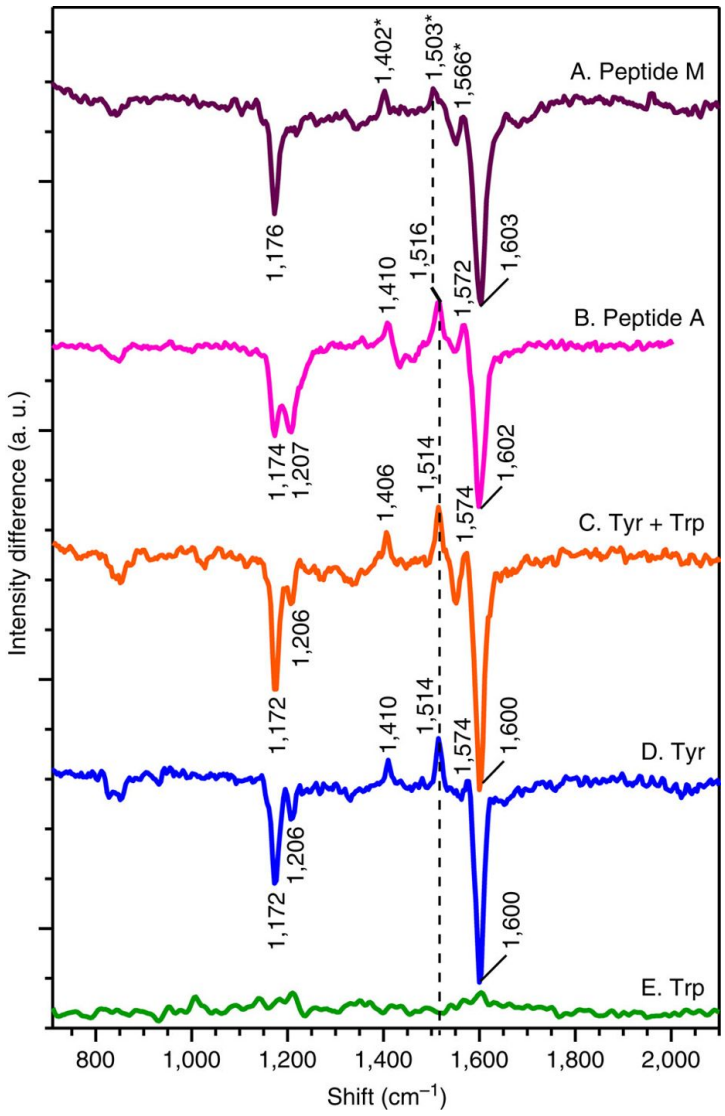

Figure 4.10 UVRR difference spectra derived from Peptide M, Peptide A and model compounds. Data were acquired from Peptide M (A), Peptide A (B), a tyrosine-tryptophan solution (C), a tyrosine solution (D) or a tryptophan solution (E). The analyte concentration was 1 mM, and the buffer was 5 mM borate, pH 11. The difference spectrum was obtained by subtracting an averaged low-power scan (340 µW) from an averaged high-power scan (3.4 mW). The tick marks denote 50 intensity units. The data were averaged from at least two independent measurements. The asterisks in A denote unique frequencies of the YO·-W dyad.

Table 4.6 Vibrational frequencies (cm^{-1}) and assignments for tyrosyl radical in Peptide M, other model compounds and *E. coli* β2 as defined by UVRR spectroscopy.

Sample	RingY8a	CO Y7a	Ring Y19a
Tyr*	1,574	1,514	1,410
Tyr+Trp*	1,574	1,514	1,406
Trp*	NO†	NO†	NO†
Peptide A*	1,572	1,516	1,410
Peptide M*	1,566	1,503	1,402
RNR‡	1,556	1,499	NO†

*This work; † NO, not observed; ‡ Values from ref [13]

Figure 4.10a presents UVRR difference spectrum of Peptide M. The frequencies and intensities of the singlet Raman bands were identifiable using data acquired from the tryptophan–tyrosine mixture and a tyrosine solution. A shift in the frequency of the singlet Y8a, from 1,600 cm^{-1} in tyrosine (Figure 4.10d) to 1,603 cm^{-1} in Peptide M (Figure 4.10a), may not be significant, relative to the uncertainty in peak position (±2 cm^{-1}). The Y9a band is conformationally sensitive and exhibits a modest shift (4 cm^{-1}) when Peptide M is compared with tyrosine.

In contrast, the frequencies of the positive radical bands were significantly shifted in Peptide M, compared with those derived from tyrosine, a solution of tyrosine and tryptophan, and Peptide A (Figure 4.10b and Table 4.6).[13, 30] For example, the radical ring stretch (Y19a) shifts from 1,410 cm^{-1} in tyrosine to 1,402 cm^{-1} in Peptide M (Table 4.6). In addition, the radical CO stretch (Y7a) and the ring stretch (Y8a) bands were 1,514 and 1,574 cm^{-1} in the tyrosine model compound (Figure 4.10d) but were 1,503 and 1,566 cm^{-1} in Peptide M (Figure 4.10a, peaks labelled with asterisks). Radical frequencies in Peptide A were indistinguishable from that of tyrosine and were 1,410 (Y19a), 1,516 (Y7a) and 1,572 (Y8a) cm^{-1} (Table 4.6 and see also ref. [30]). We conclude that substantial 8–11 cm^{-1} Raman shifts are diagnostic for an aromatic–aromatic interaction between the tyrosyl radical and a tryptophan side chain in a YO·-W dyad.

4.5 Discussion

In β2 or other complex proteins, a detailed picture of interaction between Y and W is difficult to obtain, because of background signals from other tyrosines, tryptophans and the peptide backbone. *De novo* designed peptides provide structurally tractable backgrounds in which to elucidate function (for examples, see refs [38, 41-42]). For instance, studies of the β-hairpin, Peptide A, have demonstrated that the peptide environment accelerates the rate of electron and proton-coupled electron transfer[43] and provide a model system for investigating orthogonal proton and electron transfer involving tyrosine and histidine.[14, 18] Also, UVRR spectroscopy has shown that a reversible conformational change accompanies electron or proton-coupled electron transfer in Peptide A.[30]

To understand the spectroscopic and functional properties of a tyrosine–tryptophan dyad, we designed and synthesized a β-hairpin maquette, Peptide M, which contains a tyrosine–tryptophan cross-strand interacting pair. Peptide M forms a β-hairpin at pH 6.5 and 11 and can be reversibly folded and unfolded at both pH values. NMR experiments show that the tyrosine and tryptophan are ~6 Å apart and exhibit a pi-stacked, staggered interaction, which is similar to the tyrosine/tryptophan orientation observed in β2. The ultraviolet and CD spectra of the peptide exhibit spectral shifts and splittings that are characteristic of S_0 state stabilization and of a dipole–dipole-mediated electronic interaction between the indole and phenol groups, respectively. The peak potential and singlet Raman spectrum of Peptide M are not significantly perturbed, compared with the isolated amino acids or Peptide A. However, the Raman spectrum of the radical, Y5·-W14, dyad in Peptide M is distinct from that of tyrosine and Peptide A.

In model tyrosine, production of tyrosyl radical is associated with a dramatic upshift of the CO vibrational band (from ~1,260 to 1,514 cm^{-1}) and a downshift of the highest energy aromatic ring stretching mode (from ~1,600 to 1,574 cm^{-1}).[13, 44-46] The Y5·-W14 dyad in Peptide M (Figure 4.10a) exhibits downshifted CO and ring stretching bands, relative to those of tyrosyl radical in aqueous solution (Figure 4.10d) and Peptide A (Figure 4.10b). Interestingly, downshifted CO and ring stretching frequencies have also been reported for Y122O·-W48 in *E. coli* β2 (refs [13, 44, 47]). The CO band of the Y122O·-W48 dyad was detected at 1,498/1,499 cm^{-1} (refs [13, 44, 47]), and the ring stretching mode was detected at 1,556 cm^{-1}. The substantial downshifts observed in the Peptide M dyad suggest that the shifted Raman frequencies in *E. coli* β2 are due, at least in part, to an interaction between Y122O· and W48. The CO band has also been reported to be sensitive to hydrogen

bonding and electrostatics,[48-49] but a factor that downshifts the frequency of the ring stretching bands has not been successfully modelled until this work (reviewed in ref. [50]) Note that in the Peptide M structural ensemble calculated via NOE, there are no conformers showing the presence of an H-bond between Y5 and W14. However, seven of the lowest energy conformers show the presence of an H-bond between the side chains of Y5 and R16. Therefore, intramolecular hydrogen bonding does not provide an explanation for the downshifted Raman bands of Peptide M, when compared with Raman bands of Peptide A.

We attribute the downshift of the CO and ring frequencies of the tyrosyl radical to charge transfer from the tyrosyl radical in the Y·-W dyad. Precedent is established in previous studies of Old Yellow Enzyme, in which charge transfer between flavin cofactor and phenolic compounds resulted in shifts of phenol Raman bands.[51] Subtle changes in angle and distance are observed in the met state of *E. coli* and mouse β2; these changes in orientation could influence the amount of charge transfer. UVRR studies to detect both the ring and CO stretching mode in mammalian β2 will be useful in evaluating this possibility. Such subtle changes in orientation may be the foundation of the 4–8 cm^{-1} differences in band position, when RNR and Peptide M are compared. Note that the idea of conformational gating and tyrosyl radical movement has been proposed to explain the EPR and FTIR spectra of hydrogen peroxide-treated crystals[7] and hydroxyurea-treated solution samples[45], respectively. Therefore, the met Y122OH structure may not be predictive of all the interactions in the radical state.

4.6 Conclusions

In summary, Peptide M is the first reported model system that accounts for the downshifted CO and ring stretching vibrations of Y122O· in *E. coli* β2. The results presented here suggest that the *E. coli* β2 Y122O· radical interacts with W48. The decrease in vibrational frequencies for Y122O· is characteristic of an overall decrease in radical bond strength. This decrease can be associated with delocalization of electron density onto the W48 indole ring or onto another nearby site in the protein. Note that a small amount of charge transfer from the tyrosyl radical to another site would be difficult to detect with magnetic resonance techniques. However, this transfer of charge may be an important element in guiding electron transfer through the hydrogen-bonding network of β2. This charge transfer motif may also operate in other metalloproteins, which employ redox-active tyrosine residues.

4.7 References

1. Dempsey, J. L.; Winkler, J. R.; Gray, H. B. Proton-Coupled Electron Flow in Protein Redox Machines. *Chem. Rev.* **2010,** *110*, 7024-39.

2. Stubbe, J.; van der Donk, W. A. Ribonucleotide Reductases: Radical Enzymes with Suicidal Tendencies. *Chem Biol* **1995,** *2*, 793-801.

3. Minnihan, E. C.; Nocera, D. G.; Stubbe, J. Reversible, Long-Range Radical Transfer in *E. Coli* Class Ia Ribonucleotide Reductase. *Acc. Chem. Res.* **2013,** *46*, 2524-35.

4. Larsson, A.; Sjöberg, B. M. Identification of the Stable Free Radical Tyrosine Residue in Ribonucleotide Reductase. *EMBO Journal* **1986,** *5*, 2037-2040.

5. Atkin, C. L.; Thelander, L.; Reichard, P.; Lang, G. Iron and Free Radical in Ribonucleotide Reductase: Exchange of Iron and Mössbauser Spectroscopy of the Protein B2 Subunit of the *Escherichia Coli* Enzyme. *J. Biol. Chem.* **1973,** *248*, 7464-7472.

6. BollingerJr., J. M.; Edmondson, D. E.; Huynh, B. H.; Filley, J.; Norton, J. R.; Stubbe, J. Mechanism of Assembly of the Tyrosyl Radical-Dinuclear Iron Cluster Cofactor of Ribonucleotide Reductase. *Science* **1991,** *253*, 292-298.

7. Högbom, M.; Galander, M.; Andersson, M.; Kolberg, M.; Hofbauer, W.; Lassmann, G.; Nordlund, P.; Lendzlan, F. Displacement of the Tryosyl Radical Cofactor in Ribonucleotide Reductase Obtained by Single-Crystal High-Field Epr and 1.4-a X-Ray Data. *Proc. Nat. Acad. Sci. USA* **2003,** *100*, 3209-3214.

8. Kauppi, B.; Nielsen, B. B.; Ramaswamy, S.; Larsen, I. K.; Thelander, M.; Thelander, L.; Eklund, H. The Three-Dimensional Structure of Mammalian Ribonucleotide Reductase Protein R2 Reveals a More-Accessible Iron-Radical Site Than *Escherichia Coli* R2. *J. Mol. Biol.* **1996,** *262*, 706-20.

9. Strand, K. R.; Karlsen, S.; Kolberg, M.; Rohr, A. K.; Gorbitz, C. H.; Andersson, K. K. Crystal Structural Studies of Changes in the Native Dinuclear Iron Center of Ribonucleotide Reductase Protein R2 from Mouse. *J Biol Chem* **2004,** *279*, 46794-801.

10. Saleh, L.; Kelch, B. A.; Pathickal, B. A.; Baldwin, J.; Ley, B. A.; Bollinger, J. M., Jr. Mediation by Indole Analogues of Electron Transfer During Oxygen Activation in Variants of *Escherichia Coli* Ribonucleotide Reductase R2 Lacking the Electron-Shuttling Tryptophan 48. *Biochemistry* **2004,** *43*, 5943-52.

11. Krebs, C.; Chen, S.; Baldwin, J.; Ley, B. A.; Patel, U.; Edmondson, D. E.; Huynh, B. H.; J. Martin Bollinger, J. Mechanism of Rapid Electron Transfer During Oxygen Activation in the R2 Subunit of *Escherichia Coli* Ribonucleotide Reductase. 2. Evidence for and Consequences of Blocked Electron Transfer in the W48f Variant. *J. Am. Chem. Soc.* **2000,** *122*, 12207-12219.

12. Rova, U.; Goodtzova, K.; Ingemarson, R.; Behravan, G.; Graslund, A.; Thelander, L. Evidence by Site-Directed Mutagenesis Supports Long-Range Electron Transfer in Mouse Ribonucleotide Reductase. *Biochemistry* **1995,** *34*, 4267-75.

13. Barry, B. A.; Chen, J.; Keough, J.; Jenson, D. L.; Offenbacher, A. R.; Pagba, C. V. Proton Coupled Electron Transfer and Redox Active Tyrosines: Structure and Function of the Tyrosyl Radicals in Ribonucleotide Reductase and Photosystem Ii. *J. Phys. Chem. Lett.* **2012,** *3*, 543-554.

14. Sibert, R.; Josowicz, M.; Porcelli, F.; Veglia, G.; Range, K.; Barry, B. A. Proton-Coupled Electron Transfer in a Biomimetic Peptide as a Model of Enzyme Regulatory Mechanisms. *J Am Chem Soc* **2007,** *129*, 4393-400.

15. Smith, P.; Zhou, B.; Ho, N.; Yuan, Y. C.; Su, L.; Tsai, S. C.; Yen, Y. 2.6 a X-Ray Crystal Structure of Human P53r2, a P53-Inducible Ribonucleotide Reductase. *Biochemistry* **2009,** *48*, 11134-41.

16. Umena, Y.; Kawakami, K.; Shen, J.-R.; Kamiya, N. Crystal Structure of Oxygen-Evolving Photosystem Ii at a Resolution of 1.9 Angstrom. *Nature* **2011,** *473*, 55-60.

17. Ito, N.; Phillips, S. E. V.; Stevens, C.; Ogel, Z. B.; McPherson, M. J.; Keen, J. N.; Yadav, K. D. S.; Knowles, P. F. Novel Thioether Bond Revealed by a 1.7a Crystal Structure of Galactose Oxidase. *Nature* **1991,** *350*, 87-90.

18. Sibert, R. S.; Josowicz, M.; Barry, B. A. Control of Proton and Electron Transfer in De Novo Designed, Biomimetic Beta Hairpins. *ACS Chem Biol* **2010,** *5*, 1157-68.

19. Makwana, K. M.; Mahalakshmi, R. Nmr Analysis of Tuning Cross-Strand Phe/Tyr/Trp–Trp Interactions in Designed B-Hairpin Peptides: Terminal Switch from L to D Amino Acid as a Strategy for B-Hairpin Capping. *The Journal of Physical Chemistry B* **2015,** *119*, 5376-5385.

20. Wu, L.; McElheny, D.; Takekiyo, T.; Keiderling, T. A. Geometry and Efficacy of Cross-Strand Trp/Trp, Trp/Tyr, and Tyr/Tyr Aromatic Interaction in a B-Hairpin Peptide. *Biochemistry* **2010,** *49*, 4705-4714.

21. Polizzi, N. F.; Migliore, A.; Therien, M. J.; Beratan, D. N. Defusing Redox Bombs? *Proc Natl Acad Sci USA* **2015,** *112*, 10821-2.

22. Gray, H. B.; Winkler, J. R. Hole Hopping through Tyrosine/Tryptophan Chains Protects Proteins from Oxidative Damage. *Proc Natl Acad Sci USA* **2015,** *112*, 10920-5.

23. Jenson, D. L.; Barry, B. A. Proton-Coupled Electron Transfer in Photosystem Ii: Proton Inventory of a Redox Active Tyrosine. *J Am Chem Soc* **2009,** *131*, 10567-73.

24. Bax, A.; Davis, D. G. Mlev-17 Based Two-Dimensional Homonuclear Magnetization Transfer Spectroscopy. *J. Magn. Res.* **1985,** *65*, 355-360.

25. Bax, A.; Davis, D. G. Practical Aspects of Two-Dimensional Transverse Noe Spectroscopy. *Journal of Magnetic Resonance* **1985,** *63*, 207-213.

26. Delaglio, F., Grzesiek, S., Vuister, G.W., Zhu, G., Pheifer, J., Bax, A. Nmrpipe: A Nultidimensional Spectral Processng System Based on Unix Pipes. *J. Biomol. NMR* **1995,** *6*, 277-293.

27. Goddard, T. D.; Kneller, D. G. Sparky 3. **1999**.

28. Wuthrich, K., *Nmr of Proteins and Nucleic Acids*. Wiley: 1986.

29. Schwieters, C. D.; Kuszewski, J. J.; Tjandra, N.; Clore, G. M. The Xplor-Nih Nmr Molecular Structure Determination Package. *J. Magn. Res.* **2003,** *160*, 65-73.

30. Pagba, C. V.; Barry, B. A. Redox-Induced Conformational Switching in Photosystem-Ii-Inspired Biomimetic Peptides: A Uv Resonance Raman Study. *J. Phys. Chem. B* **2012,** *116*, 10590-9.

31. Chen, J.; Barry, B. Ultraviolet Resonance Raman Microprobe Spectroscopy of Photosystem Ii. *Photochem. Photobiol.* **2008,** *84*, 815-818.

32. Braun, J.; Neusser, H. J.; Hobza, P. N− H⊙⊙⊙ Π Interactions in Indole⊙⊙⊙ Benzene-H 6, D 6 and Indole⊙⊙⊙ Benzene-H 6, D 6 Radical Cation Complexes. Mass

Analyzed Threshold Ionization Experiments and Correlated Ab Initio Quantum Chemical Calculations. *The Journal of Physical Chemistry A* **2003,** *107*, 3918-3924.

33. Kumar, S.; Biswas, P.; Kaul, I.; Das, A. Competition between Hydrogen Bonding and Dispersion Interactions in the Indole··· Pyridine Dimer and (Indole) 2··· Pyridine Trimer Studied in a Supersonic Jet. *The Journal of Physical Chemistry A* **2011,** *115*, 7461-7472.

34. Hill, J. G.; Das, A. Interaction in the Indole··· Imidazole Heterodimer: Structure, Franck–Condon Analysis and Energy Decomposition. *Physical Chemistry Chemical Physics* **2014,** *16*, 11754-11762.

35. Grishina, I. B.; Woody, R. W. Contributions of Tryptophan Side Chains to the Circular Dichroism of Globular Proteins: Exciton Couplets and Coupled Oscillators. *Faraday Discuss* **1994**, 245-62.

36. Khan, M. A.; Neale, C.; Michaux, C.; Pomes, R.; Prive, G. G.; Woody, R. W.; Bishop, R. E. Gauging a Hydrocarbon Ruler by an Intrinsic Exciton Probe. *Biochemistry* **2007,** *46*, 4565-79.

37. Harriman, A. Further Comments on the Redox Potentials of Tryptophan and Tyrosine. *J. Phys. Chem.* **1987,** *91*, 6102-6104.

38. Tommos, C.; Skalicky, J. J.; Pilloud, D. L.; Wand, A. J.; Dutton, P. L. De Novo Proteins as Models of Radical Enzymes. *Biochemistry* **1999,** *38*, 9495-507.

39. Barry, B. A.; El-Deeb, M. K.; Sandusky, P. O.; Babcock, G. T. Tyrosine Radicals in Photosystem Ii and Related Model Compounds. *J. Biol. Chem.* **1990,** *265*, 20139-20143.

40. Stoll, S.; Shafaat, H. S.; Krzystek, J.; Ozarowski, A.; Tauber, M. J.; Kim, J. E.; Britt, R. D. Hydrogen Bonding of Tryptophan Radicals Revealed by Epr at 700 Ghz. *J Am Chem Soc* **2011,** *133*, 18098-101.

41. Handel, T.; DeGrado, W. F. De Novo Design of a Zn^{2}+-Binding Protein. *J. Am. Chem. Soc.* **1990,** *112*, 6710-6711.

42. Reedy, C. J.; Gibney, B. R. Heme Protein Assemblies. *Chem. Rev.* **2004,** *104*, 617-650.

43. Pagba, C. V.; Chi, S. H.; Perry, J.; Barry, B. A. Proton-Coupled Electron Transfer in Tyrosine and a Beta-Hairpin Maquette: Reaction Dynamics on the Picosecond Time Scale. *J Phys Chem B* **2015,** *119*, 2726-36.

44. Offenbacher, A. R.; Vassiliev, I. R.; Seyedsayamdost, M. R.; Stubbe, J.; Barry, B. A. Redox-Linked Structural Changes in Ribonucleotide Reductase. *J. Am. Chem. Soc.* **2009,** *131*, 7496-7497.

45. Offenbacher, A. R.; Burns, L. A.; Sherrill, C. D.; Barry, B. A. Redox-Linked Conformational Control of Proton-Coupled Electron Transfer: Y122 in the Ribonucleotide Reductase Beta2 Subunit. *J. Phys. Chem. B* **2013,** *117*, 8457-68.

46. Offenbacher, A. R.; Minnihan, E. C.; Stubbe, J.; Barry, B. A. Redox-Linked Changes to the Hydrogen-Bonding Network of Ribonucleotide Reductase Beta2. *J Am Chem Soc* **2013,** *135*, 6380-3.

47. Backes, G.; Sahlin, M.; Sjoberg, B. M.; Loehr, T. M.; Sanders-Loehr, J. Resonance Raman Spectroscopy of Ribonucleotide Reductase. Evidence for a Deprotonated Tyrosyl Radical and Photochemistry of the Binuclear Iron Center. *Biochemistry* **1989,** *28*, 1923-9.

48. Spanget-Larsen, J.; Gil, M.; Gorski, A.; Blake, D. M.; Waluk, J.; Radziszewski, J. G. Vibrations of the Phenoxyl Radical. *J. Am. Chem. Soc.* **2001,** *123*, 11253-61.

49. Tomter, A. B.; Zoppellaro, G.; Schmitzberger, F.; Andersen, N. H.; Barra, A. L.; Engman, H.; Nordlund, P.; Andersson, K. K. Hf-Epr, Raman, Uv/Vis Light Spectroscopic, and Dft Studies of the Ribonucleotide Reductase R2 Tyrosyl Radical from Epstein-Barr Virus. *PloS One* **2011,** *6*, e25022.

50. Barry, B. A. Reaction Dynamics and Proton Coupled Electron Transfer: Studies of Tyrosine-Based Charge Transfer in Natural and Biomimetic Systems. *Biochim. Biophys. Acta* **2015,** *1847*, 46-54.

51. Kitagawa, T.; Nishina, Y.; Shiga, K.; Watari, H.; Matsumura, Y.; Yamano, T. Resonance Raman Evidence for Charge-Transfer Interactions of Phenols with the Flavin Mononucleotide of Old Yellow Enzyme. *Journal of the American Chemical Society* **1979,** *101*, 3376-3378.

CHAPTER 5. STRUCTURE AND FUNCTION OF TRYPTOPHAN-TYROSINE DYADS IN BIOMIMETIC BETA HAIRPINS

Reprinted with permission from *The Journal of Physical Chemistry B*

McCaslin, T. G.; Pagba, C. V.; Chi, S- H.; Hwang, H. J.; Gumbart, J. C.; Perry, J. W.; Olivieri, C.; Porcelli, F.; Veglia, G.; Guo, Z.; McDaniel, M.; Barry, B.A. Structure and Function of Tryptophan-Tyrosine Dyads in Biomimetic Beta Hairpins. *J. Phys. Chem. B*

In press

5.1 Abstract

Tyrosine-tryptophan (YW) dyads are ubiquitous structural motifs in enzymes and play roles in proton coupled electron transfer (PCET) and, possibly, protection from oxidative stress. Here, we describe the function of YW dyads in *de novo* designed 18-mer, beta hairpins. In Peptide M, a YW dyad is formed between W14 and Y5. A UV hypochromic effect and an excitonic Cotton signal are observed, in addition to singlet, excited state (W*), and fluorescence emission spectral shifts. In a second peptide, Peptide MW, a Y5-W13 dyad is formed diagonally across the strand and distorts the backbone. On the picosecond timescale, the W* excited state decay kinetics are similar in all the peptides, but are accelerated relative to amino acids in solution. In Peptide MW, the W* spectrum is consistent with increased conformational flexibility. In Peptide M and MW, the EPR spectra obtained after UV photolysis are characteristic of tyrosine and tryptophan radicals at 160 K. Notably, at pH 9, the radical photolysis yield is decreased in Peptide M and MW, compared to a tyrosine and tryptophan mixture. This protective effect is not observed at pH 11 and is not observed in peptides containing a tryptophan-histidine dyad or tryptophan alone. The YW dyad protective effect is attributed to an increase in radical recombination rate. This increase in rate can be facilitated by hydrogen-bonding interactions, which lower the barrier for the PCET reaction at pH 9. These results suggest that the YW dyad structural motif promotes radical quenching under conditions of reactive oxygen stress.

5.2 Introduction

Proton coupled electron transfer (PCET) and electron transfer (ET) reactions are ubiquitous in biology and play essential roles in respiration, photosynthesis, and DNA

synthesis.[1] In photosynthesis and DNA synthesis, these reactions involve the transient oxidation and reduction of the aromatic amino acids, tryptophan and tyrosine. When produced in solution, these reactive aromatic species have microsecond lifetimes. However, the protein environment can stabilize the radicals and extend lifetimes out to the hours or days time scale.[2-3] In addition, cellular reactions involving oxygen can produce singlet oxygen species, which are potentially reactive and damaging to biological macromolecules. Cells have evolved mechanisms to avoid these deleterious side reactions of reactive oxygen, which can damage proteins (for examples, see refs [4-6]).

Tyrosine-tryptophan (YW) dyads are conserved structural motifs in a variety of oxidoreductases and other enzymes.[7-8] These dyads are identified as pairs or clusters of tyrosine-tryptophan side chains in which the inter-ring distance is less than 10 Å (for example, see [9]). A conserved tyrosine-tryptophan dyad is found in class 1a RNRs (Figure 5.1A) and involves the tyrosyl radical initiator, Y122· and W48 (*E. coli* numbering).[10] In PSII, two redox active tyrosines, YD and YZ (Figure 5.1B-E) [11-13] conduct light-induced ET and PCET reactions via a hopping mechanism in photosynthetic oxygen evolution. The placement of tryptophan side chains near the two tyrosines, YD and YZ, distinguishes the two redox-active sites (Figure 5.1B-E). This is of interest because, while YZ is essential in function, YD forms a more stable radical, which persists in the dark for hours after illumination.[14]

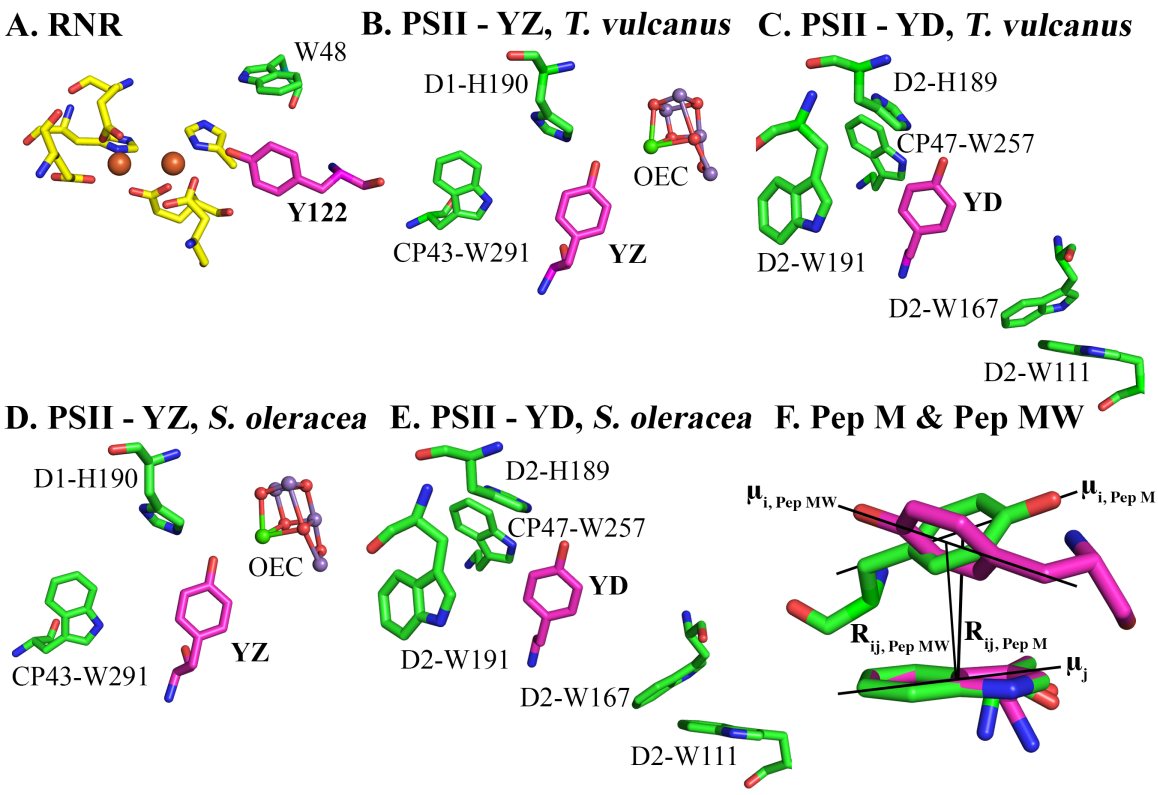

Figure 5.1 YW interactions in X-ray structures of RNR (A, Y122, PDB 1MXR, ref [15]), cyanobacterial (*T. vulcanus*) PSII (B, YZ, and C, YD, PDB 4UB6, ref [12]) and spinach (*S. oleracea*) PSII (D, YZ and E, YD, PDB 3JCU, ref [13]). F shows dihedral angles between tyrosine and tryptophan transition moments (μ_i and μ_j, respectively) and the inter-ring vector, R_{ij}, in the lowest energy NMR structures of Peptide M (green) and Peptide MW (purple). The orientation of the transition moments is defined in refs [16-18].

Due to the wide distribution of the YW dyad motif in enzymes, it has been proposed that these dyads may serve a protective function, possibly by minimizing oxidative damage caused by reactive oxygen species. One protective mechanism could involve rapid radical transfer, through the dyad, to the protein surface. At the surface, the oxidizing equivalents could be scavenged in cellular metabolism.[7-8] In this case, the rate at which oxidizing equivalents are transferred to the surface must be slower than the catalytic reaction. This mechanism could involve quenching of reactive oxygen species. Reactive oxygen is

produced as a byproduct of UV damage and cellular reactions, which involve molecular oxygen. The production of hydroxyl, superoxide, and singlet oxygen is facilitated by the presence of metal ions and known to involve oxidative damage of tryptophan.[5, 19] Tyrosine-tryptophan dyads could function as radical scavengers for these diffusive species.

To test the function of YW dyads in a structurally well-defined system, we have used 18-mer, *de novo* designed beta hairpin peptides. Biomimetic peptide models or maquettes provide an incisive tool for studying non-covalent interactions (reviewed in ref [20]). Previously, designed peptide and adapted protein models have been utilized to define the photochemical properties of tryptophan and tyrosine. For example, the fluorescence emission of tryptophan has been studied in engineered beta hairpin peptides [21] and the ET properties of tryptophan have been studied in modified variants of azurin. [22] For tyrosine, redox properties and excited state spectra have been reported for a beta hairpin peptide, called Peptide A.[23-24] The PSII-inspired hairpin, Peptide A, contains tyrosine and histidine and conducts a proton transfer from tyrosine to histidine when the tyrosine is oxidized in the mid-pH range. The coupling of the PCET and ET reactions with conformational dynamics has been investigated in Peptide A with UV resonance Raman and molecular dynamics simulations.[25-26] Time-resolved spectroscopy has been used to investigate the effects of non-covalent interactions on ET and PCET kinetics.[27-28] The effect of a hydrophobic environment on PCET and ET of tyrosine has also been investigated in alpha helical peptides.[29-31]

UV resonance Raman (UVRR) studies of a RNR-inspired β-hairpin maquette, Peptide M, have also been reported previously. This peptide contains a single tyrosine and a single tryptophan, which exhibit dipole-dipole coupling. The unique UVRR spectrum of

Peptide M was suggested to be characteristic of charge transfer between tyrosyl radical and tryptophan.[32] The UVRR spectrum of Peptide M was reported to be similar to the spectrum of the Y122-W48 in RNR.[33] Here, we use this peptide and its sequence variants to examine the broader role of the YW dyads in structure and function. The results suggest a role for dyads in structural stabilization and in radical scavenging.

5.3 Materials and Methods

5.3.1 Overview of Materials and Methods

Peptides were synthesized by solid-phase synthesis (Genscript, Piscataway, NJ). NMR structures were determined using previously described methods.[23, 32] CD spectra were collected in a Peltier-type cell using a Jasco J-810 spectropolarimeter.[32] EPR spectroscopy was performed on a Bruker EMX spectrometer equipped with a liquid nitrogen cryostat. A frequency quadrupled Nd-YAG laser was used for photolysis (266 nm) methods.[23, 32] TRAS were measured using a HELIOS spectroscopy system.[27-28] The system consisted of a regeneratively amplified Ti:sapphire laser (100 fs pulse width) and a computer-controlled optical parametric amplifier (OPA) pumped by the amplified laser. The 280 nm photolysis pulse was generated by the fourth harmonic of the OPA. Molecular dynamics simulations were performed using previously described methods.[26] A more detailed summary of methods and spectroscopic approaches is given below.

5.3.2 Samples

Boric acid (99% purity), sodium hydroxide (99.5%), 2-(*N*-morpholino)ethanesulfonic acid (MES, >99.5% purity), tyrosine (99.9% purity), and

tryptophan (≥98% purity) were purchased from Sigma (St. Louis, MO). Peptides were synthesized by solid-state synthesis and were purchased from Genscript (Piscataway, NJ; >95% purity). The sequences of peptides employed in this study are shown in Figure 5.2, including Peptide A, Peptide M, Peptide MW, Peptide W, and Peptide WA14.

5.3.3 Effect of pH

In this work, peptide experiments were conducted at pH 9 and 11. The pK_a of tyrosine is 10.[34] Therefore, in experiments conducted at pH 9, tyrosine is expected to be primarily in the neutral (YH) state. The amino terminus will also titrate in this pH range. The terminal NH_2- group has a pK_a of 9.3 and will be ~50% protonated at pH 9, but unprotonated at pH 11.[34] Histidine has a pK_a of 6 [23-24] and will be unprotonated in the singlet state of all the peptides at pH 9 and 11. The tryptophan indole side chain does not titrate in this pH range.

5.3.4 UV-Visible (UV-Vis) Spectroscopy

Optical absorption spectra were recorded on a Shimadzu (Columbia, MD) UV-1700 spectrometer at room temperature. The slit width and spectral resolution were 1 nm.[32]

5.3.5 Circular Dichroism (CD) Spectroscopy

CD spectra were acquired on a Jasco J-810 CD spectropolarimeter. The instrument was equipped with a Peltier-type cell. Spectra were collected from 250 to 193 nm in 1 mm quartz cuvettes. Eight accumulations per scan were averaged in triplicate from independent measurements. Parameters: sensitivity, 100 mdeg; data pitch, 2 nm; scan speed, 50 nm min^{-1}; response time, 1 s; bandwidth, 1 nm.[32]

5.3.6 Electron Paramagnetic Resonance (EPR) Spectroscopy

EPR spectra [23] were recorded on a Bruker (Billerica, MA) EMX spectrometer with a Bruker ER 4102ST cavity and Bruker ER 4131VT temperature controller at 160 K. Field swept spectra were acquired after ten UV flashes. Parameters: microwave frequency, 9.4 GHz; microwave power, 200 μW; modulation amplitude, 4 G; modulation frequency, 100 kHz; scan time, 164 s; number of scans, 3-12; time constant, 655 ms. A microwave power saturation curve was monitored for each sample; samples exhibited no signal saturation at the microwave power employed here. The 266 nm flash (~7 nsec) was supplied by a Nd-YAG (Continuum, San Jose, CA) laser, equipped with two harmonic generators. The laser energy was 35 mJ, and the beam dimensions were approximately 1 cm by 1 cm. Some of the spectra were smoothed with a 13-point algorithm for presentation purposes. Experiments were conducted on at least two different samples.

5.3.7 Fluorescence Spectroscopy

Fluorescence spectra were recorded at room temperature on a Shimadzu (Columbia, MD) RF-5301PC fluorimeter in 1 cm cuvettes. Samples were excited at 266 nm with an excitation and emission slit width of 3 cm; the sampling interval was 1 nm. Emission spectra were recorded from 280 to 450 nm; experiments were conducted in triplicate.

5.3.8 Transient Absorption Spectroscopy (TRAS)

TRAS data were acquired with a pump−white-light- continuum probe spectroscopy system (HELIOS, Ultrafast Systems, Sarasota, FL) using procedures previously described.[27-28] The 280-nm photolysis pulse was generated using the fourth-harmonic

output of the OPA. A white-light-continuum (WLC) probe beam with a spectral range of 350−750 nm was generated by focusing less than 5% of the 800-nm amplified beam into a CaF_2 crystal. The probe signal was collected using a fiber-optic cable coupled to a spectrometer with a multichannel CMOS (complementary metal−oxide−semiconductor) sensor (spectral range of 300−900 nm). The maximum time delay was 3.2 ns. The pump beam was chopped at 500 Hz to obtain the WLC spectrum without the pump and alternately with the 280- nm pump. These data were used to calculate the transient spectra, represented as the changes in optical density or absorbance unit (AU). Each transient spectrum at a given time delay was averaged for 4 s. The excitation pulse energy was 2−3 μJ. The optical path length of the quartz cuvette was 2 mm. The solutions had an optical density at 280 nm (OD280) of 0.25−0.50 in 2-mm-path-length cuvettes and were stirred throughout data acquisition to prevent photoinduced degradation. To verify the integrity of the sample, steady-state absorption spectra were recorded before and after the ultrafast measurements on a Shimadzu UV-3101PC spectrophotometer. No significant change in the steady-state spectrum was observed. Data were fit using IGOR 6.43A software (Wavemetrics Inc., Oswego, OR). In some cases, sinusoidal oscillations were observed as noise on the kinetic transients; these oscillations were not fit during data analysis. Formation of all the signals was complete in 3 ps. Fits to the transient data, associated with decay, began at 3 ps.

5.3.9 Nuclear Magnetic Resonance (NMR) Spectroscopy

The NMR samples were prepared by dissolving 1.0 mg of the lyophilized peptide in 350 μM sodium phosphate buffer at pH ~5 with 5% D_2O. All the NMR experiments were performed at 278 K on a Bruker 600 MHz spectrometer (Bruker Biospin, Billerica, MA). The homonuclear two dimensional TOCSY with 40 or 70 ms of mixing time and spectral

widths of 8000 Hz for both dimensions, was used to assign all resonances. The inter-nuclear distances were determined using a series of homo-nuclear ROESY experiments with mixing times of 50, 100, 200, 250, 300 and 400 ms. Spectra were processed using NMRPipe and analyzed using Sparky software. The fingerprint region of the ROESY acquired at a mixing time of 250 ms is shown in Figure 5.7.

NMR structural analysis was conducted by methods previously described.[23, 32] A total of 125 ROEs consisting of 66 inter- and 59 intra-residues, and 154 ROEs, 74 inter- and 80 intra-residues, respectively for Peptide MW and Peptide W, were used for structure calculations. The complete resonance assignment is reported in Table 5.2 and Table 5.3. Table 5.4 includes measured coupling constants for Pep W and Pep MW. Peak volumes were classified as strong, medium and weak corresponding to distance restraints of 1.8-2.9, 1.8-3.6 and 1.8-6.0 Å, respectively. For residues showing $^{3}J_{NH\text{-}H\alpha} > 8.0\ Hz$ angles were restricted to a range of -160 to -80 degrees. For both peptides, structural ensembles were calculated starting from extended structure and minimized using a hybrid simulated annealing (SA) protocol present in XPLOR-NIH package. 50 conformers were generated using an initial temperature of 1000K with 50000 high temperature steps and 6000 cooling steps. Generated conformers were minimized by introducing Lennard-Jones potential, van der Waals, and electrostatic interactions using an initial temperature T_i of 1000K with 45000 cooling steps. The 20 lowest energy conformers with no NOE violations greater than 0.5 Å, no bond violations greater than 0.05 Å, and no bond violation greater than 4°, were selected for further analysis and reported in Figure 5.4.

5.3.10 Molecular Dynamics (MD) Simulations

MD simulations were conducted by methods previously described.[26] Briefly, the starting states of the peptides were based upon the NMR structure determined here. All simulations utilize the CHARMM36 force field for proteins.[35] Parameters for the tyrosyl radical were determined by us previously.[26] Simulations were carried out with NAMD [36] at 300 K and 1 atm, maintained using Langevin dynamics and the Langevin piston methods, respectively. A 2-fs time step was used with bonded and short-range non-bonded interactions calculated every time step. Long-range interactions were calculated every two time steps using the particle-mesh Ewald (PME) method.[37] The long-range cutoff was 12 Å with a switching function beginning at 10 Å. System setup and analysis were done using VMD.[38] For Peptide M, MW, and W, simulations were conducted for charge states represented at pH 9.0 (YW). For Peptide M, simulations were also conducted in the charge state generated at pH 11 (Y^-W). Replica-Exchange with Solute Tempering (REST2) simulations[39-40] were also run for 100 ns each for Peptide M, MW, and W. A total of 12 replicas covering a temperature range from 300 K to 600 K were used with exchange rates of 20-40%. All analysis and plots presented are for the lowest temperature replica only.

5.4 Results

5.4.1 Sequences and NMR Structures

Figure 5.2 presents the primary sequences of the β-hairpin peptides investigated in this paper, named Peptides M (B), MW (C), W (D), and WA14 (E). As a control in some experiments, Peptide A, was used (Figure 5.2A). Peptide A is a stably folded beta hairpin.[23-24] Peptide A does not contain a YW dyad, but is a tyrosine-histidine containing peptide. In the lowest energy NMR structures, Peptide A forms a beta hairpin with a pi-pi

interaction between tyrosine (Y5) and histidine (H14) (Figure 5.2A). The average structure shows that Peptide A is stabilized by two D-R salt bridges and contains an arginine at position 12, which has a pi-cation interaction with H14. Peptide M (Figure 5.2B) is a sequence variant of Peptide A, which is designed to contain a dyad and in which tryptophan has been substituted for H14 (W14).

A. Peptide A

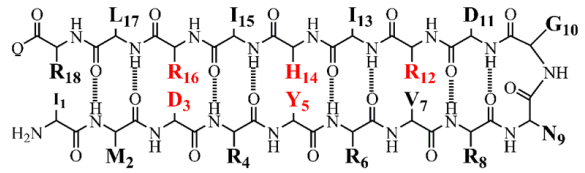

B. Peptide M

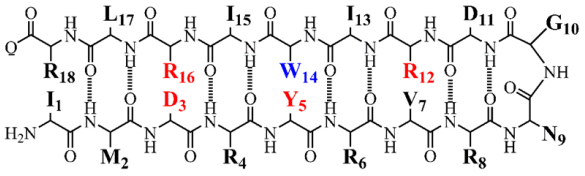

C. Peptide MW

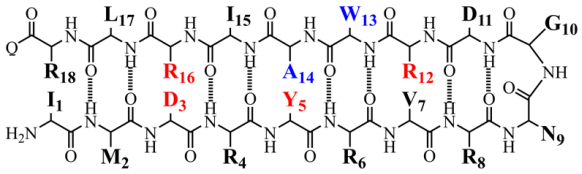

D. Peptide W

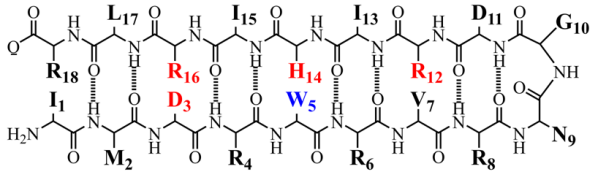

E. Peptide WA14

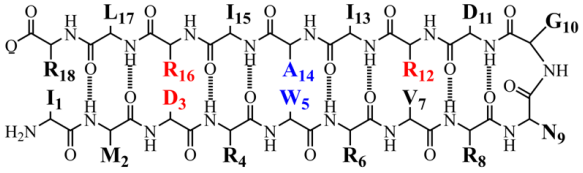

Figure 5.2 Primary sequences and predicted beta turn in Peptide A (A), Peptide M (B), Peptide MW (C), Peptide W (D), and Peptide WA14 (E).

Previously, we determined the NMR structure of Peptide M [32]. This structure shows that the Y5 and W14 aromatic rings do indeed interact as a dyad and exhibit a pi-pi interaction (Figure 5.3B and ref [32]). Note that Y5 and W14 are not hydrogen bonded to each other in the lowest energy structure. In the sequence variant, Peptide MW (Figure 5.2C), the tryptophan side chain is placed at position 13, with an alanine substituted at position 14. The NMR structure of Peptide MW reported here reveals a folded beta hairpin, in which Y5 and W13 form a dyad from opposite sides of the hairpin (Figure 5.3C). Peptide W contains a tryptophan substituted at position 5 and a histidine at position 14 (Figure 5.2D). The NMR structure of Peptide W confirms the formation of a WH interacting, cofacial pair in this peptide, formed from the same side of the beta hairpin (Figure 5.3D). Peptide WA14 was used as a control; this peptide contains only one aromatic group, W5 (Figure 5.2E). Peptide WA14 forms a beta hairpin (Figure 5.3E) as predicted by the program, PEP-FOLD.[41]

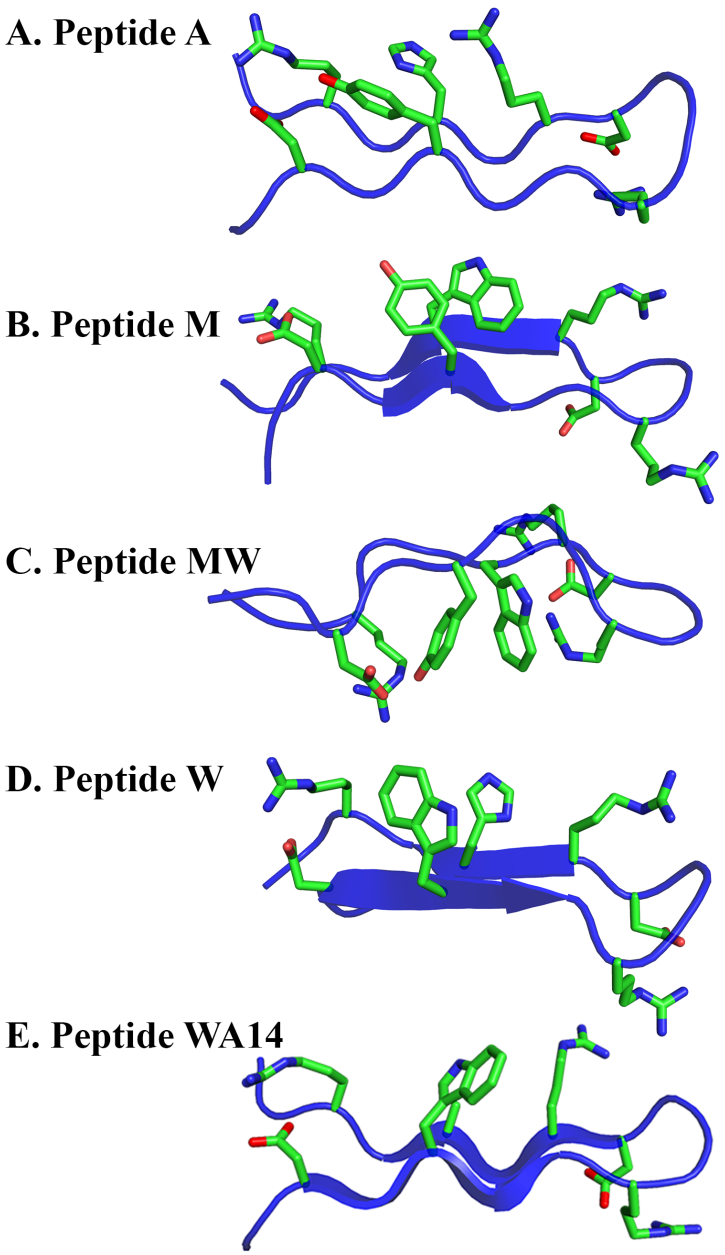

Figure 5.3 Lowest energy NMR structures of (A) Peptide A, (B) Peptide M, (C) Peptide MW, and (D) Peptide W. In (E), a PEP-FOLD [41] model of Peptide WA14.

Figure 5.3 and Figures 5.4-5.7 provide a summary of the NMR data on these peptides and compare the results with the NMR structure of the original Peptide A. The orientation of the aromatic rings in Peptide M and MW is cofacial (Figure 5.3 and Figure 5.4). The cofacial arrangement and inter-ring distances are similar in the 20 lowest energy

structures (Figure 5.4). The chemical shifts reflect the average of all of the possible conformations that are in solution. Although there is a population still folded as reflected by the dipolar contacts (Figure 5.5), in the mutated peptides, the folded population is lower. As shown in the chemical shift index (Figure 5.6), the chemical shifts change with the mutations. Table 5.1 summarizes the distance between aromatic groups in the lowest energy structures of Peptide MW (Table 5.1A), W (Table 5.1B) and Peptide M (Table 5.1C). In Peptide M, the average distance between the phenolic oxygen of Y5 and the indole nitrogen of W14 is ~6 Å, as reported previously.[32] For Peptide MW, the average distance between the phenolic oxygen of Y5 and the indole nitrogen of W13 is ~7 Å. W5 and H14 in Peptide W are measured to be ~6 Å apart. Resonance assignments for Peptide W and Peptide MW are given in Table 5.2 and 5.3, respectively. Table 5.4 shows the measured coupling constants for Peptide W and Peptide MW.

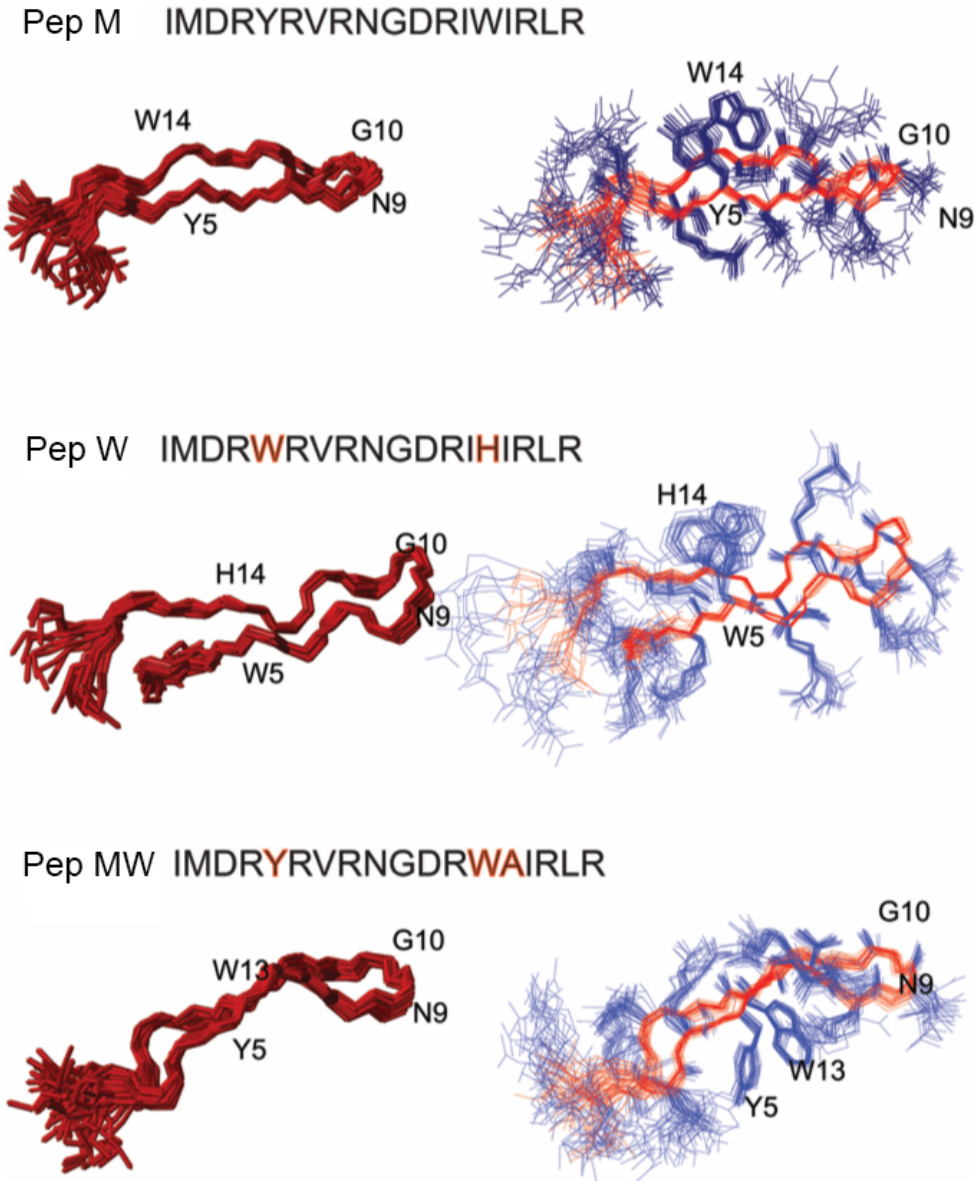

Figure 5.4 Twenty lowest energy NMR structures of Peptide M, Peptide W, and Peptide MW.

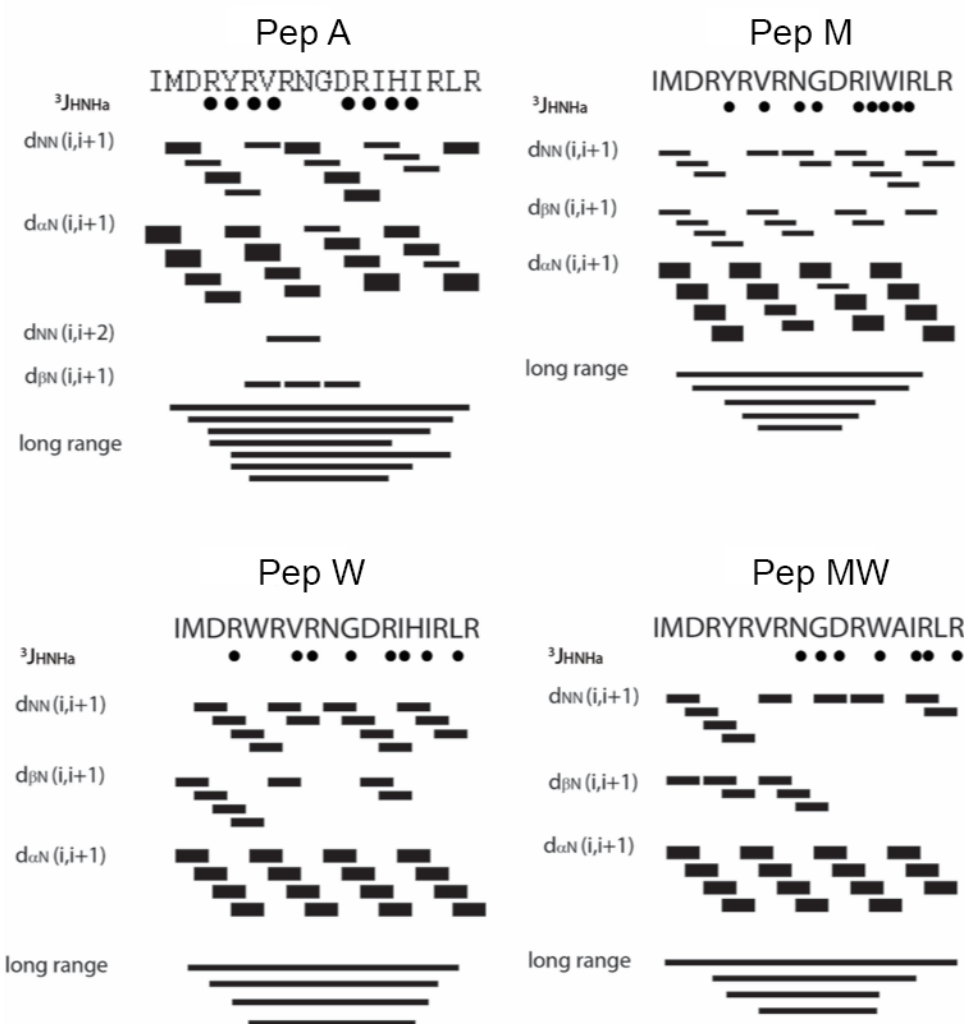

Figure 5.5 Graphical summary of NMR constraints for beta hairpins. Short and long range coupling for the backbone and sidechains of Peptide A, Peptide M, Peptide W, and Peptide MW. The NMR structure of Peptide A was reported previously in ref [23], and the NMR structure of Peptide M was reported in ref [32].

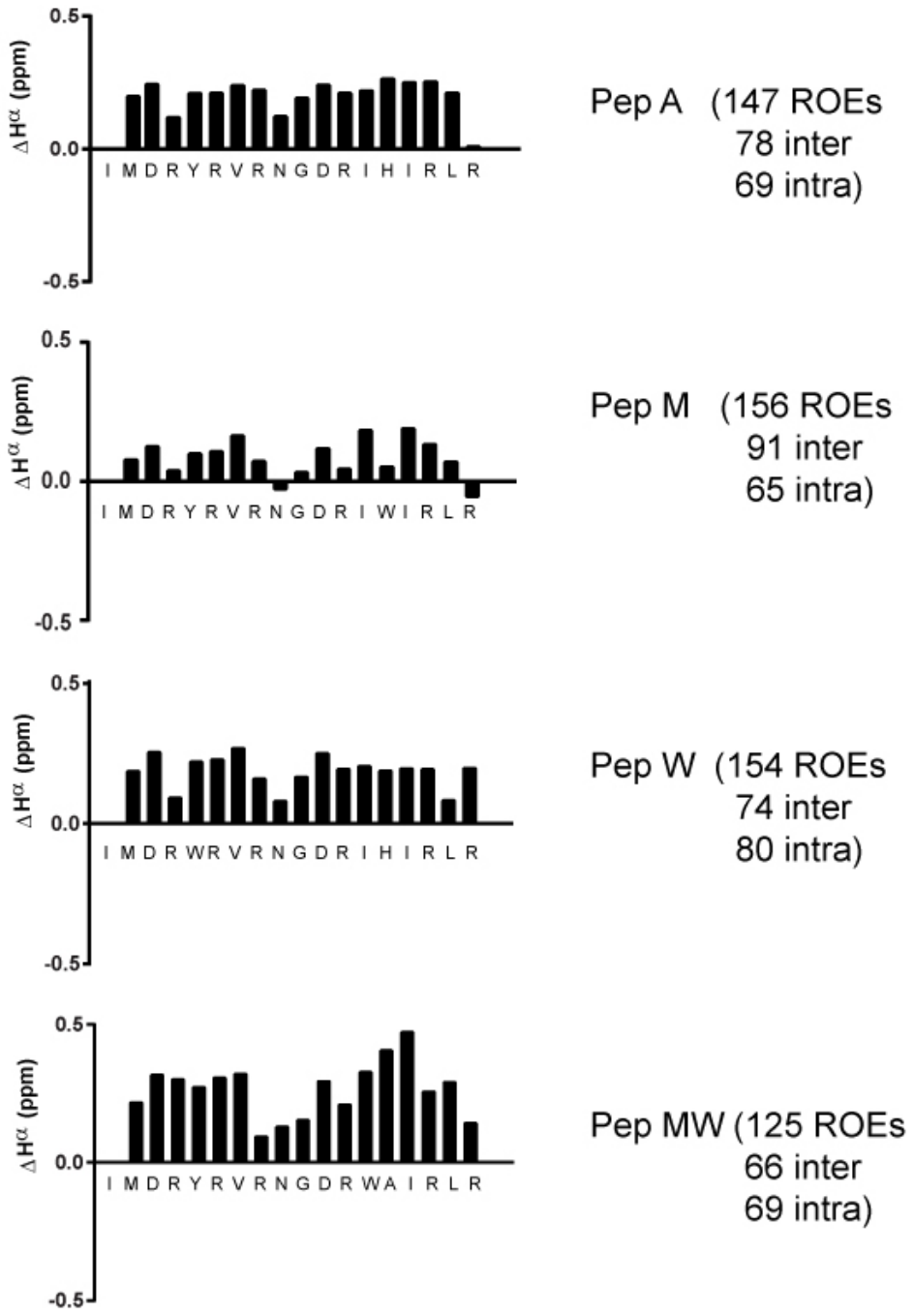

Figure 5.6 Chemical shift index derived from the NMR structures of Peptide A, Peptide M, Peptide W, and Peptide MW. The chemical shifts for random coil were obtained according to the tool at https://spin.niddk.nih.gov/bax/nmrserver/Poulsen_rc_CS/ (ref [42-43]).

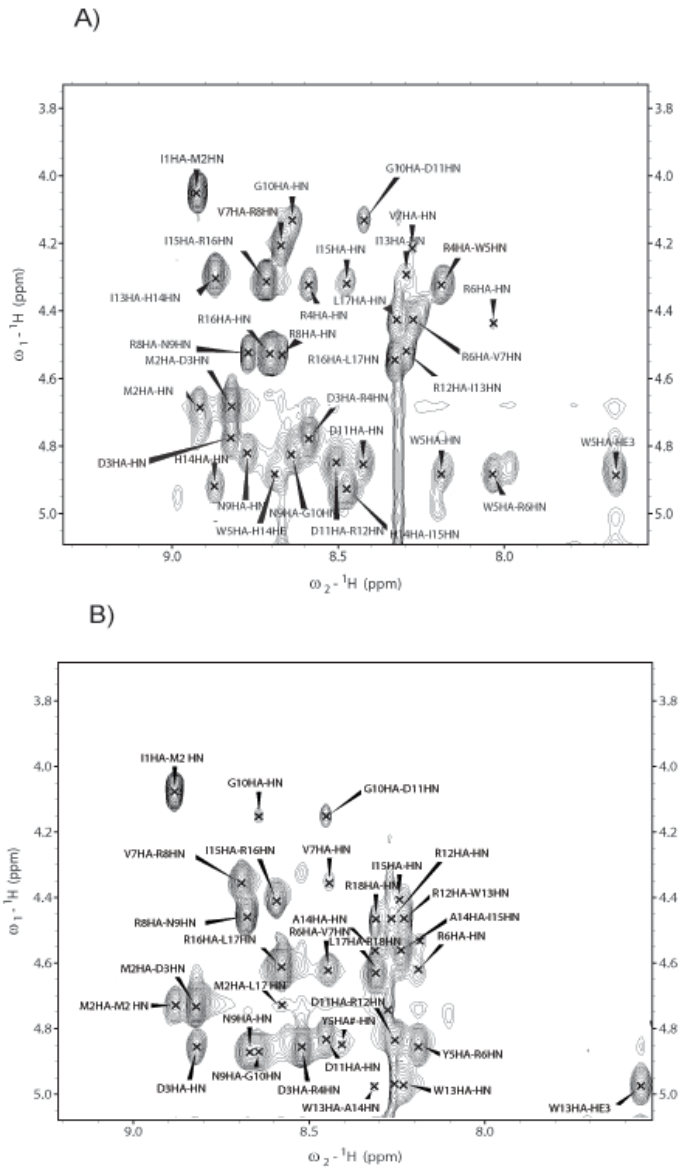

Figure 5.7 Fingerprint regions of A) Pep W and B) Pep MW extracted from the 2D [^{1}H-^{1}H] ROESY experiments acquired at a mixing time of 250 ms.

Table 5.1 Distances (Å) derived from the 20 lowest energy NMR structures of Peptide MW (A), Peptide W (B), and Peptide M (C)

A. Peptide MW

Model #	Y5O-W13NH	Y5O-R16NεH	Y5OH-R16Nε	Y5O-R16NH*	Y5OH-R16N*
1	7.3	1.6	2.9	4.0	3.3
2	7.4	1.7	3.1	2.0	3.2
3	7.5	2.3	2.9	3.7	3.3
4	6.9	4.9	4.1	5.2	5.3
5	7.3	5.6	4.2	3.2	3.4
6	7.3	1.5	2.9	2.9	3.1
7	7.4	5.1	4.0	3.2	3.3
8	7.3	6.0	4.7	5.7	5.2

Table 5.1 continued

9	7.4	1.7	3.2	3.1	3.9
10	7.4	5.1	5.1	1.4	3.2
11	7.4	2.7	3.3	3.0	3.0
12	7.3	5.2	4.0	3.2	2.4
13	7.5	5.9	4.8	4.1	4.3
14	7.3	2.3	3.1	1.5	3.1
15	7.3	2.9	2.5	1.6	2.8
16	7.4	4.6	3.9	3.5	3.6
17	7.4	2.4	3.0	3.5	3.5
18	7.2	3.7	3.8	1.4	3.1
19	7.3	6.3	5.0	5.3	5.0
20	7.4	6.0	5.0	4.4	4.7

Table 5.1 continued

B. Peptide W

Model #	W5NH-H14Nε2	W5N-R16NεH	W5NH-R16Nε	W5N-R16NH*	W5NH-R16N*
1	5.9	6.9	8.5	8.7	9.6
2	4.5	7.6	6.5	5.8	6.5
3	5.3	7.7	6.3	6.1	5.6
4	5.2	9.4	8.3	8.2	8.5
5	6.6	6.0	4.8	3.1	3.3
6	5.5	7.0	7.5	4.4	5.7
7	6.0	9.1	9.8	7.4	9.1
8	5.2	9.6	8.7	8.7	9.3

Table 5.1 continued

9	6.0	11.7	12.0	10.6	12.2
10	5.4	7.0	7.9	5.0	6.3
11	5.9	12.4	12.5	11.7	12.9
12	6.2	11.1	11.3	9.9	11.5
13	6.1	11.7	11.9	10.4	12.0
14	4.8	6.9	5.8	4.0	4.5
15	5.7	11.1	11.8	11.6	13.2
16	5.7	11.7	11.8	10.9	12.1
17	5.1	7.3	6.1	5.8	6.3
18	5.8	6.6	7.7	5.8	7.3
19	5.9	9.3	9.7	8.1	9.8
20	6.0	12.5	12.8	11.1	12.9

Table 5.1 continued

C. Peptide M, ref [32]

Model #	Y5O-W14NH	Y5O-R16NεH	Y5OH-R16Nε	Y5O-R16NH*	Y5OH-R16N*
1	6.1	9.3	9.7	9.7	10.9
2	5.9	6.4	7.2	8.2	9.2
3	6.2	5.4	5.2	1.5	3.1
4	6.0	9.3	9.7	7.9	9.6
5	6.4	2.8	3.7	1.4	3.1
6	6.3	4.2	4.2	1.5	3.1
7	6.3	8.5	6.9	5.5	5.4
8	6.5	5.1	5.3	1.4	3.2

Table 5.1 continued

9	6.7	5.7	4.2	3.7	3.3
10	6.2	4.9	4.4	2.9	2.9
11	6.5	5.1	4.8	7.3	6.8
12	6.4	7.0	6.0	7.4	7.0
13	6.4	8.4	7.5	9.5	9.0
14	6.9	7.8	8.0	7.7	8.8
15	6.7	4.8	4.4	2.7	2.8
16	6.7	6.5	6.1	5.0	5.3
17	6.0	9.2	7.6	7.1	6.5
18	6.6	6.9	5.7	5.7	5.8
19	6.6	4.9	5.1	1.4	3.1

Table 5.1 continued

20	6.3	6.7	6.0	7.3	7.1

*The distance to the closest–NH group (η1 or η2) of R16 is presented.

Table 5.2 Resonance assignments of ^{1}H chemical shifts of Pep W at pH 5.0 using solution NMR experiments.

Residue	NH (ppm)	CαH (ppm)	CβH (ppm)	Others (ppm)
I1	NA	4.049	2.091	NA
M2	8.926	4.681	2.206-2.138	γ -CH_2 2.732
D3	8.822	4.783	2.852	
R4	8.591	4.321	1.782	γ -CH_2 1.504
				δ-CH_2 3.0.88
				NH 7.165

Table 5.2 continued

W5	8.186	4.883	3.424/3.529	5-H 7.205 ζ3
				6-H 7.301 η2
				7-H 7.531 ζ2
				4-H 7.672 ε
R6	8.034	4.424	1.957 – 1.834	γ -CH_2 1.645
				δ-CH_2 3.224
				NH 7.346
V7	8.271	4.195	2.250	γ -CH_3 1.127

Table 5.2 continued

R8	8.669	4.521	1.948	γ -CH_2 1.771 δ-CH_2 3.254 NH 7.343
N9	8.772	4.819	2.947- 3.021	
G10	8.637	4.130		
D11	8.424	4.851	2.998	
R12	8.509	4.521	1.965	γ -CH_2 1.797 δ-CH_2 3.25186 NH 7.346
I13	8.292	4.288	1.996	γ -CH 1.587 δ-CH_3 1.344

Table 5.2 continued

H14	8.872	4.916	3.383 - 3.308	γ-H 7.442 ε-H 8.672
I15	8.474	4.313	1.988	γ -CH 1.628 δ-CH_3 1.341
R16	8.714	4.528	1.965	γ -CH_2 1.827 δ-CH_2 3.251 NH 7.346
L17	8.330	4.425	2.067	γ -CH 1.793 δ-CH_3 --
R18	8.704	4.521	1.856	γ -CH_2 -- δ-CH_2 3.250

Table 5.3 Resonance assignments of ^{1}H chemical shifts of Pep MW at pH 5.0 using solution NMR experiments.

Residue	NH (ppm)	CαH (ppm)	CβH (ppm)	Others (ppm)
I1	NA	4.079	1.999	NA
M2	8.881	4.711	2.254	γ -CH_2 2.781
D3	8.823	4.858	3.023 -2.876	
R4	8.587	4.547	1.856	γ -CH_2 1.595
				δ-CH_2 3.128
				NH 7.141
Y5	8.402	4.851	3.294 - /3.142	3,5-H 7.257 δ
				2,6-H 7.118 ε

Table 5.3 continued

R6	8.190	4.615	1.856	γ -CH_2 1.705 δ-CH_2 2.962 NH 7.133
V7	8.442	4.350	2.253	γ -CH_3 1.153
R8	8.691	4.455	1.959/1.834	γ -CH_2 1.689 δ-CH_2 3.070 NH 7.166
N9	8.674	4.868	3.005 -2.937	
G10	8.643	4.118		
D11	8.451	4.827	2.985	

Table 5.3 continued

R12	8.255	4.457	1.849	γ -CH_2 1.574
				δ-CH_2 3.188
				NH 7.145
W13	8.224	4.976	3.491 – 3.368	5-H 7.115 ζ3
				6-H 7.439 η2
				7-H 7.479 ζ2
				4-H 7.557 ε
A14	8.313	4.564	1.504	
I15	8.237	4.416	1.840	γ -CH 1.722
				δ-CH_3 1.102

Table 5.3 continued

R16	8.597	4.601	2.019	γ -CH_2 1.800 δ-CH_2 3.109 NH 7.261
L17	8.573	4.633	1.879	γ -CH 1.761 δ-CH_3 1.099
R18	8.307	4.465	1.977	γ -CH_2 1.823 δ-CH_2 3.201 NH 7.264

Table 5.4 Measured coupling constant $^3J_{HN\alpha}$ (Hz) for Pep W and Pep MW.

Pep W	**$^3J_{HN\alpha}$ (Hz)**	**Pep MW**	**$^3J_{HN\alpha}$ (Hz)**
I1		**I1**	

Table 5.4 continued

M2	7.2	**M2**	6.1
D3	7.0	**D3**	7.0
R4	10.1	**R4**	6.4
W5	7.0	**Y5**	6.8
R6	7.4	**R6**	6.5
V7	11.1	**V7**	9.9
R8	8.1	**R8**	7.1
N9	6.8	**N9**	8.6
G10	12.0	**G10**	11.0
D11	7.1	**D11**	8.2
R12	8.3	**R12**	7.4

Table 5.4 continued

I13	9.8	**W13**	9.2
H14	7.4	**A14**	6.4
I15	9.8	**I15**	10.2
R16	7.1	**R16**	9.0
L17	9.1	**L17**	6.7
R18	7.2	**R18**	9.5

5.4.2 Molecular Dynamics Simulations

Simulations of Peptide M, MW, and W were conducted over 200 ns, repeated four times for each peptide (2.4 μs in total; Figure 5.8). Additionally, one 100-ns Replica-Exchange with Solute Tempering (REST2) simulation was run for each peptide (Figure 5.9), which allows for enhanced sampling at increased computational cost. [39-40] These simulations represent the charge state at pH 9, in which the W and Y side chains are net neutral. The simulations of Peptide M are consistent with a stable folded structure in most of the simulation runs (Figure 5.9A). In Peptide MW, interactions between Y and W are formed and distort the peptide backbone (Figure 5.9B). Peptide W simulations are consistent with a stable folded structure in all four equilibrium simulation runs (Figure 5.8);

however, in the REST2 run the β-sheet is lost for most of the simulation, although the hairpin is still compact (Figure 5.9A). A summary of average distance and hydrogen bonding, as derived from the simulations, is presented graphically in Figure 5.10. The distance between tryptophan and tyrosine or tryptophan and histidine is relatively invariant on the 200-ns time scale at pH 9. Simulations of Peptide M at pH 11 were also conducted; at this pH, the tyrosine side chain is deprotonated (Figure 5.11). The change in charge state did not alter the results of the simulation, when compared to Peptide M at pH 9.

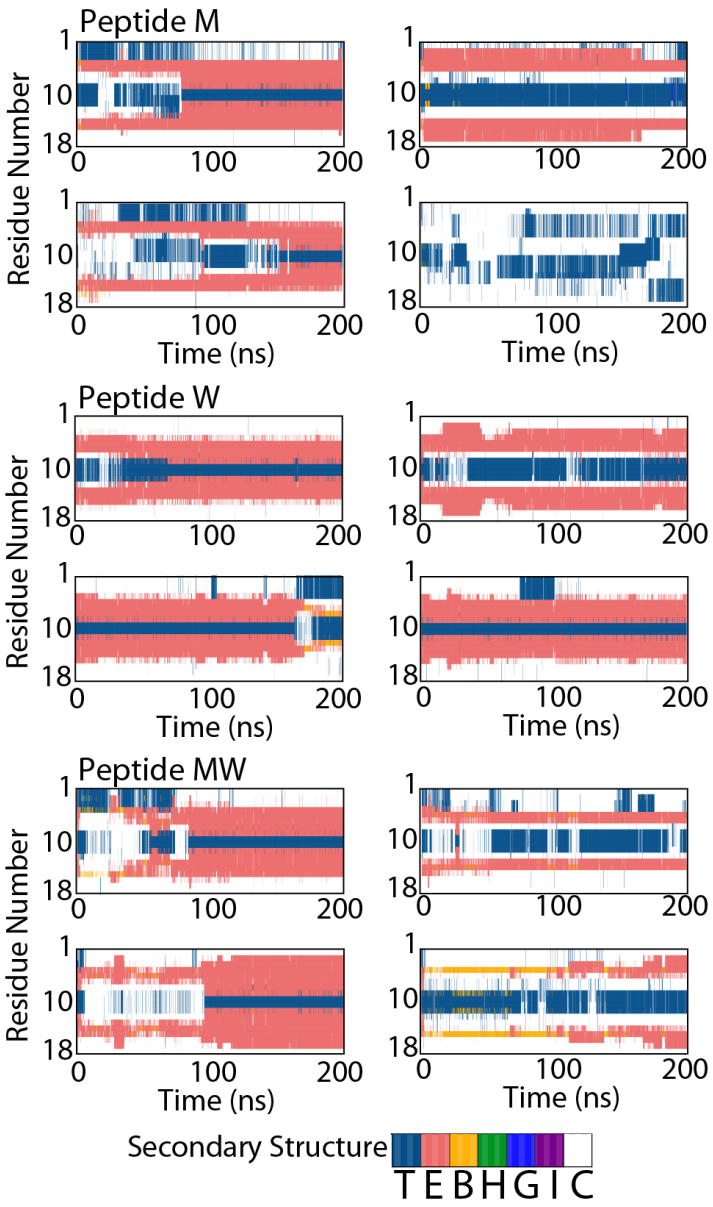

Figure 5.8 Time evolution of secondary-structure assignment per residue of Peptide M (top), Peptide W (middle), and Peptide MW (bottom). Simulation runs 1-4 are shown for each peptide. The legend uses DSSP classification: T is β turn, E is β sheet, B is β bridge, H is α helix, G is 3_{10} helix, I is π helix, and C is unstructured coil.

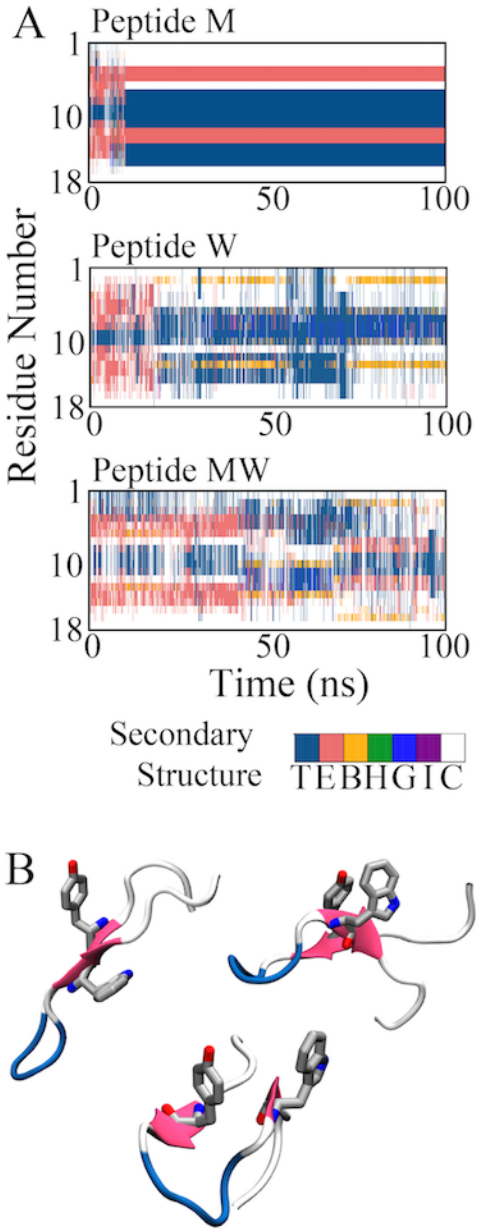

Figure 5.9 MD simulations of Peptide M, W, and MW. (A) Time evolution of secondary-structure assignment per residue of Peptide M (top), Peptide W (middle), and Peptide MW (bottom) during REST2 simulations. The legend uses DSSP classification: T is β turn, E is β sheet, B is β bridge, H is α helix, G is 3_{10} helix, I is π helix, and C is unstructured coil. (B) Snapshots of the YW dyad structure in Peptide MW.

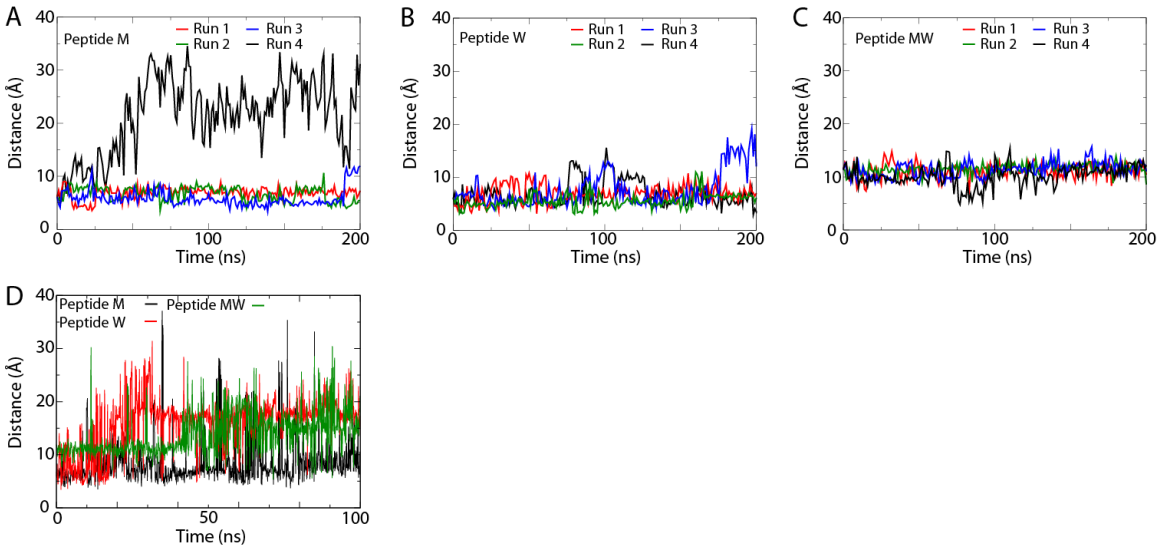

Figure 5.10 Results from MD simulations of beta hairpins at pH 9.0. Distance between the (A) side-chain oxygen of Y5 and side-chain nitrogen of W14 for four runs of Peptide M, (B) side-chain nitrogen of W5 and the side-chain epsilon nitrogen of H14 for four runs of Peptide W, and (C) side-chain oxygen of Y5 and the side-chain nitrogen of W13 for four runs of Peptide MW. The charge state is YW, corresponding to pH 9. (D) Distances in the REST2 runs. We note that replica-exchange trajectories are not guaranteed to be continuous in time, but they do sample from the canonical ensemble.

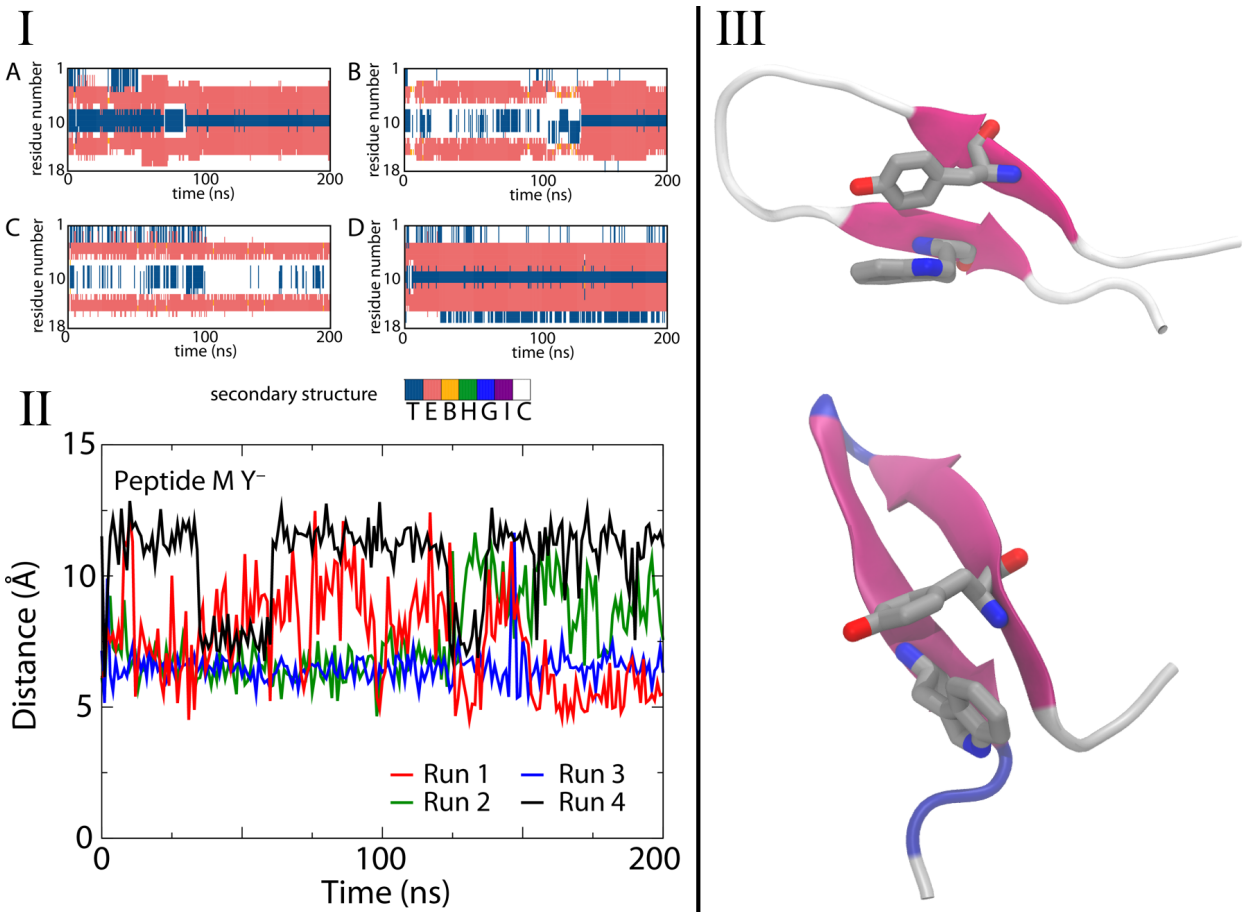

Figure 5.11 Results of MD simulations of Peptide M at pH 11. In (I), time evolution of secondary-structure assignment per residue, in (II), the distance between the side-chain oxygen of Y5 and side-chain nitrogen of W14 for four runs, and in (III), snapshots of structures. The legend at the bottom of (I) uses DSSP classification in which T is β turn, E is β sheet, B is β bridge, H is α helix, G is 3_{10} helix, I is π helix, and C is unstructured coil. The charge state of the dyad is Y^- W, in which the tyrosinate side chain is negatively charged, as expected at pH 11.

5.4.3 CD and Excitonic Splitting

Figure 5.12 presents CD data derived from the beta hairpin peptides. For comparison, the signal from Peptide A (I, pink, solid line), derived at pH 9 and 20 °C, is presented. This signal exhibits negative ellipticity at 200 nm and is characteristic of a *β*-hairpin. Similar results were obtained from Peptide M (IIA, purple, solid line) and Peptide MW (IIIA, black, solid line). After heating to 80 °C, negative ellipticity at 200 nm is lost

in all three peptide samples (Figure 5.12, I, II, III, dot-dashed lines). All samples refold reversibly with cooling back to 20 °C, as assessed by recovery of the CD signal (Figure 5.12, I, II, III, dashed lines). A similar signal was also observed in Peptide W and WA14 at 20 °C and pH 9. We conclude that all the peptides form thermally stable beta hairpins at 20 °C.

We previously reported a CD-detected Cotton signal, derived from excitonic coupling within the YW dyad of Peptide M. This signal arises from coupling between the ^1B_b band of tryptophan and the ^1L_a band of tyrosine. The exciton splitting depends on the magnitude and directions of the transition dipole vectors, $\boldsymbol{\mu}_i$ and $\boldsymbol{\mu}_j$, and the interchromophore distance ($\boldsymbol{R}_{ij}$) vectors (Figure 5.1F) between the aromatic side chains.[16-17] This signal is apparent in Figure 5.12, IIB, solid, which presents the difference CD signal between Peptide M and Peptide A. The Peptide M excitonic splitting is sensitive to melting (Figure 5.12, IIB, dashed), consistent with loss of the excitonic interaction when the peptide unfolds. As observed in Panel IIIB, the difference spectrum derived from Peptide MW also exhibits an excitonic coupling signal (solid), which is sensitive to melting (dashed). Given the signal to noise ratio, the signal in Peptide MW is similar to the excitonic splitting found in Peptide M. This result indicates that the average electronic interaction between the tyrosine ^1L_a and tryptophan ^1B_b states are similar, when averaged over the solution conformers of Peptide M and MW.

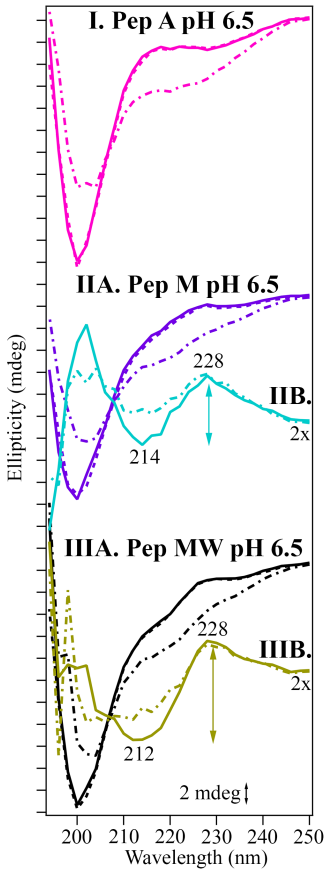

Figure 5.12 CD spectra of Peptide A (I, pink), Peptide M (IIA, purple), and Peptide MW (IIIA, black), pH 6.5. The spectra were acquired at 20 °C (solid line, pre-melt), 80 °C (dot-dashed line) or 20 °C (dashed line, post-melt). In IIB, difference CD spectra are shown in cyan, corresponding to Peptide M (IIA, purple)-minus-Peptide A (I, pink). In IIIB, difference CD spectra are shown in gold, corresponding to Peptide MW (III, black)-minus-Peptide A (I, pink). Data were obtained at 20 °C (IIB, cyan; IIIB, gold; solid line; pre-melt) or at 80 °C (IIB, cyan; IIIB, gold; dot-dashed line). Amplitude of differential signal noted as a vertical line (IIB, cyan, 3.1 mdeg; IIIB, gold, 4.5 mdeg). Analyte concentration, 200 µM; buffer, 5 mM MES, pH 6.5. The tick marks on the y axis denote 2 mdeg. Difference CD spectra (B, cyan and C, gold) are multiplied by a factor of 2 for presentation purposes.

5.4.4 UV-Vis Spectrum

The UV spectra of Peptides M, MW, W, and WA14 are compared to tryptophan and a tyrosine-tryptophan mixture in Figure 5.13, I-II. At the same concentration, the UV absorbance of the peptides is decreased. The 266 nm extinction coefficient of the peptides

was therefore determined at pH 9 (Figure 5.13, IV) and found to be reduced by approximately a factor of 2, relative to tryptophan, in all the peptides (5000 M^{-1} cm^{-1} in tryptophan, average 2700 M^{-1} cm^{-1} in the peptides). Such hypochromism is well documented in nucleic acids and also alters the UV absorption bands of peptides and proteins. This effect has been attributed to exciton coupling (dipole-dipole), dipole-induced dipole effects, and/or electrostatic effects.[44-46] After normalization to account for the difference in their extinction coefficients, red shifts of the Peptide M and MW spectra are observed, relative to tryptophan, Peptide W, and Peptide WA14 (Figure 5.13, III). For Peptide M, this red shift was reported previously and attributed to a dipole-dipole interaction.[32] Note that previous work has shown that the peak potentials of the aromatic amino acids in Peptide M are similar to the peak potential of a mixture of aqueous tyrosine and tryptophan, so the impact of dipole-dipole interactions in the ground and radical states must be compensating.[32]

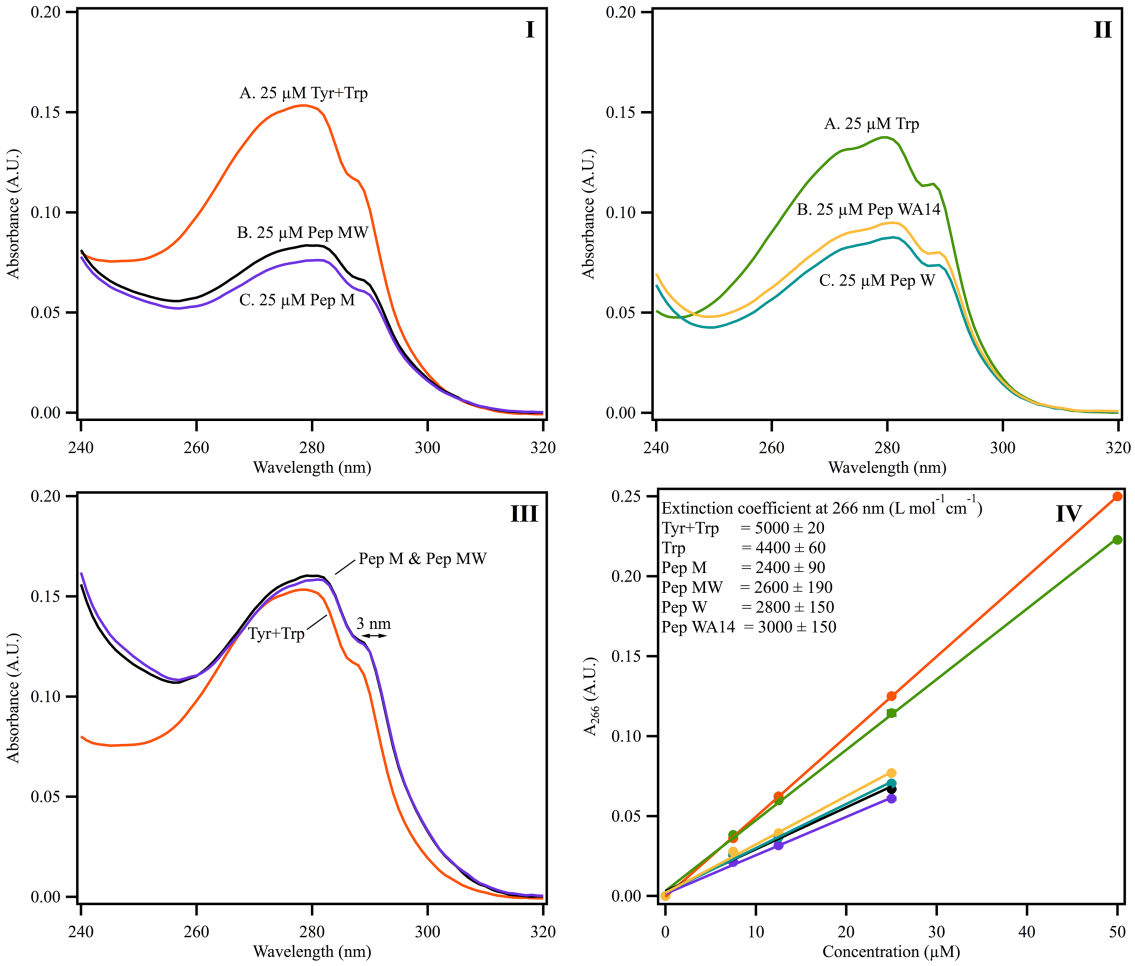

Figure 5.13 UV spectra of amino acids and peptides (I, II, III) and hypochromic effect in peptides (IV). Samples in (I-IV): a 1:1 mixture of tyrosine and tryptophan (orange), Peptide M (purple), Peptide MW (black), tryptophan (green), Peptide W (teal), and Peptide WA14 (yellow). In III, traces from I are replicated and normalized by the extinction coefficient at 266 nm (in IV) to highlight the red-shifted UV spectrum of Peptide M and Peptide MW. In (IV), determination of 266 nm extinction coefficients. The buffer contained 5 mM borate, pH 9. Error bars represent the standard deviation of three replicate measurements.

5.4.5 Fluorescence Emission Spectrum

The fluorescence spectrum of tryptophan is known to be sensitive to the placement of charges near the indole ring.[47] For example, in crystallins, tryptophan-tryptophan interactions red shift the emission spectrum [19], and it has been reported that electron

transfer to the amide backbone can quench fluorescence [48]. To investigate any impact of the YW dyad on the fluorescence emission spectrum, spectra of Peptide M and MW (Figure 5.14A, purple and black, respectively) were compared to an equimolar mixture of amino acids (orange), tyrosine in solution (blue), and tryptophan in solution (green) with fluorescence excitation at 266 nm. After correction for the extinction coefficient change in the peptides (Figure 5.13, IV), there is little significant quenching of *tryptophan* fluorescence in the peptides, relative to an aqueous solution of tryptophan. However, *tyrosine* fluorescence is quenched in the YW dyad peptides; this effect is attributed to Förster transfer from tyrosine to tryptophan in the dyad. In addition, the fluorescence emission spectrum of Peptide M (purple) is significantly blue shifted (5 nm), compared to a mixture of amino acids (orange), under the same conditions. The blue shift is observed at three different concentrations (Figures 5.14B and C), and Peptide MW (Figure 5.14C) behaved similarly to Peptide M (Figure 5.14B). The blue shift is attributed to interaction between the pi systems of Y and W in the dyad.

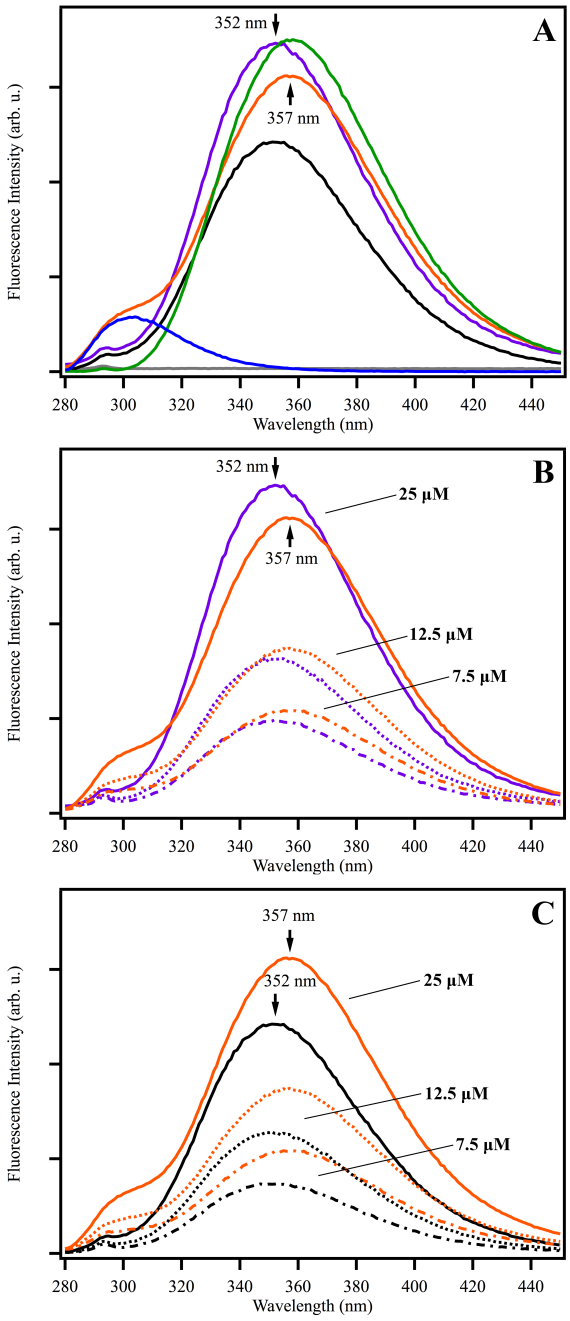

Figure 5.14(A) Fluorescence emission spectra derived from a 1:1 tyrosine and tryptophan mixture (orange), tyrosine (blue), tryptophan (green), Peptide M (purple), Peptide MW (black) and a buffer background (grey). The Peptide M and Peptide MW fluorescence spectra were normalized using the UV absorption extinction coefficients shown in Figure S9. The analyte concentration was 25 µM. In (B), concentration dependence of the emission spectrum derived from a 1:1 mixture of tyrosine and tryptophan (orange) or Peptide M (purple). In (C), concentration dependence of the emission spectrum derived from a 1:1 mixture of tyrosine and tryptophan (orange) or Peptide MW (black). In (B and C), the analyte concentration

was 25 μM (solid), 12.5 μM (dotted), or 7.5 μM (dot-dashed). The buffer contained 5 mM borate, pH 9. Tick marks denote 100 intensity units.

5.4.6 TRAS, Tryptophan and Tyrosine Amino Acid Solutions

Figure 5.15A presents TRAS, obtained from aqueous solutions of tryptophan after a femtosecond UV (280 nm) photolysis flash at pH 9.0. The spectra were acquired on the picosecond time scale, starting 3 ps (black) after the 280-nm pulse. The 3-ps spectrum (black) is dominated by three bands at ~360, 450, and 580 nm (Figure 5.15A). The band at 340 nm arises from the S_1 excited state of the indole ring in tryptophan. The 450- and 580-nm bands have also been assigned to the W* tryptophan excited state by picosecond spectroscopy and electronic structure calculations.[49] In the spectral region shown in Figure 5.15A, there are possible overlapping contributions from photoionization products, namely the tryptophan cation radical at 580 nm and the tryptophan neutral radical at 510 nm. The pK_a of the tryptophan cation radical is 4.3; the deprotonation time is expected to be 10^{-6} s^{-1}, so the neutral radical is not expected to contribute on the ps time scale.[49] Similarly, formation of the triplet species, which absorbs at 430 nm, is not expected in oxygen-containing buffers on this time scale. The solvated electron makes a spectral broad contribution in the range from 650 to 700 nm.

Decay kinetics were monitored at selected wavelengths as a function of time, at 15 (blue), 33 (green), 513 (orange), 1033 (purple), and 2033 (pink) ps after the 280 nm flash. Biexponential fits and residuals are shown in Figure 5.16A; the data are presented on a semi-logarithm scale in Figure 5.17. On this time scale, the 360 nm band does not significantly decay in tryptophan (Figure 5.17A). The decay kinetics of the 520 nm band (Figure 5.17D) can be fit with a biexponential function with rate constants of 4 ps (4%)

and 1000 ps (38%) (Table 5.5). Decay kinetics at 410, 460, 580, and 650 nm were also monitored (Figure 5.17B-C, E-F), and the wavelengths at which appreciable decay occurred were also fit with two exponentials. The need for two exponentials may be explained by a distribution of backbone conformers in solution.[50-51] The fits were consistent at all wavelengths, with fast phases in the 3-10 ps range and slow phases in the 1000-1900 ps range (Table 5.5). In tryptophan at pH 9, a new signal grows in on the 3 ps to 2 ns time scale (Figure 5.15A) as a band at 420 nm. Previously, this signal has been assigned to a photoproduct, produced as a result of indole ring protonation by the amino terminus of tryptophan.[52] TRAS and kinetic data were also derived from an aqueous mixture of tryptophan and tyrosine (Figures 5.15B and Figure 5.16B). The bands and kinetics were indistinguishable when compared to those acquired from tryptophan alone, because spectral contributions derived from tyrosine are less intense compared to tryptophan (Figures 5.18 and 5.19). TRAS and kinetics were acquired from tryptophan at pH 11 (Table 5.6 and Figures 5.20 and 5.21). The photoproduct was not formed at pH 11, as expected, because the amino group is not protonated.

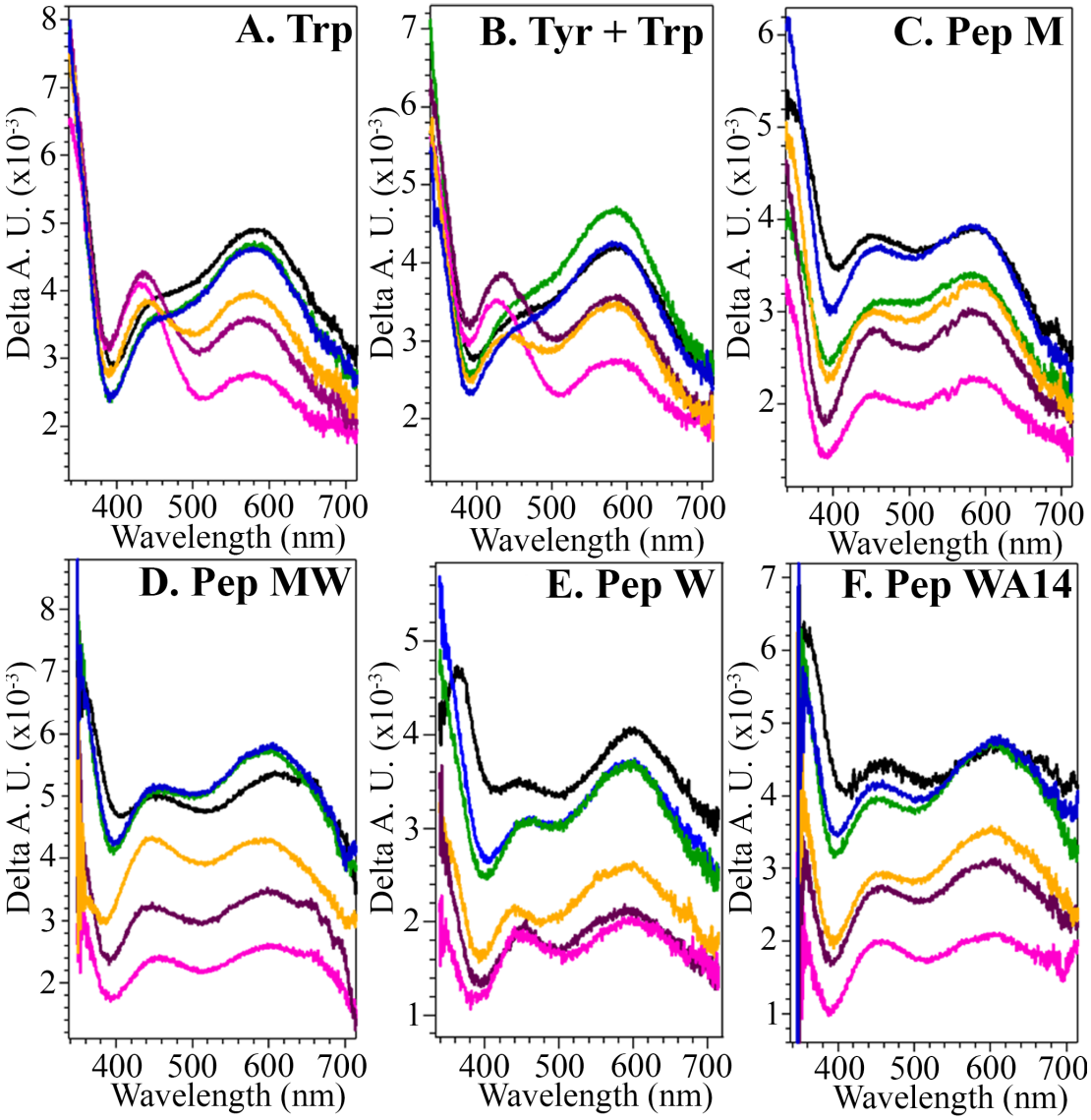

Figure 5.15 TRAS derived from (A) tryptophan, (B) a 1:1 mixture of tryptophan and tyrosine, (C) Peptide M, (D) Peptide MW, (E) Peptide W, and (F) Peptide WA14 after UV photolysis at pH 9. Spectra were obtained at 3 (black), 15 (blue), 33 (green), 513 (orange), 1033 (purple), 2033 ps (pink). Analyte concentration, 1 mM; buffer, 5 mM borate-NaOH.

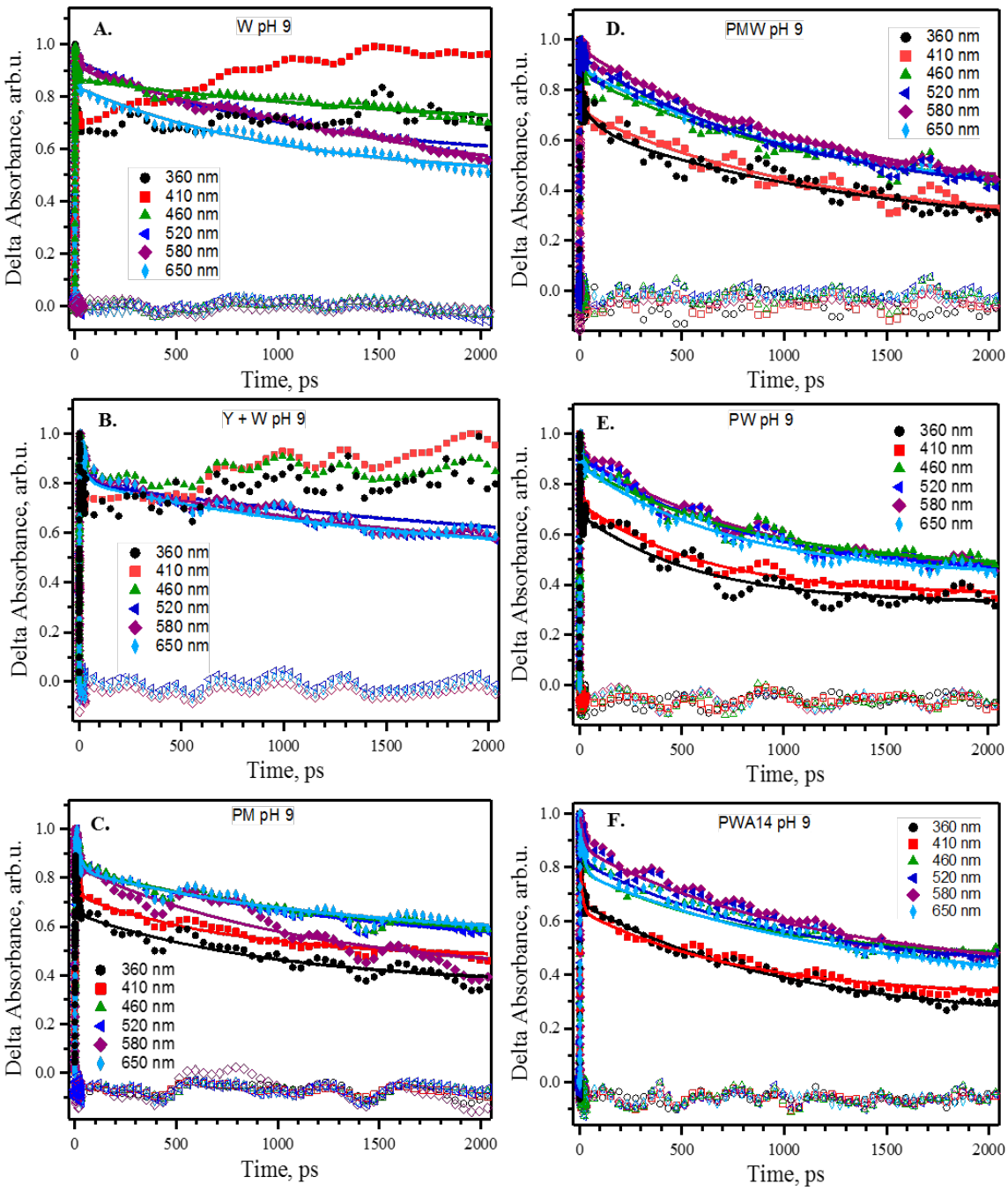

Figure 5.16 Decay kinetics obtained from TRAS of amino acid and beta hairpins after UV photolysis at pH 9. Data were acquired from (A) tryptophan, (B) a 1:1 mixture of tyrosine and tryptophan, (C) Peptide M, (D) Peptide MW, (E) Peptide W, and (F) Peptide WA14. Spectra were monitored at selected wavelengths; 360 nm (black circles), 410 nm (red squares), 460 nm (green triangles), 520 nm (blue triangles), 580 nm (purple diamonds) and 650 nm (cyan diamonds). Bi-exponential fits (starting from 3 ps) are superimposed as solid lines, and the open symbols at the bottom of each panel are the corresponding residuals. The data were averaged from at least two

independent measurements. The averaged data were normalized with respect to the maximum absorbance, which occurred at 2-3 ps. Fitting parameters are presented in Table 5.5. Selected data are reproduced in Figure 5.17 on a semi-logarithm plot. Analyte concentration, 1 mM; buffer, 5 mM borate-NaOH.

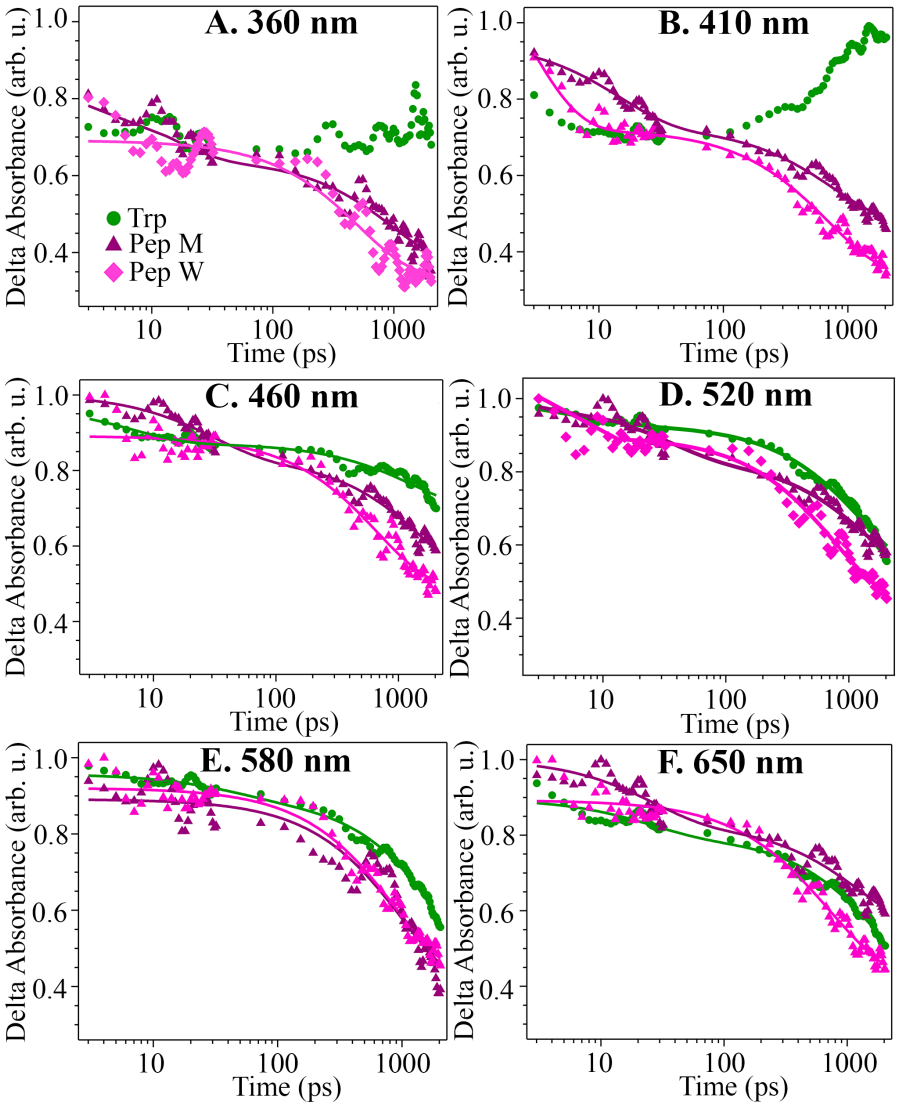

Figure 5.17 Decay kinetics obtained from TRAS of amino acid and selected peptides after UV photolysis at pH 9. Data were acquired from tryptophan (green), Peptide M (purple), and Peptide W (pink). Spectra were monitored at 360 nm (A), 410 nm (B), 460 nm (C), 520 nm (D), 580 nm (E) and 650 nm (F). Bi-exponential fits (starting from 3 ps) are superimposed as solid lines (Table 5.5). The averaged data were normalized with respect to the maximum absorbance, which occurred at 2-3 ps. A comparison of all the kinetic data with residuals is shown in Figure 5.16. Analyte concentration, 1 mM; buffer, 5 mM borate-NaOH.

Table 5.5 Kinetic constants derived from biexponential fits to TRAS of amino acids and peptides at pH 9 (τ, time constant, A, amplitude)

	τ_1	A_1 (%)	τ_2	A_2 (%)	y_0 (%)	χ^2
Tryptophan						
345 nm	n.d.*					
410 nm	n.d.					
460 nm	10 ± 2.9	0.06 ± 0.01	1933 ± 103	0.21 ± 0.01	0.66	0.0164
520 nm	4 ± 3	0.04 ± 0.01	1050 ± 27	0.38 ± 0.01	0.56	0.0248
580 nm	10 ± 7.4	0.03 ± 0.00	1270 ± 30	0.42 ± 0.01	0.51	0.0194
650 nm	3.2 ± 0.9	0.08 ± 0.01	1021 ± 21	0.35 ± 0.01	0.48	0.0192

Table 5.5 continued

Tyr + Trp						
345 nm	n.d.					
410 nm	n.d.					
460 nm	n.d.					
520 nm	18 ± 4	0.14 ± 0.02	925 ± 67	0.26 ± 0.01	0.56	0.0517
580 nm	23 ± 10	0.09 ± 0.02	861 ± 64	0.28 ± 0.02	0.58	0.0571
650 nm	21 ± 8	0.10 ± 0.02	751 ± 57	0.28 ± 0.02	0.59	0.0561
Peptide M						

Table 5.5 continued

345 nm	24 ± 9	0.09 ± 0.2	1345 ± 64	0.42 ± 0.01	0.48	0.0526
360 nm	15 ± 4	0.14 ± 0.02	1000 ± 70	0.30 ± 0.01	0.36	0.0632
410 nm	16 ± 2	0.19 ± 0.01	1130 ± 185	0.29 ± 0.02	0.42	0.0193
460 nm	28 ± 5	0.15 ± 0.01	1406 ± 349	0.32 ± 0.03	0.52	0.0282
520 nm	33 ± 8	0.14 ± 0.02	1515 ± 500	0.35 ± 0.05	0.49	0.0435
580 nm	15 ± 6	0.12 ± 0.00	1413 ± 80	0.51 ± 0.02	0.33	0.1436
650 nm	26 ± 5	0.15 ± 0.02	1350 ± 94	0.29 ± 0.02	0.54	0.0528

Table 5.5 continued

Peptide MW						
360 nm	90 ± 60	0.10 ± 0.04	1413 ± 121	0.43 ± 0.02	0.22	0.1032
410 nm	20 ± 10	0.08 ± 0.02	1126 ± 213	0.45 ± 0.03	0.27	0.0604
460 nm	32 ± 30	0.05 ± 0.03	1122 ± 251	0.49 ± 0.03	0.37	0.0863
520 nm	53 ± 68	0.03 ± 0.02	1245 ± 208	0.59 ± 0.03	0.32	0.0433
580 nm	60 ± 88	0.02 ± 0.01	1197 ± 25	0.60 ±0.01	0.35	0.0168

Table 5.5 continued

650 nm	13 ± 14	0.04 ± 0.02	1278 ± 103	0.54 ± 0.02	0.33	0.0081
Peptide W						
345 nm	1.0 ± 0.5	0.11 ± 0.03	450 ± 32	0.40 ± 0.01	0.38	0.0549
360 nm	2.0 ± 1.4	0.10 ± 0.00	571 ± 36	0.35 ± 0.01	0.33	0.1081
410 nm	2.0 ± 0.4	0.20 ± 0.02	601 ± 42	0.36 ± 0.01	0.36	0.0326
460 nm	2.0 ± 0.7	0.14 ± 0.03	828 ± 84	0.42 ± 0.02	0.46	0.0584
520 nm	1.0 ± 0.5	0.11 ± 0.02	776 ± 62	0.46 ± 0.01	0.44	0.0500

Table 5.5 continued

580 nm	1.0 ± 0.8	0.09 ± 0.02	907 ± 81	0.49 ± 0.02	0.42	0.0537
650 nm	3.0 ± 0.7	0.14 ± 0.02	747 ± 57	0.45 ± 0.01	0.43	0.0433
Peptide WA14						
360 nm	8.2 ± 1.9	0.13 ± 0.01	809 ± 72	0.40 ± 0.01	0.23	0.0318
410 nm	11 ± 2.2	0.16 ± 0.01	776 ± 89	0.32 ± 0.01	0.32	0.0300
460 nm	15 ± 4.7	0.14 ± 0.02	835 ± 160	0.33 ± 0.02	0.46	0.0666

Table 5.5 continued

520 nm	19 ± 6.2	0.12 ± 0.02	1020 ± 183	0.42 ± 0.02	0.41	0.0586
580 nm	21 ± 5.0	0.12 ± 0.01	1154 ± 152	0.48 ± 0.02	0.39	0.0305
650 nm	20 ± 3.0	0.17 ± 0.01	1300 ± 196	0.44 ± 0.03	0.34	0.0258

*n.d., Not Decaying

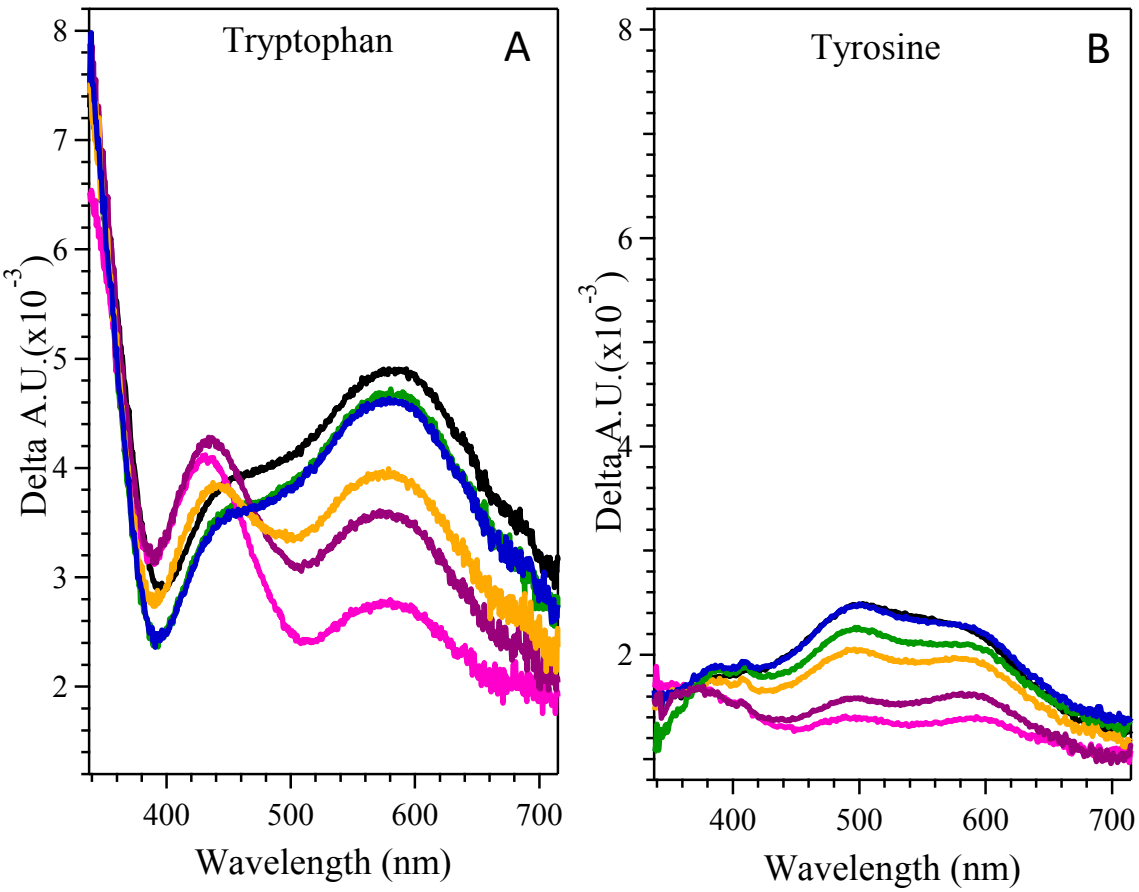

Figure 5.18 TRAS of (A) tryptophan and (B) tyrosine at pH 9 after UV photolysis. Spectra were obtained at 3 (black), 15 (blue), 33 (green), 513 (orange), 1033 (purple), 2033 (pink) ps. The spectra in (A) and (B) are plotted on the same scale. The spectra were averaged from at least three independent measurements. Analyte concentration, 1 mM; buffer, 5 mM borate-NaOH. Figure 5.18A is repeated from main text, and Figure 5.18B was reported in ref [27].

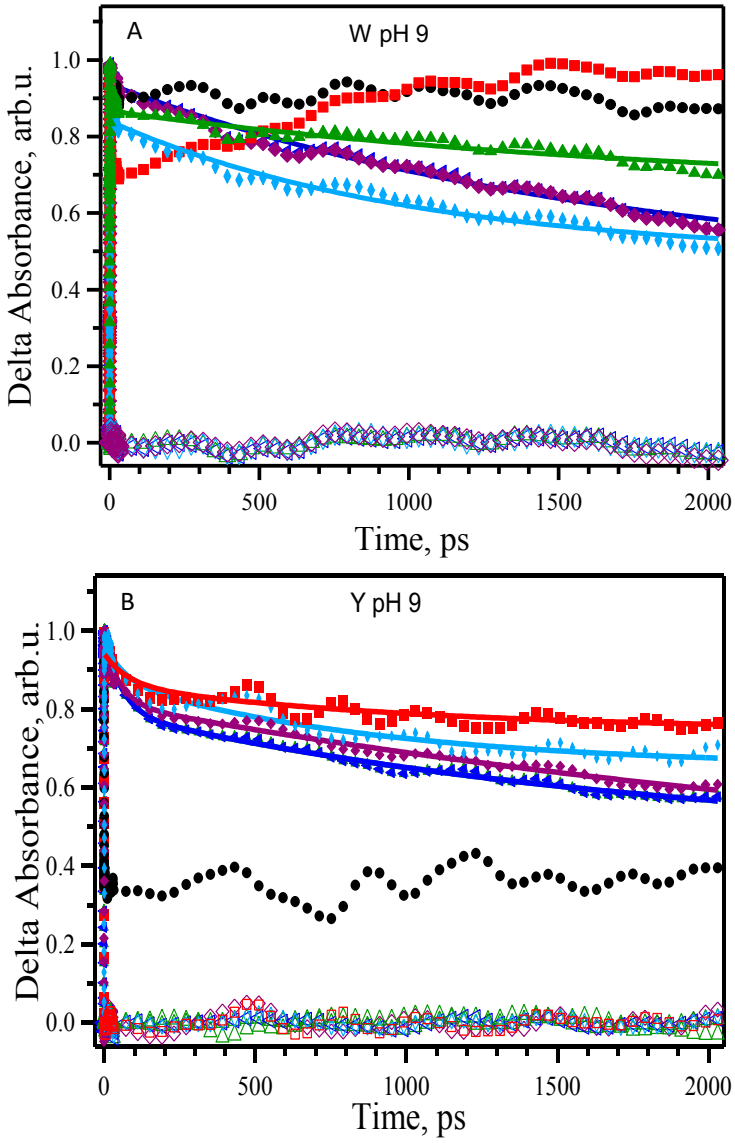

Figure 5.19 Decay kinetics obtained from TRAS of amino acids after UV photolysis. Data were acquired from (A) tryptophan and (B) tyrosine at pH 9. Spectra were monitored at selected wavelengths; 345 nm (black circles), 410 nm (red squares), 460 nm (green triangles), 520 nm (blue triangles), 580 nm (purple diamonds) and 650 nm (cyan diamonds). Bi-exponential fits (starting from 3 ps) are superimposed as solid lines, and the open symbols at the bottom of each panel are the corresponding residuals. The data were averaged from at least two independent measurements. The averaged data were normalized with respect to the maximum absorbance, which occurred at 2-3 ps. Fitting parameters for (A) are presented in Table 5.5. Analyte concentration, 1 mM; buffer, 5 mM borate-NaOH.

Table 5.6 Kinetic constants derived from biexponential fits to TRAS of amino acids and peptides at pH 11 (τ, time constant, A, amplitude)

	τ_1	A_1 (%)	τ_2	A_2 (%)	y_0 (%)	χ^2
Tryptophan						
345 nm	125 ± 84	0.04 ± 0.01	1978 ± 401	0.10 ± 0.01	0.82	0.0173
410 nm	3.0 ± 0.5	0.08 ± 0.01	2698 ± 107	0.15 ± 0.01	0.58	0.0054
460 nm	9.0 ± 0.0	0.04 ± 0.01	3199 ± 139	0.21 ± 0.01	0.66	0.0091
650 nm	9.5 ± 2.0	0.06 ± 0.01	3209 ± 191	0.24 ± 0.01	0.65	0.0150
Peptide M						

Table 5.6 continued

345 nm	46 ± 22	0.14 ± 0.03	1139 ± 88	0.47 ± 0.02	0.32	0.1560
410 nm	21 ± 2.1	0.26 ± 0.01	804 ± 91	0.33 ± 0.01	0.26	0.0218
460 nm	32 ± 3.3	0.26 ± 0.02	1123 ± 225	0.31 ± 0.02	0.30	0.0274
520 nm	32 ± 4.5	0.29 ± 0.02	1104 ± 72	0.38 ± 0.02	0.30	0.0792
580 nm	51 ± 8.3	0.23 ± 0.02	1224 ± 69	0.37 ± 0.01	0.32	0.0475
650 nm	60 ± 12	0.23 ± 0.02	1109 ± 85	0.32 ± 0.02	0.42	0.0608

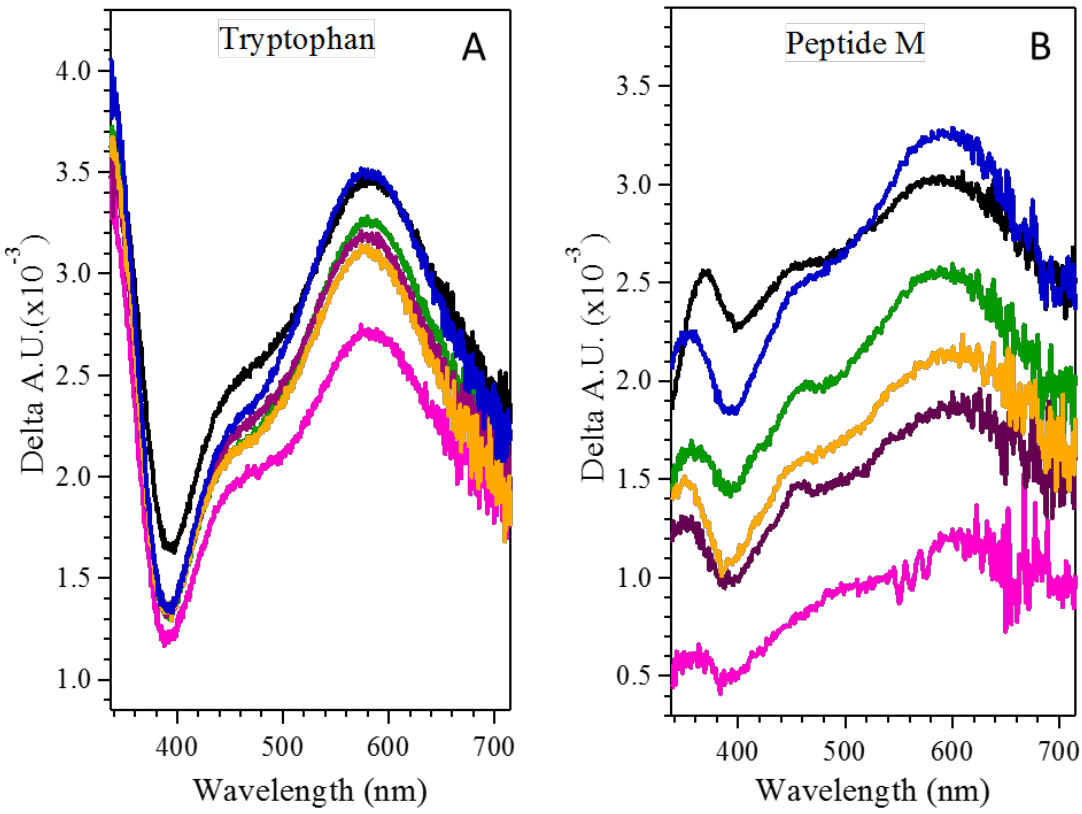

Figure 5.20 TRAS of (A) tryptophan and (B) Peptide M at pH 11 after UV photolysis. Spectra were obtained at 3 (black), 15 (blue), 33 (green), 513 (orange), 1033 (purple), 2033 ps (pink). The spectra were averaged from at least three independent measurements. Analyte concentration, 1 mM; buffer, 5 mM borate-NaOH.

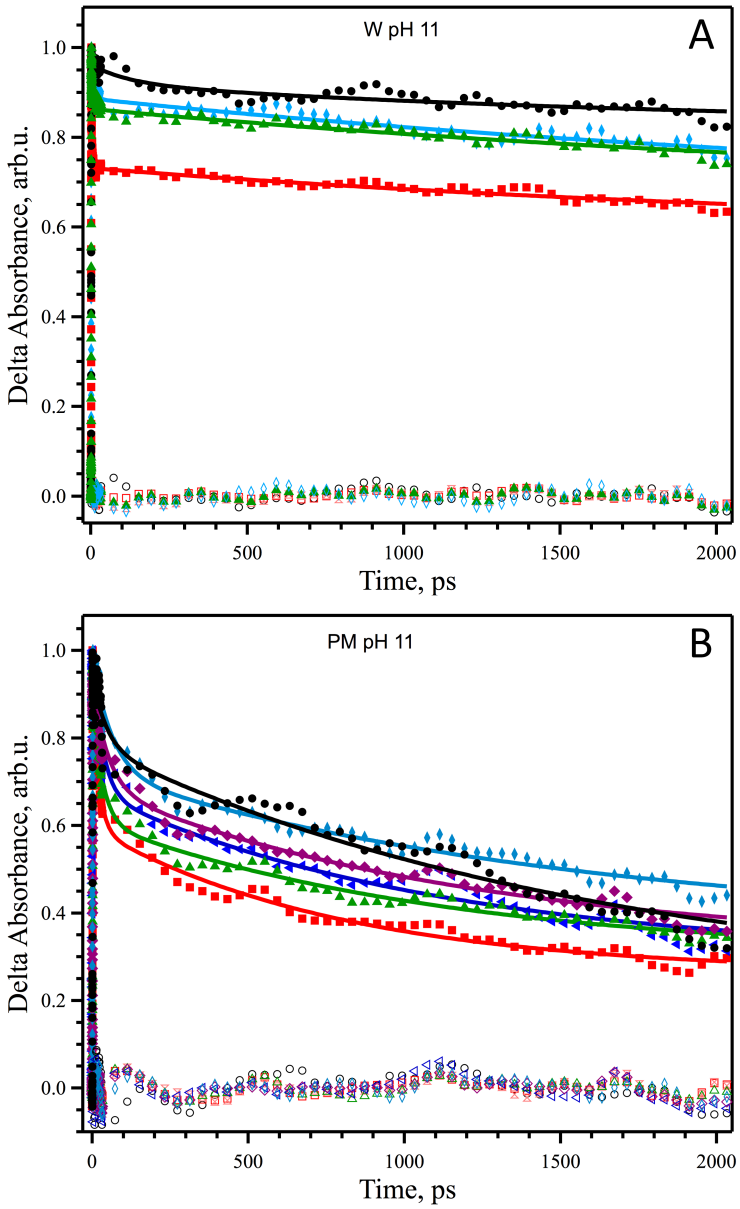

Figure 5.21 Decay kinetics obtained from TRAS of amino acid and beta hairpins after UV photolysis at pH 11. Data were acquired from (A) tryptophan and (B) Peptide M. Spectra were monitored at selected wavelengths; 345 nm (black circles), 410 nm (red squares), 460 nm (green triangles), 520 nm (blue triangles), 580 nm (purple diamonds) and 650 nm (cyan diamonds). Bi-exponential fits (starting from 3 ps) are superimposed as solid lines (Table S6), and the open symbols at the bottom of each panel are the corresponding residuals. The data were averaged from at least two independent measurements. The averaged data were normalized with respect to the maximum absorbance, which occurred at ~ 2-3 ps. Analyte concentration, 1 mM; buffer, 5 mM borate-NaOH.

5.4.7 TRAS, Peptides M, W and WA14

Figure 5.15C shows TRAS data, obtained following 280 nm excitation of a Peptide M sample, which contains a YW dyad. Bands at 360, 450, and 580 nm are observed at 3 ps, and, overall, the peak positions are similar to those observed in aqueous tryptophan (Figure 5.15A) and the mixture of tryptophan and tyrosine (Figure 5.15B). In spectra acquired from Peptide M at pH 9, the 420 nm peak, characteristic of a photoproduct, does not appear. Kinetic data were derived from the Peptide M TRAS spectra after UV photolysis at pH 9 (Figure 5.16C). The TRAS data at 360, 410, 460, 520, 560, and 650 nm are shown on a semi-log plot in Figure 5.17 and were fit with a biexponential function (Table 5.5). When compared to tryptophan, the 360 nm-derived decay of W* is accelerated in Peptide M with time constants of 15 ps (14%) and 1000 ps (30%) (Figure 5.16C, Table 5.5). There are also changes when the kinetic fits are compared at other wavelengths (Figure 5.17). For example, at 520 nm, while Peptide M exhibited time constants of 33 $\pm$ 8 ps, 14%; 1500 $\pm$ 500 ps, 35%), the tryptophan sample yielded time constants of 4 $\pm$ 3 ps, 4%; 1000 $\pm$ 30, 38%. Notably, these changes on the picosecond timescale are not associated with a significant increase in fluorescence quenching in the peptide, as discussed above. TRAS and spectra were also obtained from Peptide M at pH 11 (Figures 5.20 and 5.21). At pH 11, the Peptide M sample exhibits mainly the 580-nm band at the 3-ps time point (Figure 5.20B). The decay kinetics in the peptide are accelerated relative to tryptophan in solution at this pH (Figure 5.21).

TRAS data were then obtained from Peptide W (Figure 5.15E). From the NMR structure, Peptide W is predicted to exhibit a tryptophan-histidine pi-pi interaction. The spectra obtained on the picosecond time scale show changes in relative amplitudes of the

450- and 600-nm bands, when compared to spectra derived from Peptide M (Figure 5.15C). The decay is accelerated relative to tryptophan when analyzed at 360, 460, and 520 nm (Figures 5.17 and 5.16E). Peptide WA14 (Figures 5.15F and 5.16F) behaves similarly when compared to Peptide W (Figures 5.15E and 5.16E). Both spectra and kinetics are similar to Peptide W. For example, fits to the 520-nm decay show that this peptide (Table 5.5) yields time constants of 1 ps (11%) and 780 ps (46%).

5.4.8 TRAS, Peptide MW

Peptide MW, which contains a YW dyad formed from opposite sides of the beta strand, was examined using TRAS. In spectra derived on the picosecond time scale, Peptide MW (Figure 5.15D) exhibits a red shift of the ~580-nm band, when compared to Peptide M (Figure 5.15C). Also, complex dynamics are observed in an evolution of the W* spectrum on the picosecond time scale (Figure 5.22). This spectral complexity is attributable to the conformational flexibility predicted by NMR spectroscopy and molecular dynamic simulations. The decay kinetics were monitored at various wavelengths, including 520 and 360 nm (Figure 5.16D). In Peptide MW, the W* decay kinetics are similar to the kinetics observed in Peptides M, Peptide W, Peptide WA14, and are again faster than the decay kinetics observed in amino acid solutions (Table 5.5). Although the overall amount of decay at 2 ns does not change significantly, fits to the Peptide MW data show that only a small contribution from a fast phase (53 ps, 3%) is necessary to account for the data. Instead, the decay is dominated by a 1200-ps component, which is 59% of the amplitude. Changes in the time constants derived from biexponential fits may reflect average conformer selection in different peptide environments.

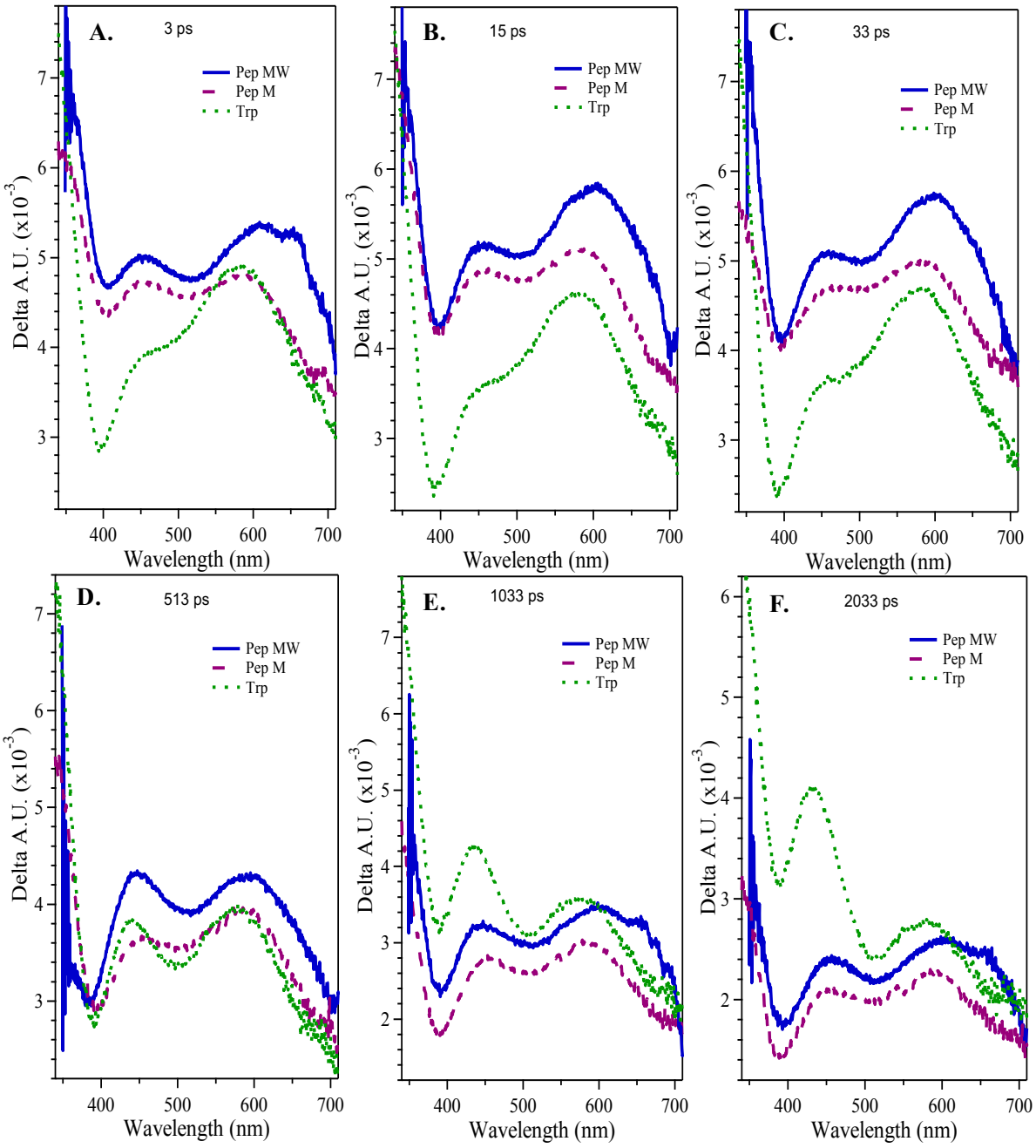

Figure 5.22 Overlay of TRAS derived from tryptophan (black dotted-line), Peptide M (blue dashed-line), and Peptide MW (green solid-line) and obtained at 3 (A), 15 (B), 33 (C), 513 (D), 1033 (E), 2033 ps (F). Analyte concentration, 1 mM; buffer, 5 mM borate-NaOH (pH 9). Spectra are reproduced from Figure 5.15.

5.4.9 Summary of TRAS and pH Dependence of TRAS Data Derived from Tryptophan and Peptide M

When compared to tryptophan, TRAS obtained from tyrosine at pH 9 exhibit no significant intensity at 340-360 nm and reduced signal intensity in the rest of the visible region (Figure 5.18). Kinetic data obtained from tyrosine are shown in Figure 5.19B and are compared to data acquired from tryptophan (Figure 5.19A). There is no significant contribution to the decay kinetics when wavelengths in the 345-360 nm region are probed in tyrosine. As expected if the tyrosine contribution is less intense compared to tryptophan, fits to the tryptophan-tyrosine mixture data (Table 5.5) are similar to fits derived from tryptophan alone. TRAS were also acquired from tryptophan solutions at pH 11 (Figure 5.20). At this pH, the amino group is not protonated, and the photoproduct is not formed. This is confirmed by the spectra presented in Figure 5.20A. Note that the observation of the 580 nm band at pH 11 provides support for assignment of this band to tryptophan S_1 excited state. Also, the 450 nm band is diminished in amplitude relative to the 580 nm band at pH 11 (Table 5.6 and Figure 5.19A). Figure 5.21 compares kinetic data derived from tryptophan and Peptide M at pH 11. The decay of spectral components in Peptide M is accelerated at all monitored wavelengths, when compared to tryptophan at this pH.

5.4.10 EPR Spectroscopy

To investigate any impact of the YW dyad on ET or PCET, EPR spectroscopy and UV photolysis were used to generate tryptophan and tyrosyl radicals in frozen aqueous samples at 160 K according to prior methods.[53] UV-Vis absorption spectra were recorded before and after UV photolysis (Figure 5.23) and showed no significant changes to the spectrum, either in a mixture of tyrosine and tryptophan (Figure 5.23A) or in the peptides (see Peptide M example, Figure 5.23B). Figure 5.24A shows the result of an EPR spectrum recorded after 266 nm UV photolysis (10 flashes) of tyrosine at pH 9. The spectrum is

characteristic of a neutral tyrosyl radical. The tyrosyl radical EPR spectrum is dominated by coupling to the beta-methylene protons and the 3,5-ring protons, with a g value of ~2.004.[54] Figure 5.24E shows the results of photolysis of tryptophan at pH 9. The photochemistry of tryptophan is more complex than that of tyrosine, because the radical form of the indole side chain has a pK_a value of 4.3.[55] This complexity is evident when spectra at pH 4.3, 9, and 11 are compared (Figure 5.25). At pH 9 (Figure 5.25B), the spectrum corresponds to the neutral radical, W•. The EPR spectrum at pH 9 (Figure 5.25B) has a g value of 2.003, partially resolved hyperfine splittings, and an overall linewidth of $\geq$20 G. This spectrum is similar to those reported in the literature, and, at lower microwave power, exhibits the additional hyperfine splittings, which have been assigned to the beta protons and the indole nitrogen.[56-58] At pH 4.3 (Figure 5.25A), the UV photolysis-induced spectrum is expected to reflect an approximately equal contribution from $WH\bullet^+$ and W•. At pH 4.3, the EPR signal (Figure 5.25A) has an overall 60 G linewidth, a g value of 2.006, and exhibits a new 1:1:1 splitting, which may represent a coupling to the indole nitrogen. The observed g value shift, when pH 4.3 and 9 are compared, is expected based on previous studies of tryptophan radicals.[59-60] An additional experiment was performed to investigate the origin of the spectrum obtained at pH 9 in tryptophan (Figure 5.25D). As observed, UV photolysis at 160 K followed by warming to 200 K results in a g shift and the loss of a narrow g = 2.002 signal. At pH 11, the EPR spectrum is similar to the pH 9 spectrum, except for the superposition of a more intense g = 2.002 narrow signal (Figure 5.25C).

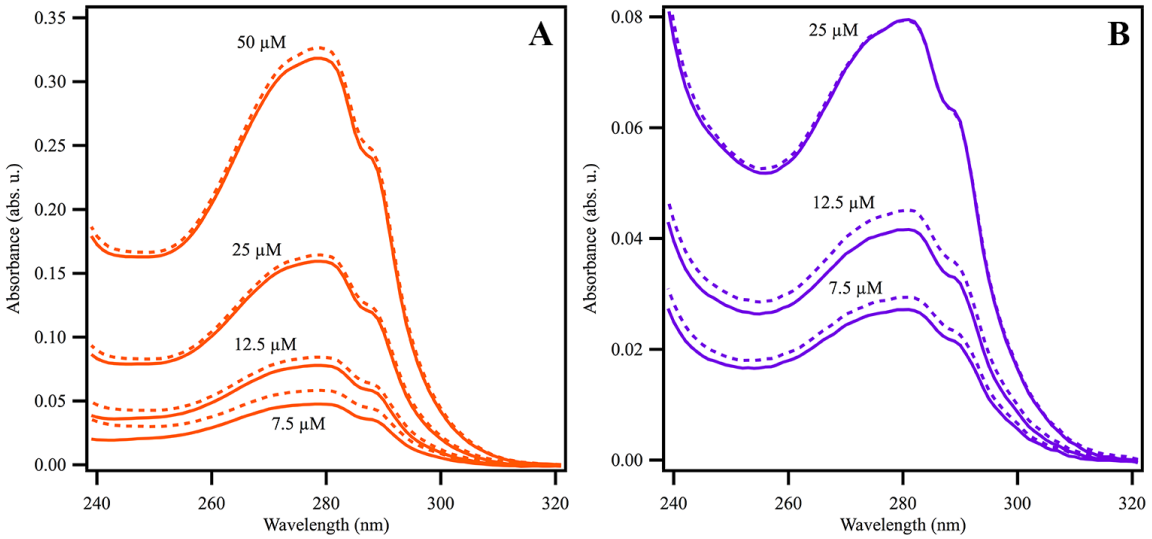

Figure 5.23 UV-Vis absorption spectra recorded before (solid) and after (dashed) UV photolysis at 160 K (EPR experiment). In (A), spectra were acquired from an equimolar mixture of tryptophan and tyrosine and in (B), spectra were acquired from Peptide M. Note the scale change on the y axis and see Figure 5.13 for the magnitude of the hypochromic effect in Peptide M. The buffer contained 5 mM borate, pH 9, and the spectra were acquired at room temperature.

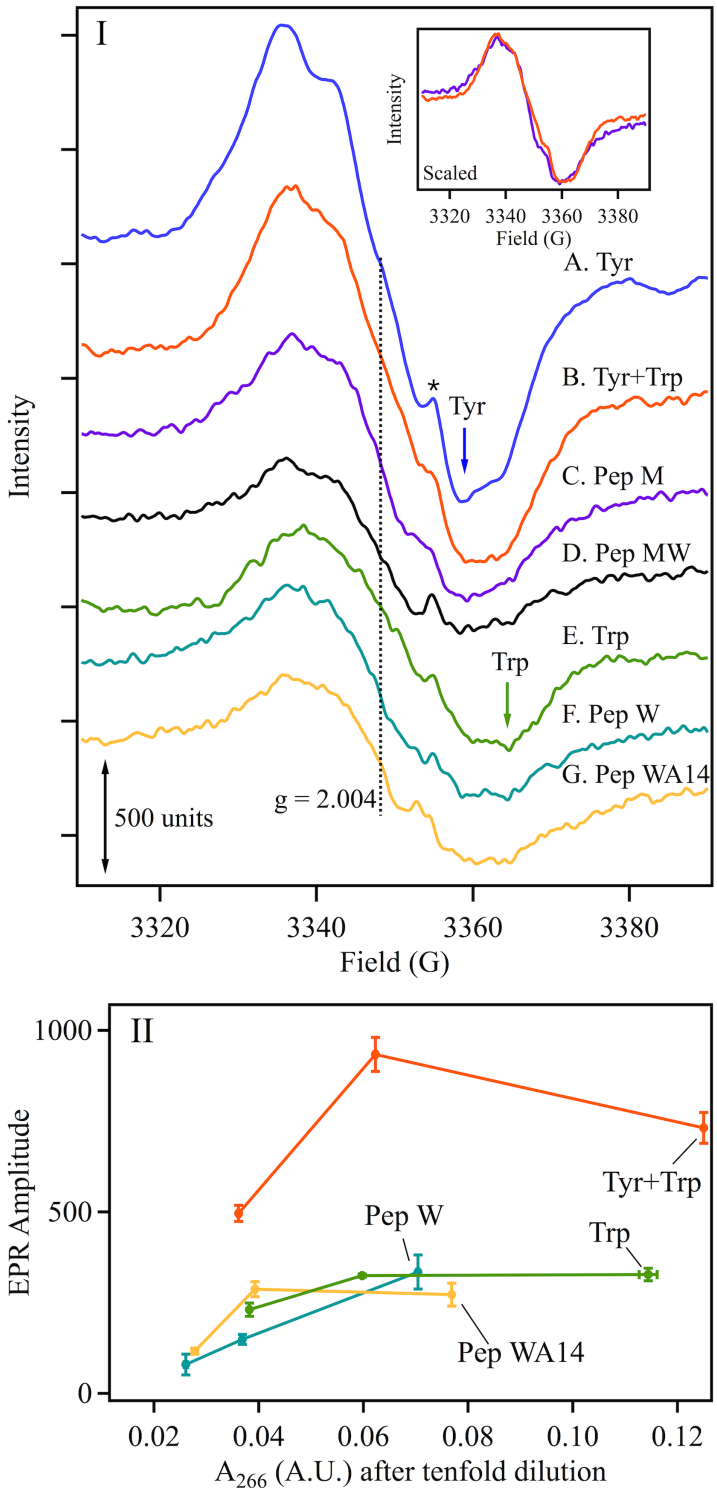

Figure 5.24 In (I), EPR spectra derived from amino acid and beta hairpins after UV photolysis at 160 K and pH 9. Samples: (A) tyrosine, (B) a 1:1 molar mixture of tryptophan and tyrosine (orange), (C) Peptide M (purple), (D) Peptide MW (black),

(E) tryptophan (green), (F) Peptide W (teal), and (G) Peptide WA14 (yellow). The concentration was 250 μM, as determined gravimetrically. Tick marks denote 500 intensity units. The asterisk marks a spectral artifact from the quartz EPR tube. The inset shows an overlay of the spectra of Peptide M (C) and the 1:1 mixture (B); the inset spectra have been arbitrarily scaled to facilitate comparison. The arrows in I emphasize a difference in overall hyperfine coupling between neutral tyrosyl and tryptophan radicals. In (II), EPR amplitude at 3336 G (minus the zero offset at 3315 G) as a function of measured 266 nm absorbance, after a 1 to 10 dilution, at pH 9. Samples: a 1:1 molar mixture of tryptophan and tyrosine (orange), tryptophan (green), Peptide W (teal), and Peptide WA14 (yellow). Error bars represent the standard deviation of 3 replicate measurements.

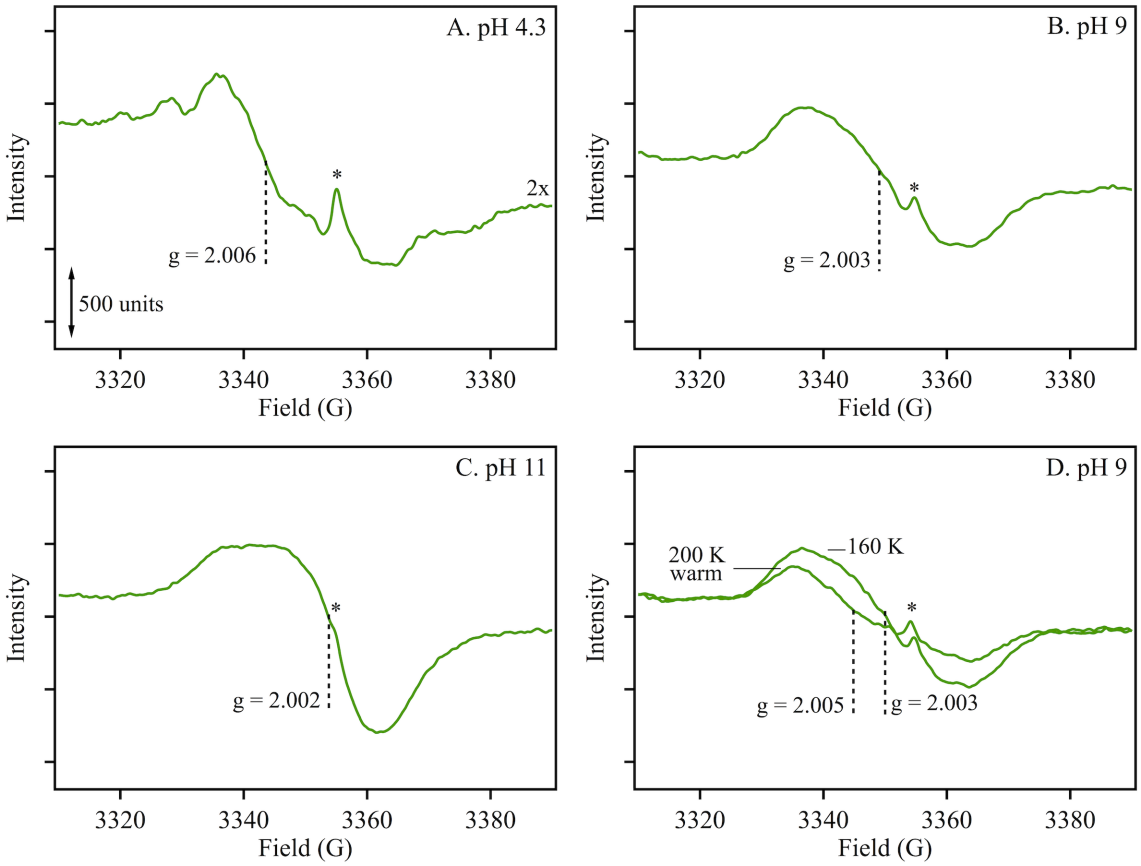

Figure 5.25 The pH dependence of EPR spectra derived from UV photolysis of tryptophan at 160 K. In (A), the sample was pH 4.3, 5 mM acetate with spectra representing a mixture of the protonated $WH\bullet^{+}$ and neutral W• radicals, in (B), the sample was pH 9.0, 5 mM borate with spectra representing the neutral W• radical, and in (C), the sample was pH 11.0, 5 mM borate with spectra representing the neutral W• radical and a superimposed, narrow radical. In (D), UV photolysis of tryptophan was performed at 160 K and pH 9. The sample was then warmed to 200 K, and additional spectra were acquired. Most of the signal amplitude is retained,

but a narrow signal at g=2 loses intensity with warming. The concentration was 250 μM. Tick marks denote 500 intensity units. The asterisk marks a spectral artifact from the quartz EPR tube.

As expected, the EPR spectra of Peptide W (Figure 5.24F) and WA14 (Figure 5.24G) at pH 9 are similar to spectra acquired from tryptophan at the same pH (Figure 5.24E). EPR experiments were conducted on a 1:1 mixture of tyrosine and tryptophan (Figures 5.26A and 5.24B). The EPR spectra of tyrosyl and tryptophan radicals are both produced in the mixture and overlap near g = 2 with a narrow signal. (Figures 5.26A and 5.24B). In Peptide M (Figures 5.26A and 5.24C), UV photolysis produces a radical lineshape that is similar, but not identical, to the mixture spectrum at pH 9 (Figure 5.24, inset). A similar result is obtained when Peptide MW is compared to the mixture (Figure 5.24D).

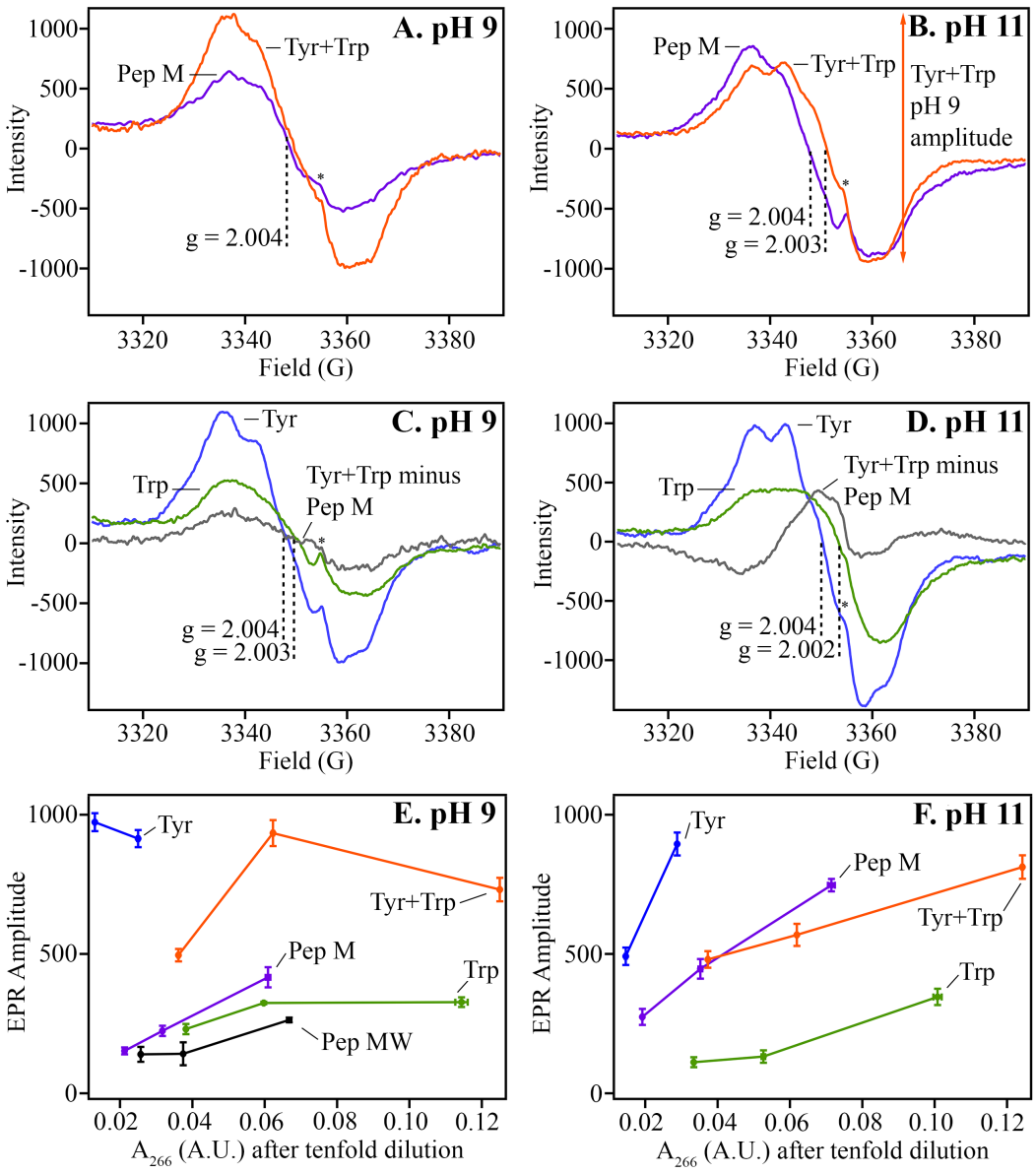

Figure 5.26 EPR spectra of peptides and amino acids at 160 K. In (A and B), EPR spectra derived after UV photolysis from a 1:1 tyrosine-tryptophan mixture (orange, 125 µM, A_{266} = 0.6) and Peptide M (purple, 250 µM, A_{266} = 0.6) at pH 9 (A) or pH 11 (B). In (C and D), the difference spectra, mixture-minus-Peptide M, at pH 9 (C) or pH 11 (D) are compared to EPR spectra derived from tyrosine (blue) and tryptophan (green) at the same pH. In (E and F), EPR amplitude at 3336 G, after subtraction of the zero offset at 3315 G, as a function of measured 266 nm absorbance and after a 1 to 10 dilution, at pH 9 (E) or pH 11 (F). Samples: tyrosine (blue), a 1:1 molar mixture of tryptophan and tyrosine (orange), Peptide M (purple), Peptide MW (black), and tryptophan (green). Error bars represent the standard deviation of 3 replicate measurements. The asterisk marks a spectral artifact from the quartz EPR tube.

The amplitudes of the spectra acquired from Peptide M and the amino acid mixture at pH 9 are compared in Figure 5.26A. These spectra were derived from solutions with an equivalent 266 nm absorbance of 0.6 AU (125 μM mixture; 250 μM Peptide M). The yield of radical appears to be decreased when Peptide M is compared to the mixture. At 3336 G (minus the baseline offset), the intensity of Peptide M is approximately 45% the intensity of the amino acid mixture at pH 9. To investigate this change in yield, the EPR amplitude is plotted versus 266-nm absorption, as measured in each EPR sample after a 1 to 10 dilution (Figure 5.26E). These data confirm that the radical yield is decreased in Peptide M at pH 9 (purple), when compared to the 1:1 mixture of tyrosine and tryptophan (orange). A similar decrease in yield is observed in Peptide MW, compared to the mixture at pH 9 (Figure 5.26E, black). Subtraction of the pH 9 spectra (mixture-minus-Peptide M) gives a difference spectrum that reflects a significant contribution from the tryptophan neutral radical (Figure 5.26C), which has a slightly larger, characteristic splitting compared to tyrosyl radical (see annotation in Figure 5.24). Subtractions using the pH 9 Peptide MW spectra gave a similar lineshape. Note that in Peptide W (Figure 5.24II, teal) and Peptide WA14 (yellow), which lack the tyrosine, the radical yield is similar to the yield obtained in tryptophan alone (green). Importantly, at pH 11, the Peptide M protective effect on radical yield is not observed. At 3336 G, the intensity in the mixture is similar (76%) to the intensity in Peptide M (Figures 5.26B and F). Moreover, at pH 11, the difference spectrum, generated from the mixture and the peptide, resembles mainly a narrow radical (Figure 5.26D). The results are consistent with the conclusion that Peptide M lowers the barrier for radical recombination at 160 K and pH 9 (see Discussion below).

5.5 Discussion

This work defines the spectroscopic and functional impact of inter-aromatic interactions in a pair of YW dyads. The structural effects of aromatic-aromatic interactions in beta hairpin model peptides have been investigated previously.[61] For example, in octamer beta hairpins [62], NMR analysis revealed side chain interactions between the tyrosine and tryptophan rings even at non-hydrogen bonding sites and in organic solvents. In another study, aromatic edge-to-face-interactions were found to have a stabilizing effect on the free energy of beta hairpins.[63] In a third example, time-resolved infrared spectroscopy was used to probe the effect of tryptophan mutagenesis in Trpzip2 beta hairpins.[64] These stabilizing effects of aromatic-aromatic interactions occur in globular proteins. For example, in proteins, it has been concluded that 60% of aromatic residues are involved in aromatic pairs, the majority of which form networks of three or more aromatic side chains.[65] Phenyl ring centroids are typically separated by 4.5 to 7 Å, and dihedral angles of approximately 90^{o} are preferred. The contribution of these interactions to the free energy was deduced to depend on the environment, but varied from 0.6 to 2 kcal/mole.

The YW aromatic-aromatic dyad is a structural motif found in many enzymes, particularly oxidoreductases.[7-8] There are likely to hold functional significance, as evident in examination of two proteins, photosystem II and RNR (Figure 5.1). In RNR, Y122 in the beta subunit acts as a catalytic initiator (reviewed in ref [66]). In the absence of the alpha subunit, Y122 forms a stable radical. The X-ray structure of the singlet state shows that the tyrosine is in close proximity to the beta subunit residue, W48.[15] Mutation shows that W48 plays an important role in RNR, in particular, in the assembly of the tyrosyl radical-diferric cluster.[66-67] In photosystem II, there are two redox-active tyrosines, YZ and YD

(Y161 of the D1 subunit and Y160 of the D2 subunit, respectively), with different functional roles.[20] The YD radical forms a stable neutral tyrosyl radical with a lifetime on the hours time scale.[68] Mutagenesis of this tyrosine leads to a decrease in the steady state rate of oxygen evolution, but the sample is not completely inactivated. It has been proposed that YD may be important in maintaining a high oxidation state of manganese in the active site. On the other hand, YZ is an essential electron transfer intermediate between the primary donor and the metal cluster with a microsecond to millisecond radical lifetime.[69-70] The environment of YZ contains one tryptophan, while YD has multiple interactions with tryptophan residues at interaction distances of ~10 Å [11-13] (Figure 5.1). Interestingly, these interactions are observed both in cyanobacterial and spinach PSII structures.[12-13]

It has been suggested that YW dyads may act as defusers or radical scavengers. In this proposal, the YW dyads catalyze inter-ring electron transfer and conduct excess oxidizing equivalents from catalytic sites to the protein surface.[7-8] Inter-ring transfer is possible, depending on orientation and midpoint potential of the tyrosine and tryptophan. Tyrosine has a pH-independent midpoint potential above the phenolic oxygen pK_a (~10) and has a midpoint potential that varies linearly with pH below this pK_a. Tryptophan can function either in ET or PCET in proteins.[55] Between pH 4 and 10, the midpoint potential of the neutral tryptophan radical is more positive than tyrosine.[55] For example, at pH values between 6 and 10, the neutral tryptophan radical oxidized tyrosine in dipeptides.[55] In azurin, it was also concluded that a W radical could be reduced by tyrosine.[22] For an intra-dyad ET or PCET reaction to be protective, the rates of these defusing reactions must be less than that of the catalytic reactions.

Here, we examine *de novo* designed, YW dyad-containing peptides in which the Y and W rings are in the range of 6-7 Å apart. A significant YW inter-aromatic interaction is evident from our CD experiments on the YW dyad-containing peptides. Tryptophan has multiple singlet excited states, termed B_a, B_b, L_a, and L_b, with absorption maxima of 195, 218 and 278 nm at pH 7.[71] A far UV CD signal is characteristic of excitonic splitting between the ^1B_b band of tryptophan and the ^1L_a band of tyrosine.[72] Previously, such excitonic coupling between tryptophans has been modeled in 12-mer model peptides using time dependent density functional calculations.[18] In addition, a tyrosine-tryptophan excitonic signal has been observed previously in the protein, PagP.[17] To give rise to the CD signal of Peptide M and MW, the ^1L_a and ^1B_b states of tyrosine and tryptophan, respectively, must couple to give two excited states. The splitting energy, Δ_{ij} [17], equals $(\delta_{ij}^2 + 4V_{ij}^2)^{1/2}$, where V_{ij} is the interaction energy. The difference in transition energy, δ_{ij}, is calculated from the positive and negative components of the spectrum (σ_i and σ_j) and corresponds to 228 and 214/212 nm in our spectra of Peptide M and MW. V_{ij} is calculated from the dipole-dipole interaction between the transition dipole moments ($\boldsymbol{\mu}$) and equals:

$$V_{ij} = \boldsymbol{\mu}_i \bullet \boldsymbol{\mu}_j / R_{ij}^3 - 3(\boldsymbol{\mu}_i \bullet \mathbf{R}_{ij})(\boldsymbol{\mu}_j \bullet \mathbf{R}_{ij})/R_{ij}^5 \qquad (5.1)$$

in which the bold face symbols denote vectors (Figure 5.1F).

The rotational strength, R_o, which is the amplitude of the signal, depends on the triple product.

$$R_{ij} = \pm \pi V_{ij} (\sigma_i \sigma_j)^{1/2} [\mathbf{R}_{ij} \bullet (\boldsymbol{\mu}_i \times \boldsymbol{\mu}_j)]/\Delta_{ij} \qquad (5.2)$$

In the NMR structures of Peptide M and MW, the tyrosine phenolic group is oriented in opposite directions, relative to the indole ring (Figure 5.1F). One component of the tyrosine transition dipole moment is oriented along this CO bond.[17] The tryptophan transition dipole moment is oriented parallel to the long dimension of the indole ring, bisecting the ring system.[18] Use of the dihedral angles derived from the lowest energy NMR structures (Figure 5.1F) predicts that the value of V_{ij} will be within a factor of 2 when Peptide M and MW are compared. This is in agreement with the observed Cotton signal amplitudes.

The UV absorption band, assignable to $^1L_{a/b}$, is red-shifted in Peptide M and MW. The fluorescence emission spectrum of the YW dyad peptides is also shifted. In proteins, tryptophan fluorescence occurs mainly from the singlet L_a state with a lifetime in the nanosecond time regime.[73] The fluorescence yield varies dramatically in proteins.[48] We show here that the YW dyad has the effect of blue shifting the fluorescence emission spectrum of W by approximately 5 nm. Negative charges near the benzene ring or positive charges near the pyrrole ring are expected to shift the emission to shorter wavelengths.[47] In the lowest energy NMR structures of Peptide M and MW, the nearest functional group to the tryptophan ring is the phenol moiety. Specifically, Y5 is positioned with pi electron density proximal to the benzene portion of the indole ring. Based on the lowest energy NMR structures, the nearest C-C distances from Y5 to W14 (Peptide M) or W13 (Peptide MW) are 3.0 and 2.9 Å, respectively. Therefore, the YW interaction can account for the fluorescence emission blue shift. We also find that fluorescence emission from the tyrosine phenol ring is quenched in the YW dyad-containing peptides. This is attributable to a Förster dipole-dipole transfer mechanism between the tryptophan and tyrosine rings.

While quenching of tryptophan fluorescence via electron transfer can also sometimes be observed in tryptophan-containing proteins [48, 74] and peptides, [21] we show that quenching of the tryptophan fluorescence is not significant in Peptide M and MW. The amount of quenching will depend on the electronic coupling and the energy gap, and these factors are sensitive to the detailed protein environment.

We measured the spectra and lifetime of the W* produced in peptide and aqueous amino acid samples after UV photolysis on the picosecond time scale.[27-28] The spectra are dominated by contributions from the S_1 excited state of the indole ring, W*. This W* decays by multiple mechanisms, which include photoproduct formation, electron transfer, and other mechanisms. Photoionization is expected and is accompanied by production of a solvated electron with absorption at 650 nm, as observed here. The formation of the W* signal is complete in 3 ps, and the solvated electron signal decays on the picosecond time scale. The spectra that we report from tryptophan and tryptophan-tyrosine mixtures are similar to previous reports of the indole S_1 excited state, with absorption at 345/360 and 520 nm.[49, 52, 75-76] In tryptophan and in the mixture, the formation of a H^+indole photoproduct is also evident as a 420 nm spectral feature that grows in ~500 ps. The source of the proton has been attributed to the tryptophan amino group.[52, 75] This photoproduct is not observed in the peptide samples studied here. The lifetime of the W* state in tryptophan, as reported here, is consistent with previous reports of the nanosecond fluorescence lifetime of tryptophan.[49, 52, 75-76]

The TRAS data acquired on the picosecond time scale show that the excited spectra of Peptide M, MW, W, and WA14 are all distinguishable by minor intensity changes at 450 and 600 nm. These are most likely attributable to changes in electrostatic interactions

in the peptides. In addition, the spectrum of Peptide MW is red shifted when compared to Peptide M or tryptophan and exhibits complex spectral changes on the picosecond time scale. This red shift and the picosecond-time dependent alterations are attributed to the unique conformational landscape sampled by this peptide. We conclude that the structural relaxation in Peptide MW influences the S_1 excited state surface and reflects the detailed arrangement of charged groups near the indole ring. Note that the excited state spectrum of Peptide M is pH dependent, indicating that the deprotonation state of amino acid side chains is an important determinant in this process.

The decay rate of the W* state is similar in all four peptides. However, the rate observed in the peptides is accelerated, when compared to tryptophan solutions or tryptophan-tyrosine mixtures. For example, at 360 nm, there is no appreciable signal decay in an aqueous solution of tryptophan; however, significant spectral decay is observed in all the peptides on the picosecond time scale. This is a wavelength at which tyrosine excited state decay makes no significant contribution. Because this acceleration is independent of the tryptophan's non-covalent interactions, the effect is attributable to the influence of the peptide backbone. The tryptophan radical can decay by recombination with the solvated electron.[46, 55] The tryptophan radical is most likely formed with 280 nm photolysis on the 2 ns timescale, even if not directly detected under the intense W* absorption, because our spectra provide evidence for the production of a solvated electron. Previous studies of tyrosyl radical decay in beta hairpins have demonstrated a peptide backbone-induced increase in PCET and ET rate, which alters the rate of radical recombination. In that case, this increase in decay rate was attributed to an increase in electronic coupling.[27-28] Such

an increase in electronic coupling can accelerate the rate of tryptophan radical decay in Peptide M and thus accelerate W* decay, as well.

To test if the YW dyads in the beta hairpins have unique electron and proton transfer characteristics, radical yield was measured using EPR spectroscopy after UV photolysis at 160 K. UV photolysis can produce reactive oxygen species, which lead to damage of the indole ring. Such oxidative damage may alter the UV spectrum and is expected to be evident in spectra obtained from tryptophan solutions after UV laser flashes. However, in our experiments, the spectra acquired from tryptophan-containing peptides or the tyrosine-tryptophan mixture were not significantly altered by UV photolysis. The 266-nm flash is expected to generate a neutral radical in tyrosine and tryptophan solutions at pH 9. This was confirmed by comparison of radical lineshapes produced at pH 4.3, 9.0, and 11.0 in tryptophan.

At pH 9.0, the radical yield is substantially reduced in Peptide M and MW, when compared to a mixture of tyrosine and tryptophan. The majority of the pH 9 effect appears to be on the yield of tryptophan radical, as assessed from the difference spectrum. However, significantly, at pH 11, the yield of neutral tryptophan radical, W•, is similar in Peptide M, when compared to a 1:1 mixture. Notably, MD simulations of Peptide M indicate that the structure of the peptide at pH 11 is similar to the structure at pH 9. In addition, at pH 9.0, the yield of W• is indistinguishable in Peptides W and WA14, when compared to the radical yield in tryptophan.

In UV flash photolysis, the radical yield equals the number of radicals formed per number of photons absorbed. The number of photons absorbed in dilute solution is linearly

proportional to the absorbance at 266 nm, the pathlength, and concentration. With pathlength and incident intensity held constant, a plot of amplitude versus 266 nm absorption shows a quenching effect specific to Peptide M and MW. What is the origin of this quenching effect at pH 9? The effect could be on the formation rate or on the recombination rate. Because the tyrosyl and tryptophan radicals are formed in the excited state, alterations in the description of the S_1 excited state or in the rates of S_1 decay, internal conversion, and radical formation could impact the EPR yield. The TRAS and kinetic experiments provide evidence that the S_1 excited states decay more slowly in the amino acid mixture, compared to the peptides. This could contribute to a difference in yield; however, the effect on the excited state decay rate was observed both at pH 9 and 11, and was observed in peptides in which no protective effect was detected (Peptide W and WA14). Therefore, a change in the formation rate due to alterations in the excited state seems an unlikely explanation of Peptide M radical quenching in the EPR experiment. In addition, fluorescence experiments confirm that the YW dyad has little effect on tryptophan fluorescence quenching. Note that the midpoint potential of Peptide M is similar to that of amino acids.[32]

Based on the considerations above, we propose that the protective effect observed on radical yield in Peptide M and MW is due to alteration in radical recombination rate at pH 9 (Figure 5.27). Tyrosyl radicals decay by recombination with the solvated electron and a proton at pH 9, but with solvated electron alone at pH 11. Tryptophan neutral radical decays by a PCET reaction, involving H^+ and e^-, at both pH values. From the EPR difference spectra of Peptide M and MW, the majority of the protective effect appears to be on tryptophan radical. At pH 9, the tyrosine side chain is protonated, and the protective

effect can be attributed to rapid PCET through a hydrogen-bonding network, which contains the tyrosine and hydrogen-bonded water molecules (Figure 5.27). Consistent with a role for this protonated tyrosine side chain, there is no significant effect on yield when Peptides W and WA14 are compared to tryptophan. Also, the YW protective effect is not evident at pH 11, where the negative charge on the tyrosinate may disrupt hydrogen-bonding interactions (Figure 5.27). This speculative model proposes that the interactions of the YW side chains with nearby water molecules are important kinetically and lower a barrier for PCET. A similar model has been proposed to explain PCET reactions in a DNA photolyase [77] and in donor-acceptor supramolecules assembled through a hydrogen bonded interface (reviewed in ref [78]).

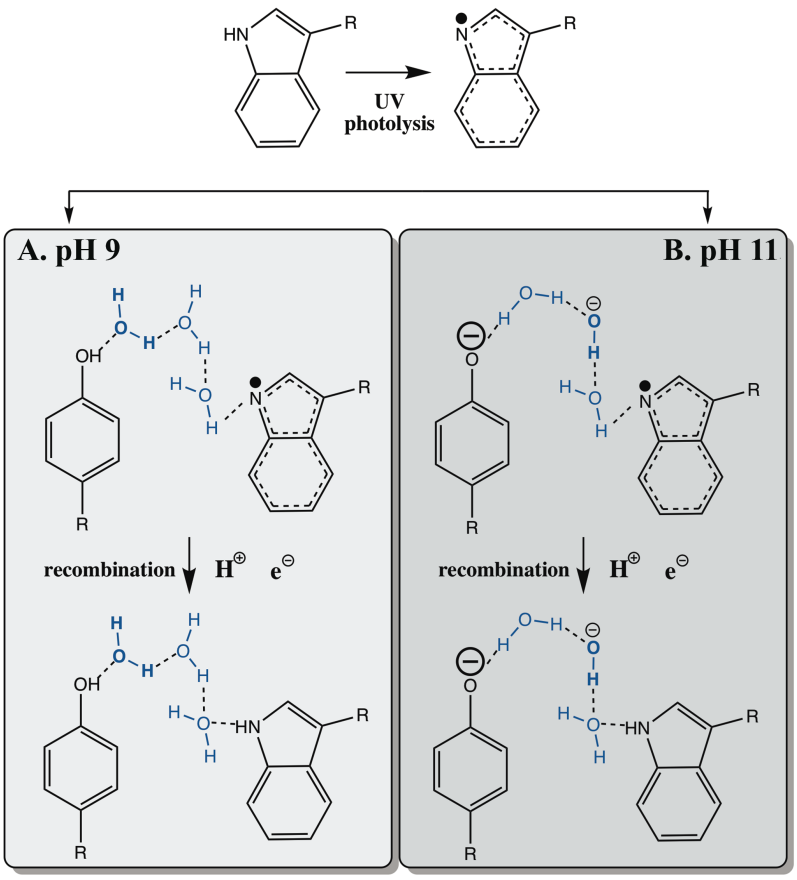

Figure 5.27 Schematic illustrating UV photolysis, radical generation, a pH-induced change in a hydrogen bonding network containing Y and W, and a speculative protective mechanism in the YW dyad-containing peptides.

Previous studies of azurin have provided evidence that the presence of tyrosine in the protein can quench a stable tryptophan radical. This was attributed to intramolecular ET from tyrosine to the tryptophan radical.[22] A similar process has been proposed to rationalize the UV spectrum of Peptide M by another group.[32] In DNA photolyase from *Anacystis nidulans*, a microsecond ET pathway was proposed to involve a tyrosine to tryptophan radical transfer step, but only in ~40% of the sample.[60] However, tyrosine to tryptophan radical ET is not a consistent explanation of our EPR results, because oxidation of tyrosine at the expense of tryptophan radical would still generate an overlapping $g = 2$ radical and would not decrease the overall intensity of the EPR spectrum in Peptide M and

MW at pH 9. Instead, we favor the explanation that the barrier for radical recombination with the solvated electron is decreased.

Distances of 6-7 Å, as found here in Peptide M and MW, have been described in extensive aromatic wires in cytochrome c oxidase and human superoxide dismutase. In PSII and RNR, the Y-W distance is ~10 Å (Figures 5.1A-E). While distances of 10 Å are expected to support electron exchange on the microsecond time scale (□G = 0, λ□ = 1 eV, T = 295 K), distances of 7.5 Å have been proposed to support much faster ET rates.[7-8] In cyanobacterial and spinach PSII (Figures 5.1B and D), YZ interacts at a distance of ~10 Å with a single tryptophan and decays on the microsecond-millisecond time scale. YD (Figures 5.1C and E) has multiple tryptophan interactions predicted at 10 Å and decays on the hours time scale. Y122 radical in the isolated *E. coli* RNR beta subunit is stable for days; in the singlet structure, Y122 is ~10 Å from a surface exposed tryptophan (Figure 5.1A). The reason for these distinctions in stability is not known, but has been proposed to be due to access of water to the radical site.[33] This comparison underlines the importance of modeling YW interactions at distinct OH-N distances and orientations.

5.6 Conclusions

The distribution and prevalence of YW dyads in enzymes suggest that solvent exposed dyads and aromatic clusters play important roles in structure and function. Here, we show that the energetics of a YW aromatic interaction is sufficient to destabilize the backbone fold and to introduce spectrally detectable, conformational dynamics on the picosecond time scale. The peptide backbone is observed to accelerate the rate of W* decay. We also provide evidence that peptides, containing these YW dyads, exhibit a

decreased yield of free radicals after UV photolysis at pH 9. These results support a protective role for YW dyads (6-7 Å distances) as ROS scavengers and free radical quenchers.

5.7 References

1. Dempsey, J. L.; Winkler, J. R.; Gray, H. B. Proton-Coupled Electron Flow in Protein Redox Machines. *Chem. Rev.* **2010,** *110*, 7024-39.

2. Keough, J.; Jenson, D. L.; Zuniga, A.; Barry, B. A. Proton Coupled Electron Transfer and Redox-Active Tyrosine Z in the Photosynthetic Oxygen Evolving Complex. *J. Am. Chem. Soc.* **2011,** *133*, 11084-11087.

3. Keough, J.; Zuniga, A.; Jenson, D. L.; Barry, B. A. Redox Control and Hydrogen Bonding Networks: Proton-Coupled Electron Transfer Reactions and Tyrosine Z in the Photosynthetic Oxygen-Evolving Complex. *J. Phys. Chem. B* **2013,** *117*, 1296−1307.

4. Kasson, T. M.; Barry, B. A. Reactive Oxygen and Oxidative Stress: N-Formyl Kynurenine in Photosystem Ii and Non-Photosynthetic Proteins. *Photosynth Res* **2012,** *114*, 97-110.

5. Ehrenshaft, M.; Deterding, L. J.; Mason, R. P. Tripping up Trp: Modification of Protein Tryptophan Residues by Reactive Oxygen Species, Modes of Detection, and Biological Consequences. *Free Radic Biol Med* **2015,** *89*, 220-8.

6. Taylor, R. M.; Sallans, L.; Frankel, L. K.; Bricker, T. M. Natively Oxidized Amino Acid Residues in the Spinach Cytochrome B 6 F Complex. *Photosynth Res* **2018**, 10.1007/s11120-018-0485-0.

7. Gray, H. B.; Winkler, J. R. Hole Hopping through Tyrosine/Tryptophan Chains Protects Proteins from Oxidative Damage. *Proc Natl Acad Sci USA* **2015,** *112*, 10920-5.

8. Winkler, J. R.; Gray, H. B. Could Tyrosine and Tryptophan Serve Multiple Roles in Biological Redox Processes? *Philos Trans A Math Phys Eng Sci* **2015,** *373*.

9. Bradley, J. M.; Svistunenko, D. A.; Moore, G. R.; Le Brun, N. E. Tyr25, Tyr58 and Trp133 of Escherichia Coli Bacterioferritin Transfer Electrons between Iron in the Central Cavity and the Ferroxidase Centre. *Metallomics* **2017,** *9*, 1421-1428.

10. Nordlund, P.; Sjöberg, B.-M.; Eklund, H. Three-Dimensional Structure of the Free Radical Protein of Ribonucleotide Reductase. *Nature* **1990,** *345*, 593-598.

11. Umena, Y.; Kawakami, K.; Shen, J.-R.; Kamiya, N. Crystal Structure of Oxygen-Evolving Photosystem Ii at a Resolution of 1.9 Angstrom. *Nature* **2011,** *473*, 55-60.

12. Suga, M.; Akita, F.; Hirata, K.; Ueno, G.; Murakami, H.; Nakajima, Y.; Shimizu, T.; Yamashita, K.; Yamamoto, M.; Ago, H., et al. Native Structure of Photosystem Ii at 1.95 a Resolution Viewed by Femtosecond X-Ray Pulses. *Nature* **2015,** *517*, 99-103.

13. Wei, X.; Su, X.; Cao, P.; Liu, X.; Chang, W.; Li, M.; Zhang, X.; Liu, Z. Structure of Spinach Photosystem Ii-Lhcii Supercomplex at 3.2 Angstrom Resolution. *Nature* **2016,** *534*, 69-74.

14. Barry, B. A. Proton Coupled Electron Transfer and Redox Active Tyrosines in Photosystem Ii. *J. Photochem. Photobiol. B* **2011,** *104*, 60-71.

15. Högbom, M.; Galander, M.; Andersson, M.; Kolberg, M.; Hofbauer, W.; Lassmann, G.; Nordlund, P.; Lendzlan, F. Displacement of the Tryosyl Radical Cofactor in Ribonucleotide Reductase Obtained by Single-Crystal High-Field Epr and 1.4-a X-Ray Data. *Proc. Nat. Acad. Sci. USA* **2003,** *100*, 3209-3214.

16. Grishina, I. B.; Woody, R. W. Contributions of Tryptophan Side Chains to the Circular Dichroism of Globular Proteins: Exciton Couplets and Coupled Oscillators. *Faraday Discuss* **1994**, 245-62.

17. Khan, M. A.; Neale, C.; Michaux, C.; Pomes, R.; Prive, G. G.; Woody, R. W.; Bishop, R. E. Gauging a Hydrocarbon Ruler by an Intrinsic Exciton Probe. *Biochemistry* **2007,** *46*, 4565-79.

18. Roy, A.; Bour, P.; Keiderling, T. A. Td-Dft Modeling of the Circular Dichroism for a Tryptophan Zipper Peptide with Coupled Aromatic Residues. *Chirality* **2009,** *21 Suppl 1*, E163-71.

19. Schafheimer, N.; King, J. Tryptophan Cluster Protects Human Gammad-Crystallin from Ultraviolet Radiation-Induced Photoaggregation in Vitro. *Photochem Photobiol* **2013,** *89*, 1106-15.

20. Barry, B. A. Reaction Dynamics and Proton Coupled Electron Transfer: Studies of Tyrosine-Based Charge Transfer in Natural and Biomimetic Systems. *Biochim. Biophys. Acta* **2015,** *1847*, 46-54.

21. McMillan, A. W.; Kier, B. L.; Shu, I.; Byrne, A.; Andersen, N. H.; Parson, W. W. Fluorescence of Tryptophan in Designed Hairpin and Trp-Cage Miniproteins: Measurements of Fluorescence Yields and Calculations by Quantum Mechanical Molecular Dynamics Simulations. *J Phys Chem B* **2013,** *117*, 1790-809.

22. Larson, B. C.; Pomponio, J. R.; Shafaat, H. S.; Kim, R. H.; Leigh, B. S.; Tauber, M. J.; Kim, J. E. Photogeneration and Quenching of Tryptophan Radical in Azurin. *J. Phys. Chem. B* **2015,** *119*, 9438-49.

23. Sibert, R.; Josowicz, M.; Porcelli, F.; Veglia, G.; Range, K.; Barry, B. A. Proton-Coupled Electron Transfer in a Biomimetic Peptide as a Model of Enzyme Regulatory Mechanisms. *J Am Chem Soc* **2007,** *129*, 4393-400.

24. Sibert, R. S.; Josowicz, M.; Barry, B. A. Control of Proton and Electron Transfer in De Novo Designed, Biomimetic Beta Hairpins. *ACS Chem Biol* **2010,** *5*, 1157-68.

25. Pagba, C. V.; Barry, B. A. Redox-Induced Conformational Switching in Photosystem-Ii-Inspired Biomimetic Peptides: A Uv Resonance Raman Study. *J. Phys. Chem. B* **2012,** *116*, 10590-9.

26. Hwang, H.; Tyler G. McCaslin; Pagba, C. V.; Nevin, C. M.; Pavlova, A.; Barry, B. A.; Gumbart, J. C. Redox-Driven Conformational Dynamics in a Photosystem-Ii-Inspired B-Hairpin Maquette Determined through Spectroscopy and Simulation. *J. Phys. Chem. B* **2017,** *121*, 3536-3545.

27. Pagba, C. V.; Chi, S. H.; Perry, J.; Barry, B. A. Proton-Coupled Electron Transfer in Tyrosine and a Beta-Hairpin Maquette: Reaction Dynamics on the Picosecond Time Scale. *J Phys Chem B* **2015,** *119*, 2726-36.

28. Pagba, C. V.; McCaslin, T. G.; Chi, S. H.; Perry, J. W.; Barry, B. A. Proton-Coupled Electron Transfer and a Tyrosine-Histidine Pair in a Photosystem Ii-Inspired Beta-Hairpin Maquette: Kinetics on the Picosecond Time Scale. *J Phys Chem B* **2016,** *120*, 1259-72.

29. Martinez-Rivera, M. C.; Berry Bruce, W.; Valentine, K. G.; Westerlund, K.; Hay, S.; Tommos, C. Electrochemical and Structural Properties of a Protein System Designed to Generate Tyrosine Pourbaix Diagrams *J. Am. Chem. Soc.* **2011,** *133*, 17786-17795

30. Ravichandran, K. R.; Liang, L.; Stubbe, J.; Tommos, C. Formal Reduction Potential of 3,5-Difluorotyrosine in a Structured Protein: Insight into Multistep Radical Transfer. *Biochemistry* **2013,** *52*, 8907-15.

31. Glover, S. D.; Jorge, C.; Liang, L.; Valentine, K. G.; Hammarstrom, L.; Tommos, C. Photochemical Tyrosine Oxidation in the Structurally Well-Defined Alpha3y Protein: Proton-Coupled Electron Transfer and a Long-Lived Tyrosine Radical. *J. Am Chem Soc* **2014,** *136*, 14039-51.

32. Pagba, C. V.; McCaslin, T. G.; Veglia, G.; Porcelli, F.; Yohannan, J.; Guo, Z.; McDaniel, M.; Barry, B. A. A Tyrosine-Tryptophan Dyad and Radical-Based Charge Transfer in a Ribonucleotide Reductase-Inspired Maquette. *Nature Comm.* **2015,** *10010.*

33. Barry, B. A.; Chen, J.; Keough, J.; Jenson, D. L.; Offenbacher, A. R.; Pagba, C. V. Proton Coupled Electron Transfer and Redox Active Tyrosines: Structure and Function of the Tyrosyl Radicals in Ribonucleotide Reductase and Photosystem Ii. *J. Phys. Chem. Lett.* **2012,** *3*, 543-554.

34. Edsall, J. T.; Martin, R. B.; Hollingworth, B. R. Ionization of Individual Groups in Dibasic Acids, with Application to the Amino and Hydroxyl Groups of Tyrosine *Proc. Natl. Acad. Sci. USA* **1958,** *44*, 505-519.

35. Best, R. B.; Zhu, X.; Shim, J.; Lopes, P. E.; Mittal, J.; Feig, M.; MacKerell Jr, A. D. Optimization of the Additive Charmm All-Atom Protein Force Field Targeting Improved Sampling of the Backbone Φ, Ψ and Side-Chain X1 and X2 Dihedral Angles. *Journal of chemical theory and computation* **2012,** *8*, 3257-3273.

36. Phillips, J. C.; Braun, R.; Wang, W.; Gumbart, J.; Tajkhorshid, E.; Villa, E.; Chipot, C.; Skeel, R. D.; Kale, L.; Schulten, K. Scalable Molecular Dynamics with Namd. *Journal of computational chemistry* **2005,** *26*, 1781-1802.

37. Darden, T.; York, D.; Pedersen, L. Particle Mesh Ewald: An N· Log (N) Method for Ewald Sums in Large Systems. *The Journal of chemical physics* **1993,** *98*, 10089-10092.

38. Humphrey, W.; Dalke, A.; Schulten, K. Vmd: Visual Molecular Dynamics. *Journal of molecular graphics* **1996,** *14*, 33-38.

39. Jo, S.; Jiang, W. A Generic Implementation of Replica Exchange with Solute Tempering (Rest2) Algorithm in Namd for Complex Biophysical Simulations. *Computer Physics Communications* **2015,** *197*, 304-311.

40. Wang, L.; Friesner, R. A.; Berne, B. J. Replica Exchange with Solute Scaling: A More Efficient Version of Replica Exchange with Solute Tempering (Rest2). *The Journal of Physical Chemistry B* **2011,** *115*, 9431-9438.

41. Maupetit, J.; Derreumaux, P.; Tuffery, P. Pep-Fold: An Online Resource for De Novo Peptide Structure Prediction. *Nucleic Acids Res* **2009,** *37*, W498-503.

42. Kjaergaard, M.; Brander, S.; Poulsen, F. M. Random Coil Chemical Shift for Intrinsically Disordered Proteins: Effects of Temperature and Ph. *Journal of biomolecular NMR* **2011,** *49*, 139-149.

43. Kjaergaard, M.; Poulsen, F. M. Sequence Correction of Random Coil Chemical Shifts: Correlation between Neighbor Correction Factors and Changes in the Ramachandran Distribution. *Journal of Biomolecular NMR* **2011,** *50*, 157-165.

44. Devoe, H.; Tinoco, I., Jr. The Hypochromism of Helical Polynucleotides. *J Mol Biol* **1962,** *4*, 518-27.

45. Rhodes, D.; Burley, S. K. Protein-Nucleic Acid Interactions. *Curr Opin Struct Biol* **1997,** *7*, 73-5.

46. Blanco-Rodriguez, A. M.; Towrie, M.; Sykora, J.; Zalis, S.; Vlcek, A., Jr. Photoinduced Intramolecular Tryptophan Oxidation and Excited-State Behavior of [Re(L-Aa)(Co)3(Alpha-Diimine)](+) (L = Pyridine or Imidazole, Aa = Tryptophan, Tyrosine, Phenylalanine). *Inorg Chem* **2011,** *50*, 6122-34.

47. Vivian, J. T.; Callis, P. R. Mechanisms of Tryptophan Fluorescence Shifts in Proteins. *Biophys J* **2001,** *80*, 2093-109.

48. Adams, P. D.; Chen, Y.; Ma, K.; Zagorski, M. G.; Sonnichsen, F. D.; McLaughlin, M. L.; Barkley, M. D. Intramolecular Quenching of Tryptophan Fluorescence by the Peptide Bond in Cyclic Hexapeptides. *J Am Chem Soc* **2002,** *124*, 9278-86.

49. Kandori, H.; Borkmann, R. F.; Yoshihara, K. Picosecond Transient Absorption of Aqueous Tryptophan. *J. pHys. Chem.* **1993,** *97*, 9664-9667.

50. Sharma, B.; Asher, S. A. Uv Resonance Raman Investigation of the Conformations and Lowest Energy Allowed Electronic Excited States of Tri- and Tetraalanine: Charge Transfer Transitions. *The journal of physical chemistry. B* **2010,** *114*, 6661-8.

51. Gord, J. R.; Hewett, D. M.; Hernandez-Castillo, A. O.; Karl N. Blodgett; Rotondaro, M. C.; Varuolo, A.; Kubasik, M. A.; Zwier, T. S. Conformation-Specific Spectroscopy of Capped, Gas-Phase Aib Oligomers: Tests of the Aib Residue as a 310-Helix Former. *Phys Chemi Chem Phys* **2016,** *18*.

52. Leonard, J.; Sharma, D.; Szafarowicz, B.; Torgasin, K.; Haacke, S. Formation Dynamics and Nature of Tryptophan's Primary Photoproduct in Aqueous Solution. *Phys Chem Chem Phys* **2010,** *12*, 15744-50.

53. Barry, B. A.; El-Deeb, M. K.; Sandusky, P. O.; Babcock, G. T. Tyrosine Radicals in Photosystem Ii and Related Model Compounds. *J. Biol. Chem.* **1990,** *265*, 20139-20143.

54. Barry, B. A.; El-Deeb, M.; Sithole, I.; Debus, R.; McIntosh, L.; Babcock, G. T., *Current Research in Photosynthesis*, Baltscheffsky, M., Ed. Kluwer Academic Publishers: Dordrecht, 1990; Vol. I, pp 483-486.

55. Reece, S. Y.; Stubbe, J.; Nocera, D. G. Ph Dependence of Charge Transfer between Tryptophan and Tyrosine in Dipeptides. *Biochim. Biophys. Acta* **2005,** *1706*, 232-8.

56. Walden, S. E.; Wheeler, R. A. Distinguishing Features of Indolyl Radical and Radical Cation: Implications for Tryptophan Radical Studies. *The Journal of Physical Chemistry* **1996,** *100*, 1530-1535.

57. Shafaat, H. S.; Leigh, B. S.; Tauber, M. J.; Kim, J. E. Spectroscopic Comparison of Photogenerated Tryptophan Radicals in Azurin: Effects of Local Environment and Structure. *J. Am. Chem. Soc.* **2010,** *132*, 9030-9.

58. Stoll, S.; Shafaat, H. S.; Krzystek, J.; Ozarowski, A.; Tauber, M. J.; Kim, J. E.; Britt, R. D. Hydrogen Bonding of Tryptophan Radicals Revealed by Epr at 700 Ghz. *J Am Chem Soc* **2011,** *133*, 18098-101.

59. Kim, S. T.; Sancar, A.; Essenmacher, C.; Babcock, G. T. Time-Resolved Epr Studies with DNA Photolyase: Excited-State Fadh0 Abstracts an Electron from Trp-306 to Generate Fadh-, the Catalytically Active Form of the Cofactor. *Proc Natl Acad Sci U S A* **1993,** *90*, 8023-7.

60. Aubert, C.; Mathis, P.; Eker, A. P.; Brettel, K. Intraprotein Electron Transfer between Tyrosine and Tryptophan in DNA Photolyase from Anacystis Nidulans. *Proc Natl Acad Sci U S A* **1999,** *96*, 5423-7.

61. Waters, M. L. Aromatic Interactions in Model Systems. *Current Opin. Chem. Biol.* **2002,** *6*, 736-741.

62. Mahalakshmi, R.; Raghothama, S.; Balaram, P. Nmr Analysis of Aromatic Interactions in Designed Peptide Beta-Hairpins. *J Am Chem Soc* **2006,** *128*, 1125-38.

63. Tatko, C.; Waters, M. L. Comparison of C-H Pi and Hydrophobic Interactions in a Beta Hiarpin Peptide: Impact on Stability and Specificity. *Journal of the American Chemical Society* **2004,** *126*, 2028-2034.

64. Popp, A.; Wu, L.; Keiderling, T. A.; Hauser, K. Effect of Hydrophobic Interactions on the Folding Mechanism of Beta-Hairpins. *J Phys Chem B* **2014,** *118*, 14234-42.

65. Burley, S. K.; Petsko, G. A. Aromatic-Aromatic Interaction: A Mechanism of Protein Structure Stabilization. *Science* **1985,** *229*, 23-8.

66. Minnihan, E. C.; Nocera, D. G.; Stubbe, J. Reversible, Long-Range Radical Transfer in *E. Coli* Class Ia Ribonucleotide Reductase. *Acc. Chem. Res.* **2013,** *46*, 2524-35.

67. Krebs, C.; Chen, S.; Baldwin, J.; Ley, B. A.; Patel, U.; Edmondson, D. E.; Huynh, B. H.; J. Martin Bollinger, J. Mechanism of Rapid Electron Transfer During Oxygen Activation in the R2 Subunit of *Escherichia Coli* Ribonucleotide Reductase. 2. Evidence for and Consequences of Blocked Electron Transfer in the W48f Variant. *J. Am. Chem. Soc.* **2000,** *122*, 12207-12219.

68. Barry, B. A.; Babcock, G. T. Tyrosine Radicals Are Involved in the Photosynthetic Oxygen-Evolving System. *Proc. Nat. Acad. Sci. USA* **1987,** *84*, 7099-7103.

69. Dekker, J. P.; Gorkom, H. J. V.; Brok, M.; Ouwehand, L. Optical Characterization of Photosystem Ii Electron Donors. *Biochimica et Biophysica Acta* **1984,** *764*, 301-309.

70. Gerken, S.; Brettel, K.; Schlodder, E.; Witt, H. T. Optical Characterization of the Immediate Donor to Chlorophyll A_{ii}^{+} in O_2-Evolving Photosystem Ii Complexes. *FEBS Letters* **1988,** *237*, 69-75.

71. Sweeney, J. A.; Asher, S. A. Tryptophan Uv Resonance Raman Excitation Profiles. *J. Phys. Chem.* **1990,** *94*, 4784-4791.

72. Woody, R. W. Contributions of Tryptophan Side Chains to the Far-Ultraviolet Circular Dichroism of Proteins. *Eur Biophys J* **1994,** *23*, 253-62.

73. Callis, P. R. 1la and 1lb Transitions of Tryptophan: Applications of Theory and Experimental Observations to Fluorescence of Proteins. **1997,** *278*, 113-150.

74. Kosinski-Collins, M. S.; Flaugh, S. L.; King, J. Probing Folding and Fluorescence Quenching in Human Gammad Crystallin Greek Key Domains Using Triple Tryptophan Mutant Proteins. *Protein Sci* **2004,** *13*, 2223-35.

75. Sharma, D.; Leonard, J.; Haacke, S. Ultrafast Excited-State Dynamics of Tryptophan in Water Observed by Transient Absorption Spectroscopy. *Chem Phys Letters* **2010,** *489*, 99-102.

76. Ovejas, V.; Fernandez-Fernandez, M.; Montero, R.; Castano, F.; Longarte, A. Ultrafast Nonradiative Relaxation Channels of Tryptophan. *J Phys Chem Lett* **2013,** *4*, 1928-32.

77. Müller, P.; Ignatz, E.; Kiontke, S.; Brettel, K.; Essen, L.-O. Sub-Nanosecond Tryptophan Radical Deprotonation Mediated by a Protein-Bound Water Cluster in Class Ii DNA Photolyases. *Chemical Science* **2018,** *9*, 1200-1212.

78. Reece, S. Y.; Nocera, D. G. Proton-Coupled Electron Transfer in Biology: Results from Synergistic Studies in Natural and Model Systems. *Annual Review of Biochemistry* **2009,** *78*, 673-699.

CHAPTER 6. ULTRAVIOLET RESONANCE RAMAN AND CIRCULAR DICHROISM STUDIES OF METALLO-PROTEIN INTERACTIONS IN HISTATIN-5, AN INTRINSICALLY DISORDERED SALIVARY PEPTIDE

McCaslin, T. G.; Pagba, C. V.; Yohannan, J.; Barry, B.A. Ultraviolet Resonance Raman and Circular Dichroism Studies of Metallo-Protein Interactions in Histatin-5, an Intrinsically Disordered Salivary Peptide. **In preparation**

6.1 Abstract

Intrinsically disordered proteins function as components of signaling networks and of the innate immune system. As an example, histatin-5 (Hst5) is an antimicrobial, salivary protein involved in the host defense system. Hst5 has been proposed to bind functionally relevant zinc and copper but presents challenges in structural studies due to its disordered conformation in aqueous solution. Here, we use circular dichroism (CD) and UV resonance Raman (UVRR) spectroscopy to define the interactions of copper and zinc with Hst5 in aqueous solution. When zinc is added to Hst5, the CD spectrum is altered and becomes resistant to thermal melting. This result is consistent with a zinc-induced increase in the concentration of stable conformers. The addition of zinc to Hst5 causes shifts of histidine Raman bands. Based on comparison to model compounds and to a family of designed, zinc-binding beta hairpins, the alterations in the Hst5 UVRR spectrum are attributed to zinc coordination by imidazole side chains. Zinc addition to Hst5 shifted a tyrosine aromatic ring UVRR band, consistent with an alteration in tyrosine pK_a due to an electrostatic interaction between tyrosine and bound zinc. The tyrosine and histidine band shifts are not observed with copper. The data suggest that the copper and zinc binding sites in Hst5 are distinct. To define the metal binding site in more detail, a sequence variant, H18A/H19A, was employed; this mutant, which still contains five histidine residues, has less potent antifungal activity, when compared to Hst5. The CD signal of this mutant was altered compared to wildtype, and zinc addition had a less pronounced effect on the thermal stability of the mutant. Interestingly, in this mutant, both zinc and copper addition shifted histidine UVRR bands in a manner diagnostic for metal coordination. However, results obtained with a K13E/R22G mutant were similar to those obtained with wildtype. These

experiments support the conclusion that H18 and H19 contribute to a zinc binding site in Hst5 and that coordination of zinc at this binding favors stable conformers. In the H18A/H19A mutant, low affinity zinc binding still occurs but the specificity of the copper/zinc binding sites is lost. The experiments implicate specific zinc binding to be important to the antimicrobial activity of Hst5.

6.2 Introduction

Intrinsically-disordered proteins (IDPs) play key roles in human health and disease ([1] and reviewed in [2-3]). IDPs are inherently difficult to study, because their dynamic conformational landscapes interconvert between different structures on a variety of timescales.[4-6] Histatins are a class of histidine-rich salivary peptides, which are important in the innate immune system and play an antimicrobial role (reviewed in [7]). These peptides are antimicrobial against various bacteria and fungi such as multi-drug-resistant *Staphlococcus aureus* (MRSA)[8], *Candida albicans*[9-10], *Cryptococcus neoformans*[11], and can regulate *Porphyroromonas gingivalis*, which is associated with periodontal disease[12]. Amongst the histatin family, the two primary sequences are histatin-1 and histatin-3 which are genetically encoded by *his1* and *his2*, respectively.[13] Histatin-5 is proposed to be a 24-amino acid proteolytic product of histatin-3.[13] Histatin-2 is likely derived from histatin-1, while histatin-4 through histatin-12 are likely fragments of histatin-3.[14] Histatin-1 has been shown to undergo post-translational modifications. Ser2 phosphorylation has been identified for histatin-1[15], and polysulfation of the terminal four tyrosines (Tyr27, 30, 34, and 36) of histatin-1 has been detected[16].

Within this family of peptides, histatin-5 (Hst5) has been proposed to bind functionally relevant Cu^{2+} and Zn^{2+}. Copper zinc binding sites are found in enzymes, such as superoxide dismutase (Figure 6.1A) and can consist of histidine side chains. (reviewed in [17]) Cu^{2+} binding by Hst5 has been proposed to occur to the amino terminus.[18] Copper has been proposed to provide oxidative activity and may be responsible for the antimicrobial properties of Hst5.[19] Nickel has been shown to bind to histatin-5, and may implicate histatin-5 in nickel allergies.[20] Zinc interactions have also been proposed to enhance antimicrobial activity.[21]

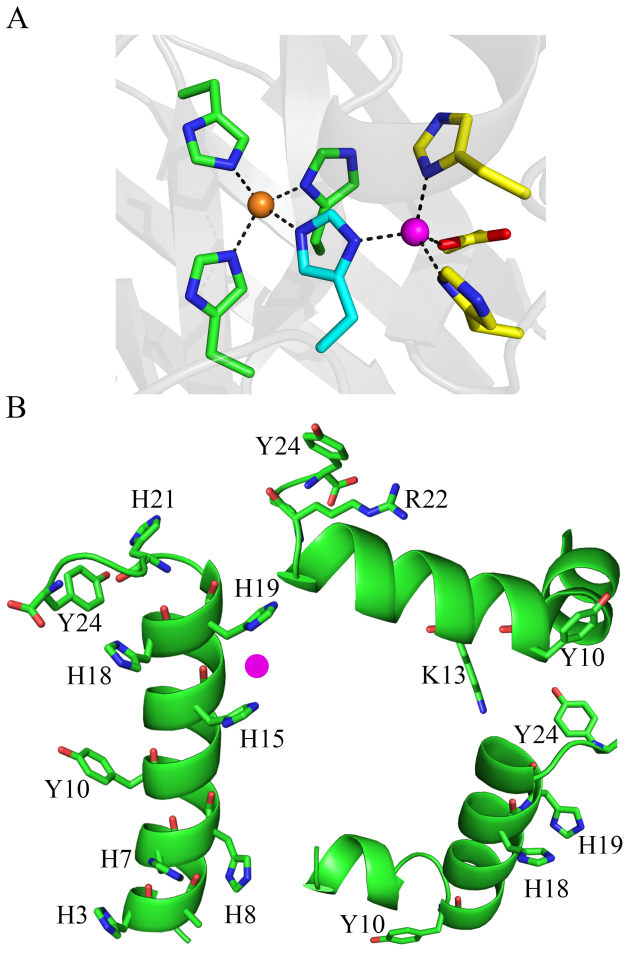

Figure 6.1 In (A), Copper/zinc coordination site in superoxide dismutase (SOD) (PDB, 2SOD).[22] Cu^{2+} (light brown sphere) is ligated by His44, His46, His61 and His118,

while Zn^{2+} (magenta sphere) is ligated by His61, His69, His78 and Asp81. His61 (blue residue) bridges Cu^{2+} and Zn^{2+} ions. In (B), speculative PEP-FOLD models of Hst5. Side chain labeling: left, all seven histidine and both tyrosine side chains are labeled; top, K13, R22, and both tyrosine residues; bottom right, H18, H19, and both tyrosines are labeled. The mutants, Hst5 K13E/R22G (top) and Hst5 H18A/H19A (bottom) are investigated here. A speculative binding site for Zn^{2+} ion is shown in pink.

In aqueous solution, the conformation of Hst5 is disordered. However in trifluoroethanol[23] or d_6-DMSO[24], Hst5 adopts a helical conformation. The functional and structural role of metal binding in salivary peptides needs clarification. In this work, circular dichroism (CD) and UV resonance Raman (UVRR) spectroscopic measurements are used to obtain new information concerning the structure and function of Hst5 and its interactions with zinc and copper. Two mutants of Hst5 are also studied, K13E/R22G and H18A/H19A. Compared to the wild type sequence of Hst5 (ED_{50} = 6-8 μM), Hst5 K13E/R22G has approximately 7-fold less potency (ED_{50} = 50 μM) as a candidacidal agent[10]. In the second mutant, Hst5 H18A/H19A, this sequence has approximately 20-fold less potency (ED_{50} = 150 μM) against *Candida*.[9]

The Hst5 spectroscopic results presented here are interpreted by comparison to amino acid model compounds in solution and to a family of conformationally dynamic beta hairpin models.[25-28] The beta hairpins contain two antiparallel beta strands connected by a turn motif. These peptides spontaneously fold in solution[25-26] and, in this work, have been engineered to contain a low affinity zinc binding site. Zinc interactions in proteins and peptides are particularly challenging to study because zinc is non-chromogenic and non-paramagnetic. Our experiments provide new information concerning metal interactions and structure and function in conformationally flexible proteins such as Hst5. This work shows

that a combination of spectroscopic techniques can identify low affinity metal-binding in intrinsically disordered peptides.

6.3 Materials and Methods

6.3.1 Materials

The 18-mer peptides, Peptides P, J, and J/F were synthesized by solid-state synthesis and were obtained from Genscript, USA, Inc (Piscataway, NJ) or New England Peptide (Gardner, MA). The sequences are: Peptide A, IMDRYRVRNGDRIHIRLR; Peptide P, IHDHYRVRNGDRIHHRHR; Peptide J, IDDHYRVRNGDRIHHRHR; Peptide J/F, IDDHFRVRNGDRIHHRHR. Histatin-5 (Hst5) and the two double mutants, K13E/R22G and H18A/H19A, were synthesized by solid-state synthesis and were obtained from Genscript, USA, Inc (Piscataway, NJ). The sequences are Hst5, DSHAKRHHGYKRKFHEKHHSHRGY; Hst5 K13E/R22G, DSHAKRHHGYKREFHEKHHSHGGY; Hst5 H18A/H19A, DSHAKRHHGYKRKFHEKAASHRGY. Mass spectrometry was used to verify the molecular weights of the peptides. The molecular weights matched the theoretical prediction from the sequence.

Peptide samples were suspended either in a H_2O or D_2O buffer containing 5 mM 2-[4-(2-hydroxyethyl)piperazin-1-yl]ethanesulfonic acid (HEPES), pH/pD 7.5, to give 1 mM solutions. Acetic acid (VWR, Radnor, PA)/sodium acetate (Thermo Fisher Scientific, Inc., Waltham, MA) and sodium borate (Mallinckrodt, Paris, KY)/NaOD were used to make buffers at pD 5 and pD 11, respectively. The pH/pD was adjusted using NaOH or NaOD. HEPES, histidine, and tyrosine were purchased from Sigma-Aldrich (St. Louis,

MO), and D_2O and NaOD were purchased from Cambridge Isotopes (Tewksbury, MA, 99.9% D). The pD is reported as the uncorrected meter reading, because the small solvent isotope shift effects on weak acid pK_a values are compensated by the D_2O-induced change in response of the glass pH electrode[29]. In some experiments, $ZnCl_2$ (Alfa Aesar, Tewksbury, MA), $CuCl_2$ (Alfa Aesar, Tewksbury, MA), $MnCl_2$ (ICN Biomedicals, Aurora, OH), $CaCl_2$ (EMD Millipore, Billerica, MA) were used in buffered solutions.

6.3.2 UV-Vis Absorbance Spectroscopy

UV-Vis absorption spectra were recorded on a Shimadzu UV 1700 spectrometer. The slit width was 1 nm, the resolution was 1 nm, and the scan speed was 6.5 nm/s. The peptide concentration was 500 μM. The zinc concentration ranged from 500 μM (1:1 Peptide to Zn ratio) to 4 mM (1:8 Peptide to Zn ratio). The buffer contained 5 mM HEPES, pH 7.5 or pD 7.5. The spectra were averaged from two independent measurements.

6.3.3 Circular Dichroism (CD) Spectroscopy

A Jasco J-810 CD spectropolarimeter equipped with a Peltier-type cell was employed. Spectra were collected from 250 nm to 193 nm in 1 mm quartz cells. Eight accumulations per scan were averaged in three to nine independent measurements for each of the conditions. Parameters used were: sensitivity, 100 mdeg; data pitch, 2 nm; scan speed, 50 nm/min; response time, 1 s; bandwidth, 1 nm.

6.3.4 UV-Resonance Raman (UVRR) Spectroscopy

The spectra were obtained at room temperature using a 244 nm (3.4 to 3.7 mW) probe beam.[27, 30] The probe beam was generated from an intracavity frequency-doubled Argon

ion laser (Cambridge LEXEL 95, Fremont, CA) and was coupled to a Raman microscope system (Renishaw inVia, Hoffman Estates, IL) equipped with UV-coated, deep depletion charge-coupled device. The spectral resolution was 6 cm^{-1} and the separation between the data points was 3.8 cm^{-1}. The peak positions are reported to a precision of ±2 cm^{-1}. Peptide samples (1 mL) were recirculated using a peristaltic pump through a nozzle (~120 μm inner diameter) to prevent sample damage due to UV irradiation. The flow rate was 4.5 ml/min, and the pump was plumbed with silicone tubing. The spectra were averaged from at least two independent measurements.

6.4 Results

6.4.1 UV-Vis and CD Spectroscopy

Hst5 was synthesized by solid state synthesis (Figure 6.2A). Though Hst5 is intrinsically disordered, PEP-FOLD[31] models of the wild type sequence were generated and are shown as speculative examples in Figure 6.1B. Three different models are shown and display amino acid side chains of relevance to this study, namely Tyr10, Tyr24, His3, His7, His8, His15, His18, His19, His21, Lys13, and Arg22.

A. Histatin-5 (Hst5)

DSHAKRHHGYKRKFHEKHHSHRGY

B. Peptide J

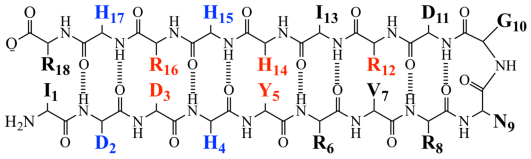

C. Peptide P

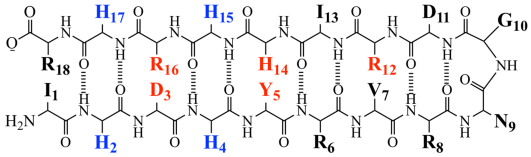

D. Peptide J/F

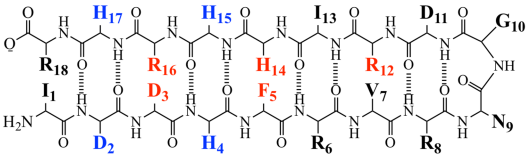

Figure 6.2 Sequences of Hst5 (A), Peptide J (B), Peptide P (C), and Peptide J/F (D). In (A), red denotes K13E/R22G mutation sites and blue denotes H18A/H19A mutation sites. In (B-D), blue denotes metal-binding residues and red denotes possible non-covalent interactions with Tyr5.

Hst5 contains an amino terminal copper and nickel binding motif as well as a proposed binding site for zinc (HEXXH).[7] The peptide contains two tyrosines and seven histidines, and shows absorbance in the UV region of the spectrum (Figure 6.3A, solid line). The addition of Zn^{2+} (Figure 6.3B), Cu^{2+} (Figure 6.3C) or a mixture of Zn^{2+} and Cu^{2+} (Figure 6.3D) alter the spectrum of Hst5.

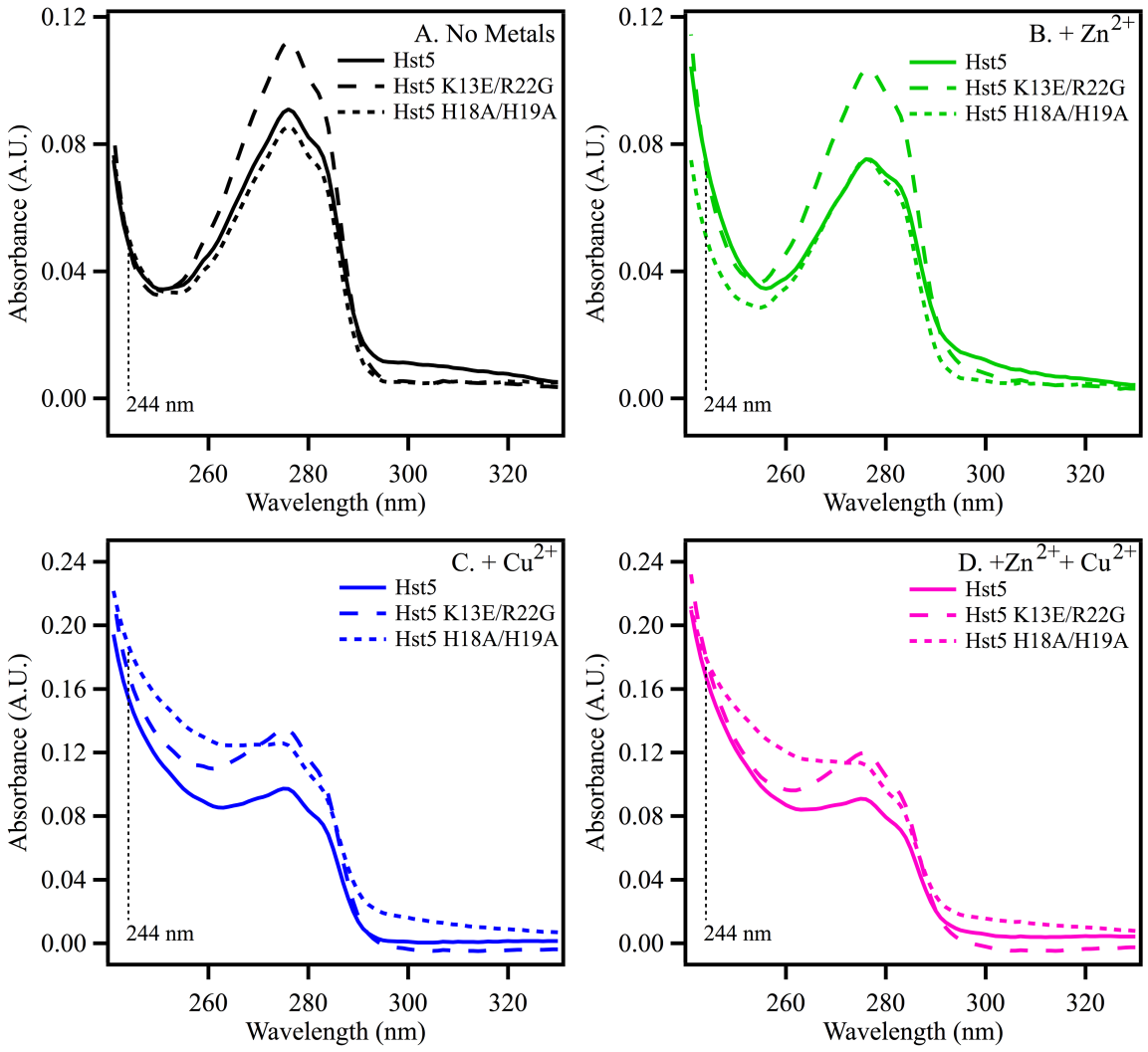

Figure 6.3 UV absorption spectra of Hst5 and mutants. In (A), Hst5 (solid line), Hst5 K13E/R22G (dashed line), and Hst5 H18A/H19A (dotted line) in the absence of added metals (black). In (B), Hst5 (solid line), Hst5 K13E/R22G (dashed line), and Hst5 H18A/H19A (dotted line) in the presence of equimolar Zn^{2+} (green). In (C), Hst5 (solid line), Hst5 K13E/R22G (dashed line), and Hst5 H18A/H19A (dotted line) in the presence of equimolar Cu^{2+}(blue). In (D), Hst5 (solid line), Hst5 K13E/R22G (dashed line), and Hst5 H18A/H19A (dotted line) in the presence of equimolar Zn^{2+} and Cu^{2+}. The peptide concentration was 50 μM, and the buffer contained 5 mM HEPES pH 7.5 and 50 μM $ZnCl_2$ and/or $CuCl_2$ where noted and the metal- or non-metal-containing buffers were used in a reference cell during spectrum acquisition. Spectra are an average of three measurements; resolution, 1 nm; tick marks denote 0.04 absorbance units.

The peptide was characterized by CD experiments and thermal melting. In Figure 6.4A (solid line), the pre-melt spectrum at 20 ^{o}C (solid line) of Hst5 shows two features: a band of negative ellipticity at 198 nm and a broad positive feature at approximately 220 nm. With heating to 80 °C, these features are lost (Figure 6.4A, dot-dashed line), but regained after cooling (Figure 6.4A, dashed line). The addition of zinc in a 1:1 ratio is associated with as less significant change with heating and cooling (Figure 6.4B). Such an effect can be associated with zinc driven stabilization of peptide conformation. These results are similar to previous CD experiments reported[32] such that the binding of zinc decreases the magnitude of ellipticity of Hst5 at approximately 198 nm; however, the results presented here do not reproduce the increase in magnitude of ellipticity of the band centered at approximately 220 nm reported previously[32].

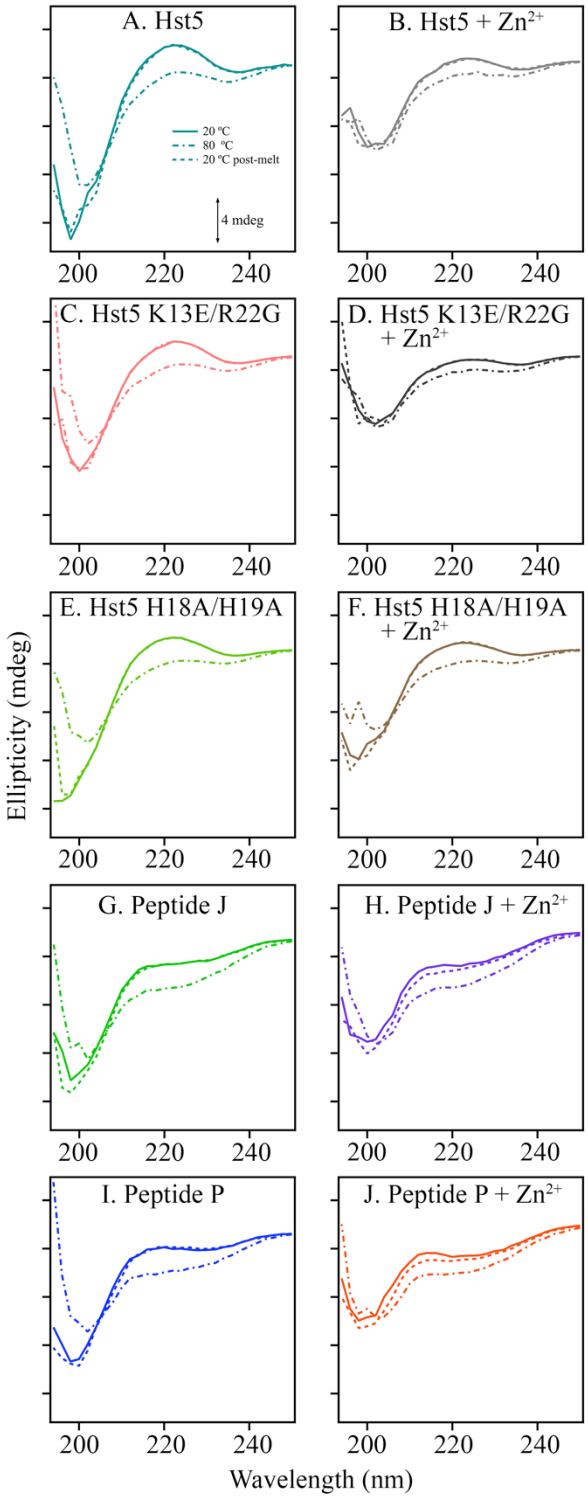

Figure 6.4 CD spectra of peptides in the absence (left) or presence of (right) Zn^{2+}. Samples are Hst5 (A, teal), Hst5 + Zn^{2+} (B, grey), Hst5 K13E/R22G (C, peach), Hst5 K13ER22G + Zn^{2+} (D, black), Hst5 H18A/H19A (E, light green), Hst5 H18A/H19A + Zn^{2+} (F, brown), Peptide J (G, green), Peptide J + Zn^{2+} (H, purple), Peptide P (I, blue),

and Peptide P + Zn^{2+} (J, orange). Spectra were acquired at 20 °C (solid trace), then the samples were melted in the Peltier cell at 80 °C (dot-dashed trace), and subsequently cooled back to 20 °C (dashed trace). Tick marks denote 4 mdeg. Spectra were averaged from three to nine replicates. The peptide concentration was 100 μM, and equimolar $ZnCl_2$ was added where noted. The buffer contained 5 mM HEPES pH 7.5.

To interpret these results, a metal binding site was engineered into a family of beta hairpin peptides. The original peptide, Peptide A, is known to be a beta hairpin from NMR spectroscopy.[25] This peptide contains a tyrosine-histidine pair, which conducts a proton coupled electron transfer reaction when tyrosine is oxidized in the mid pH range.[25-26] As discussed above (Figure 6.1A), zinc binding sites in proteins can be composed of histidine and carboxylate groups.[33] Therefore, three types of zinc binding sites were engineered into Peptide A. The first, giving Peptide P, contains a four histidine motif (H2, H4, H15, and H17) (Figure 6.2C). The UV spectrum of Peptide P is shown in Figure 6.5C (pH 7.5) and S1D (pD 7.5) and represents the contributions of five histidines and Y5. Difference spectra of Peptide P with varying ratios of peptide to metal were generated (Figure 6.6A and 6.6C) and exhibit a red-shifted UV absorption as Zn^{2+} concentration increases (Figure 6.6B and 6.6D). The CD spectrum of Peptide P in the absence of zinc exhibits negative ellipticity at 198 nm (Figure 6.4I, solid). This band is lost with heating and regained by cooling (Figure 6.4I, dot-dashed and dashed). In the presence of zinc (1:1 stoichiometry), the CD spectrum of Peptide P is reduced in amplitude and exhibits only a modest change with an increase in temperature (Figure 6.4J). This is consistent with stabilization of peptide structure by the divalent metal ion. Overall, the CD results obtained with Peptide P are similar to the behavior observed in Hst5.

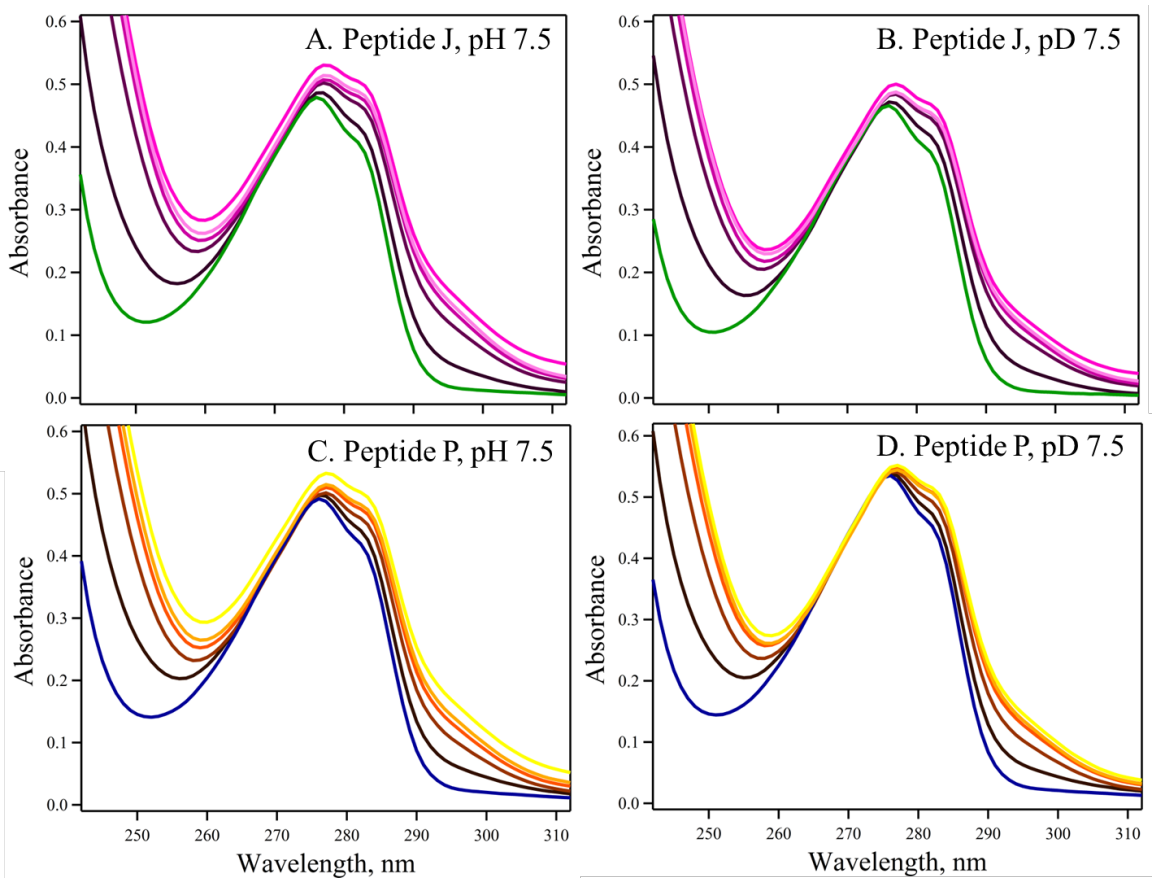

Figure 6.5 UV absorption spectra of Peptide J (A and B) and Peptide P (C and D) with increasing concentrations of Zn^{2+} (500 µM, dark purple and dark brown; 1mM, purple and brown; 2 mM, light purple and orange, 3 mM, pink and light orange; 4 mM, light pink and yellow) at pH 7.5 (A and C) and pD 7.5 (B and D). The analyte concentration was 500 µM. The buffer contained 5 mM HEPES. The spectra were averaged from two independent measurements.

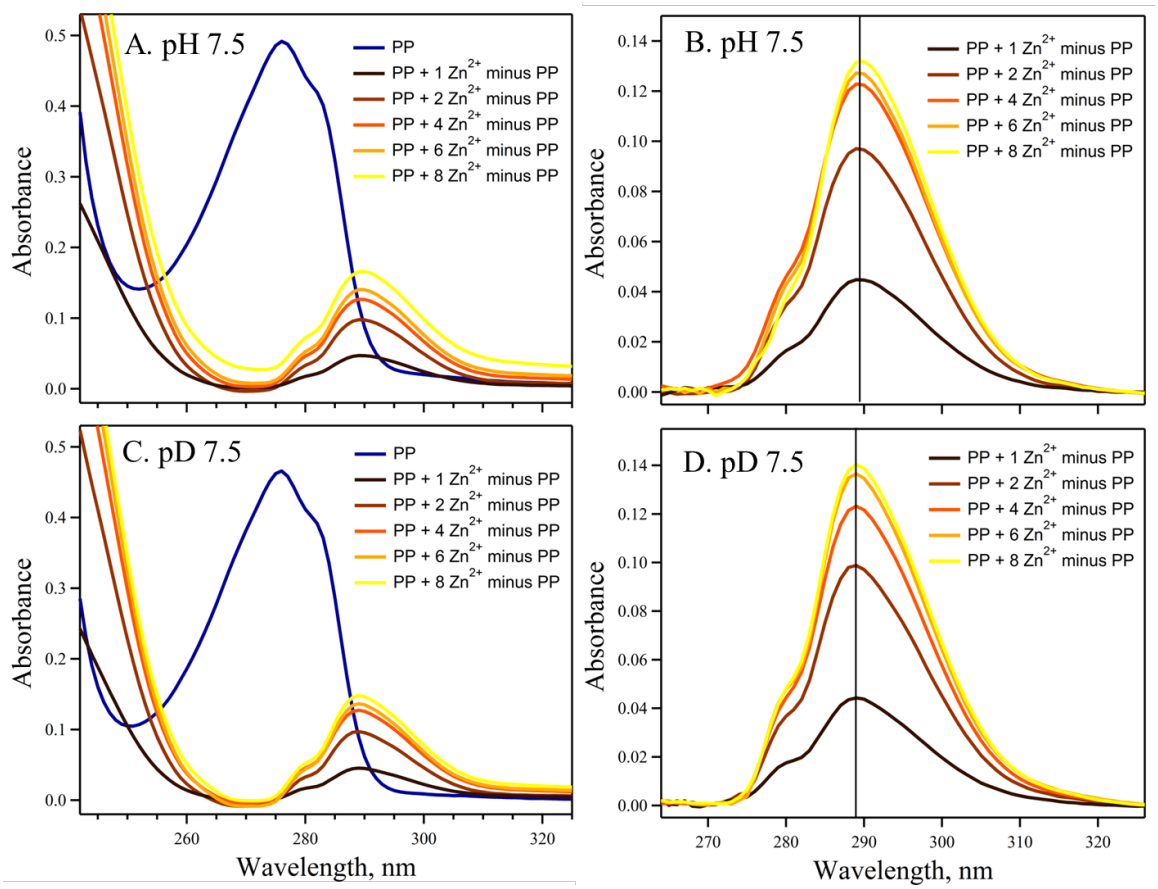

Figure 6.6 UV absorption spectra of Peptide P (A and C) (green) and difference absorption spectra obtained by subtracting Peptide P spectrum from that of Peptide P and Zn^{2+} solution with variation in the Peptide:Zn^{2+} stoichiometry ratios, 1:1 (dark brown), 1:2 (brown), 1:4 (orange) and 1:6 (light orange), 1:8 (yellow). The difference spectra (baseline corrected) are expanded in panels B and D. The measurements were performed at pH 7.5 (A and B) and pD 7.5 (C and D). The peptide concentration was 500 µM. The buffer contained 5 mM HEPES. The spectra were averaged from two independent measurements.

Two additional metal binding peptides were characterized with UV absorbance and CD spectroscopy. In Peptide J, the putative metal binding site contains three histidines (H4, H15, H17), with the fourth position occupied by an aspartate (D2) (Figure 6.2B). In Peptide J/F, a three-histidine-aspartate binding site is retained (Figure 6.2D), but the tyrosine at position 5 is replaced with phenylalanine, which cannot coordinate metals. UV absorbance spectra of Peptide J are presented in Figure 6.5A and 6.5B and difference

spectra with varying ratios of peptide to metal are shown at pH 7.5 (Figure 6.7A) and pD 7.5 (Figure 6.7C). Again, addition of metal causes a red shift of the Peptide J UV spectrum (Figure 6.7B and 6.7D), similar to the response observed in Peptide P (Figure 6.6B and 6.6D). CD data derived from Peptide J/F (data not shown) and Peptide J (Figure 6.4G and 6.4H solid line) exhibit similar behavior when compared to Hst5 and Peptide P. Note that control CD experiments were performed with Peptide A (Figure 6.8) and there was no significant effect of zinc on the stability of this beta hairpin, which does not contain a metal binding site. In addition, Peptide P and J samples were frozen, thawed, and filtered before some of the measurements (data not shown). No change was observed. The results support the conclusion that a soluble form of each peptide is interacting with zinc, not an aggregated oligomeric form.

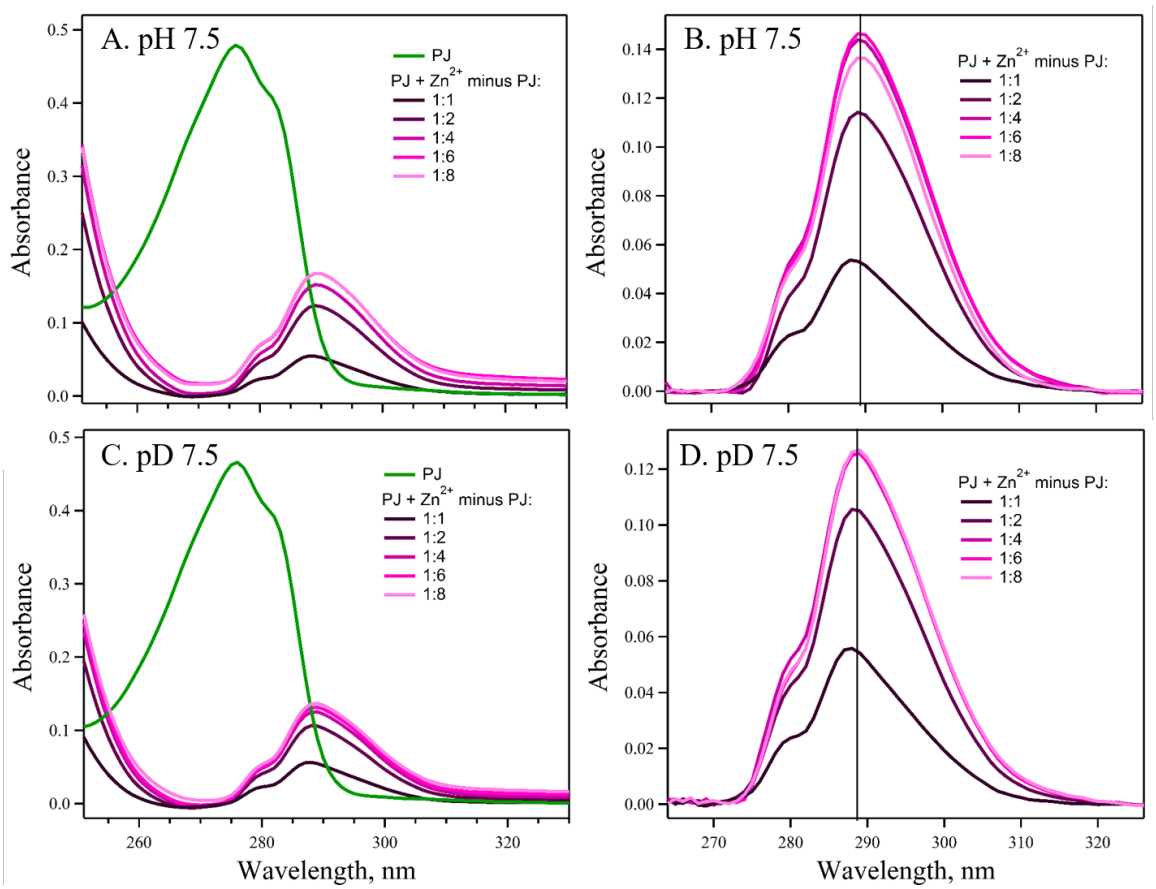

Figure 6.7 UV absorption and difference spectra of Peptide J (green) at pH 7.5 (A) and pD 7.5 (C). Difference spectra, showing the effects of zinc addition, were obtained by subtracting the Peptide J spectrum from that of a Peptide J and Zn^{2+} mixture (A, pH 7.5 and C, pD 7.5). The ratios were 1: 1 (dark purple), 1:2 (purple), 1:4 (light purple), and 1:6 (pink), 1:8 (light pink). The difference spectra are expanded in panels B and D. The analyte concentration was 500 µM, and the buffer contained 5 mM HEPES, pL 7.5. The spectra were averaged from two independent measurements.

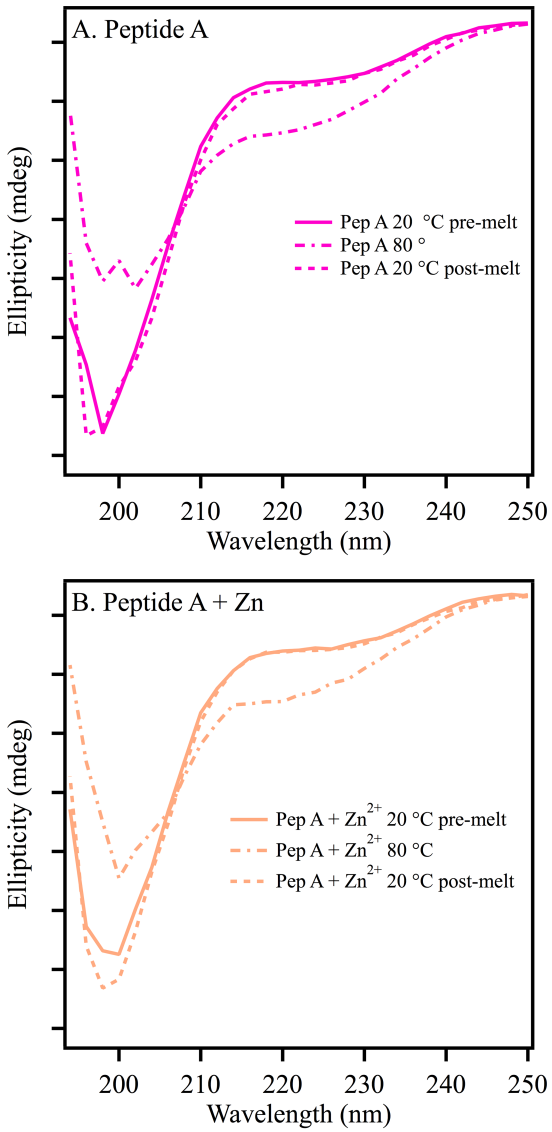

Figure 6.8 CD spectra of Peptide A (A) and Peptide A and Zn^{2+} (B). Spectra were acquired at 20 °C (solid trace), then the samples were melted in the Peltier cell at 80 °C (dot-dashed trace), and subsequently cooled back to 20 °C (dashed trace). Tick marks denote 4 mdeg. Spectra were averaged from three replicates. The peptide concentration was 100 μM, and equimolar $ZnCl_2$ was added where noted. The buffer contained 5 mM HEPES pH 7.5.

Two mutants of Hst5 were selected for characterization: K13E/R22G and H18A/H19A (Figure 6.1B and Figure 6.2A, red and blue). These mutants have been shown to exhibit less potent antimicrobial activity [9-10], when compared to wildtype. The UV

spectrum of the mutants in shown in Figure 6.3. Note the small change in extinction coefficient at 280 nm in the K13E/R22G mutant (Figure 6.3, dashed line), which is most likely associated with an electrostatic perturbation to the environment of one or more of the tyrosines. The spectrum of the aromatic ring is known to be sensitive to protonation state and exhibits a red shift when the phenol form is converted to phenolate.[27, 34] The CD spectra of the K13E/R22G mutant (Figure 6.4C, solid line) are similar to wild type Hst5; the addition of zinc causes a change in the spectrum consistent with an overall increase in stability (Figure 6.4D, solid line). However, in the H18A/H19A mutant (Figure 6.4E, solid line), zinc addition has a less significant effect on the CD spectrum (Figure 6.4F, solid line), particularly in the thermal melt (Figure 6.4E and 6.4F, dot-dashed line). This result implies that the overall affinity for Zn^{2+} binding is reduced in the H18A/H19A mutant. Note that the change in the CD signal in the histidine mutant in the absence of zinc is consistent with an alteration in the average conformation in solution.

6.4.2 UVRR Spectroscopy of Hst5 and variants

As a more detailed probe of zinc peptide interactions, UV resonance Raman spectroscopy was employed. In particular, a 244 nm probe in D_2O buffer allows specific interactions with histidine and tyrosine side chains to be observed because the bands are resonantly enhanced. The UV spectrum of Hst5 (Figure 6.3, solid line) shows significant absorption at 244 nm. A microcell recirculating device is used to prevent UV damage to the sample.[27, 30] Previous work has shown that the use of D_2O enhances the vibrational contributions of histidine in the UVRR spectrum [35-36]. Note that the pD is reported here as the uncorrected pH meter reading, according to a standard protocol.[29] The UVRR spectrum of Hst5 in D_2O solution is presented in Figure 6.9IA and 6.9IIA and exhibits bands at 1315

cm^{-1}, 1334 cm^{-1}, 1371 cm^{-1}, and 1565 cm^{-1}, which are candidates for assignment to the histidine side chain. Bands at 1176 cm^{-1}, 1210 cm^{-1}, and 1612 cm^{-1} are candidates to be assigned to tyrosine.

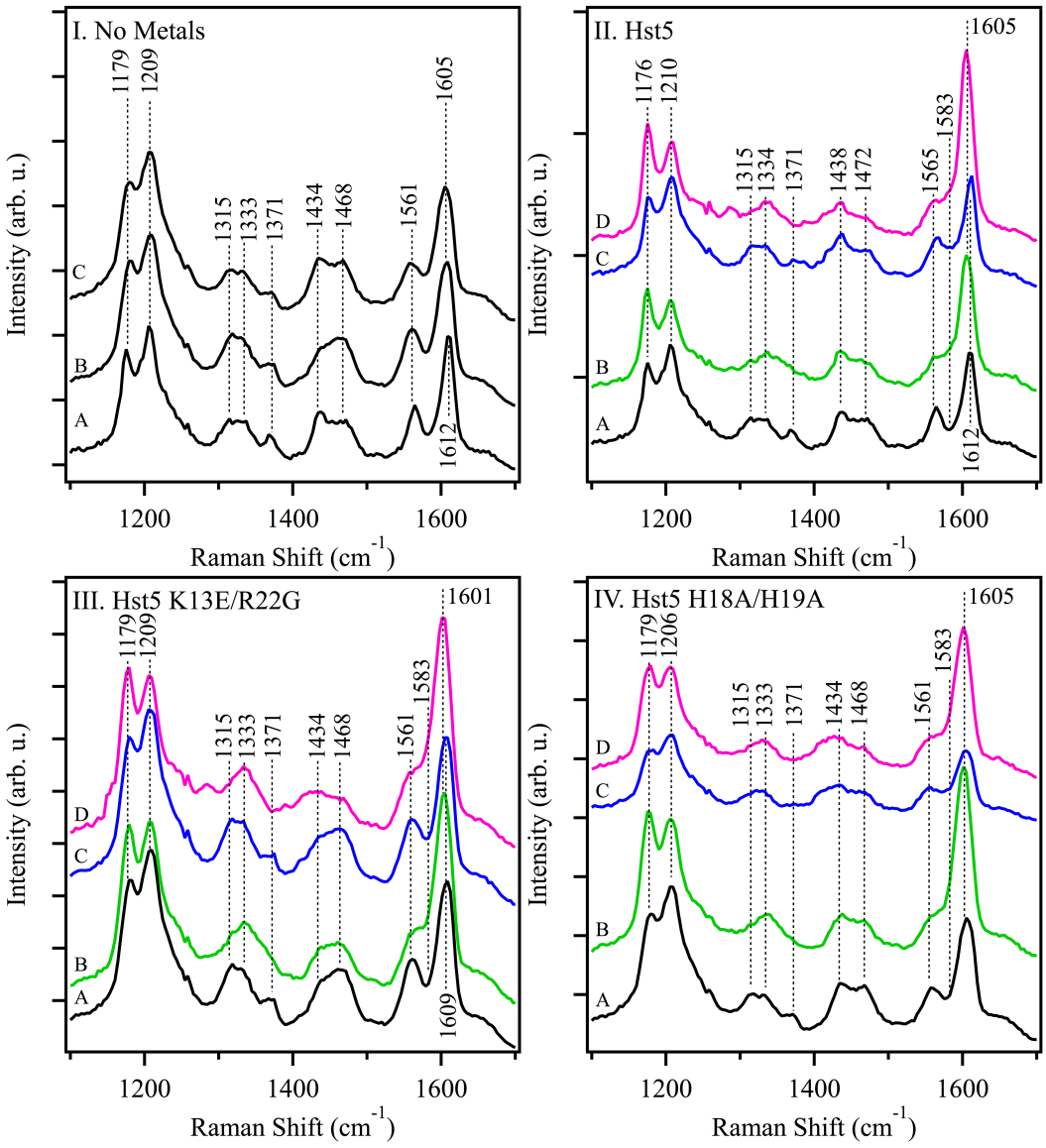

Figure 6.9 UVRR spectra of Histatin-5 (Hst5) and mutants K13E/R22G and H18A/H19A in the presence or absence of Zn^{2+} and Cu^{2+}. In (I), wild type Hst5 (A), Hst5 K13E/R22G (B) and Hst5 H18A/H19A (C) in the absence of added metals. In (II), Hst5 in the absence of added metals (A, black), presence of Zn^{2+} (B, green), Cu^{2+} (C, blue), or Zn^{2+} and Cu^{2+} (D, pink). In (III), Hst5 K13E/R22G in the absence of added metals (A, black), presence of Zn^{2+} (B, green), Cu^{2+} (C, blue), or Zn^{2+} and Cu^{2+}

(D, pink). In (IV), Hst5 H18A/H19A in the absence of added metals (A, black), presence of Zn^{2+} (B, green), Cu^{2+} (C, blue), or Zn^{2+} and Cu^{2+} (D, pink). The peptide concentration was 1 mM, and the samples contained equimolar $ZnCl_2$ and/or $CuCl_2$ where noted. The buffer contained 5 mM HEPES pD 7.5. The sample was recirculated using a peristaltic pump to prevent UV damage. Laser wavelength, 244 nm; laser power, 3.7 mW; scan time, 120 s; accumulations, 4. Data were averaged from two independent measurements (using two 1 mL samples) and normalized to the intensity of the amide II' band at ~1434 cm^{-1}. Tick marks denote 1000 intensity units.

To support these assignments, model compound data were acquired from histidine in D_2O solution as a function of pD (Figure 6.10). At pD 5 (Figure 6.10A), histidine is cationic, with a protonated imidazolium cation side chain, a protonated amino terminus, and an anionic carboxylate at the carboxyl terminus. At pD 7.5 (Figure 6.10B), histidine is zwitterionic with an unprotonated imidazole side chain. At pD 11 (Figure 6.10C), histidine is anionic, with a deprotonated amino and imidazole group, and negative charge remaining on the carboxyl terminus. In D_2O, the spectrum of the protonated imidazolium cation (pD 5) exhibits bands at 1408 and 1601 cm^{-1}, while the spectrum of the deprotonated imidazole side chain exhibits new bands at 1317, 1370, 1479, and 1564 cm^{-1}. These data are similar to results reported previously [35-36]. The normal mode assignments of the bands are: 1166 cm^{-1} in-plane ring modes mixing with N_1-H,[37] 1323 cm^{-1} and 1351 cm^{-1} in-plane ring modes,[37] 1457 cm^{-1} ring N_1-H,[37] 1484 cm^{-1} N-H in-plane bend of the protonated imidazole side chain,[38], 1568 cm^{-1} C=C stretching mode of the neutral imidazole sidechain in one tautomer,[38] 1577 cm^{-1} mixture of the in-plane ring mode with the N_1-H,[37] 1585 cm^{-1} C=C stretch of the ring in one tautomer of histidine,[38] 1573-1588 cm^{-1} C_4=C_5 stretch when N_p coordinates a metal,[39] and 1594-1606 cm^{-1} C_4=C_5 stretch when N_t coordinates a metal[39].

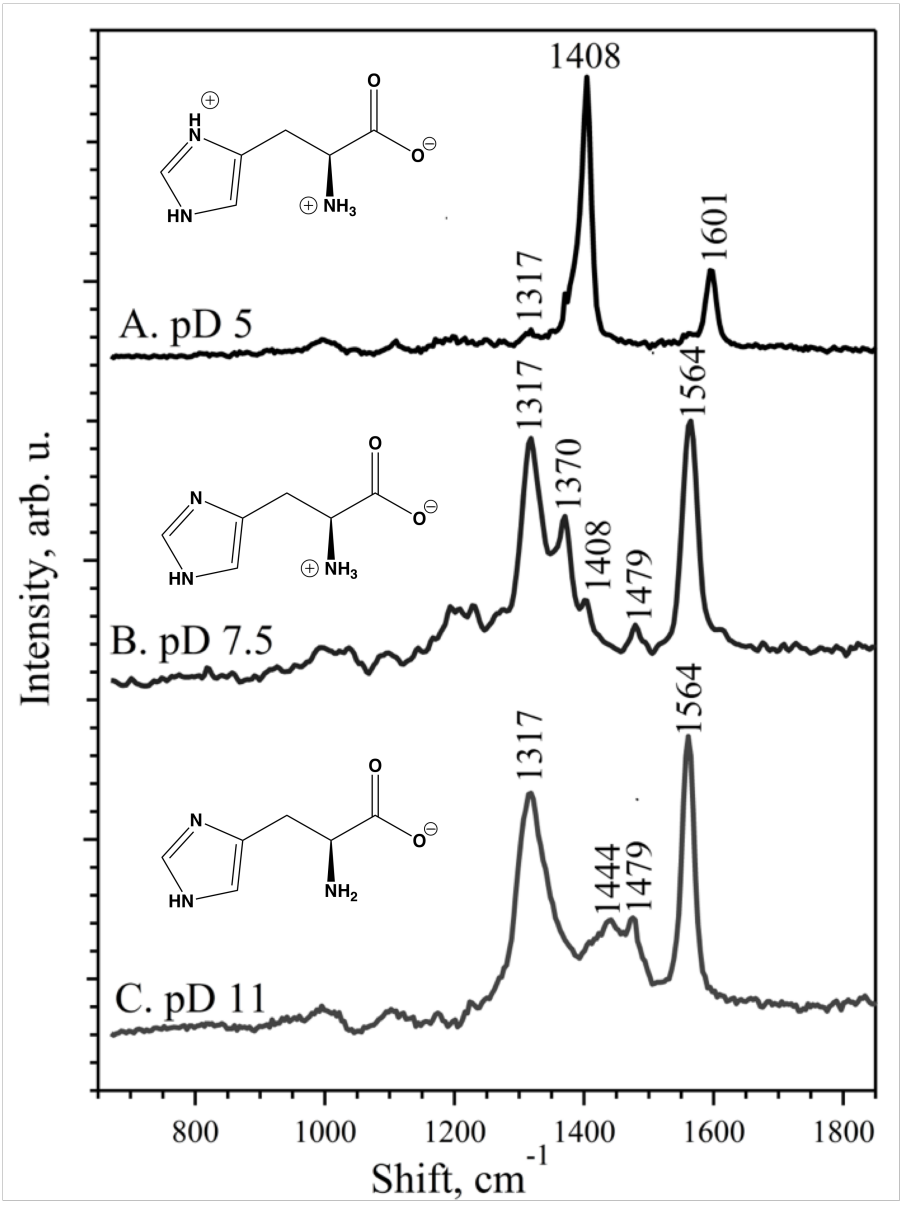

Figure 6.10 UV Raman spectra of 5 mM Histidine at (A.) pD 5, (B.) pD 7.5 and (C.) pD 11 The buffer contained 5 mM of acetate (pD 5), HEPES (pD 7.5) and Borate (pD 11). The spectra are normalized with respect to most intense peak for each sample. Each tick mark is 0.1 unit.

Characteristic bands of tyrosine are also observed in the Hst5 spectrum (Figure 6.9IA and 6.9IIA) arising from Y10 and Y24. These bands include 848 (not shown), 1176, 1210, and 1612 cm^{-1}. To support the assignment to tyrosine, UVRR spectra were acquired from tyrosine and tyrosinate in H_2O and D_2O buffers (Figure 6.11). At pH/pD 8.5 (Figure 6.11A

and 6.11B), the compound has a protonated phenolic ring, while at pH/pD 11 the aromatic ring is deprotonated (Figure 6.11C and 6.11D). The contributions from the tyrosine and tyrosinate ring are resonantly enhanced at 244 nm. The highest energy ring stretching mode, Y8a, of the deprotonated phenolate is observed at 1602 cm^{-1} and is insensitive to the addition of D_2O. Other characteristic bands are also D_2O insensitive and are observed at 845, 1174, and 1207 cm^{-1}.[34, 40] At pH/pD 8.5, when the phenol ring is protonated, Y8a is observed at 1614 cm^{-1} in H_2O and downshifts to 1610 cm^{-1} in D_2O. In summary, model compound studies of tyrosine and histidine in solution support assignment of the Hst5 spectrum to vibrational contributions of the phenol/phenolate and imidazole side chains.

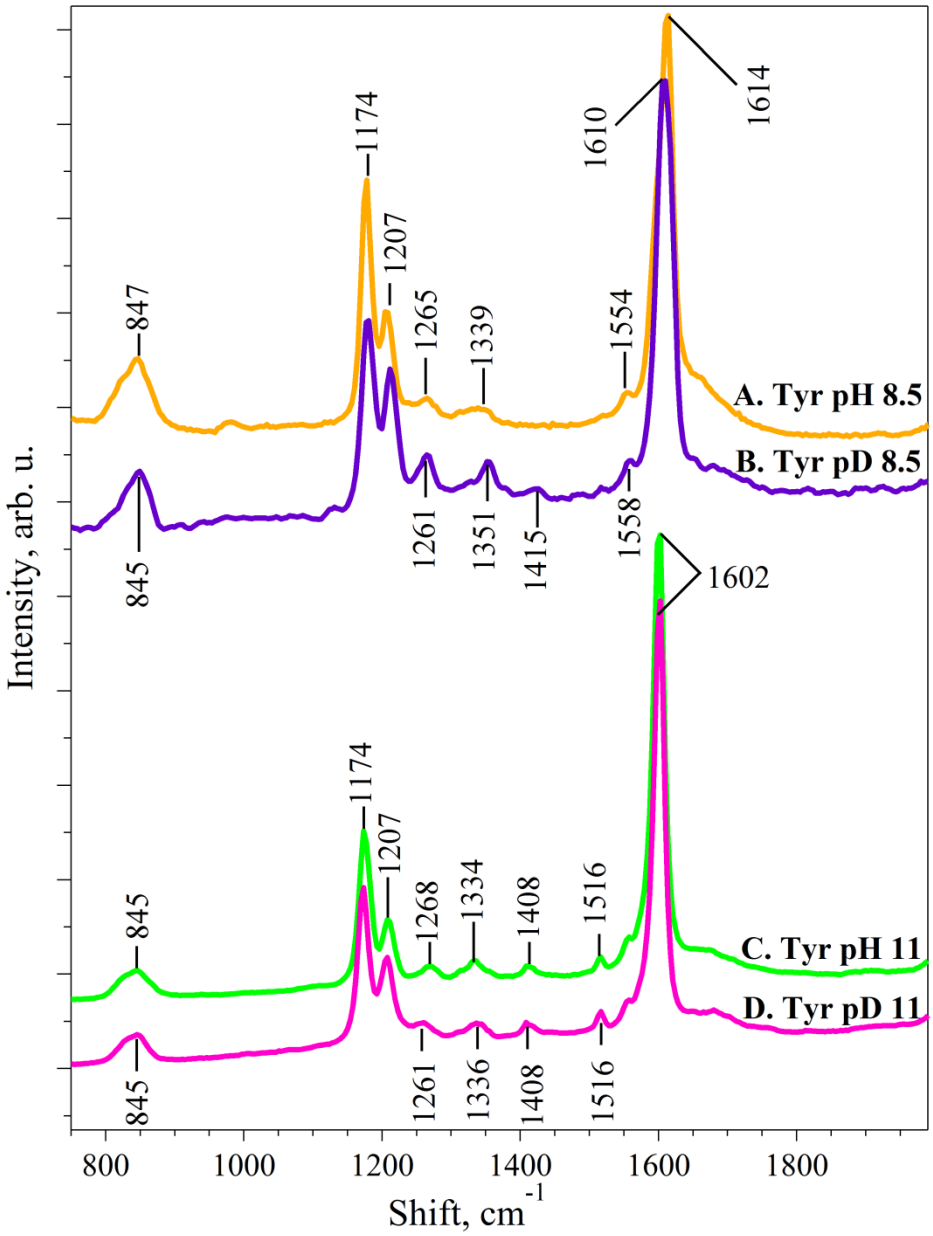

Figure 6.11 UV Raman spectra of 1 mM tyrosine at (A.) pH 8.5, (B.) pD 8.5, (C.) pH 11 and (D.) pD 11. The spectra are normalized with respect to the most intense peak. Each tick mark is 0.05 unit. The buffer contained 5 mM of TAPS (pL 8.5) or 5 mM borate (pL 11).

The UVRR spectra of the Hst5 mutants, K13E/R22G (Figure 6.9IB and 6.9IIIA) and H18A/H19A (Figure 6.9IC and 6.9IVA), were obtained. The UV spectrum (Figure 6.3) reveals that the extinction coefficient at 244 nm is approximately 1000 L mol^{-1} cm^{-1} which

is consistent with similar resonance enhancement factor in each sample. It has been shown that the enhancement factors for imidazole bound to copper are similar to the unbound state.[37] A band at 1440 cm^{-1} is observed in each spectrum. In D_2O buffer, this band arises from amide II' (C-N stretch) and is expected to be invariant to the mutation.[27] Accordingly, the intensity of this band was used to normalize the spectra for comparison. After normalization, the spectrum of the K13E/R22G mutant is similar to that of wild type. In particular, the histidine and tyrosine bands have similar intensities and frequencies. On the other hand, the spectrum of the H18A/H19A mutant is distinguishable in the relative intensity of amide II' to the 1313, 1371, and 1561 cm^{-1} bands, which arise from imidazole (Table 6.1B). The H18A/H19A mutant also exhibits a 7 cm^{-1} shift of the Y8a tyrosine band, while a smaller and possibly not significant change is observed in the K13E/R22G mutant. The shift is due to a pK_a shift when the imidazole ring is changed to alanine. This change is accompanied by alterations in the 1179 and 1210 cm^{-1} bands, suggestive of hydrogen bonding and conformational changes.[34, 40]

Table 6.1 Vibrational bands of aromatic amino acids and comparison to model compounds, peptides and proteins

A. Tyrosine

Sample	**CH bend (Y9a) (cm^{-1})**	**Ring C-CH2 (Y7a) (cm^{-1})**	**Ring (Y8a) (cm^{-1})**
Hst5	1176	1210	1612
Hst5 + Zn	1176	1210	1605
Hst5 + Cu	1176	1210	1612
Hst5 + Zn + Cu	1176	1210	1605
Hst5 K13E/R22G	1179	1209	1609

Table 6.1 continued

Hst5	1179	1209	1601
K13E/R22G +			
Zn			
Hst5	1179	1209	1609
K13E/R22G +			
Cu			
Hst5	1179	1209	1601
K13E/R22G +			
Zn + Cu			
Hst5	1179	1206	1605
H18A/H19A			
Hst5	1179	1206	1605
H18A/H19A +			
Zn			

Table 6.1 continued

Hst5 H18A/H19A + Cu	1179	1206	1605
Hst5 H18A/H19A + Zn + Cu	1179	1206	1605
Peptide P	1177	1207	1612
Peptide P + Zn	1177	1207	1604
Peptide J	1177	1207	1612
Peptide J + Zn	1177	1207	1604
Cu/Zn SOD (240 nm, pD 9)[41]	1177	1206	1616

Table 6.1 continued

B. Histidine

Sample	**~1315 cm^{-1}**	**~1335 cm^{-1}**	**~1370 cm^{-1}**	**~1390 cm^{-1}**	**~1565 cm^{-1}**	**~1580 cm^{-1}**
Hst5	1315	1334	1371		1565	
Hst5 + Zn		1334			1565	1583
Hst5 + Cu	1315	1334	1371		1565	
Hst5 + Zn + Cu		1334			1565	1583
Hst5 K13E/R22G	1315	1333	1371		1561	

Table 6.1 continued

Hst5 K13E/R22G + Zn		1333		1561	1583
Hst5 K13E/R22G + Cu	1315	1333	1371	1561	
Hst5 K13E/R22G + Zn + Cu		1333		1561	1583
Hst5 H18A/H19A	1315	1333	1371	1561	
Hst5 H18A/H19A + Zn		1333		1561	1583

Table 6.1 continued

Hst5 H18A/H19A + Cu		1333			1561	
Hst5 H18A/H19A + Zn + Cu		1333			1561	1583
Peptide P	1317	1336	1370		1564	
Peptide P + Zn		1336		1388	1564	1583
Peptide J	1317	1336	1370		1564	
Peptide J + Zn		1336		1388	1564	1583
Cu/Zn SOD [42]	1320 (est., pD 9, 229 nm ex.)	1340 (est., pD 9, 229 nm ex.)	1360 (His-Zn, pD 9, 229 nm ex.)	1396 (His-Zn, pD 9, 229 nm ex.)	1564 (His-M, His61, pD 7.3, 229 ex.)	1580 (sh, est., pD 7.3, 229 ex.)

1352 cm^{-1} = N_{τ}-Ligated His (Cu(II)- βAlaHis)[41]

6.4.3 Effects of Metal Addition on the UVRR Spectrum

The effects of copper and zinc on the Hst5 UVRR spectrum were evaluated. From previous studies of superoxide dismutase and 27-mer zinc finger peptide, the expectation is that ligating histidine bands will shift in frequency (Figure 6.1A and refs [35, 39, 43-44]) with metal coordination. Upon addition of Zn^{2+} (Figure 6.9IIB) to the wildtype Hst5 sample, the 1315 cm^{-1} band undergoes an upshift to 1334 cm^{-} , and the 1371 cm^{-1} band is decreased in intensity. Additionally, the 1565 cm^{-1} band is reduced in intensity, and a zinc-induced shoulder is present at 1583 cm^{-1}. Upon addition of Cu^{2+} (Figure 6.9IIC), the spectral features are unaltered compared to the control (Figure 6.9IIA), indicating that histidine does not provide coordination to copper in the wildtype. Upon addition of both Zn^{2+} and Cu^{2+} (Figure 6.9IID), the spectral changes are similar to those observed with zinc alone. The results are consistent with coordination of zinc at a binding site that contains histidine. Interactions with copper are deduced to occur at a distinct, non-imidazole binding site. Shifts of the tyrosine Y8a band, from 1612 to 1605 cm^{-1} are also observed with zinc addition. These are attributed to electrostatic interactions. Note that while the UV spectrum is not significantly altered by zinc addition (Figure 6.3B), the spectrum is sensitive to the addition of copper (Figure 6.3C and 6.3D). A similar set of zinc and copper induced changes are observed in the K13E/R22G mutant, indicating that the metal binding sites are relatively unchanged in this mutant. However, the H18A/H19A mutant shows a different pattern of spectral changes. Addition of zinc shifts imidazole bands, as observed in wildtype, but this effect is no longer specific to zinc. Notably, in the mutant, copper and zinc have a similar effect on the spectrum. These results are attributed to loss of metal binding specificity in the H18A/H19A mutant.

6.4.4 Modelling the Conformationally Dynamic Site, Metal Addition to Beta Hairpin Samples

The CD and thermal melting of the H18A/H19A variant are altered, when compared to wild type and K13E/R22G mutant. We hypothesized that this result is due to a different distribution of conformers in the H18A/H19A mutant, which still provide a dynamic, low affinity zinc binding site. To test this hypothesis, we used UVRR spectroscopy to measure the effect of zinc addition on Peptide P, J, and J/F, which exhibit similar CD properties when compared to Hst5.

The UVRR spectrum of Peptide J/F was obtained (Figure 6.12IIIA)**.** This peptide contains no tyrosine, but has the four histidine metal binding motif. Most of the spectral bands are readily assignable by comparison to the histidine model spectrum at pD 7.5 (Figure 6.10). In the Peptide J/F UVRR spectrum, imidazole bands are observed at 1321, 1369, and 1567 cm^{-1} and are similar to bands observed in histidine solution at pD 7.5. Zinc was added at a one to one stoichiometry to Peptide J/F, and the UVRR spectrum was obtained (Figure 6.12IIIB). At a one to one stoichiometry, a band at 1321 cm^{-1} decreases in intensity, and new bands appear at 1048 (not shown), 1200, 1287, 1350 cm^{-1}. The band at 1567 broadens and shifts to 1555 and 1575 cm^{-1}. UVRR spectra of Peptide P and J (Figure 6.12II and 6.12I) exhibited similar imidazole bands and similar zinc induced shifts.

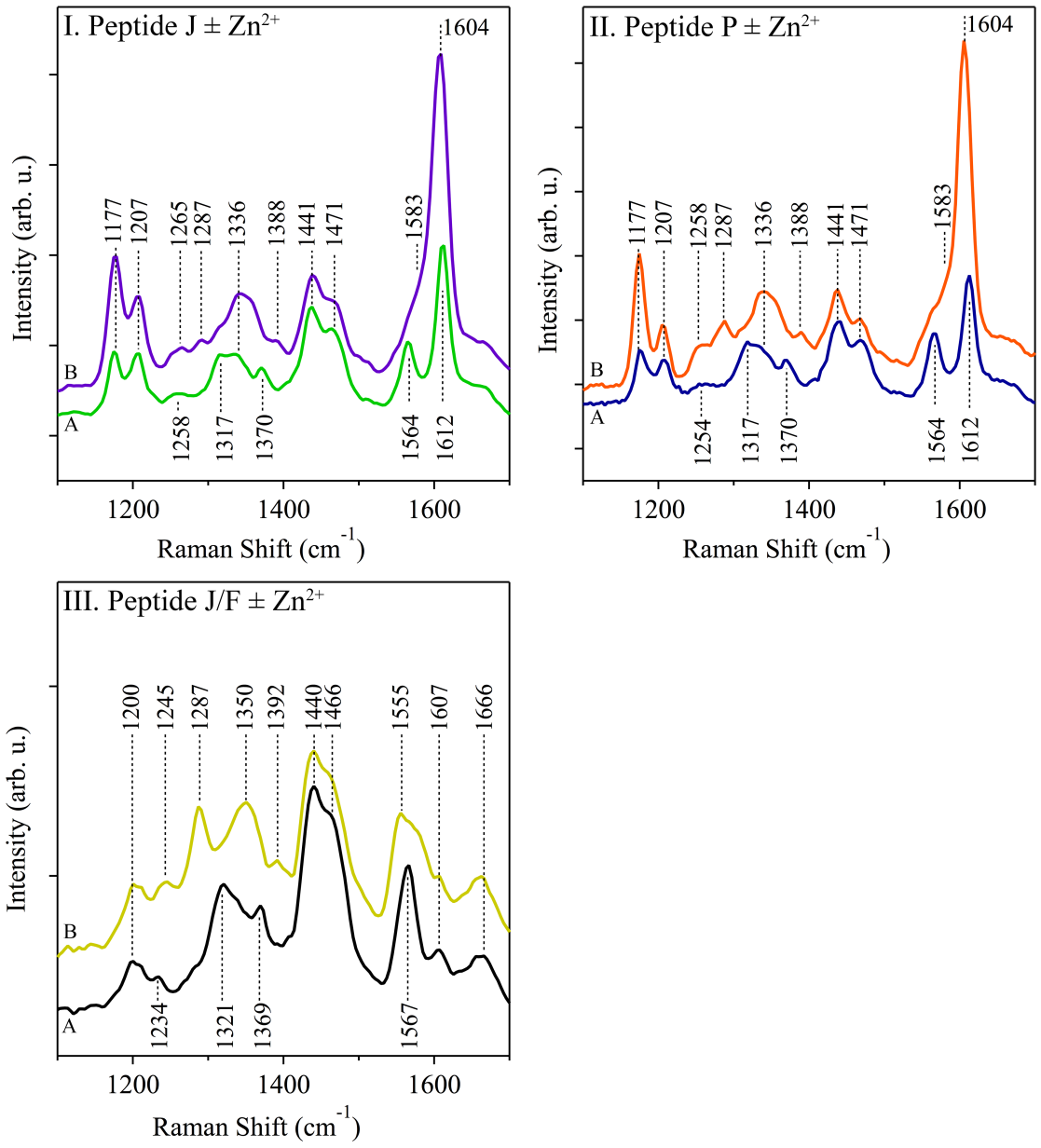

Figure 6.12 UVRR spectra of beta hairpin peptides. Samples: Peptide J (I) in the absence (A, green) or presence (B, purple) of equimolar $ZnCl_2$; Peptide P (II) in the absence (A, blue) or presence (B, orange) of equimolar $ZnCl_2$; Peptide J/F (III) in the absence (A, black) or presence (B, gold) of equimolar $ZnCl_2$. The peptide concentration was 1 mM, and the samples contained equimolar $ZnCl_2$ where noted. The buffer contained 5 mM HEPES pD 7.5. Sample was recirculated using a peristaltic pump to prevent UV damage. Laser wavelength, 244 nm; laser power, 3.4 mW; scan time, 120 s; accumulations, 4. Data were averaged from at least two independent measurements (using at least two 1 mL samples). Tick marks denote 200 intensity units.

Peptide P and J also contain a tyrosine side chain, and the UVRR spectra of these peptides exhibits bands assignable to Y5. Interestingly, the bands display zinc induced shifts, similar to the results obtained with Hst5. The tyrosine side chain is protonated at pD 7.5, and contributes to the spectrum at 848, 1177, 1207, and 1612 (Figure 6.11). With zinc addition at a one to ratio (Figure 6.12IB and 6.12IIB), a dramatic increase in intensity and small decrease in frequency for the ring stretching mode of tyrosine occurs. The tyrosinate band is now observed at 1604 cm^{-1} in the presence of zinc. The intensity increase is attributed to red shift observed of tyrosine UV band, which increases absorption at 244 nm (Figure 6.5). The frequency downshift is attributed to deprotonation and a change in the pK_a of tyrosine. The results are similar to those observed in the histatins. Experiments were conducted to evaluate if the low affinity zinc binding site in the model peptides is specific to zinc. The UVRR spectra reflected no significant change when manganese or calcium are added to a Peptide J sample in H_2O buffer (Figure 6.13). Also note that modification of the sequence to contain the four histidine or three histidine-aspartate binding site is necessary to observe these spectral changes**.** The addition of zinc to Peptide A, which contains the cross strand Y5-H14 pair, has no significant effect on the spectrum in H_2O buffer (Figure 6.14).

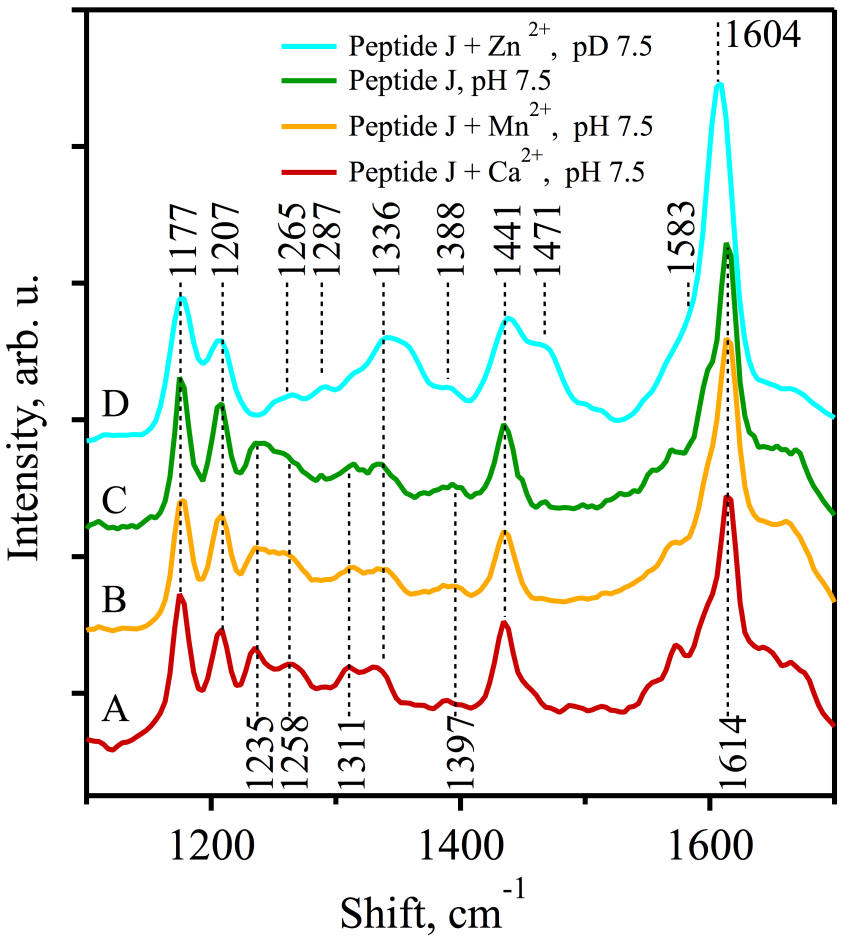

Figure 6.13 UVRR spectra of Peptide J and Ca^{2+} (A, red), Peptide J and Mn^{2+} (B, light orange) and Peptide J (C, green) at pH 7.5. In (D), Peptide J and Zn^{2+} pD 7.5 is reproduced from Figure 6 in the main text. In A-C, the peptide concentration was 1 mM, when present, the calcium and manganese concentrations were 5 mM, and the buffer contained 5 mM HEPES in H_2O (pH 7.5). In (D), the peptide concentration was 1 mM, and the sample contained equimolar Zn^{2+}. The data were averaged from at least two independent measurements. Tick marks denote 200 intensity units.

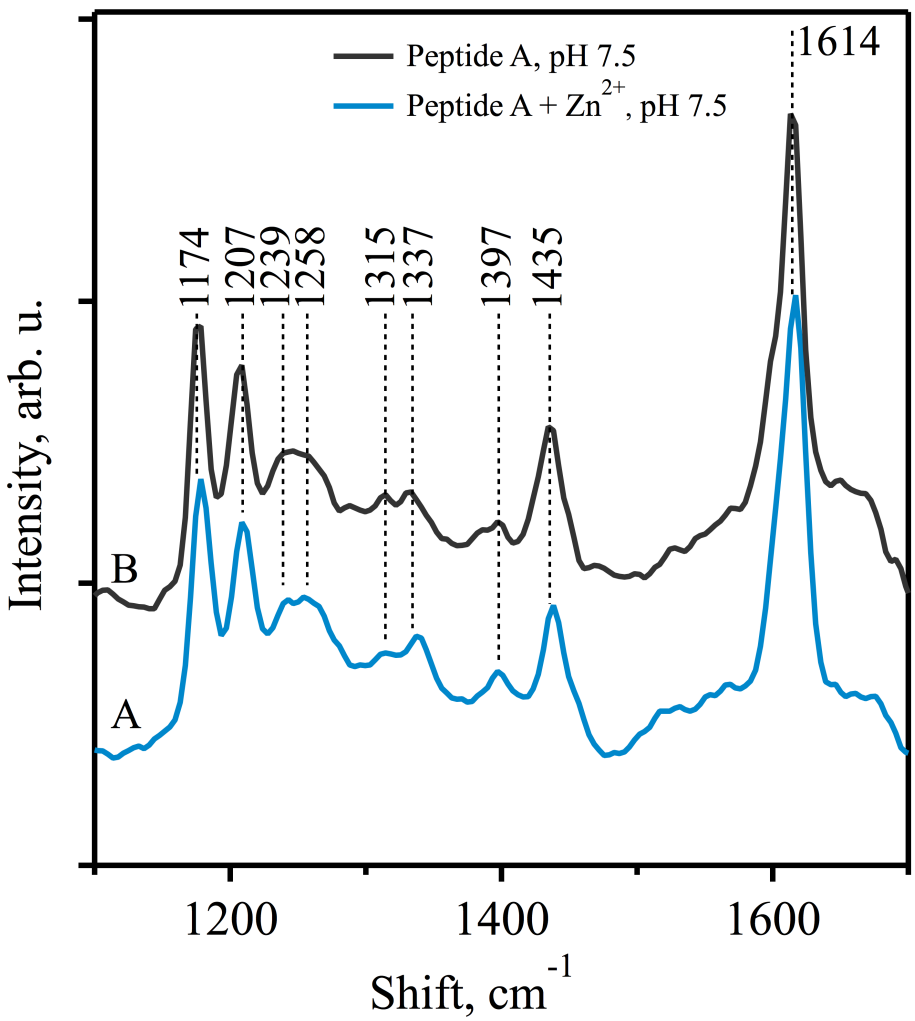

Figure 6.14 UVRR spectra of Peptide A in the presence (A, blue) or absence (B, black) of Zn^{2+} at pH 7.5. The peptide concentration was 1 mM, and the zinc concentration was 5 mM. The buffer contained 5 mM HEPES in H_2O (pH 7.5). The data were averaged from at least two independent measurements. Tick marks denote 200 intensity units.

6.5 Discussion

The histatins play an important role in human health. The oral cavity presents a site for opportunistic infections. Antimicrobial immune peptides, like Hst5, have been shown to differ in concentrations in some immunocompromised individuals. It has been shown that oral fungal infection by *Candida albicans* is increased in an HIV-positive population

that also exhibited lower salivary histatin-5 concentration.[45] Additionally, it has been observed by proteomic analysis that patients with both primary and secondary Sjögren's syndrome have lower levels of identifiable salivary histatins.[46] The Hst5 K13E/R22G and Hst5 H18A/H19A mutants significantly decrease candidacidal activity compared to wild type.[9-10] Binding of nickel, zinc, and copper is proposed to influence the activity of Hst-5. While zinc and copper are present in blood at a concentration of approximately 1 ppm,[47] in saliva, zinc is present at approximately 0.1-0.2 ppm [47-48] and copper has been measured to be approximately 2-100 ppb.[48] Incubation of Zn^{2+} and Cu^{1+} have been shown to increase the antifungal properties of the peptide.[49] Ni^{2+} is also believed to be coordinated by Hst5, though the proposed binding sites for Ni^{2+} compete with the proposed binding sites for both Zn^{2+} and Cu^{2+}. Histatin-5 could possibly be relevant for allergies to nickel.[20]

Here, we report CD and UVRR studies of Hst5 and those two sequence variants. We find that the addition of zinc to wild type Hst5 stabilizes the peptide against thermal denaturation. Further, frequency shifts are observed in characteristic Raman vands when zinc is added to wild type Hst5. These bands are assigned to the imidazole side chain by comparison to spectra of the amino acid in solution and to a family of conformationally dynamic beta hairpins. The H18/H19 mutant exhibits altered behavior with CD and thermal melting, when compared to wild type. This change is consistent with an alteration in the distribution of stable conformers in the mutant. In this H18/H19 mutant and the K13E/R22G mutant, UVRR spectroscopy reveals an electrostatic perturbation of tyrosine, which is evident as a downshift of the highe-t energy ring stretching mode. This effect is also reproduced in tyrosine-containing, zinc binding beta hairpins. We also find that the

H18A/H19A mutant loses metal specificity and appears to bind copper to a imidazole containing binding site.

Three models have been proposed for the bioactivity of histatins (reviewed in ref [7]) In one, histatins interrupt fungal mitochondrial electron transfer. In a second, histatins generate reactive oxygen species, which is toxic and antimicrobial. In a third, histatins act as membrane permeant peptides and disrupt the electrochemical gradient. Based on our results, the change in antifungal activity in H18A/H19A is most likely due to change in stability of peptide and a loss of metal specificity.

Previous studies have been conducted on Hst5 (reviewed in ref [7]) and the two mutants Hst5 K13E/R22G and Hst5 H18A/H19A. The structure of wild type Hst5 has been studied by NMR in trifluorethanol/water and DMSO/water mixtures.[23, 50] In these hydrophobic environments, the peptide adopts a helical conformation, though the peptide is considered to be disordered in purely aqueous solvent. Isothermal titration calorimetry has identified at least one binding site for Zn^{2+} and one for Cu^{2+}. The measured binding constants for the wild type peptide for Zn^{2+} and Cu^{2+} are 10^{-5} and 10^{-7} M, respectively.[51] NMR experiments on Hst5 in aqueous solvent in the presence of three equivalents of Zn^{2+} revealed a broadening of three histidine peaks along with one glutamate peak. In the presence of three equivalents of Cu^{2+}, the reduction in intensity of an aspartate resonance was apparent.[18]. Mass spectrometry characterization of Hst5 has revealed information regarding the stoichiometry of metal-binding.[32] At pH 7.5, a 2:1 ratio results in 73% relative abundance of a dicopper-Hst5 complex and 27% monocopper-Hst5.[32] For the case of 2:1 Zn^{2+}:peptide samples, only 22% of the sample was found to bind Zn^{2+}, and the stoichiometry of this complex was 1:1.[32] In sample preparations with higher Zn^{2+}:peptide

ratios, a greater percentage of the sample was found to bind at least one equivalent of Zn^{2+}.[32] This previous work also investigated the CD spectra of Hst5 in the presence of 5 equivalents of Zn^{2+} and Cu^{2+} at 25 °C, pH 7.2. In the presence of either Cu^{2+} or Zn^{2+}, the CD spectrums was altered, although the decrease in magnitude of the CD signal, noted here with zinc addition, was not observed.[32]

The peptides used here were inspired by the zinc binding sites in carbonic anhydrase[52] and superoxide dismutase.[22] Zinc binding proteins are ubiquitous in biology and can be divided into two main classes.[53] In structural zinc proteins, such as the zinc finger, the divalent ion is coordinated by cysteine and zinc.[54] In catalytic zinc proteins, such as carbonic anhydrase[52] and superoxide dismutase[22], zinc coordination involves histidine, aspartate, and active site water molecule. Peptide mimics of zinc binding peptides have been described previously, based on zinc finger cysteine/histidine motifs.[55-56] For example, CP-1 has hydrophobic core and have a dissociation constant of 10^{-7} for Co^{2+} and 10^{-12} for Zn^{2+}.[55] Peptide mimics of carbonic anhydrase, based on ZnN_3O coordination, have also been constructed.[57-58] Recently, it has been shown that heptapeptides, can form zinc-containing amyloid fibrils and catalyze the hydrolysis of esters, in a manner similar to carbonic anhydrase.[59-60] The K_M was 1.8 mM.[59] A similar strategy has beeinx used to introduce a specific zinc binding site into a 16-mer beta hairpin[61] and a octapeptide[62]. Zinc coordination was verified by metal induced changes in the CD spectrum and by NMR spectroscopy.[61-62]

Previous studies of Cu/Zn containing superoxide dismutase (SOD) and its relevant model compounds have shown that D_2O exchange intensifies UVRR bands of histidine and makes them more easily detectable at 229 nm and [42-43] 240 nm [44] In SOD, the Cu ion

is coordinated by four histidine residues, and the Zn ion is coordinated by three histidine residues and one aspartic acid residue. Among the coordinated histidines, His61 has a unique imidazolate structure (His-) and bridges between copper and zinc.[63-64] The UVRR spectrum of SOD reveals characteristic changes with metal binding in bands assignable to Cu-His, Zn-His, and the bridging His61.[63]

In the case of SOD wild type, the bridging imidazolate His61 has been assigned to the UVRR bands observed at 986 cm^{-1}, 1050 cm^{-1}, 1282 cm^{-1}, 1292 cm^{-1}, and 1564 cm^{-1}. [42] In the apoenzyme, these frequencies are not observed. [42] Additional histidine-zinc vibrational bands at 1360 cm^{-1} and 1396 cm^{-1} are perturbed in the apoenzyme as well. [42] Histidine-metal bands at approximately 1340 cm^{-1} are downshifted to approximately 1320 cm^{-1} in the apo complex. [42] The normal mode assignments have been described previously. [65] Imidazolium-d_0 exhibits a ring expansion and N-H wag 1322 cm^{-1} and a $C^{(+)}N$ + C-N stretch at 1590 cm^{-1}. [65] Imidazole-d_0 modes include C_2N_1 + C_5N_1 stretch + N-H wag at 1578. [65] A C-H wag is calculated to occur at 1394 cm^{-1} for imidazole-d_1. [65] Perturbation of the frequency or intensity of these histidine ring modes is consistent with metal-binding and is observed when wild type and apo SOD are compared. In SOC, there is a single tyrosine Y108, which has an elevated pK_a when metal is bound. A shift of the Y8a band was reported with metal binding.[35]

While intrinsically disordered proteins are ubiquitous (reviewed in [2-3, 66]). new paradigms are needed to link structure and function in these proteins. To model and interpret the histatin results, we employed a family of designed beta hairpin peptides, which were engineered to provide a bindig site for zinc. In beta hairpins, the formation of the antiparallel beta structure is spontaneous.[67] Beta hairpins are dynamic in solution, and

sample an ensemble of structural states.[28, 68-69] When the samples are treated with zinc, a change in the UVRR spectrum is observed, which is similar to the change observed in the histatin peptides. In addition, a change in vibrational spectrum of an adjacent tyrosine is observed, which is consistent with a decrease in its pK_a and the observed red shift of its electronic spectrum. Interesiingly, the UVRR bands are similar to the Hst5 observed here.

Designed beta hairpins also provide a promising avenue in the development of new treatments. For example, the antimicrobial peptide, arenicin, is a beta hairpin and use of analogs of the sequence as a pharmaceutical agent against Gram positive bacteria is under investigation.[70] Also, the use of beta hairpins as scaffolds to catalyze biomimetic reactions has been explored.[71] To widen the field of accessible uses and reactions, specific metal binding is a valuable goal. Because beta hairpins are often dynamic molecules, which exhibit conformational flexibility on multiple time scales, detailed structural studies are not always possible via NMR or X-ray crystallography. This is especially true for non-paramagnetic and non-chromogenic metal ions like zinc, which do not lend themselves to electron spin resonance techniques. In addition, short beta-turn-beta peptides are important in human health. For example, antimicrobial peptides of the beta hairpin family are components of the innate immune system.[72] An example is defensin, which contains at least one pair of two beta strands.[73] Defensins play a role in host defense and are 18-45 amino acids in length.[74] Another example, hepcidin, is a 25 amino acid peptide, which is a regulator of iron metabolism.[75]

6.6 Conclusions

In summary, the results presented here provide new information concerning metal binding sites in intrinsically disordered peptides. A combination of spectroscopic studies of the biological sample and peptide models provides a robust framework for interpretation. The results support the conclusion that Hst5 is a conformationally dynamic peptide, with bioactive forms that are preferentially stabilized by zinc interactions. The stability of the peptide is responsive to the addition of divalent metal ions, and zinc binds to histidine residues in the peptide. The copper and zinc sites are distinct, and a loss of specificity and conformational destabilization are associated with a decrease in antimicrobial activity.

6.7 References

1. Uversky, V. N. Intrinsically Disordered Proteins and Their (Disordered) Proteomes in Neurodegenerative Disorders. *Frontiers in Aging Neuroscience* **2015,** *7*.

2. Uversky, V. N.; Oldfield, C. J.; Dunker, A. K. Intrinsically Disordered Proteins in Human Diseases: Introducing the D2 Concept. *Annu. Rev. Biophys.* **2008,** *37*, 215-246.

3. Wright, P. E.; Dyson, H. J. Intrinsically Disordered Proteins in Cellular Signalling and Regulation. *Nature Reviews Molecular Cell Biology* **2014,** *16*, 18.

4. Dunker, A. K.; Babu, M. M.; Barbar, E.; Blackledge, M.; Bondos, S. E.; Dosztányi, Z.; Dyson, H. J.; Forman-Kay, J.; Fuxreiter, M.; Gsponer, J., et al. What's in a Name? Why These Proteins Are Intrinsically Disordered. *Intrinsically Disordered Proteins* **2013,** *1*, e24157.

5. Eliezer, D. Biophysical Characterization of Intrinsically Disordered Proteins. *Current Opinion in Structural Biology* **2009,** *19*, 23-30.

6. Baker, J. M. R.; Hudson, R. P.; Kanelis, V.; Choy, W.-Y.; Thibodeau, P. H.; Thomas, P. J.; Forman-Kay, J. D. Cftr Regulatory Region Interacts with Nbd1 Predominantly Via Multiple Transient Helices. *Nature Structural &Amp; Molecular Biology* **2007,** *14*, 738.

7. Melino, S.; Santone, C.; Di Nardo, P.; Sarkar, B. Histatins: Salivary Peptides with Copper (Ii)-and Zinc (Ii)-Binding Motifs. *The FEBS journal* **2014,** *281*, 657-672.

8. Welling, M. M.; Brouwer, C. P.; Veerman, E. C.; Amerongen, A. V. N. Histatin-Derived Monomeric and Dimeric Synthetic Peptides Show Strong Bactericidal Activity

Towards Multidrug-Resistant Staphylococcus Aureus in Vivo. *Antimicrobial agents and chemotherapy* **2007,** *51*, 3416-3419.

9. Tsai, H.; Bobek, L. A. Studies of the Mechanism of Human Salivary Histatin-5 Candidacidal Activity with Histatin-5 Variants and Azole-Sensitive and-Resistant Candida Species. *Antimicrobial agents and chemotherapy* **1997,** *41*, 2224-2228.

10. Tsai, H.; Raj, P. A.; Bobek, L. A. Candidacidal Activity of Recombinant Human Salivary Histatin-5 and Variants. *Infection and immunity* **1996,** *64*, 5000-5007.

11. Tsai, H.; Bobek, L. A. Human Salivary Histatin-5 Exerts Potent Fungicidal Activity against Cryptococcus Neoformans. *Biochimica et Biophysica Acta (BBA)-General Subjects* **1997,** *1336*, 367-369.

12. Imatani, T.; Kato, T.; Minaguchi, K.; Okuda, K. Histatin 5 Inhibits Inflammatory Cytokine Induction from Human Gingival Fibroblasts by Porphyromonas Gingivalis. *Oral microbiology and immunology* **2000,** *15*, 378-382.

13. Sabatini, L.; Azen, E. Histatins, a Family of Salivary Histidine-Rich Proteins, Are Encoded by at Least Two Loci (His1 and His2). *Biochemical and biophysical research communications* **1989,** *160*, 495-502.

14. Troxler, R.; Offner, G.; Xu, T.; Vanderspek, J.; Oppenheim, F. Structural Relationship between Human Salivary Histatins. *Journal of Dental Research* **1990,** *69*, 2-6.

15. Oppenheim, F.; Xu, T.; McMillian, F.; Levitz, S.; Diamond, R.; Offner, G.; Troxler, R. Histatins, a Novel Family of Histidine-Rich Proteins in Human Parotid Secretion. Isolation, Characterization, Primary Structure, and Fungistatic Effects on Candida Albicans. *Journal of Biological Chemistry* **1988,** *263*, 7472-7477.

16. Cabras, T.; Fanali, C.; Monteiro, J. A.; Amado, F.; Inzitari, R.; Desiderio, C.; Scarano, E.; Giardina, B.; Castagnola, M.; Messana, I. Tyrosine Polysulfation of Human Salivary Histatin 1. A Post-Translational Modification Specific of the Submandibular Gland. *Journal of proteome research* **2007,** *6*, 2472-2480.

17. Abreu, I. A.; Cabelli, D. E. Superoxide Dismutases—a Review of the Metal-Associated Mechanistic Variations. *Biochimica et Biophysica Acta (BBA) - Proteins and Proteomics* **2010,** *1804*, 263-274.

18. Grogan, J.; McKnight, C. J.; Troxler, R. F.; Oppenheim, F. G. Zinc and Copper Bind to Unique Sites of Histatin 5. *FEBS letters* **2001,** *491*, 76-80.

19. Tay, W. M.; Hanafy, A. I.; Angerhofer, A.; Ming, L.-J. A Plausible Role of Salivary Copper in Antimicrobial Activity of Histatin-5—Metal Binding and Oxidative Activity of Its Copper Complex. *Bioorganic & Medicinal Chemistry Letters* **2009,** *19*, 6709-6712.

20. Kurowska, E.; Bonna, A.; Goch, G.; Bal, W. Salivary Histatin-5, a Physiologically Relevant Ligand for Ni(Ii) Ions. *Journal of Inorganic Biochemistry* **2011,** *105*, 1220-1225.

21. Rydengård, V.; Nordahl, E. A.; Schmidtchen, A. Zinc Potentiates the Antibacterial Effects of Histidine-Rich Peptides against Enterococcus Faecalis. *The FEBS journal* **2006,** *273*, 2399-2406.

22. Tainer, J. A.; Getzoff, E. D.; Beem, K. M.; Richardson, J. S.; Richardson, D. C. Determination and Analysis of the 2 Å Structure of Copper, Zinc Superoxide Dismutase. *Journal of molecular biology* **1982,** *160*, 181-217.

23. Melino, S.; Rufini, S.; Sette, M.; Morero, R.; Grottesi, A.; Paci, M.; Petruzzelli, R. Zn2+ Ions Selectively Induce Antimicrobial Salivary Peptide Histatin-5 to Fuse Negatively Charged Vesicles. Identification and Characterization of a Zinc-Binding Motif Present in the Functional Domain. *Biochemistry* **1999,** *38*, 9626-9633.

24. Raj, P. A.; Marcus, E.; Sukumaran, D. K. Structure of Human Salivary Histatin 5 in Aqueous and Nonaqueous Solutions. *Biopolymers: Original Research on Biomolecules* **1998,** *45*, 51-67.

25. Sibert, R.; Josowicz, M.; Porcelli, F.; Veglia, G.; Range, K.; Barry, B. A. Proton-Coupled Electron Transfer in a Biomimetic Peptide as a Model of Enzyme Regulatory Mechanisms. *J Am Chem Soc* **2007,** *129*, 4393-400.

26. Sibert, R. S.; Josowicz, M.; Barry, B. A. Control of Proton and Electron Transfer in De Novo Designed, Biomimetic Beta Hairpins. *ACS Chem Biol* **2010,** *5*, 1157-68.

27. Pagba, C. V.; Barry, B. A. Redox-Induced Conformational Switching in Photosystem-Ii-Inspired Biomimetic Peptides: A Uv Resonance Raman Study. *J. Phys. Chem. B* **2012,** *116*, 10590-9.

28. Hwang, H.; Tyler G. McCaslin; Pagba, C. V.; Nevin, C. M.; Pavlova, A.; Barry, B. A.; Gumbart, J. C. Redox-Driven Conformational Dynamics in a Photosystem-Ii-Inspired B-Hairpin Maquette Determined through Spectroscopy and Simulation. *J. Phys. Chem. B* **2017,** *121*, 3536-3545.

29. Jenson, D. L.; Barry, B. A. Proton-Coupled Electron Transfer in Photosystem Ii: Proton Inventory of a Redox Active Tyrosine. *J Am Chem Soc* **2009,** *131*, 10567-73.

30. Chen, J.; Barry, B. Ultraviolet Resonance Raman Microprobe Spectroscopy of Photosystem Ii. *Photochem. Photobiol.* **2008,** *84*, 815-818.

31. Maupetit, J.; Derreumaux, P.; Tuffery, P. Pep-Fold: An Online Resource for De Novo Peptide Structure Prediction. *Nucleic Acids Res* **2009,** *37*, W498-503.

32. Brewer, D.; Lajoie, G. Evaluation of the Metal Binding Properties of the Histidine-Rich Antimicrobial Peptides Histatin 3 and 5 by Electrospray Ionization Mass Spectrometry. *Rapid Communications in Mass Spectrometry* **2000,** *14*, 1736-1745.

33. Alberts, I. L.; Nadassy, K.; Wodak, S. J. Analysis of Zinc Binding Sites in Protein Crystal Structures. *Protein Science* **1998,** *7*, 1700-1716.

34. Barry, B. A.; Chen, J.; Keough, J.; Jenson, D. L.; Offenbacher, A. R.; Pagba, C. V. Proton Coupled Electron Transfer and Redox Active Tyrosines: Structure and Function of the Tyrosyl Radicals in Ribonucleotide Reductase and Photosystem Ii. *J. Phys. Chem. Lett.* **2012,** *3*, 543-554.

35. Wang, D.; Zhao, X.; Vargek, M.; Spiro, T. G. Metal-Bound Histidine Modes in Uv Resonance Raman Spectra of Cu, Zn Superoxide Dismutase. *Journal of the American Chemical Society* **2000,** *122*, 2193-2199.

36. Hashimoto, S.; Ono, K.; Takeuchi, H. Uv Resonance Raman Scattering from Metal-Coordinating Histidine Residues in Cu, Zn-Superoxide Dismutase. *Journal of Raman spectroscopy* **1998,** *29*, 969-975.

37. Caswell, D. S.; Spiro, T. G. Ultraviolet Resonance Raman Spectroscopy of Imidazole, Histidine, and Cu(Imidazole)$_4^{2+}$: Implications for Protein Studies. *Journal of the American Chemical Society* **1986,** *108*, 6470-6477.

38. Ashikawa, I.; Itoh, K. Raman Spectra of Polypeptides Containing L-Histidine Residues and Tautomerism of Imidazole Side Chain. *Biopolymers: Original Research on Biomolecules* **1979,** *18*, 1859-1876.

39. Miura, T.; Satoh, T.; Hori-i, A.; Takeuchi, H. Raman Marker Bands of Metal Coordination Sites of Histidine Side Chains in Peptides and Proteins. *Journal of Raman Spectroscopy* **1998,** *29*, 41-47.

40. Barry, B. A. Reaction Dynamics and Proton Coupled Electron Transfer: Studies of Tyrosine-Based Charge Transfer in Natural and Biomimetic Systems. *Biochim. Biophys. Acta* **2015,** *1847*, 46-54.

41. Hashimoto, S.; Ono, K.; Takeuchi, H. Uv Resonance Raman Scattering from Metal-Coordinating Histidine Residues in Cu,Zn-Superoxide Dismutase. *J. Raman Spec.* **1998,** *29*, 969-975.

42. Wang, D. J.; Zhao, X. J.; Vargek, M.; Spiro, T. G. Metal-Bound Histidine Modes in Uv Resonance Raman Spectra of Cu, Zn Superoxide Dismutase. *J Am Chem Soc* **2000,** *122*, 2193-2199.

43. Zhao, X.; Wang, D.; Spiro, T. G. Detection of Metal-Bound Histidine in Ultraviolet Resonance Raman Spectra: Superoxide Dismutase. *Inorg. Chem.* **1998,** *37*, 5414-5415.

44. Hashimoto, S.; Ohsaka, S.; Takeuchi, H.; Harada, I. Ultraviolet Resonance Raman-Spectra of Cu,Zn-Superoxide Dismutase - Detection of an Imidazolate Bridge between the Metal-Ions in Solution. *J. Am. Chem. Soc.* **1989,** *111*, 8926-8928.

45. Torres, S. R.; Garzino-Demo, A.; Meiller, T. F.; Meeks, V.; Jabra-Rizk, M. A. Salivary Histatin-5 and Oral Fungal Colonisation in Hiv+ Individuals. *Mycoses* **2009,** *52*, 11-15.

46. Peluso, G.; De Santis, M.; Inzitari, R.; Fanali, C.; Cabras, T.; Messana, I.; Castagnola, M.; Ferraccioli, G. F. Proteomic Study of Salivary Peptides and Proteins in Patients with Sjögren's Syndrome before and after Pilocarpine Treatment. *Arthritis & Rheumatism* **2007,** *56*, 2216-2222.

47. Lane, H. W.; Warren, D. C.; Squyres, N. S.; Cotham, A. C. Zinc Concentrations in Hair, Plasma, and Saliva and Changes in Taste Acuity of Adults Supplemented with Zinc. *Biological Trace Element Research* **1982,** *4*, 83-93.

48. Ayinampudi, B.; Narsimhan, M. Salivary Copper and Zinc Levels in Oral Pre-Malignant and Malignant Lesions. *Journal of Oral and Maxillofacial Pathology* **2012,** *16*, 178-182.

49. Conklin, S. E.; Bridgman, E. C.; Su, Q.; Riggs-Gelasco, P.; Haas, K. L.; Franz, K. J. Specific Histidine Residues Confer Histatin Peptides with Copper-Dependent Activity against Candida Albicans. *Biochemistry* **2017,** *56*, 4244-4255.

50. Brewer, D.; Hunter, H.; Lajoie, G. Nmr Studies of the Antimicrobial Salivary Peptides Histatin 3 and Histatin 5 in Aqueous and Nonaqueous Solutions. *Biochemistry and cell biology* **1998,** *76*, 247-256.

51. Gusman, H.; Lendenmann, U.; Grogan, J.; Troxler, R. F.; Oppenheim, F. G. Is Salivary Histatin 5 a Metallopeptide? *Biochimica et Biophysica Acta (BBA) - Protein Structure and Molecular Enzymology* **2001,** *1545*, 86-95.

52. Eriksson, A. E.; Jones, T. A.; Liljas, A. Refined Structure of Human Carbonic Anhydrase Ii at 2.0 Å Resolution. *Proteins: Structure, Function, and Bioinformatics* **1988,** *4*, 274-282.

53. Karlin, S.; Zhu, Z.-Y. Classification of Mononuclear Zinc Metal Sites in Protein Structures. *Proceedings of the National Academy of Sciences* **1997,** *94*, 14231-14236.

54. Laity, J. H.; Lee, B. M.; Wright, P. E. Zinc Finger Proteins: New Insights into Structural and Functional Diversity. *Current Opinion in Structural Biology* **2001,** *11*, 39-46.

55. Krizek, B. A.; Amann, B. T.; Kilfoil, V. J.; Merkle, D. L.; Berg, J. M. A Consensus Zinc Finger Peptide: Design, High-Affinity Metal Binding, a Ph-Dependent Structure, and a His to Cys Sequence Variant. *Journal of the American Chemical Society* **1991,** *113*, 4518-4523.

56. Kim, C. A.; Berg, J. M. Thermodynamic B -Sheet Propensities Measured Using a Zinc-Finger Host Peptide. *Nature* **1993,** *362*, 267-270.

57. Cangelosi, V. M.; Deb, A.; Penner-Hahn, J. E.; Pecoraro, V. L. A De Novo Designed Metalloenzyme for the Hydration of Co2. *Angewandte Chemie* **2014,** *126*, 8034-8037.

58. Zastrow, M. L.; Peacock, A. F. A.; Stuckey, J. A.; Pecoraro, V. L. Hydrolytic Catalysis and Structural Stabilization in a Designed Metalloprotein. *Nature Chemistry* **2011,** *4*, 118.

59. Rufo, C. M.; Moroz, Y. S.; Moroz, O. V.; Stöhr, J.; Smith, T. A.; Hu, X.; DeGrado, W. F.; Korendovych, I. V. Short Peptides Self-Assemble to Produce Catalytic Amyloids. *Nature Chemistry* **2014,** *6*, 303.

60. Lee, M.; Wang, T.; Makhlynets, O. V.; Wu, Y.; Polizzi, N. F.; Wu, H.; Gosavi, P. M.; Stöhr, J.; Korendovych, I. V.; DeGrado, W. F., et al. Zinc-Binding Structure of a Catalytic Amyloid from Solid-State Nmr. *Proceedings of the National Academy of Sciences* **2017,** *114*, 6191-6196.

61. Platt, G.; Chung, C.-W.; Searle, M. S. Design of Histidine-Zn^{2+} Binding Sites within a B-Hairpin Peptide: Enhancement of B-Sheet Stability through Metal Complexation. *Chem. Commun.* **2001**, 1162-1163.

62. Imperiali, B.; Kapoor, T. M. The Reverse Turn as a Template for Metal Coordination. *Tetrahedron* **1993,** *49*, 3501-3510.

63. Tainer, J. A.; Getzoff, E. D.; Richardson, J. S.; Richardson, D. C. Structure and Mechanism of Copper, Zinc Superoxide Dismutase. *Nature* **1983,** *306*, 284-287.

64. Ascone, I.; Castañer, R.; Tarricone, C.; Bolognesi, M.; Stroppolo, M. E.; Desideri, A. Evidence of His61 Imidazolate Bridge Rupture in Reduced Crystalline Cu,Zn Superoxide Dismutase. *Biochemical and Biophysical Research Communications* **1997,** *241*, 119-121.

65. Markham, L. M.; Mayne, L. C.; Hudson, B. S.; Zgierski, M. Z. Resonance Raman Studies of Imidazole, Imidazolium, and Their Derivatives: The Effect of Deuterium Substitution. *Journal of Physical Chemistry* **1993,** *97*, 10319-10325.

66. Oldfield, C. J.; Dunker, A. K. Intrinsically Disordered Proteins and Intrinsically Disordered Protein Regions. *Annual Review of Biochemistry* **2014,** *83*, 553-584.

67. Jang, S.; Shin, S.; Pak, Y. Molecular Dynamics Study of Peptides in Implicit Water: Ab Initio Folding of B-Hairpin, B-Sheet, and Bβα-Motif. *Journal of the American Chemical Society* **2002,** *124*, 4976-4977.

68. Constantine, K. L.; Mueller, L.; Andersen, N. H.; Tong, H.; Wandler, C. F.; Friedrichs, M. S.; Bruccoleri, R. E. Structural and Dynamic Properties of A. Beta.-Hairpin-Forming Linear Peptide. 1. Modeling Using Ensemble-Averaged Constraints. *Journal of the American Chemical Society* **1995,** *117*, 10841-10854.

69. Garcia, A. E.; Sanbonmatsu, K. Y. Exploring the Energy Landscape of a B Hairpin in Explicit Solvent. *Proteins: Structure, Function, and Bioinformatics* **2001,** *42*, 345-354.

70. Panteleev, P. V.; Bolosov, I. A.; Balandin, S. V.; Ovchinnikova, T. V. Design of Antimicrobial Peptide Arenicin Analogs with Improved Therapeutic Indices. *Journal of Peptide Science* **2015,** *21*, 105-113.

71. Matsumoto, M.; Lee, S. J.; Waters, M. L.; Gagné, M. R. A Catalyst Selection Protocol That Identifies Biomimetic Motifs from B-Hairpin Libraries. *Journal of the American Chemical Society* **2014,** *136*, 15817-15820.

72. Ganz, T. The Role of Antimicrobial Peptides in Innate Immunity1. *Integrative and Comparative Biology* **2003,** *43*, 300-304.

73. Ganz, T. Defensins: Antimicrobial Peptides of Innate Immunity. *Nature Reviews Immunology* **2003,** *3*, 710.

74. Lehrer, R. I.; Lu, W. A-Defensins in Human Innate Immunity. *Immunological Reviews* **2012,** *245*, 84-112.

75. Ganz, T. Hepcidin, a Key Regulator of Iron Metabolism and Mediator of Anemia of Inflammation. *Blood* **2003,** *102*, 783-788.